The role of the Southern Ocean in past global biogeochemical cycling

Anne Morée

Thesis for the degree of Philosophiae Doctor (PhD)
University of Bergen, Norway
2020

UNIVERSITY OF BERGEN

The role of the Southern Ocean in past global biogeochemical cycling

Anne Morée

Thesis for the degree of Philosophiae Doctor (PhD)

at the University of Bergen

Date of defense: 27.04.2020

Year: 2020

Title: The role of the Southern Ocean in past global biogeochemical cycling

Name: Anne Morée

Print: Skipnes Kommunikasjon / University of Bergen

Scientific environment

The doctoral research presented in this work was carried out at The Geophysical Institute of the University of Bergen (UoB). Climate research at the Geophysical Institute is brought together with NORCE Climate, the Nansen Environmental and Remote Sensing Center and the Institute for Marine Research in the Bjerknes Centre for Climate Research (BCCR). This cooperation provides a Bergen-based community of around 200 climate scientists, in which I found advice and support throughout my PhD. More specifically, I have been part of the research theme that studies the Carbon System at the BCCR, where approximately 50 researchers across the four different institutes are gathered. On the national level, I was able to participate at The Norwegian Research School in Climate Dynamics (ResClim) and The Norwegian Research School on Changing Climates in the coupled Earth System (CHESS) (partly organized and funded by BCCR). The SciSnack group, the writing group that writes brief popular science articles at BCCR, taught me many valuable lessons about writing. Internationally, I have built a network and received invaluable input for this study, made possible by the generous funding from UiB and others. I am particularly thankful for the opportunity to stay at ETH Zürich for 4 months, the chance to participate in the Advanced Course for Climate Dynamics (ACDC) 2018, as well as the possibility to attend three major international conferences over the course of the doctoral research (10th International Carbon Dioxide Conference 2017, Gordon Research School and Conference on Polar Science 2018, American Geophysical Union Fall Meeting 2019). For my modelling work, I received plentiful computational and storage resources through UNINETT Sigma2 - the National Infrastructure for High Performance Computing and Data Storage in Norway (project numbers ns2980k and ns2345k).

Acknowledgements

This thesis would not have been where it is now if it had not been for the support of many. Thank you for reading this work – I encourage you to read more of it.

First, the community at the Bjerknes Centre and the Geophysical Institute has made me feel welcome from the start and provided me with countless opportunities to grow, learn and build a network. I expect that having people gathered under one roof from so many different Earth science disciplines and cultural backgrounds will be valuable for many in the future too. I particularly want to thank Kakeklubben (the cake club to practice Norwegian) and hope they will continue being a fun and welcoming environment with great cake.

Thank you to my supervisors; Christoph, Jörg and Mario. Thank you Christoph, for always being available for questions and advice, for keeping me from getting distracted too much, and for patiently giving me the time I needed when I had to interrupt my research. You were invaluable to keep an eye on the bigger picture. Thank you Jörg, for the many hours of teaching me HAMOCC and NorESM, for being patient and positive and for consistently making an effort to give detailed feedback on my work - and always ask some tricky questions. Thank you Mario for being there from Bremerhaven and checking up on my progress – I wish we had been able to work together more. It has been great to have you all as a supervisor and I hope there will be many upcoming PhD students as lucky as I have been.

There are many people to name outside of work, too: those who could get my mind off work (BSI Seiling-folk, and in specific the trips on Albin Express boat Schmelnick), those providing a listening ear (you know), and those lovely people I regularly shared dinners with (Wednesday dinner). Big thanks also to my Dutch friends and family, who have kept in contact by video calling and/or visits to Bergen - despite the rain.

And, thank you to my fantastic partner Wouter. Dankjewel voor de steun die je me hebt gegeven de afgelopen zes jaar. Ik had dit avontuur niet zonder je willen ondernemen. Op nog vele avonturen samen. Skål!


The Southern Ocean

Abstract

This thesis describes several recent advances on the role of the Southern Ocean in past global biogeochemical cycling. We focus on the ocean of the Last Glacial Maximum (LGM) and the Pleistocene epoch and apply proxies of long-term climate variability (particularly the deep-sea sediment records of $\delta^{13}C$ and $\delta^{18}O$). Specifically, we aim to explore how the physical and biogeochemical state of the Southern Ocean influenced past global marine tracer distributions, such that we can better interpret proxy data and improve our understanding of the drivers of long-term climate variability.

The focus on the ocean realm is motivated by the large carbon reservoir in the (deep) ocean, which is able to interact with the atmosphere and govern atmospheric pCO_2 on millennial timescales – particularly through Southern Ocean processes. The LGM and Pleistocene represent the most recent glacial extreme and glacial-interglacial cycles, respectively. Therefore, relatively many proxy data are available, and their recorded climate variability is likely indicative of long-term natural climate variability.

We applied global ocean models of different complexities (NorESM-OC, HAMOCC2s and TMI) to study the drivers that shape the benthic $\delta^{13}C$ and $\delta^{18}O$ records. Applying these, we studied the role of the Southern Ocean in shaping vertical marine $\delta^{13}C$ gradients (Paper I), as well as its contribution to the $\delta^{18}O$ archive of glacial-interglacial cycles (Paper IV) using idealized model experiments. Besides these, the LGM ocean and its circulation and biological changes are studied to reveal and explore their relative importance in a more complex model setup (NorESM-OC; Papers II and III).

A central conclusion of this thesis is that knowledge of the relevant water mass end-member characteristics is fundamental for interpretation of the benthic $\delta^{13}C$ and $\delta^{18}O$ records. We show that Southern source waters (waters originating in the Southern Ocean) have a particularly large potential to influence the records of both $\delta^{13}C$ and $\delta^{18}O$, through changes in the biogeochemical or physical state of the Southern Ocean. We find that biogeochemical changes in the Southern Ocean (of particularly air-sea gas

exchange and nutrient utilisation) have the potential to affect $\delta^{13}C$ globally and with a magnitude relevant for global $\delta^{13}C$ deep-sea records (Paper I). Such major biogeochemical changes are indeed implied by the estimated near doubling of the global mean biological carbon pump efficiency required to satisfy LGM proxy records of $\delta^{13}C$, besides the changes in ocean circulation (Papers II and III). Last, Southern source water characteristics are also highly relevant for deep-sea $\delta^{18}O$ records – and have likely been incompletely archived due to interference with out-of-phase cyclic signals from Northern source water during the Early Pleistocene (Paper IV).

These findings have direct implications for the interpretation of $\delta^{13}C$ and $\delta^{18}O$ records, as well as for (paleo)-modelling efforts of global climate. Regarding the first, we see the need for increased (interdisciplinary) efforts to constrain the drivers of long-term end-member variability (Papers I-IV) as well as the need for an improved understanding of what part of the end-member signal is recorded (Paper IV). Regarding (paleo)-modelling, we anticipate that only models that contain the processes and/or components that realistically change both ocean circulation and biogeochemistry will be able to simulate long-term climate variability in satisfactory agreement with (proxy) data. Furthermore, we note that these processes and/or components are currently not (fully) represented in Earth System Models.

List of Papers

I. Morée, A. L., J. Schwinger, and C. Heinze: Southern Ocean controls of the vertical marine $\delta^{13}C$ gradient – a modelling study, Biogeosciences, 15, 7205-7223, 10.5194/bg-15-7205-2018, 2018.

II. Morée, A. L., and J. Schwinger: A Last Glacial Maximum forcing dataset for ocean modelling, Earth System Science Data Discussions, 10.5194/essd-2019-79, in review, 2019.

III. Morée, A. L., J. Schwinger, U. Ninneman, A. Jeltsch-Thömmes, I. Bethke, and C. Heinze: Evaluating the Biological Pump Efficiency of the Last Glacial Maximum Ocean using $\delta^{13}C$, submitted to Climate of the Past.

IV. Morée, A. L., T. Sun, A. Bretones, E.O. Straume, K. Nisancioglu, and G. Gebbie: Cancellation of the precessional cycle in benthic $\delta^{18}O$ records during the Early Pleistocene, under review at Geophysical Research Letters[1].

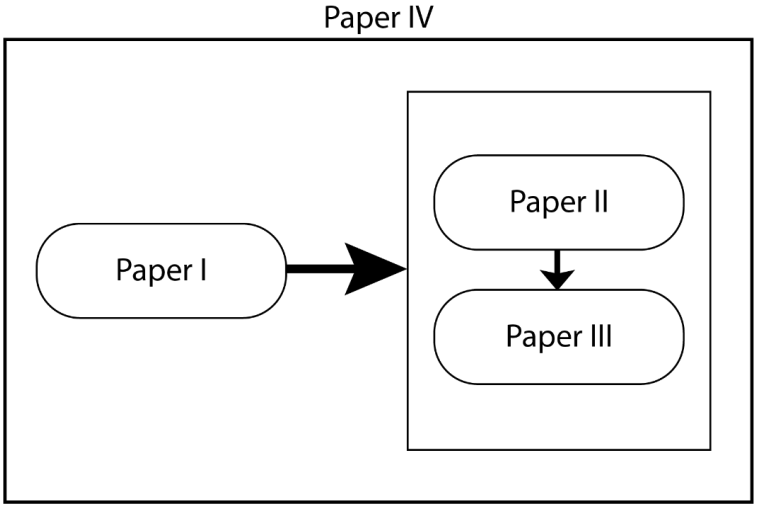

In addition, the technical description of the implementation of the carbon isotopes in NorESM-OC, as used in Paper III, is described in Tjiputra et al. (2020).

[1]Available as preprint at Earth and Space Science Open Archive (ESSOAr), 10.1002/essoar.10501616.1

Contents

Chapter 1

Introduction

1.1 (Paleo)-climatology

A central question in climate science is how the Earth System responds to changes in atmospheric CO_2 concentrations. Being a greenhouse gas, atmospheric CO_2 influences atmospheric temperatures (IPCC, 2014), and is involved in many Earth System feedbacks (Heinze et al., 2019). Atmospheric pCO_2 (pCO_2^{atm}) naturally varied by ~100 ppm over the past 800 000 years, as recorded in Antarctic ice cores (Lüthi et al., 2008). At present, land-use change and fossil emission of carbon alter the contemporary global carbon cycle (Le Quéré et al., 2018). pCO_2^{atm} is currently ~130 ppm above pre-industrial levels and increases by another ~2.5 ppm yr^{-1} (NOAA ESRL, 2019). Alongside the perturbations to the carbon cycle, other biogeochemical cycles such as those of oxygen, phosphorus and nitrogen are also affected by anthropogenic perturbations on a global scale (Ciais et al., 2013).

In order to understand these observed changes and our contributions to them, and in order to know what to expect for the 21st century (Collins et al., 2013), a major challenge is to understand the natural variability of the Earth System.

Nearly all direct observations have been made at a time where natural systems already had been perturbed. The study of past biogeochemical cycling makes it possible to extend and interpret observational records beyond the few decades of data we have from satellites and direct measurements – and hence into the natural state. In paleoclimatology, proxies such as $\delta^{13}C$ and $\delta^{18}O$ are used to represent the variable of interest (e.g., $\delta^{18}O$ and temperature). Proxy data thus replace direct observational data, under the assumption that they have recorded past climate characteristics (such as for example temperature). Proxies generally have large

uncertainties and can only be interpreted if the relationship between the variable of interest and the proxy is well understood. Continuous proxy-based reconstructions of past climate variability are available for up to hundreds of thousands of years back in time - for example for pCO_2^{atm} (Zhang et al., 2019), sea surface temperatures (McClymont et al., 2013), ice sheet volume (Elderfield et al., 2012) and past nutrient distributions (Marchitto and Broecker, 2006). Particularly $\delta^{18}O$ and $\delta^{13}C$ records, obtained from ice cores and/or deep-sea sediments, have provided much information about past climate and natural climate variability. Global benthic stacks of $\delta^{18}O$ (globally compiled $\delta^{18}O$ records from different deep-sea sediment cores) for example reveal the natural cyclic behaviour of the climate system, and glacial-interglacial cycles (Fig. 1) (Ahn et al., 2017; Lisiecki and Raymo, 2005).

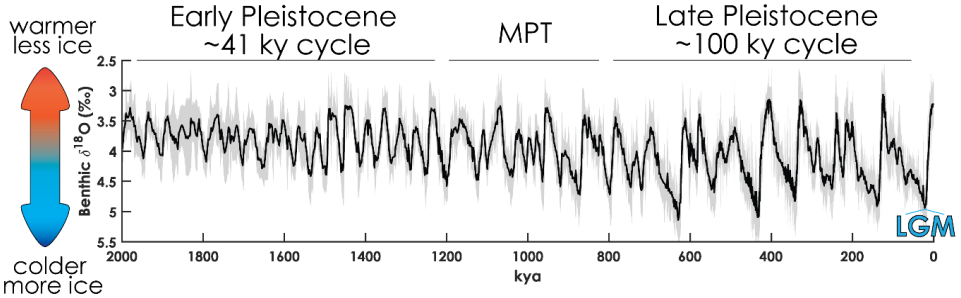

Figure 1 Probabilistic stack of 180 benthic $\delta^{18}O$ records, shown from 2 Mya to the LGM and the last deglaciation, including the 95% confidence interval in grey shading (Ahn et al., 2017). The three distinct phases of the Pleistocene (Early Pleistocene, Mid Pleistocene Transition and the Late Pleistocene) are indicated.

The peak of the most recent glacial period, the LGM (~21 kya), was a time when sea level was ~120 meters lower (Peltier and Fairbanks, 2006), land carbon storage profoundly less (Jeltsch-Thömmes et al., 2019), pCO_2^{atm} ~100 ppm lower (EPICA Project Members, 2004) and ocean circulation different from today (Adkins, 2013). The LGM is the most recent example of a vastly different climate state, and is extensively studied in order to understand the relative importance of governing processes - without obtaining a complete consensus thus far. The studies principally all revolve around one main question: What drove the ~100 ppm lower pCO_2^{atm} in the LGM as compared to pre-industrial times? This synthesis, and its underlying articles

at the end of the thesis, contribute to several central questions in paleoclimatology (Chapter Motivation and Objectives): It addresses the interpretation and sensitivity of the (marine) $\delta^{13}C$ (Papers I and III) and $\delta^{18}O$ (Paper IV) proxies, and the state and role of the ocean in the LGM (Papers II and III). In the remainder of this introductory section, the (past) ocean is introduced, and in specific the Southern Ocean. Last, the basic principles of the proxies $\delta^{13}C$ and $\delta^{18}O$ are described, useful as a broader introduction to Papers I, III and IV.

1.2 (Paleo)-oceanography

The ocean is the largest reservoir of carbon available for interaction with the atmosphere on millennial timescales, and contains ~38 000 Gt of dissolved inorganic carbon (Fig. 2). As a comparison, this is at least ~20 times more carbon than what is left in global fossil reserves (Fig. 2). 1 ppm pCO_2^{atm} equals about 2.13 Gt C, revealing the enormous potential of the ocean to influence pCO_2^{atm} – *if* carbon is transferred between the ocean and atmosphere. In addition, the ocean acts as a major heat reservoir – for example taking up ~93% of the excess (anthropogenic) heat (Rhein et al., 2013).

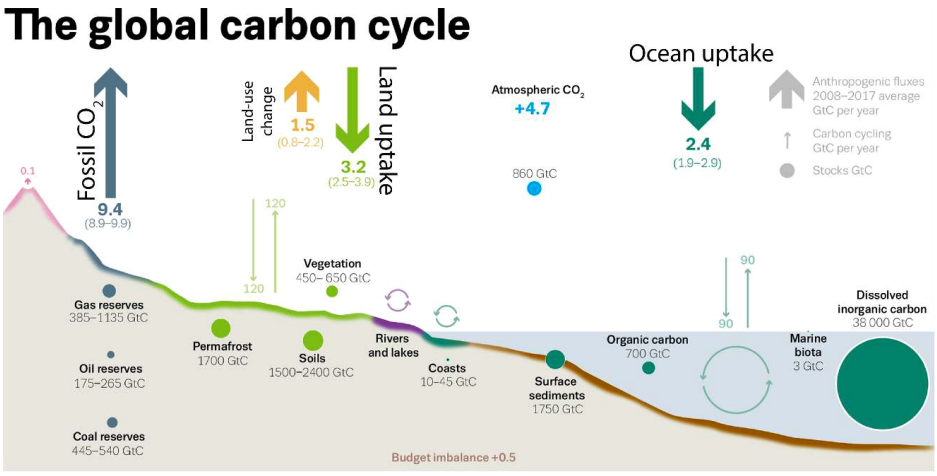

Figure 2 The contemporary global carbon cycle and carbon reservoirs, as estimated in the Global Carbon Budget 2018 (republished and adjusted with permission from Le Quéré et al., 2018). As shown, 'anthropogenic' carbon remains for ~45% in the atmosphere, while ~25% is taken up by the oceans, and ~30% is taken up by the land biosphere.

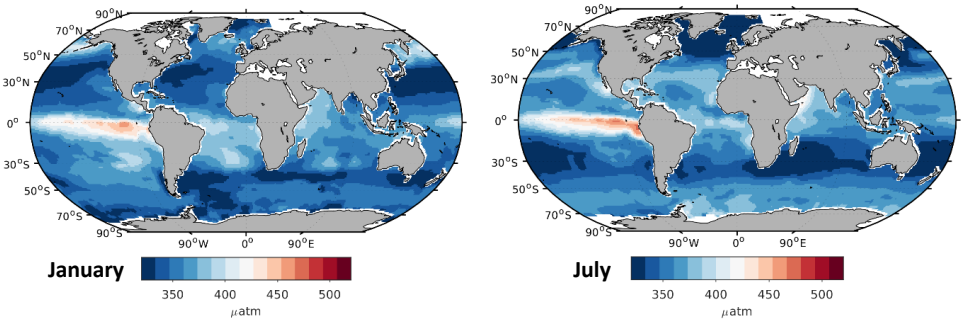

Figure 3 Contemporary surface ocean pCO_2 (climatology for the years 1985-present from Landschützer et al. (2017)), for the months January and July. The graph diverges at 420 ppm (approximate pCO_2^{atm}). Blue indicates regions where the ocean is a sink for pCO_2^{atm}, while red indicates a source region.

Indeed, about 25% of the extra carbon released by human activities is taken up by the oceans, while ~45% remains in the atmosphere and ~30% is taken up by the land biosphere (Fig. 2) (Le Quéré et al., 2018). The Southern Ocean takes up ~40% of the anthropogenic carbon emissions that enter the ocean on average, although its exact share varies significantly on seasonal, annual and decadal timescales (Takahashi et al., 2012; Gruber et al., 2019). The air-sea exchange of carbon is governed by four different carbon pumps that influence surface ocean pCO_2 and thereby the air-to-sea pCO_2 gradient and transfer: the solubility pump, the biological soft-tissue pump, the biological $CaCO_3$ counter-pump (Heinze et al., 1991; Volk and Hoffert, 1985) and the carbon pump related to ocean circulation (Levy et al., 2013). Therefore, some oceanic regions are sources of carbon to the atmosphere, while other regions behave as sinks (see Fig. 3 for the contemporary ocean). Due to variations in the relative importance of the carbon pumps, the exchange between the atmosphere and ocean varies in space and time.

Net exchange between the marine and atmospheric carbon reservoirs also played a key role in the ~100-ppm glacial-interglacial pCO_2^{atm} variability (Broecker, 1982a; Sigman et al., 2010; Broecker and Peng, 1986). The oceans must have stored extra carbon during glacials, as pCO_2^{atm} was lowered and the land carbon reservoir was likely smaller during glacials than during interglacials (Jeltsch-Thömmes et al., 2019).

On geological timescales (beyond 1000-10000 yrs), also $CaCO_3$ compensation in marine sediments and weathering of rocks play a role in the global carbon cycle. The relative importance of physical changes (e.g., ocean circulation + solubility) and biological changes (e.g., export production, remineralisation rates) in glacial-interglacial pCO_2^{atm} variability is still under debate. However, there is consensus that both must have played a role, as neither can solely explain the full variability observed in $\delta^{13}C$, $\delta^{18}O$ or other proxy records (Ganopolski and Brovkin, 2017; Buchanan et al., 2016; Bouttes et al., 2011).

Model and observational studies show that, of all ocean regions, the Southern Ocean has the greatest potential to influence pCO_2^{atm} (Sigman et al., 2010; Gruber et al., 2019; Toggweiler, 1999; Watson and Naveira Garabato, 2006). Moreover, the Southern Ocean has a major influence on lower-latitude nutrient concentrations (Marinov et al., 2006; Primeau et al., 2013; Sarmiento et al., 2004). Therefore, this work focuses on the role of the Southern Ocean in global biogeochemical cycling.

1.3 The Southern Ocean

The Southern Ocean remains a region of many unknowns due to sparse observational coverage (Lenton et al., 2013) especially in winter, few sediment cores south of ~60° S (e.g., Fig. 4) and large model biases (e.g., Marzocchi and Jansen, 2017; Mongwe et al., 2018; Downes et al., 2015). Nevertheless, there are some main characteristics of this ocean region that can be introduced here.

Zonally, the Southern Ocean is well-mixed due to the rigorous mixing by the Antarctic Circumpolar Current (ACC) that connects the Pacific, Atlantic and Indian Ocean basins in its eddying pathway. The westerly-wind driven ACC is the strongest current in the world with a transport of 173.3 ± 10.7 Sv (Donohue et al., 2016), and surface transport across the ACC is therefore strongly impeded. Meridionally, sharp physical and biogeochemical contrasts exists within the Southern Ocean, separated by oceanic fronts (Marinov et al., 2006; Marshall and Speer, 2012). These fronts have a complex

spatial structure (Belkin and Gordon, 1996) and contour the different water masses in the Southern Ocean. Driven by the strong and diverging winds, upwelling south of the ACC along steeply sloping isopycnal surfaces brings up deep waters and thereby 'closes' the global overturning circulation (Tamsitt et al., 2017). These upwelled Circumpolar Deep Waters (CDW, which originally are North-Atlantic deep waters, mixed with Antarctic water masses) then diverge into an upper northward and a lower southward cell component (Speer et al., 2000; Marshall and Speer, 2012). These components are altered by air-sea exchange (of for example heat, carbon and freshwater), vigorous mixing (along for example bathymetric features or through eddying motions) and changes in buoyancy (through precipitation and evaporation, sea ice formation, export, and melt). Facilitated by northward Ekman transport and buoyancy gain, the upwelled waters in the upper 'Deacon Cell' subduct towards the north of the ACC as intermediate and mode waters (Speer et al., 2000). Notably, this clockwise circulating upper branch of the Southern Ocean meridional circulation is the residual circulation of two opposing circulations: the wind-driven circulation and the eddy-driven circulation (Marshall and Speer, 2012). Close to the Antarctic continent, and predominantly in the Weddell and Ross Seas, downwelling of cold and saline water forms Antarctic Bottom Water (AABW) (Marshall and Speer, 2012). The occurrence of both up- and downwelling makes the Southern Ocean an important region for exchange between deep and surface ocean waters, as well as with the atmosphere.

At present, water originating in the Southern Ocean ('Southern Source Water', SSW) serves as the end-member for most of the world's bottom waters (Fig. 5). SSW, including its physical and biogeochemical signatures, therefore fill the deep ocean - and greatly affect its characteristics (e.g., Rae and Broecker, 2018; Paper I). The SSW characteristics also influence the paleoclimatological archive, which accumulates at the sediment-bottom water interface (Papers I and IV). Moreover, SSW generally expands during glacials (Adkins, 2013) – increasing its influence on interior water mass characteristics and paleoclimatic archives.

The particulars of the Southern Ocean circulation shape its distinct biogeochemical characteristics, relevant for its role in past biogeochemical cycling. First, the upwelling CDW water masses bring large amounts of nutrients to the surface. However, biological processes are unable to fully utilize these nutrients due to light and micronutrient (iron) limitation. Therefore, the Southern Ocean is a so-called high nutrient, low chlorophyll (HNLC) region. Consequently, a large fraction of macronutrients leaves the Southern Ocean in unused form (referred to as preformed nutrients, see also Paper III). These high preformed nutrient concentrations indicate the large - but unused - potential of the Southern Ocean to sequester carbon through photosynthesis and export production, and draw down pCO_2^{atm} (Ito and Follows, 2005). The extent to which the Southern Ocean allows communication between the (deep) ocean and the atmosphere can be seen as a 'window', and depends both on the incomplete nutrient consumption by biology as well as vertical mixing of carbon-rich deep waters to the surface (Sarmiento and Gruber, 2006). This 'Southern Ocean Window' thus determines the amount of exchange between the ocean and the atmosphere, and sets pCO_2^{atm}. Similarly, the cycling of nutrients in the Southern Ocean governs lower-latitude productivity (Sarmiento et al., 2004; Marinov et al.,

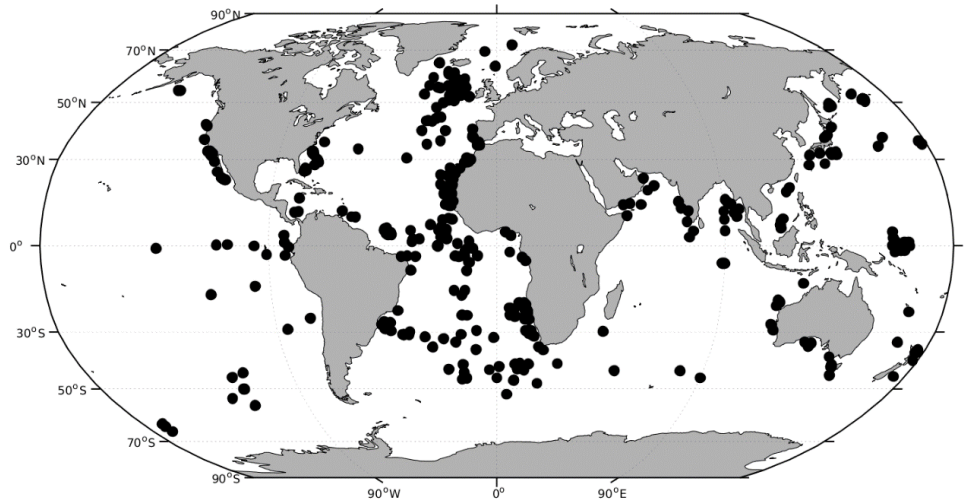

Figure 4 Location of core locations with $\delta^{13}C$ data, as used in Paper III. Note that the cores lie at different depths.

2006; Laufkötter and Gruber, 2018; Primeau et al., 2013). Thus, variations in the Southern Ocean physical and biogeochemical state have a major potential to affect global biogeochemical cycles. Indeed, the Southern Ocean played a central role in glacial-interglacial pCO_2^{atm} variations (Moy et al., 2019; Sigman et al., 2010). For the LGM, the current understanding is that Southern Ocean processes (such as increased sea ice cover, iron input, deep-water volume contribution, and stratification) facilitated the majority of the extra carbon storage in the interior ocean, allowing pCO_2^{atm} drawdown (Sigman et al., 2010; Watson and Naveira Garabato, 2006; Ferrari et al., 2014).

A large part of our understanding of paleo-oceanography and the role of the Southern Ocean in past glacial-interglacial cycling comes from $\delta^{13}C$ (e.g., Charles et al., 2010; Peterson et al., 2014). $\delta^{13}C$ is a proxy for past carbon pumping (both physical and biological), obtained from deep-sea sediment cores.

1.4 $\delta^{13}C$

Both the physical and biogeochemical state of the ocean accumulate in the $^{13}C/^{12}C$ carbon isotope ratio of foraminiferal shells (Zeebe and Wolf-Gladrow, 2001). This $^{13}C/^{12}C$ ratio is expressed in standardized form as $\delta^{13}C$, in order to facilitate comparison between different studies (Eq. 1).

$$\delta^{13}\mathrm{C} = \left(\frac{^{13}C/^{12}C}{(^{13}C/^{12}C)_{PDB}} - 1\right) * 1000\ ‰ \quad (1)$$

Standardisation is done to the Pee Dee Belemnite ratio ($^{13}C/^{12}C_{PDB} = 0.0112372$), which reveals that ^{13}C is present at concentrations typically only ~1% of the abundant ^{12}C (Zeebe and Wolf-Gladrow, 2001). The more recent Vienna-PDB standard is not used in this work because the PDB standard is still the most common in recent data products relevant for this study (Peterson et al., 2014; Eide et al., 2017). Reconstructions of the $\delta^{13}C$ of DIC provide valuable information on the past physical

and biogeochemical state of the ocean. $\delta^{13}C$ can be measured in sediment cores from the $CaCO_3$ shells of foraminifera, and are used to reconstruct $\delta^{13}C$ of water column DIC ($\delta^{13}C_{DIC}$). $\delta^{13}C_{DIC}$ is best recorded by the epifaunally-living foraminiferal genus *Cibicides*, and in specific the $\delta^{13}C$ from species *Cibicides wuellerstorfi* (Schmittner et al., 2017). Such $\delta^{13}C$ records can go back tens of millions of years (Hilting et al., 2008), and are available mainly in the Atlantic - with sparser coverage in the Pacific and Indian oceans (Fig. 4). The Pacific Ocean basin is relatively underrepresented due to $CaCO_3$ under saturation causing dissolution of the $CaCO_3$ shell material.

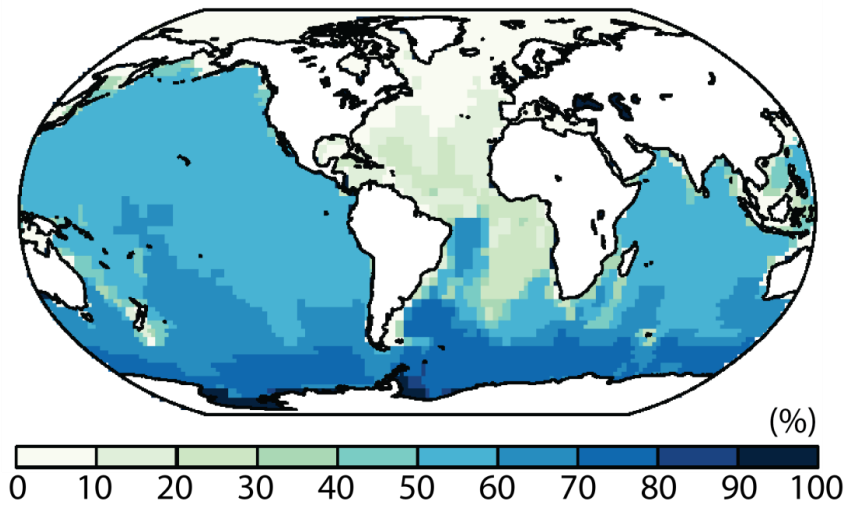

Figure 5 Volumetric contribution of Southern Source surface waters (≥ 60°S) to the ocean bottom wet layer (adjusted from Fig. S1 in the Suppelemnt to Paper IV).

Interpretation of the $\delta^{13}C$ records (and even more so, process-attribution) is not straightforward, exactly because both biogeochemical and physical processes influence $\delta^{13}C_{DIC}$ (Paper I; Broecker and McGee, 2013). Nevertheless, observational and proxy records have provided an idea of typical $\delta^{13}C_{DIC}$ values, and quantified their variability. Pre-industrial surface ocean values are in the range of 0.5-2 ‰, while interior $\delta^{13}C_{DIC}$ is lower and in the range of -0.5-1 ‰ (Eide et al., 2017). Atmospheric $\delta^{13}C$ is about -6.5 ‰, and varies by ~0.5 ‰ during glacial–interglacial cycles (Lourantou et al., 2010; Menviel et al., 2015; Bauska et al., 2016; Eggleston et al., 2016). In addition, glacial-interglacial variations in the vertical marine gradient of

$\delta^{13}C_{DIC}$ provide evidence for a glacial ocean that was both physically and biologically different from today's ocean (Paper I; Toggweiler, 1999; Curry and Oppo, 2005).

In order to interpret the reconstructed distribution and variability of $\delta^{13}C_{DIC}$, it is fundamental to understand its governing processes. The main processes are i) ocean circulation, ii) bulk exchange and thermodynamic equilibration across the air-sea interface, and iii) the efficiency of the biological carbon pump (Gruber et al., 1999; Lynch-Stieglitz et al., 1995; Toggweiler, 1999; Paper I). Important for processes ii and iii, fractionation between the ^{12}C and ^{13}C isotopes occurs during air-sea exchange and photosynthesis (Zeebe and Wolf-Gladrow, 2001). The lighter ^{12}C is namely

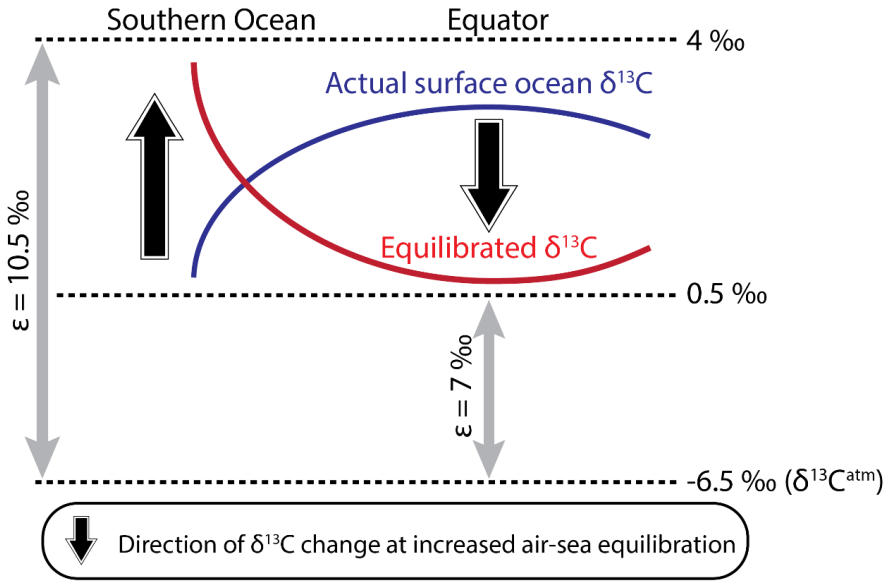

Figure 6 Simplified zonal mean concentration of surface ocean $\delta^{13}C_{DIC}$ for actual (blue) and equilibrated (red) states, with direction of air-sea equilibration (black arrows) in the Southern Ocean and low-latitude oceans. The opposing direction between the response of the SO and low-latitude oceans to equilibration is an interplay between the actual surface ocean $\delta^{13}C_{DIC}$ and the meridional contrast in the strength of air-sea fractionation (ε). Air-sea fractionation depends on latitude due to the dependency of air-sea fractionation (ε) on temperature and the CO_3^{2-}/DIC ratio.

preferentially incorporated in organic matter (increasing surface ocean $\delta^{13}C$ of DIC, and producing low-$\delta^{13}C$ organic carbon), and preferentially escapes to the atmosphere – both affecting $\delta^{13}C_{DIC}$ in interplay with ocean circulation.

Ocean circulation (its structure and rates) affects $\delta^{13}C_{DIC}$ through redistribution of $\delta^{13}C_{DIC}$, as individual water masses often have a typical $\delta^{13}C$ signature. Circulation also affects air-sea equilibration (through its effect on surface residence times) and the time available for organic matter remineralisation (releasing low-$\delta^{13}C_{DIC}$). Bulk transfer into the ocean of the low-$\delta^{13}C$ atmospheric carbon (-6.5 ‰) decreases surface ocean $\delta^{13}C_{DIC}$ – and vice versa when released from the ocean. Such exchange depends on whether the surface ocean is a source or sink of carbon to the atmosphere (Fig. 3) and can cause a ~0.6 ‰ range in surface ocean $\delta^{13}C_{DIC}$ (Lynch-Stieglitz et al., 1995). The amount of thermodynamic equilibration between atmospheric and surface ocean $\delta^{13}C_{DIC}$ will change surface ocean $\delta^{13}C_{DIC}$ in opposite directions depending on latitude, due to the strong temperature dependence of air-sea equilibration (Zhang et al., 1995) (Fig. 6 and Paper I). Last, the efficiency of the carbon pumps determines to what extent surface ocean $\delta^{13}C_{DIC}$ is increased, and interior $\delta^{13}C_{DIC}$ is decreased (which mainly occurs due to the remineralisation of low-$\delta^{13}C$ particulate organic carbon (POC) at depth). In summary, the reconstructed changes in $\delta^{13}C_{DIC}$ can only be interpreted if the relative importance of processes i-iii for a certain location (i.e., sediment core) is understood. Modelling attempts have shown that both physical and biological processes must have played a role in shaping the glacial-interglacial changes in $\delta^{13}C$ (Bouttes et al., 2011; Buchanan et al., 2016).

This work explores the governing mechanisms of $\delta^{13}C_{DIC}$ variations through idealized model experiments (Paper I) and presents an LGM simulation with the biogeochemical ocean model NorESM-OC with carbon isotopes enabled (Papers II and III) – exploring the relative role of physical and biological processes in setting $\delta^{13}C_{DIC}$.

1.5 $\delta^{18}O$

As illustrated in Fig. 1, $\delta^{18}O$ from deep-sea sediments (the standardized ratio between the ^{16}O and ^{18}O isotopes; Eq. 2) is another isotope proxy central to our understanding of past climate. Marine $\delta^{18}O$ can be measured from foraminiferal shell material in

sediment records, just like $\delta^{13}C$. Again like $\delta^{13}C$, interpretation is based on a good understanding of $\delta^{18}O$ fractionation processes and other dependencies.

$$\delta^{18}\mathrm{O} = \left(\frac{{}^{18}O/{}^{16}O}{({}^{18}O/{}^{16}O)_{standard}} - 1\right) * 1000\ ‰\ , \quad (2)$$

where ${}^{18}O/{}^{16}O_{standard}$ is the Vienna Standard mean Ocean Water (VSMOW equals 2005.20 ± 0.43 ppm; e.g. Coplen (1995)).

Aqueous $\delta^{18}O$ changes during phase transitions, and shell material $\delta^{18}O$ depends on seawater temperature at the time of shell formation (Zeebe and Wolf-Gladrow, 2001). Based on our understanding of these dependencies, $\delta^{18}O$ represents a combined signal from temperature as well as evaporation and precipitation – and thereby global ice sheet volume. The separation of the effects of temperature and global ice sheet volume is however not straightforward (e.g., Elderfield et al., 2012). Processes such as diagenesis and vital effects can namely affect fractionation, and there are uncertainties involving the paleo-temperature equations and past ocean water $\delta^{18}O$ (which is needed in the paleo-temperature equations) (Zeebe and Wolf-Gladrow, 2001). Nevertheless, it is understood that the relatively heavier ^{18}O has a higher tendency to precipitate out of a vapor phase than ^{16}O, and temperatures are lower when benthic $\delta^{18}O$ is higher.

In paleo context, the temperature dependency and relationship with the hydrological cycle make $\delta^{18}O$ a useful proxy to understand glacial-interglacial cycling. For example, the formation of large ice sheets (containing strongly depleted $\delta^{18}O$ ice of -20 to -55 ‰) leave the ocean relatively enriched in ^{18}O (~0 ‰). Larger ice sheets will thus lead to higher ocean $\delta^{18}O$, which is recorded in the benthic $\delta^{18}O$ records (Fig. 1). The variability in Fig. 1 is therefore considered to represent glacial-interglacial cycles. Indeed, the pacing of the benthic $\delta^{18}O$ record generally agrees well with the Milankovitch (Milanković) cycles of solar insolation (Imbrie et al., 1984; Hays et al., 1976; Milanković, 1920) - that drive the Earth's temperature and ice sheet volume.

The Milankovitch cycles mainly occur with a period of ~100 ky (eccentricity), 41 ky (obliquity) and ~23 ky (precession), and influence the length, intensity and timing of the seasons. Interestingly however, the Milankovitch cycles cannot explain the pronounced change in glacial-interglacial pacing recorded by $\delta^{18}O$ during the Mid-Pleistocene Transition (MPT, Fig. 1) – as this change is absent in the rhythmic solar variations. About 35 years after the discovery of the MPT in the sediment core $\delta^{18}O$ records (Shackleton and Hall, 1984), this conundrum still invites new hypothesis on the underlying causes of the MPT (e.g., Paper IV).

Chapter 2

Motivation and Objectives

In the first place, this work is motivated by the wish to understand the global Earth System, such that we can understand its sensitivity to change as well as its natural behaviour. The global Earth System is relevant to us as its components and their interactions shape our climate, and ultimately the weather we experience. Without a good understanding of the natural background state of the Earth System, we cannot understand the effects of perturbations - such as those by humankind. The study of the natural and long-term behaviour of the Earth System inevitably focuses on the past. In such study of past climate (paleoclimatology), we rely on proxies instead of direct measurement of the variable of interest. Fundamental proxies used to understand both past and present climate are isotope ratios, such as $\delta^{13}C$ and $\Delta^{14}C$ for carbon and $\delta^{18}O$ for oxygen. The study of these and other proxies has revealed a natural cyclic character of the Earth´s climate, and has helped to constrain its extremes and governing processes. Furthermore, we know from proxy data that the Southern Ocean plays a central role in both past and contemporary climate (e.g., Moy et al. (2019); Sigman et al. (2010); Ferrari et al. (2014); Hauck et al. (2015); Gruber et al. (2019)). Specifically, the Southern Ocean's role in the global overturning of water masses and biogeochemical cycling strongly influences our climate and its variability (Chapter Introduction). The governing processes and their importance for global climate are, however, still under debate. There is therefore a strong motivation to explore how the physical and biogeochemical state of the Southern Ocean influence past global marine tracer distributions, such that we can better interpret proxy data and improve our understanding of the Earth System.

A central problem in the study of the Southern Ocean is the sparsity of field data for both the past and present. Therefore, and to isolate individual processes,

mathematical models are applied to simulate the Earth System, and compared to (proxy) data (Chapter Approach). Specifically, major efforts are made to simulate past global biogeochemical cycles in state-of-the-art Earth System Models (such as those participating in the Coupled Model Intercomparison Project, CMIP) in agreement with proxy records (like the carbon isotopes) (Braconnot et al., 2012). Thanks to the advances made in proxy data collection and model development, these efforts currently allow the study of underlying processes of the global natural Earth System and its climate, and the role of the Southern Ocean therein, in more detail than ever before.

Motivated by the issues and possibilities described above, this work aims to contribute to this field of research in the following way:

I. Aid the interpretation of $\delta^{13}C_{DIC}$ reconstructions by constraining the sensitivity of the marine $\delta^{13}C_{DIC}$ distribution to biogeochemical changes, and the role of the Southern Ocean therein (Paper I);
II. Preparing an LGM minus pre-industrial atmospheric anomaly dataset for use in atmospheric forcing of LGM ocean models (Paper II);
III. Realising a model simulation of the LGM ocean in NorESM-OC with full biogeochemistry as well as carbon isotopes (Papers II and III);
IV. Exploring the role of the biological pump efficiency in the LGM ocean, as based on model-proxy comparison (Paper III);
V. Positioning I-IV in a bigger perspective by evaluating the role of Southern Ocean water in influencing global deep-sea sediment records of glacial-interglacial cycling (Paper IV).

Chapter 3

Approach

The papers bundled in this work all involve the influence of the Southern Ocean on marine biogeochemical tracer distributions, with a focus on two main paleo-oceanographic proxies - $\delta^{13}C$ and $\delta^{18}O$. We studied these tracers using several numerical ocean models evaluated and compared to qualitative and quantitative proxy data. The models made it possible to perform sensitivity experiments (Papers I and IV), in which the relative importance of governing processes and Southern Ocean surface conditions for biogeochemical tracer distributions could be explored.

We applied three models of different complexities: The Hamburg Oceanic Carbon Cycle Circulation Model Version 2s ('HAMOCC2s': Heinze and Maier-Reimer (1999) and Heinze et al. (2016)), the stand-alone ocean carbon-cycle configuration of the Norwegian Earth System Model version 1.2 ('NorESM-OC': Schwinger et al. (2016); Tjiputra et al. (2020)) and the Total Matrix Intercomparison model version 7 ('TMI': Gebbie and Huybers (2012)). In Papers I and III ($\delta^{13}C$) as well as in Paper IV ($\delta^{18}O$), the model results were evaluated against available ($\delta^{13}C/\delta^{18}O$) data from sediment cores as well as other proxies if available and relevant. This chapter summarizes each models' characteristics (detailed model descriptions are provided in the respective Papers and their technical references), and how the models were used to address the main objectives of this study.

In order to guide the work in NorESM-OC, we started with an exploratory sensitivity study on the role of the Southern Ocean in global marine $\delta^{13}C$ distributions using HAMOCC2s (Paper I). HAMOCC2s is a computationally efficient ocean biogeochemistry general circulation model that allows for long time integrations of hundred thousands of years. HAMOCC2s includes the carbon isotopes, and has a constant (modern) circulation field and a resolution of 3.5 × 3.5° with 11 depth layers.

The sensitivity of the marine $\delta^{13}C$ distribution to biogeochemical changes, and the role of the Southern Ocean therein, is explored through four groups of idealized model experiments (that cover POC sinking rates, nutrient drawdown efficiencies, sea ice extent, and air-sea gas exchange rates).

We then built on the results of Paper I, and focused on simulating and understanding the LGM ocean through model simulation using the global stand-alone ocean carbon-cycle model NorESM-OC coupled to a prognostic atmosphere for pCO_2, $\delta^{13}C$ and $\Delta^{14}C$ (Papers II and III). The fully-coupled version of NorESM contributes to major international model intercomparisons (e.g., CMIP), and is thereby one of the several tens of ESMs in the world that help to inform policy and decision makers through for example the IPCC Assessment Reports. NorESM is considered to be a state-of-the-art ESM. The stand-alone ocean carbon-cycle configuration of NorESM (that is, NorESM-OC) allows for (much) longer integration times than the fully-coupled NorESM, as well as control over the atmospheric boundary conditions of the ocean. NorESM-OC contains the isopycnal ocean circulation model MICOM, and was applied in version 1.2 with a tripolar grid with 2° nominal resolution and 53 isopycnal layers. The latitudinal spacing varies from 0.5° at the Equator to 0.35° in the Southern Ocean (Schwinger et al., 2016). The ocean is forced from the atmosphere by CORE Normal Year Forcing (CORE-NYF, Large and Yeager, 2004). The biogeochemical model HAMOCC in NorESM-OC simulates carbon, nitrogen, phosphorus, silicate, iron, and oxygen – as well as several diagnostic versions of these tracers such as saturated O_2 and preformed tracers (Schwinger et al., 2016; Tjiputra et al., 2020). Last, the sea ice model CICE is part of NorESM-OC. The simulations done for Paper III exclude the ocean sediments, due to their lengthy spin-up times (particularly for the carbon isotopes). The control over the atmospheric boundary conditions available in NorESM-OC is used to obtain a satisfactory simulation of the LGM ocean circulation (Papers II and III), something fully-coupled ESMs simulating the LGM (i.e., the Paleoclimate Modelling Intercomparison Project, PMIP) generally do not succeed in (Weber et al., 2007; Marzocchi and Jansen, 2017; Muglia and Schmittner, 2015).

Comparison with proxy data is used to evaluate the model performance in simulating the LGM ocean (see also Braconnot et al., 2012). To facilitate comparison with the common $\delta^{13}C$ proxy, the carbon isotopes ^{13}C and ^{14}C were implemented and enabled in NorESM-OC for Paper III (Tjiputra et al., 2020). Multi-model mean anomalies between LGM and pre-industrial PMIP3 simulations (Paper II) were used to adjust the CORE-NYF to provide a best estimate for the LGM atmospheric state. In addition, reconstructions of LGM dust input to the ocean (Lambert et al., 2015) and tuning of the salinity forcing was applied (Paper III). The carbon isotope-enabled NorESM-OC setup allowed for model simulations of several thousands of years, enough to create an equilibrated time-slice model simulation for the LGM and pre-industrial oceans. These two simulations formed the basis for the analysis in Paper III, and made it possible to explore the role of the biological pump efficiency in the LGM ocean (Paper III).

In order to put the work presented in Papers I-III in a more long-term perspective of glacial-interglacial cycling, we explored the relative roles of Southern and Northern end-member water masses in pacing glacial-interglacial cycles in $\delta^{18}O$ records of the Pleistocene using the TMI model (paper IV). TMI is applied in a resolution of 4° x 4° and 33 depth levels. The model is a matrix solution of mean modern arrival times to the interior ocean from any surface boundary location, as based on an inverse approach using distributions of several biogeochemical tracers. This setup of TMI can advect conservative tracers, and allows for varying boundary conditions over long timescales (millions of years). In Paper IV, the TMI model is applied to explore the effect of different end-member values (i.e., surface boundary conditions) of the deep-water formation regions in the Northern and Southern Hemisphere on the recorded interior signal. Nineteen 200-kyr experiments are performed, and their characteristics analyzed using spectral analysis (Paper IV).

Chapter 4

Summary of Results

Paper I:

Southern Ocean controls of the vertical marine $\delta^{13}C$ gradient – a modelling study

Changes in the marine $\delta^{13}C$ distribution and its surface-to-deep vertical gradient are an important proxy for past changes in ocean circulation and biogeochemical cycling. The interpretation of these changes however, is frustrated by uncertainties in the relative importance of circulation and biogeochemical cycling on $\delta^{13}C$. This study explores the effects on marine $\delta^{13}C$ of Southern Ocean and global changes in biogeochemistry. A range of idealized experiments (air–sea gas exchange rates, particulate organic carbon sinking rates, sea ice cover, and nutrient uptake efficiency) is performed with the ocean biogeochemistry general circulation model HAMOCC2s. Ocean circulation in the model is constant, and represents the pre-industrial flow field. The results show that biogeochemical changes in the Southern Ocean have a relatively large potential to affect global $\delta^{13}C$ distributions. This is especially true for more efficient Southern Ocean nutrient consumption and changes in air-sea gas exchange rates. Moreover, the results show how the regional response to biogeochemical changes especially depends on the combination of i) the contribution

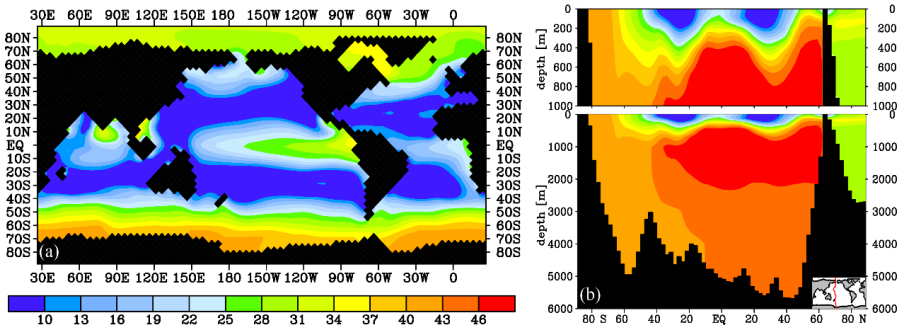

Figure 7 Percentage contributed by biological processes (photosynthesis and remineralization) to $\delta^{13}C$ at 25 m depth (a) and for a Pacific transect (b). The remainder of the signal is attributed to air-sea gas exchange and circulation. As Fig. 2 in Paper I (Morée et al., 2018).

of biology to the local $\delta^{13}C$ signal (Fig. 7), and ii) the local thermodynamic disequilibrium (Fig. 6). We conclude that past variations in the vertical $\delta^{13}C$ gradient likely were a combination of circulation and biogeochemical changes, and constrain the maximum effect of biogeochemical changes on the basin-mean vertical $\delta^{13}C$ gradient to -0.6 ‰.

Paper II:

A Last Glacial Maximum forcing dataset for ocean modelling

Model simulation of the past ocean in agreement with proxy records can help us to understand the drivers of long-term climate variability. Forcing of a stand-alone ocean model (omitting e.g. the land and atmosphere as interactive model components) drastically reduces model complexity as well as computational costs. This makes it more suitable for paleomodelling, which generally requires lengthy runtimes. The LGM ocean was the most recent time the ocean was in a very different circulation state as compared to now, driven by for example changes in the atmosphere and sea surface freshwater budget. In this data paper, we present the atmospheric anomalies between the *lgm* and *piControl* runs of the third phase of PMIP3 for application in LGM ocean modelling. We provide the multi-model mean LGM minus pre-industrial (LGM-PI) PMIP3 anomaly for specific humidity (Fig. 8), downwelling longwave and shortwave radiation, precipitation, wind (v and u components), temperature and sea surface salinity. All data are made available in a format optimized for use with the

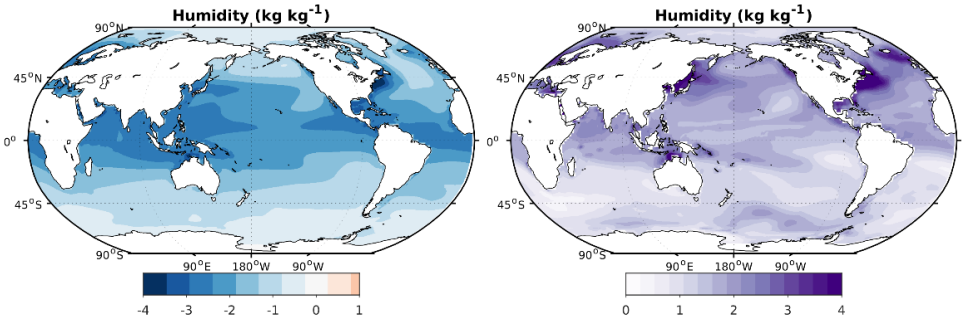

Figure 8 Annual mean 10-meter height specific humidity LGM-PI anomaly (left) and model spread (right) in kg kg^{-1} 10^{-3}. As Fig. 1 in Paper II.

common CORE ocean forcing, but can be added to any pre-industrial ocean forcing dataset. Moreover, the anomalies are presented in such a way that it should be straightforward to make changes. The anomaly fields show a colder, less humid atmosphere with weakened longwave radiation and precipitation and a generally more saline surface ocean. All multi-model mean LGM-PI anomalies show a distinct spatial pattern that we expect to be indicative of the LGM-PI changes, as well as a large inter-model spread in the amplitude of the change.

Paper III:

Evaluating the Biological Pump Efficiency of the Last Glacial Maximum Ocean using $\delta^{13}C$

The 100-ppm lower pCO_2 in the LGM atmosphere as compared to pre-industrial times has inspired many hypotheses. The marine biological pump efficiency (the ability of marine biology to consume surface ocean phosphate) is a central concept in understanding this change, as it strongly and linearly correlates with atmospheric pCO_2. This modelling study explores the relative roles of ocean circulation changes and changes in the biological pump needed to simulate an LGM ocean in satisfactory agreement with proxy data. Using the forced ocean-ice model setup of the Norwegian Earth System Model NorESM-OC, we simulate a steady state LGM and pre-industrial ocean. For the LGM simulation, we added the anomalies of Paper II to the standard atmospheric and sea surface salinity forcing of NorESM-OC. The modelled LGM-PI changes are evaluated against proxy (or model) reconstructions of $\delta^{13}C$, water mass circulation, sea surface temperature, salinity, sea ice extent, export production, vertical nutrient redistribution, atmospheric pCO_2, the change in marine dissolved inorganic carbon, and O_2. We conclude that our simulation of LGM ocean circulation agrees with proxy reconstructions within the uncertainty of the data. However, $\delta^{13}C$, O_2 and regenerated PO_4^{3-} reveal large model-proxy biases, which we interpret as a too weak remineralized signature in our LGM ocean simulation – and hence a too weak biological pump efficiency. Recognizing that agreement with the proxy data is

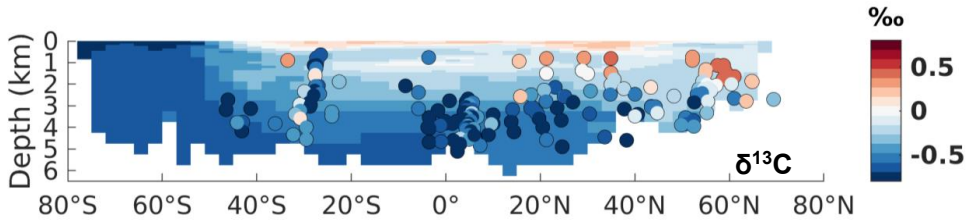

Figure 9 Adjusted simulated Atlantic $\delta^{13}C$ LGM-PI change for a biological pump efficiency of 75 %, compared to $\delta^{13}C$ data from sediment cores. Taken from Fig. 6 in Paper III.

obtained through both physical and biogeochemical changes, we explore the biological changes that would be required to minimize model-proxy bias in a theoretical framework. We find that a near doubling of the global mean biological pump efficiency from 38 % (pre-industrial) to 75 % (LGM) reduces the model-proxy $\delta^{13}C$ bias the most (Fig. 9). The remaining bias may be reduced by further circulation changes, with a major potential for Southern Source Water expansion and aging. We further conclude that only models that contain the processes and/or components that realistically change both ocean circulation and the efficiency of the biological pump will be able to simulate an LGM ocean in satisfactory agreement with proxy data – and hence be reliable for use in climate projections.

Paper IV:

Cancellation of the precessional cycle in $\delta^{18}O$ records during the Early Pleistocene

Deep-sea $\delta^{18}O$ records of Pleistocene climate variability show a marked contrast in dominant periodicity between the Early and Late Pleistocene. This transition between a dominant 41 ky cyclicity and a dominant ~100 ky cycle, referred to as the MPT, remains incompletely understood. As deep-sea $\delta^{18}O$ records are one of our key archives of long-term climate variability, this incomplete understanding suggests we have not identified the main drivers of such long-term climate system variability. A key feature of the Pleistocene $\delta^{18}O$ records is the absence of a precessional signal in the Early Pleistocene. This is unexpected, as solar insolation, considered to drive ice sheet volume and temperature, continuously contains all Milankovitch cycles

(precession, obliquity and eccentricity). A specific feature of the precession cycle is that it is out of phase between the two hemispheres for a particular season. Therefore, the precessional cycles archived in the Northern and Southern hemispheric ice sheets have the potential to cancel each other out when interfering – referred to as the Antiphase Hypothesis. We applied the TMI model to explore the potential for North Atlantic and Southern Ocean cyclic end-member signals to cancel each other out in the interior ocean. A large range of relative end-member contributions is explored in 19 model experiments. These variations, we assume, are represented by variations in sea level equivalents of ice stored in the Northern and Southern hemispheric ice sheets. The results show that widespread cancellation of precession occurs specifically for end-member contributions typical of the Early Pleistocene (Fig. 10). Therefore, we conclude that benthic $\delta^{18}O$ records incompletely archived the precessional cycle during the Early Pleistocene – and show up as an apparent contrast in periodicity across the MPT.

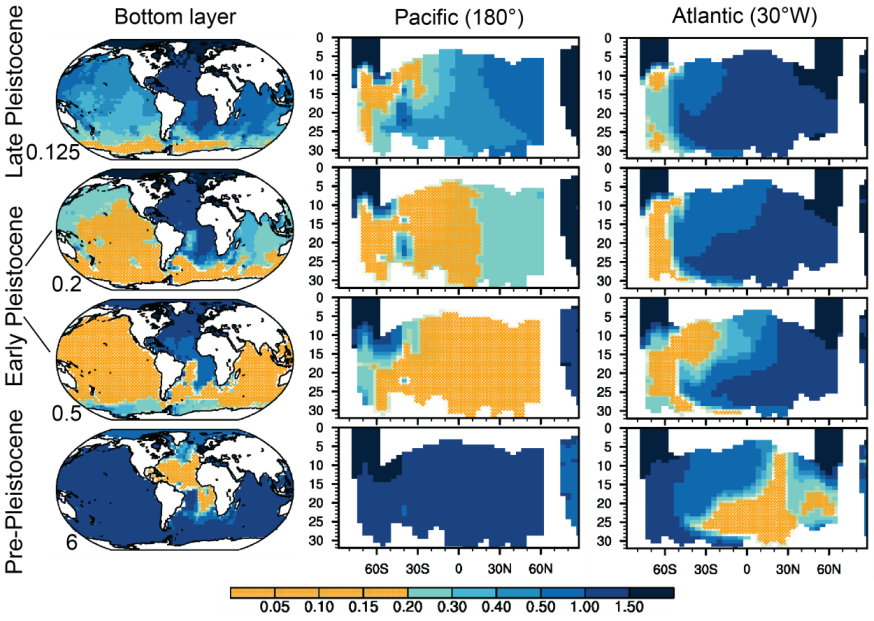

Figure 10 Cancellation of the precessional cycle relative to obliquity hatched in orange, at the sediment-ocean interface (bottom) and for a Pacific and Atlantic transect. Relative contribution of North Atlantic and Southern Ocean end-members are 0.125 (Late Pleistocene), 0.2-0.5 (Early Pleistocene) and 6 (Pre-Pleistocene).

Chapter 5

Perspectives and Outlook

Deep-sea sediment records of $\delta^{13}C$ and $\delta^{18}O$ are central for our understanding of the physical and biogeochemical state of the past ocean, and hence long-term climate variability (Chapter Introduction). The work presented in this thesis underlines that the interpretation of these records is not straightforward. Specifically, we note several factors that contribute to the uncertainties involved in the interpretation of $\delta^{13}C$ and $\delta^{18}O$ records as well as our ability to simulate the past ocean in agreement with such records.

One major uncertainty lies in the reconstruction of end-member characteristics. Knowledge of the end-member characteristics is key to unravelling their contributions to interior ocean tracers - and therefore benthic $\delta^{13}C$ and $\delta^{18}O$. Furthermore, offsets between water column $\delta^{13}C$ of DIC and the archived benthic $\delta^{13}C$ of $CaCO_3$ may result in additional uncertainty (Schmittner et al., 2017). Regarding end-member characteristics, the specifics of Southern source waters are especially important as these occupy most of the world's interior ocean and have a large potential for (biogeochemical) change (e.g., Chapter Introduction; Ito and Follows, 2005). The impacts of specifically the Southern Ocean end-member on benthic $\delta^{13}C$ and $\delta^{18}O$ records is explored and discussed in both Paper I, III and IV (Objectives I and V). Interior $\delta^{13}C$ distributions are especially sensitive to Southern Ocean nutrient uptake efficiency (Paper I). We furthermore show that cyclic signals entering the ocean at the main interior ocean end-members have the potential to get cancelled out at depth – not becoming part of the $\delta^{18}O$ records (Paper IV). Nevertheless, both Paper I and IV are idealized studies (they for example do not include dynamic ocean circulation), which in return has the advantage of low computational cost. Further efforts to identify the contributions from the main (North Atlantic and Southern Ocean) end-

members to the interior ocean, including their biogeochemical signatures (e.g., Oppo et al., 2018) will over time likely reveal the LGM ocean structure and characteristics. This is particularly true for the Atlantic basin. The limited amount of sediment core data for the Pacific ocean basin (e.g., Fig. 4) make the Pacific (and its physical and biogeochemical characteristics) a relatively unexplored ocean basin with room for new hypotheses (e.g., Jaccard et al., 2009; Umling et al., 2018). Again, Southern source waters would play a central role here, as these waters constitute up to 75% of the Pacific basin's volume (Rae and Broecker, 2018).

Uncertainties related to the relative importance of contributing processes (and disentangling their contributions) form a challenge to the interpretation of any proxy record, including the benthic archive. For example, records of $\delta^{18}O$ need information from other proxies to reliably separate temperature and ice sheet volume effects (Elderfield et al., 2012). The interpretation of $\delta^{13}C$ is aided by separating the effect of biological and physical processes – as these are the two main drivers of $\delta^{13}C$, which can be done using (proxies for) phosphate (Paper I; Gruber et al., 1999; Schmittner et al., 2013). Contributing to Objective I, we constrained the maximum effect of biogeochemical changes on the basin-mean vertical $\delta^{13}C$ gradient to -0.6 ‰ (Paper I). Specifically, we find in Paper I that biogeochemical changes in the Southern Ocean (mainly nutrient consumption and air-sea gas exchange rates) have a relatively large potential to affect global $\delta^{13}C$ distributions. In an effort to simulate and study the past ocean in a more complex model setup, we simulate the LGM ocean including carbon isotopes using NorESM-OC (Objective III). The approximate doubling of the marine biological pump efficiency (the ability of marine biology to consume surface ocean phosphate) in the LGM ocean (Paper III) confirm the conclusion of Paper I that both major circulation and major biogeochemical changes must have taken place in the ocean between the LGM and pre-industrial time.

We also note several challenges with model simulation of the past ocean. In NorESM-OC, the implementation of the carbon isotopes (as done for NorESM-OC and

described in Tjiputra et al. (2020); Objective III) is an important step towards finding model-proxy biases, as they allow direct comparison between the proxy and observational record and model simulation (Paper III; Tjiputra et al., 2020). The comparison made in Paper III shows that only when additional (biogeochemical) processes are included (e.g. ones that can increase the interior regenerated signal), satisfactory agreement with proxy data is obtained (confirming results by e.g., Ganopolski and Brovkin, 2017; Buchanan et al., 2016; Heinze et al., 2016). A major uncertainty in simulating the LGM ocean stems from the limited possibility to reconstruct the past atmospheric state. In forced ocean modelling, which is attractive because of its computational efficiency relative to fully coupled models (Chapter Approach), an atmospheric state needs to be available to drive the ocean model. For the LGM ocean however, no global data-based estimate is (or will be) available for all relevant atmospheric variables as there exist no (global) quantitative proxy archives for them (e.g., humidity, longwave and shortwave radiation, precipitation, wind speed). Therefore, we prepared a best estimate of the LGM-PI atmospheric changes by compiling the output of fully coupled Earth System Models (Paper II, Objective II). All these LGM-PI anomalies show a distinct spatial pattern that we expect to be indicative of the LGM-PI changes. Nevertheless, the large inter-model spread in the amplitude of the change indicates major uncertainties about the characteristics of the LGM atmosphere, and thus the forcing to the LGM ocean. Furthermore, the uncertainty and sensitivity to (end-member) sea surface salinity forcing in paleomodelling (Papers II and III; Weber et al., 2007) calls for improved simulation of the hydrological cycle. Specifically, the effects of meltwater and calving from ice sheets on ocean circulation may be central to this improvement – these processes are currently forced in PMIP3 (Abe-Ouchi et al., 2015). Excitingly, the first coupled ice sheet models are now included in CMIP6 (Nowicki et al., 2016).

As an outlook, we are particularly interested in the advances in Earth System modelling needed to simulate long-term climate variability with confidence. In NorESM-OC, we show that simulation of the LGM ocean in reasonable agreement

with $\delta^{13}C$ records (Objectives III and IV) is only obtained after tuning the model's sea surface salinity, and realising a near doubling of the efficiency of the biological pump (Paper III; Objective IV). Identifying specific processes that are i) relevant to the high sea surface salinity sensitivity and ii) could drive a near doubling of the biological pump efficiency, should be a focus for future marine research. Here, processes that affect both circulation and biogeochemical cycling (and carbon storage), such as increased LGM Southern Ocean sea ice cover (Jansen, 2017; Ferrari et al., 2014), could be the key to simulating an LGM ocean in agreement with proxy data. In addition, a better understanding of the sources of iron (e.g. dust, sediments, or the cryosphere) and their bioavailability in the Southern Ocean would improve our understanding of the iron fertilisation hypothesis and the LGM increase in interior regenerated nutrients (Martin et al., 1990; Tagliabue et al., 2017; Lambert et al., 2015). Besides these, the importance of imbalances between marine sedimentation and terrestrial weathering for long-term global biogeochemical cycling and marine carbon storage (Roth et al., 2014; Archer and Maier-Reimer, 1994; Broecker, 1982b; Heinze et al., 1999; Paper III) encourages the development and inclusion of these processes in ESMs (as currently done for NorESM).

Ultimately, one would want to have Earth System Models available in which the main drivers of long-term climate variability are represented. Such models would namely allow for greater confidence in their climate projections beyond a few decades. Such confidence is highly relevant for decision making on climate adaptation, as well as in climate research communication to policy makers (IPCC, 2014).

Chapter 6

Scientific Results

I

Paper I

Southern Ocean controls of the vertical marine $\delta^{13}C$ gradient – a modelling study

Morée, A. L., J. Schwinger, and C. Heinze

Biogeosciences, **15**, 7205-7223, 10.5194/bg-15-7205-2018

2018

Southern Ocean controls of the vertical marine $\delta^{13}C$ gradient – a modelling study

Anne L. Morée[1], Jörg Schwinger[2], and Christoph Heinze[1,2]

[1] Geophysical Institute, University of Bergen and Bjerknes Centre for Climate Research, 5007 Bergen, Norway

[2] Uni Research Climate, Bjerknes Centre for Climate Research, 5007 Bergen, Norway

Correspondence: Anne L. Morée (anne.moree@uib.no)

Received: 21 February 2018 – Discussion started: 26 February 2018
Revised: 26 October 2018 – Accepted: 26 November 2018 – Published: 4 December 2018

Abstract. ^{13}C, the standardised $^{13}C/^{12}C$ ratio expressed in per mille, is a widely used ocean tracer to study changes in ocean circulation, water mass ventilation, atmospheric pCO_2, and the biological carbon pump on timescales ranging from decades to tens of millions of years. $\delta^{13}C$ data derived from ocean sediment core analysis provide information on $\delta^{13}C$ of dissolved inorganic carbon and the vertical $\delta^{13}C$ gradient (i.e. $\Delta\delta^{13}C$) in past oceans. In order to correctly interpret $\delta^{13}C$ and $\Delta\delta^{13}C$ variations, a good understanding is needed of the influence from ocean circulation, air–sea gas exchange and biological productivity on these variations. The Southern Ocean is a key region for these processes, and we show here that $\Delta\delta^{13}C$ in all ocean basins is sensitive to changes in the biogeochemical state of the Southern Ocean. We conduct a set of idealised sensitivity experiments with the ocean biogeochemistry general circulation model HAMOCC2s to explore the effect of biogeochemical state changes of the Southern and Global Ocean on atmospheric $\delta^{13}C$, pCO_2, and marine $\delta^{13}C$ and $\Delta\delta^{13}C$. The experiments cover changes in air–sea gas exchange rates,

particulate organic carbon sinking rates, sea ice cover, and nutrient uptake efficiency in an unchanged ocean circulation field. Our experiments show that global mean $\Delta\delta^{13}C$ varies by up to about ±0.35 ‰ around the preindustrial model reference (1.2 ‰) in response to biogeochemical change. The amplitude of this sensitivity can be larger at smaller scales, as seen from a maximum sensitivity of about -0.6 ‰ on ocean basin scale. The ocean's oldest water (North Pacific) responds most to biological changes, the young deep water (North Atlantic) responds strongly to air–sea gas exchange changes, and the vertically well-mixed water (SO) has a low or even reversed $\Delta\delta^{13}C$ sensitivity compared to the other basins. This local $\Delta\delta^{13}C$ sensitivity depends on the local thermodynamic disequilibrium and the $\Delta\delta^{13}C$ sensitivity to local POC export production changes. The direction of both glacial (intensification of $\Delta\delta^{13}C$) and interglacial (weakening of $\Delta\delta^{13}C$) $\Delta\delta^{13}C$ change matches the direction of the sensitivity of biogeochemical processes associated with these periods. This supports the idea that biogeochemistry likely explains part of the reconstructed variations in $\Delta\delta^{13}C$, in addition to changes in ocean circulation.

1 Introduction

The vertical marine $\delta^{13}C$ gradient ($\Delta\delta^{13}C$) is the surface-to-deep difference in $\delta^{13}C$ of dissolved inorganic carbon (DIC), where the standardised $^{13}C/^{12}C$ ratio ($\delta^{13}C$) is expressed in per mille (Zeebe and Wolf-Gladrow, 2001):

$$\delta^{13}C = \left(\frac{^{13}C/^{12}C}{(^{13}C/^{12}C)_{standard}} - 1\right) \times 1000\ ‰ \quad (1)$$

Here, $^{13}C/^{12}C_{standard}$ is the Pee Dee Belemnite standard (0.0112372) (Craig, 1957). ^{13}C is slightly heavier than the ^{12}C isotope, which causes a fractionation effect during air–sea gas exchange and photosynthesis, thereby changing $\delta^{13}C$ and $\Delta\delta^{13}C$ (Laws et al., 1997; Zhang et al., 1995; Mackenzie and Lerman, 2006). Photosynthetic fractionation increases the $^{13}C/^{12}C$ ratio of surface ocean DIC (i.e. a $\delta^{13}C$ increase) due to the preferred uptake of the lighter ^{12}C into biogenic matter (which therefore has a low

$\delta^{13}C$). The deep sea DIC has a relatively low $\delta^{13}C$ signature as a result of the remineralisation of low-$\delta^{13}C$ biogenic matter at depth.

The resulting vertical $\delta^{13}C$ gradient is in addition influenced by air–sea gas exchange and circulation (Zeebe and Wolf-Gladrow, 2001; Emerson and Hedges, 2008; Ziegler et al., 2013). Both deep sea and surface ocean $\delta^{13}C$ signatures are archived in the calcareous shells of foraminifera in the sediments. Such records of $\delta^{13}C$ from planktic and benthic foraminiferal shell material cover tens of millions of years (Hilting et al., 2008). Using this archive, $\delta^{13}C$ and $\Delta\delta^{13}C$ have been used to reconstruct, for example, atmospheric CO_2 concentration, ocean circulation, and the strength of the biological pump (Broecker, 1982; Shackleton and Pisias, 1985; Zahn et al., 1986; Oppo et al., 1990; Hollander and McKenzie, 1991; Keir, 1991; Crucifix, 2005; Curry and Oppo, 2005; Lisiecki, 2010; Broecker and McGee, 2013; Ziegler et al., 2013; Hoogakker et al., 2015; Bauska et al., 2016). $\Delta\delta^{13}C$ is independent of whole-ocean $\delta^{13}C$ shifts (due to terrestrial influences), because such influences would affect $\delta^{13}C$ equally everywhere. This makes $\Delta\delta^{13}C$ a valuable proxy to study the marine carbon cycle independent of changes in carbon storage on land. Besides the use of $\delta^{13}C$ for understanding the past ocean, contemporary measurements of $\delta^{13}C$ of DIC support the quantification of anthropogenic carbon uptake by the oceans as well as the study of the effects of biology and ocean circulation on tracer distributions (Kroopnick, 1980, 1985; Gruber and Keeling, 2001; Quay et al., 2003; Holden et al., 2013; Eide et al., 2017b). However, major uncertainties remain in the interpretation of foraminiferal $\delta^{13}C$ records and $\Delta\delta^{13}C$ (Oliver et al., 2010; Broecker and McGee, 2013) as well as in the interpretation of the present-day $\delta^{13}C$ data (Eide et al., 2017b).

This article addresses part of these uncertainties by exploring the pre-industrial sensitivity of $\delta^{13}C$ and $\Delta\delta^{13}C$ to biogeochemical change in idealised model experiments. By doing so we can investigate a number of biogeochemical mechanisms that could explain (part of) the observed changes in $\delta^{13}C$ and $\Delta\delta^{13}C$. We focus on the Southern Ocean (SO), the ocean south of 45° S, because the SO plays an important

role in the global carbon cycle by regulating atmospheric CO_2 concentrations and uptake of anthropogenic CO_2 (Broecker and Maier-Reimer, 1992; Heinze, 2002; Marinov et al., 2006) as well as influencing the global efficiency of the biological pump, global primary production, and preformed nutrients (Primeau et al., 2013).

Variations in $\Delta\delta^{13}C$ over the past few 100 000 years show that $\Delta\delta^{13}C$ is generally increased during glacial periods, due to a higher contrast of deep $\delta^{13}C$ with surface and mid-depth $\delta^{13}C$ (Broecker, 1982; Shackleton and Pisias, 1985; Boyle, 1988; Charles et al., 2010; Oliver et al., 2010). Long-term $\delta^{13}C$ and $\Delta\delta^{13}C$ variations have been explained by ocean circulation changes (Duplessy et al., 1988; Jansen, 2017; Oppo et al., 1990; Toggweiler, 1999; Menviel et al., 2016). However, $\Delta\delta^{13}C$ variability cannot be explained by ocean stratification or circulation changes alone: an interaction between biogeochemical and physical processes must be at play (Keir, 1991; Boyle, 1988; Mulitza et al., 1998; Charles et al., 2010; Ziegler et al., 2013; Schmittner and Somes, 2016). $\Delta\delta^{13}C$ has been used in different ways over time: in earlier studies as the contrast between surface and deep water $\delta^{13}C$, derived from planktic versus benthic foraminifera (Broecker, 1982; Boyle, 1988; Shackleton et al., 1983; Duplessy et al., 1988), and now increasingly as the contrast of deep ocean (benthic) $\delta^{13}C$ with thermocline or intermediate ocean $\delta^{13}C$ (Mulitza et al., 1998; Charles et al., 2010; Lisiecki, 2010).

Here, we explore the sensitivity of $\delta^{13}C$ and $\Delta\delta^{13}C$ to changes in the biogeochemical state of the Global Ocean and Southern Ocean under a constant circulation field, to support the paleo-oceanographic interpretation of $\delta^{13}C$ and $\Delta\delta^{13}C$ as well as to improve the understanding of the SO role in global carbon cycling and its variability and sensitivity. In order to study biogeochemical mechanisms that could influence $\delta^{13}C$ and $\Delta\delta^{13}C$, a set of sensitivity experiments is conducted with the ocean biogeochemistry general circulation model HAMOCC2s (Heinze et al., 2016). We first estimate the contribution of biology versus air–sea gas exchange to marine $\delta^{13}C$ of DIC (Sect. 3.2). The experiments focus on one or more of the biogeochemical aspects

assumed to be important for $\delta^{13}C$ and $\Delta\delta^{13}C$, e.g. the biological pump efficiency and/or equilibration at the air–sea interface (Sect. 3.3.1–3.3.4). Together these experiments provide a broad spectrum of biogeochemical changes that could influence local and global $\delta^{13}C$ and $\Delta\delta^{13}C$. The modelling results of Sect. 3.3.1–3.3.4 are discussed in context of observational data from sediment cores (Sect. 3.4). As $\delta^{13}C$ and $\Delta\delta^{13}C$ are used to study changes in atmospheric pCO_2 (pCO_2^{atm}), a final section will cover the relationship between atmospheric $\delta^{13}C$, $\Delta\delta^{13}C$, and pCO_2^{atm} under different marine biogeochemical states (Sect. 3.5).

2 Methods

In this study we employ the ocean biogeochemistry general circulation model HAMOCC2s (Heinze et al., 1999, 2016), which simulates the inorganic and organic carbon cycle in the water column and in the sediments. The horizontal resolution of the model is 3.5° × 3.5° and there are 11 depth layers in the ocean. HAMOCC2s has an annual time step and an annually averaged fixed circulation field, as well as a one layer atmosphere component (permitting exchange of O_2, $^{13}CO_2$, and CO_2 with the ocean component), which is assumed to be longitudinally well-mixed. The model is computationally very economic and thus an ideal tool for sensitivity experiments over long integration times. Biogenic particulate matter in the model is represented as particulate organic carbon (POC), calcium carbonate ($CaCO_3$), and biogenic silica (opal). These biogenic particles are only modelled as export production due to the annual time step of the model. POC and opal export production are described by Michaelis–Menten kinetics for nutrient uptake, limited by phosphate and silicic acid respectively (Sect. 1A in the Supplement). $CaCO_3$ export production depends on the ratio between opal and POC production. POC is carried as a tracer as well as transported downwards according to a set of mass balance equations that describe POC gain through surface-layer POC production and POC losses through constant sinking and remineralisation rates (Sect. 1A in the Supplement). This is done similarly for opal and $CaCO_3$ sinking and dissolution. As the model has an annual time step, sea

ice is always present south of ~ 60° S and north of ~ 70° N in the control run (Fig. S1 in the Supplement). A more detailed model description is provided in previous studies using a similar configuration of HAMOCC2s (Heinze, 2002; Heinze et al., 2016), as well as in Sect. 1A in the Supplement.

Fractionation between ^{13}C and ^{12}C during photosynthesis is set to a constant value of -20 ‰ (Lynch-Stieglitz et al., 1995; Tagliabue and Bopp, 2008), as model results are little influenced by the chosen parameterisation (Schmittner et al., 2013; Jahn et al., 2015). The fractionation during air–sea gas exchange depends on temperature according to ε=-9.483*$10^3/T$ + 23.89 ‰, where temperature (T) is measured in Kelvin (K) (Mook, 1986), causing stronger fractionation at lower temperatures (i.e. at high latitudes). Fractionation during $CaCO_3$ formation is omitted from the model, as was done in previous studies (Lynch-Stieglitz et al., 1995; Marchal et al., 1998; Schmittner et al., 2013), as its size is uncertain but likely minor (~ 1 ‰) and effects on $\delta^{13}C$ and $\Delta\delta^{13}C$ are small (Shackleton and Pisias, 1985). In the version of HAMOCC2s used in this study, a fixed weathering input is used for ^{13}C to tune the ocean inventory to values comparable to observations. The weathering flux of ^{13}C into the ocean was determined by an iterative procedure: The model was run over 100 000 years, replacing the weathering rate with the diagnosed burial rate for ^{13}C continuously. After this, the model ^{13}C inventory was recalibrated such that the atmospheric value for ^{13}C arrived at -6.5 ‰. This procedure was repeated over three iterations. Afterwards, the weathering rate of ^{13}C was fixed to the last diagnosed value (0.36 Tmol ^{13}C yr^{-1}) – which results in a weathering flux $\delta^{13}C$ of DIC of -11 ‰ . Another 100 000-year run was carried out with this constant input rate in order to check whether the global ^{13}C distribution was stable in all reservoirs. The sensitivity experiments were then restarted from the result of that run. Weathering fluxes are added homogeneously over the first ocean layer as dissolved matter and in a fixed stoichiometric ratio for $CaCO_3$, organic carbon, PO_3^{4-}, alkalinity, and Si. Annual weathering fluxes (Tmol) are 27 for $CaCO_3$, 5 for organic carbon, $5/r_{C:P}$ for PO_3^{4-}, 2 × $CaCO_3$-$r_{N:P}$ × PO_3^{4-} for alkalinity, and 4.5 for Si (with $r_{C:P}$ = 122 and $r_{N:P}$ = 16). These

values are within the uncertainties of observational estimates for Si (5.6 Tmol yr^{-1}; Tréguer, 2002), $CaCO_3$ (~ 32 Tmol yr^{-1}; Milliman and Droxler, 1996), and organic carbon (4 Tmol yr^{-1}; Broecker and Peng, 1987) and have been adjusted to improve the fit of the respective modelled marine tracer distributions as well as burial fluxes to observational estimates. The spinup procedure described here created a model setup with close-to-observed marine and atmospheric $\delta^{13}C$ ($\delta^{13}C^{atm}$) values and freely evolving atmospheric pCO_2 and $\delta^{13}C$. This equilibrated model version is referred to as the "control run" in the remainder of this article. We define the vertical $\delta^{13}C$ gradient ($\Delta\delta^{13}C$) as follows:

$$\Delta\delta^{13}C = \delta^{13}C_{surface} - \delta^{13}C_{deep}, \quad (2)$$

where $\delta^{13}C_{surface}$ and $\delta^{13}C_{deep}$ are the volume-weighted mean $\delta^{13}C$ of DIC in the surface ocean (< 50 m depth, i.e. the model photic zone) and the deep ocean (lowermost wet layer in the model, if the top of the layer is > 3 km depth), respectively. By doing so, we can compare the $\Delta\delta^{13}C$ summarised as one number between the different sensitivity experiments.

We conducted a set of sensitivity experiments to explore changes in air–sea gas exchange rate, sea ice extent (influencing both biological production and the air–sea gas exchange of carbon), and the efficiency of the biological pump through the POC sinking rate and nutrient uptake rate (Table 1). We employ the term "efficiency of the biological pump" as a measure of the success of phytoplankton to maintain low nutrient concentrations in the surface ocean. All experiments are run for 2000 model years starting from the end of the spinup. These runtimes allowed for atmospheric quasi-equilibrium to establish (Fig. S5), with an exception for the long-term effects caused by POC sinking rate changes (as studied in more detail by Roth et al., 2014). The equilibration timescale of $\Delta\delta^{13}C$ is much shorter than that of atmospheric $\delta^{13}C$: this is the case because (1) the long-term weathering-burial equilibration of $\delta^{13}C$ affects the whole ocean reservoir simultaneously – thus keeping $\Delta\delta^{13}C$ constant – and (2) the processes that potentially influence $\Delta\delta^{13}C$ (changes in biological production

and air–sea gas exchange) affect $\Delta\delta^{13}C$ on shorter (centennial to millennial) timescales. In order to compare effects of SO change and global change, the gas exchange rate and POC sinking rate experiments are done twice – once changing the respective model parameter for the Global Ocean and once for the Southern Ocean only (SO-only). The model parameters were changed in a way that marine biogeochemical tracer distributions (e.g. PO_3^{4-}, $\delta^{13}C$) remained reasonable but did provide an estimate of the sensitivity of the respective tracer to biogeochemical change. The model has a constant sea ice cover (Fig. S1), which permits gas transfer through the ice depending on ice cover thickness (the transfer rate is divided by ice thickness in centimetres) while light transfer is inhibited at ice thicknesses over 0.01 cm. The maximum and minimum sea ice cover experiments ("ice large" and "ice small", Table 1) approximate the Last Glacial Maximum winter extent and the modern summer extent of SO sea ice, respectively (Crosta, 2009 and Fig. A22 therein) and assume full inhibition of gas and light transfer through ice for simplicity.

Table 1. Description of the sensitivity experiments. The sensitivity experiments on the CO_2 gas exchange rate and the biological pump have been done twice, once for the Global Ocean and once only making changes in the Southern Ocean (south of 45° S).

Experiment	Experiment setup
Gas fast	CO_2 gas exchange rate * 4
Gas slow	CO_2 gas exchange rate / 4
Efficient biological pump	POC sinking rate doubled to 6m/d
Inefficient biological pump	POC sinking rate halved to 1.5m/d
V_{max}	High nutrient uptake rate (control*5) in the Southern Ocean
Ice large	Southern Ocean sea ice cover south of 50° S
Ice small	Southern Ocean sea ice cover south of 70° S

The experiment on nutrient drawdown (V_{max}) alters the Michaelis–Menten kinetics of POC production by changing the maximum nutrient (i.e. PO_3^{4-}) uptake rate (V_{max}^{POC} in Sect. 1A in the Supplement). The gas exchange experiments alter the specific gas exchange rate kw, as described in more detail in Sect. 1B in the Supplement. The POC

sinking rate experiments change the sinking velocity constant w_{POC} in the POC mass balance equations (Sect. 1A in the Supplement).

The contribution of biological processes versus air–sea gas exchange to $\delta^{13}C$ is calculated using the method of Broecker and Maier-Reimer (1992) as done for observations by Eide et al. (2017b) and in a modelling context by Sonnerup and Quay (2012):

$$\delta^{13}C_{bio}[‰] = \frac{\varepsilon_{photo}}{\overline{DIC}} \times r_{c:p} \times (PO_4 - \overline{PO_4}) + \overline{\delta^{13}C}, \quad (3)$$

where $\varepsilon_{photo} = -20$ ‰, $r_{c:p} = 122$ and the following model control run mean values are used: $\overline{DIC} = 2332.284\ \mu mol\ kg^{-1}$, $\overline{PO_4} = 2.409\ \mu mol\ kg^{-1}$ and $\overline{\delta^{13}C} = 0.656$ ‰. These values result in the modelled $\delta^{13}C_{bio}$:PO_4^{3-} relationship $\delta^{13}C_{bio}$=3.18-1.05 × PO_4^{3-}. The constant 3.18 is somewhat higher than estimated for observed $\delta^{13}C$, for which a constant of 2.8 was found by Eide et al. (2017b). This higher constant originates from the over-prediction of the model mean $\delta^{13}C$ and PO_3^{4-} at depth, as seen in other models (Sonnerup and Quay, 2012). Equation (3) assumes a constant biological fractionation as well as a constant $r_{C:P}$ ratio, and these assumptions will introduce some error in the partition of biological and air–sea gas exchange signatures derived from observed $\delta^{13}C$ to PO_3^{4-} ratios (e.g. Eide et al. 2017b). For the purpose of determining $\delta^{13}C_{bio}$ in our model, these assumptions are unproblematic, since $r_{C:P}$ and ε_{photo} are actually taken to be constant in the model formulation. The air–sea gas signature ^{13}CAS is approximated as the residual ($\delta^{13}C_{AS} = \delta^{13}C_{model} - \delta^{13}C_{bio}$). $\delta^{13}C_{AS}$ is 0 ‰ when $\delta^{13}C_{model} = \delta^{13}C_{bio}$, i.e. when the $\delta^{13}C$ can be explained by biology only. We express $\delta^{13}C_{bio}$ as a percentage to aid interpretation of the results (denoted $\delta^{13}C_{bio}^{perc}$), because the values of $\delta^{13}C_{bio}$ in per mille depend strongly on the chosen "reference" values, i.e. mean DIC, PO_3^{4-} , and $\delta^{13}C$ (compare Broecker and Maier-Reimer, 1992; Lynch-Stieglitz et al., 1995; Sonnerup and Quay, 2012; Schmittner et al., 2013; Eide et al., 2017b). The conversion from $\delta^{13}C_{bio}$ to a percentage is calculated as follows:

$$\delta^{13}C_{bio}^{perc}[\%] = \frac{|\delta^{13}C_{bio}|}{|\delta^{13}C_{bio}|+|\delta^{13}C_{AS}|} \times 100\ \% \quad (4)$$

In our analysis, we define the total amount of air–sea carbon exchange as $F_{u+d}=F_{up}+F_{down}$, with F_{up} as the upward annual carbon flux from the ocean into the atmosphere and F_{down} its downward counterpart (Sect. 1B in the Supplement and Heinze and Maier-Reimer, 1999). F_{u+d} is relevant for understanding the sensitivity of $\delta^{13}C$. The net carbon exchange is defined as $F_{net}=F_{up}-F_{down}$. The sign of F_{net} indicates whether a region is a source or a sink for carbon and is relevant for understanding changes in pCO_2^{atm}.

3 Results and discussion

3.1 Model control run

The model reproduces the main features of observed marine $\delta^{13}C$, as shown in Figs. 1 and S2. The modelled global mean surface ocean $\delta^{13}C_{surface}$ of DIC is higher (1.88 ‰) than deep ocean $\delta^{13}C_{deep}$ (0.67 ‰), creating a mean ocean $\Delta\delta^{13}C$ of 1.21 ‰. In the North Atlantic and SO, $\Delta\delta^{13}C$ is the least pronounced (0.9 ‰ and 0.8 ‰ respectively) due to vertical mixing between surface and deep water during deep water formation and upwelling (Duplessy et al., 1988). $\Delta\delta^{13}C$ increases with water mass age as expected from the increased imprint of remineralisation on $\delta^{13}C$. The mean modelled ocean $\delta^{13}C$ is higher by 0.16 ‰ relative to observations (Eide et al., 2017b), which is especially pronounced in the oldest water masses (Fig. S2). This is observed in other models as well and attributed to the model's relative contribution of deep water production in the North Atlantic and Southern Ocean (Sonnerup and Quay, 2012). The modelled global export POC production is 9.6 Gt C yr^{-1}, of which 18 % is produced in the SO, which is within the uncertainty of observational estimates (MacCready and Quay, 2001; Schlitzer, 2002; Dunne et al., 2007; Lutz et al., 2007; Nevison et al., 2012). The atmosphere has a modelled equilibrium pCO_2^{atm} of 279 ppm and a $\delta^{13}C^{atm}$ of -6.50 ‰, which developed in the model from the "best-fit" weathering value F_{eq}^{w} as described above in Sect. 2. Net air–sea gas exchange is close to zero (ventilating ~ 2 ×

10^{-7} Gt of carbon to the atmosphere annually). The resulting drift of the model control over 2000 years is 7×10^{-7} ‰ for $\delta^{13}C^{atm}$, and $+2 \times 10^{-4}$ ppm for pCO_2^{atm}.

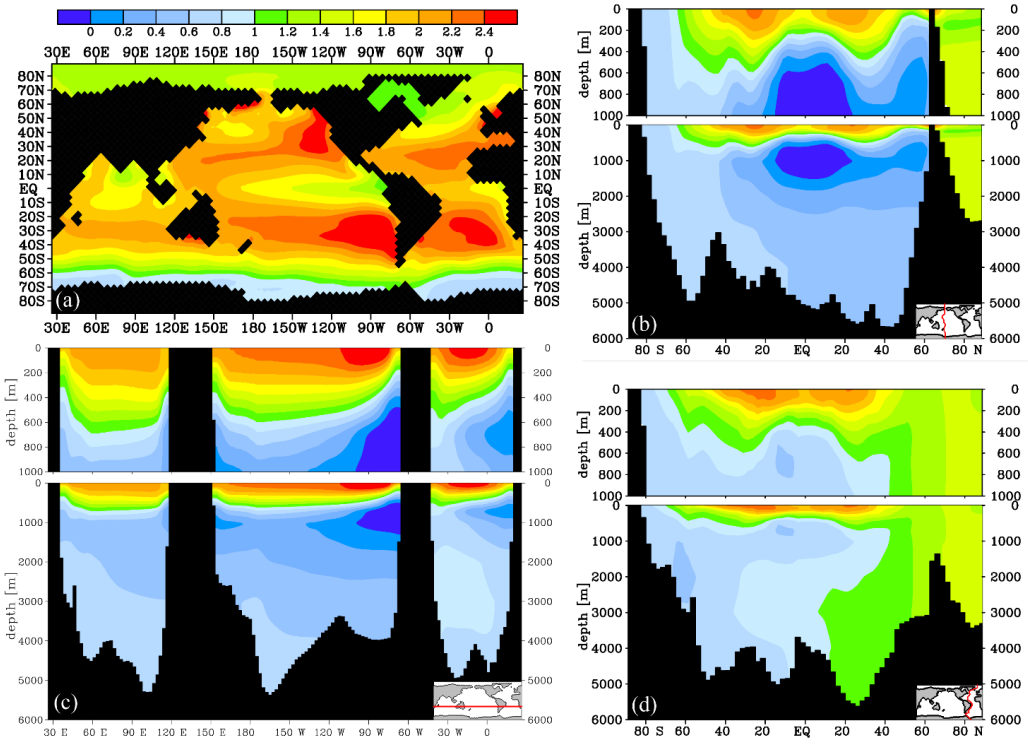

Figure 1. Modelled $\delta^{13}C$ of DIC [‰] distribution for the model control run: (a) $\delta^{13}C$ at 25 m depth, (b) Pacific transect of $\delta^{13}C$, (c) zonal transect of $\delta^{13}C$ at 26° S, and (d) Atlantic transect of $\delta^{13}C$.

3.2 Air–sea gas exchange versus biology

The contribution of biology based on Eqs. (2) and (3) to the $\delta^{13}C$ distribution is presented in Fig. 2, broadly in agreement with previous studies (Kroopnick, 1985; Schmittner et al., 2013). The contribution of biology to the modelled $\delta^{13}C$ distribution is generally below 45 % and has a steep gradient from the surface to the deep ocean. The (thermodynamic) fractionation effect of air–sea gas exchange on $\delta^{13}C$ is strongly impeded by the long equilibration time of $\delta^{13}C$, which leaves room for biological processes to contribute significantly to $\delta^{13}C$ and $\Delta\delta^{13}C$ (Lynch-Stieglitz et al., 1995; Murnane and Sarmiento, 2000; Schmittner et al., 2013; Eide et al., 2017a). In the ocean below 250 m, the influence of biology increases to 35 %–45 % due to the

remineralisation of POC, with the exception of the Arctic Ocean, where no POC production is modelled due to the sea ice cover (Figs. 2b and S1). $\delta^{13}C_{bio}^{perc}$ is close to 50 % around 1000 m depth in the northern Pacific and Indian oceans, due to the old water masses located there, which have accumulated a large fraction of remineralised DIC. At the surface, air–sea gas exchange dominates the $\delta^{13}C$ signature of DIC, as is visible from the low $\delta^{13}C_{bio}^{perc}$ (Fig. 2a). The only exception at the surface is in upwelling regions, where a relatively high $\delta^{13}C_{bio}^{perc}$ is expected due to high POC production and upwelled remineralised carbon. High $\delta^{13}C_{bio}^{perc}$ generally corresponds to a low-$\delta^{13}C$ water mass (compare Figs. 1 and 2), as expected from the upwelling of ^{13}C-depleted DIC and modelled and observed close to the Antarctic continent (Fig. 1a and observations by Eide et al., 2017a). The results presented in Fig. 2 appear to be quite robust as $\delta^{13}C_{bio}^{perc}$ typically does not change by more than 5 %–10 % for the wide range of biogeochemical states, as is explored in the sensitivity experiments presented below.

3.3 Sensitivity of $\Delta\delta^{13}C$ and $\delta^{13}C$

3.3.1 Air–sea gas exchange of carbon

Atmospheric and marine carbon isotopic ratios are generally in thermodynamic disequilibrium due to their relatively long equilibration timescales compared to the time of contact of a water parcel with the atmosphere. CO_2 equilibration through the air–sea interface takes ~ 4 months (Jones et al., 2014) and is inversely related to the Revelle buffer factor, and slowed down by a factor of ~ 20 compared to inert gases due to carbon speciation (i.e. the adjustment of the bicarbonate pool). Again ~ 10 times slower than CO_2, the air–sea equilibration of the atmospheric isotope ratio $^{13}CO_2$ / $^{12}CO_2$ (i.e. $\delta^{13}C^{atm}$) with marine $DI^{13}C$ / $DI^{12}C$ (i.e. $\delta^{13}C$) takes ~ 4 years (Jones et al., 2014). The equilibration timescale of the carbon isotopes is not facilitated by the buffering reaction of CO_2 with H_2O, but instead depends on the DIC : CO_2 ratio of seawater (Broecker and Peng, 1974; Jones et al., 2014; Galbraith et al., 2015). Over

90 % of the surface ocean $\delta^{13}C$ signature is set by air–sea gas exchange outside of upwelling regions across the world's oceans (Fig. 2), making the equilibration across the air–sea interface important for surface ocean $\delta^{13}C$. Understanding the effects of equilibration across the air–sea interface is thus key to understanding global surface ocean $\delta^{13}C$ signatures. Here we explore two extreme cases, very slow but non-zero gas exchange ("gas slow", gas exchange rate divided by 4) and very fast gas exchange to bring the air–sea equilibration close to equilibrium ("gas fast", gas exchange rate multiplied by 4).

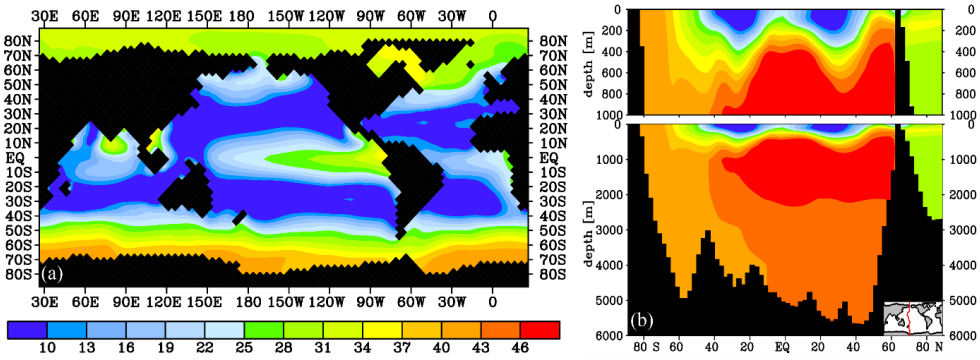

Figure 2. $\delta^{13}C_{bio}^{perc}$, the contribution of biology to the local $\delta^{13}C$ signal (%), as calculated using Eq. (4) at (a) 25 m depth and (b) a Pacific transect. The remainder of 100 % is attributed to air–sea gas exchange. The $^{13}C_{bio}$ and $^{13}C_{AS}$ values in per mille are very similar to the values found by Schmittner et al. (2013).

Our results show that the effects of changes in air–sea gas exchange on $\delta^{13}C$ mainly depend on the prior disequilibrium $\delta^{13}C_{diseq}$ ($\delta^{13}C_{diseq}$ = $\delta^{13}C$-$\delta^{13}C_{eq}$, where $\delta^{13}C_{eq}$ represents the $\delta^{13}C$ value a water parcel would have had if it would have fully equilibrated with the atmosphere; see also Gruber et al., 1999). Full isotopic equilibrium with the atmosphere results in a $\delta^{13}C_{surface}$ of ~ 0.5 to ~ 4 ‰ at low and high latitudes, respectively (Menviel et al., 2015), where the range is caused by the temperature-dependent fractionation (Mook et al., 1986; Zhang et al., 1995). In this study, modelled ε is between 7.7 ‰ and 11 ‰. This thermodynamic effect increases the difference between $\delta^{13}C_{surface}$ and $\delta^{13}C_{eq}$ at the poles (Menviel et al., 2015), thus increasing the potential of high-latitude surface water to be affected by air–sea gas exchange fluxes.

Our gas exchange experiments (Table 1) show a transient phase where the net global air–sea gas exchange flux F_{net} is non-zero, which affects pCO_2^{atm} until a new quasi-equilibrium is established (Fig. S3). We find an increase in pCO_2^{atm} by 10 ppm (slow gas exchange) and a decrease by 4 ppm (fast gas exchange) after 2000 years, respectively. If gas exchange is only changed in the SO (i.e. for 22 % of the global ice-free ocean area), an effect of 3.7 and -0.7 ppm is found after 2000 years (Table 2). Gas exchange in the SO can thus cause a disproportionate response (~ 30 % of the sensitivity) in pCO_2^{atm}. These changes occur in the first ~ 600 years of the sensitivity experiments (Fig. S3), with the strongest changes occurring after ~ 100 years. The air–sea pCO_2 difference is smaller at increased gas exchange rates and larger at reduced gas exchange rates (Fig. S4).

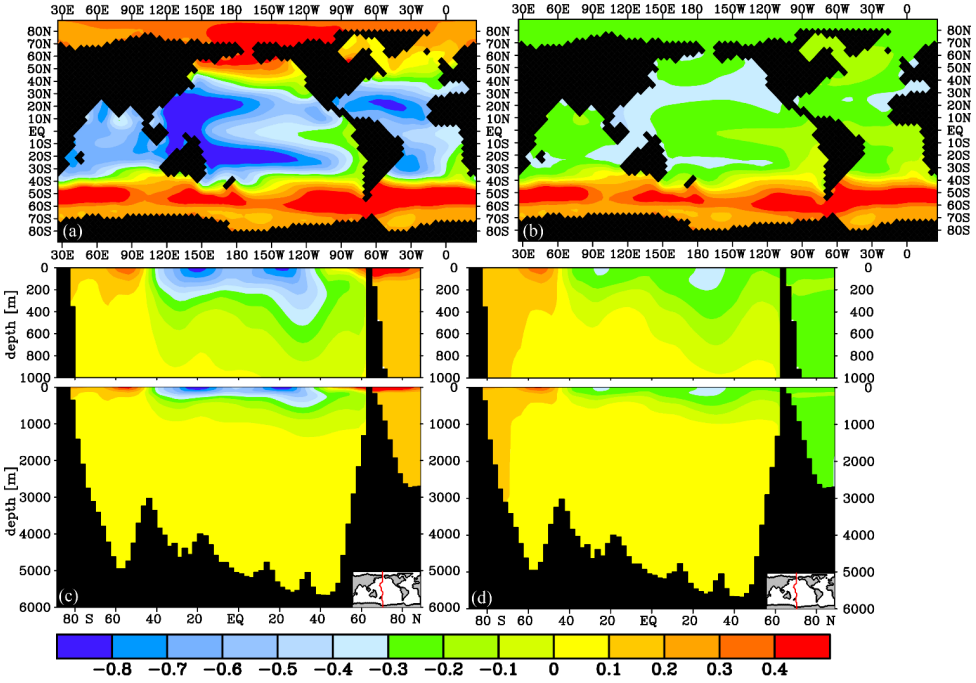

Figure 3. $\delta^{13}C$ of DIC (‰) difference after 2000 years for the fast gas exchange experiments (experiment control): global experiments (a, c) and SO-only experiments (b, d), at 25 m depth (a, b) and as a Pacific transect of $\delta^{13}C$ difference (c, d).

$\delta^{13}C^{atm}$ decreases by 0.3 ‰ during fast gas exchange and increases by 0.2 ‰ when the gas exchange rate is reduced. This is explained by the increase in the global amount of air–sea gas exchange F_{u+d} in the fast gas exchange experiment (4 times more, at 542 Gt C yr^{-1}). Such an increase leads to a smaller thermodynamic disequilibrium, which increases the mean marine $\delta^{13}C$ and lowers $\delta^{13}C^{atm}$. Slow gas exchange reduces F_{u+d} (by 73 % to 36 Gt C yr^{-1}), thus decreasing the role of air–sea gas exchange on surface ocean $\delta^{13}C$. This results in an increased contrast between atmospheric and surface ocean $\delta^{13}C$, which explains the increase in $\delta^{13}C^{atm}$. Moreover, our SO-only experiments show that these effects on $\delta^{13}C^{atm}$ are more pronounced if gas exchange only changes in the SO. This indicates that the remainder of the ocean offsets part of the atmospheric sensitivity to SO change.

Table 2. Results of pCO_2^{atm} (ppm) and $\delta^{13}C^{atm}$ (‰) for all sensitivity experiments.

	Global experiments		**SO-only experiments**	
	pCO_2^{atm}	$\delta^{13}C^{atm}$	pCO_2^{atm}	$\delta^{13}C^{atm}$
Control	279	-6.5	-	
Gas exchange				
Fast	275	-6.8	278	-7.0
Slow	289	-6.3	283	-6.2
Biological pump				
POC: Efficient	256	-6.3	275	-6.5
POC: Inefficient	292	-6.7	282	-6.5
V_{max}	-		235	-6.1
Ice				
Large	-		287	-6.2
Small	-		272	-6.6

$\delta^{13}C$ shows a different response in high latitudes compared to the lower latitudes in the surface ocean (Figs. 3a and S5): an increased air–sea gas exchange rate lowers the surface ocean $\delta^{13}C$ of DIC by 0.2 ‰ to 0.9 ‰ at the lower latitudes and increases

surface ocean $\delta^{13}C$ at high latitudes by 0.2 ‰–0.5 ‰ (Figs. 3 and 4). The direction of the response indicates whether $\delta^{13}C_{diseq}$ is positive or negative, and is in line with previous studies (Schmittner et al., 2013; Galbraith et al., 2015) that show that the disequilibrium is negative ($\delta^{13}C < \delta^{13}C_{eq}$) at high latitudes and in low-latitude upwelling regions, and positive elsewhere. The sign of $\delta^{13}C_{diseq}$, and thus the direction of the $\delta^{13}C$ response, is understood from the difference between the natural $\delta^{13}C$ distribution (Fig. 1) and the $\delta^{13}C_{eq}$, which depends on thermodynamic fractionation (Sect. 2). At increased gas exchange rates (i.e. closer to equilibrium), $\delta^{13}C$ has to increase in cool high-latitude surface waters and has to decrease in warm low-latitude surface waters in order to get closer to equilibrium (Menviel et al., 2015; Murnane and Sarmiento, 2000). The net effect of a slower gas exchange rate on surface ocean $\delta^{13}C$ is less pronounced than the effect of an increased gas exchange rate (Figs. S5, 3). The smaller effects seen for slow gas exchange indicate that the control model ocean is a "slow ocean", i.e. closer to (very) slow gas exchange than to thermodynamic equilibrium (infinitely fast gas exchange).

The effect of the gas exchange rate on marine $\delta^{13}C$ is mostly established in the top 250 to 1000 m of the water column (Figs. 3c, d, 4). Recording this air–sea gas exchange signal thus strongly depends on the reliability of planktic $\delta^{13}C$-based $\delta^{13}C_{surface}$ reconstructions and knowledge of the living depth represented by the planktic foraminifera. The signal penetrates deepest (to ~ 2000 m depth) into the North Atlantic (Fig. 4), where $\delta^{13}C$ is strongly influenced by air–sea gas exchange (Fig. 2a). However, the interpretation of variations in North Atlantic benthic $\delta^{13}C$ as coming partly from air–sea gas exchange (Lear et al., 2016) is not supported by our experiment. Due to the limited export of the $\delta^{13}C$ signal to depth, the sensitivity of $\Delta\delta^{13}C$ to the gas exchange rate mainly comes from surface ocean $\delta^{13}C$. Globally, the $\Delta\delta^{13}C$ is weakened to 0.87 ‰ when the thermodynamic disequilibrium is decreased (i.e. "Gas fast", Fig. 5) and $\Delta\delta^{13}C$ strengthens to 1.32 ‰ when the thermodynamic disequilibrium is increased ("Gas slow", Fig. 5). The extent to which thermodynamic equilibrium can develop is thus an efficient way to change the biologically induced

$\Delta\delta^{13}C$ (Murnane and Sarmiento, 2000); however, this is only true at lower latitudes where $\delta^{13}C_{diseq}$ is positive: the direction of the high-latitude SO $\Delta\delta^{13}C$ sensitivity mirrors the sensitivity of the low-latitude regions (Fig. 4) as well as the global mean due to its negative $\delta^{13}C_{diseq}$.

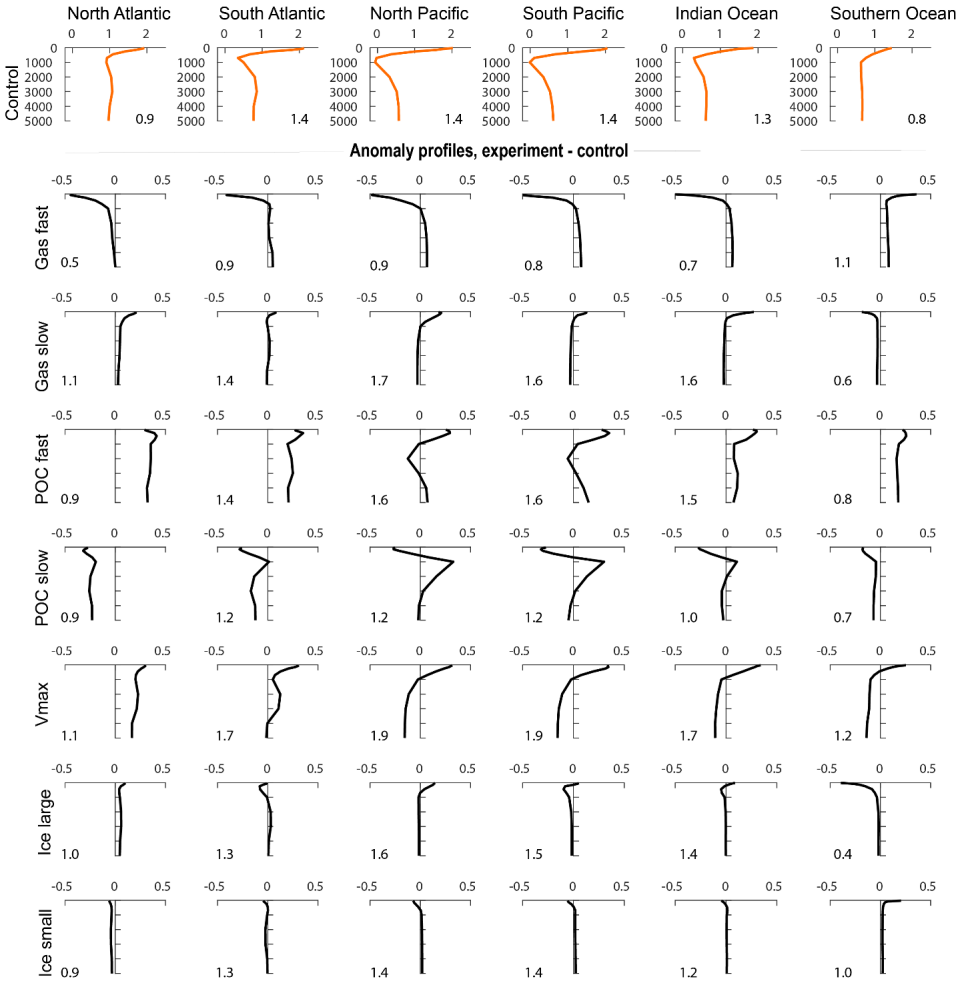

Figure 4. Volume-weighted basin mean anomaly profiles of $\delta^{13}C$ after 2000 years, with respect to the control profiles (upper row). $\Delta\delta^{13}C$ denoted per basin in the lower right (control) and lower left (sensitivity experiments) corner of each subgraph. Results are presented for the global gas exchange and POC sinking experiments. Basin extent is visualised in Fig. S8.

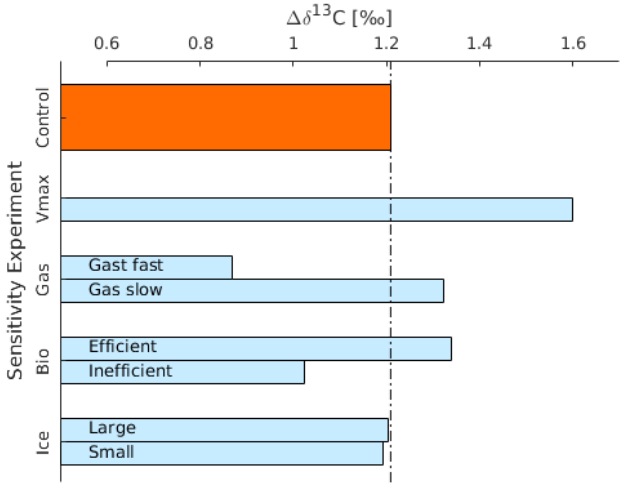

Figure 5. Global mean $\Delta\delta^{13}C$ after 2000 years for the different sensitivity experiments (Table 1). "Bio – Efficient" represents the high POC sinking rate experiment, "Bio – Inefficient" the slow POC sinking rate experiment. The results for the Southern Ocean-only experiments (Sect. 2) are described in the text.

3.3.2 The biological pump: POC sinking rate

The net effect of a regionally changed biological pump efficiency depends on the sequestration efficiency, which depends on the interplay between the biological pump and ocean circulation (DeVries et al., 2012). A more efficient biological pump (here, a higher POC sinking rate) leads to a loss of carbon to the sediments, which affects pCO_2^{atm} and $\delta^{13}C^{atm}$ on millennial timescales. Here we present results from a 2000-year simulation (as for the other experiments), which are thus transient results. A full equilibrium of the system could take as long as 200 000 years (Roth et al., 2014). On these long timescales other processes and feedbacks would occur (Tschumi et al., 2011), which complicates the attribution of changes to a primary trigger. A fast POC sinking rate leads to a pCO_2^{atm} decrease of 23 ppm and higher (+0.2 ‰) atmospheric $\delta^{13}C$ after 2000 years (Table 2, Fig. S3) as well as an increase in mean ocean $\delta^{13}C$ of 0.15 ‰, caused by the transient sediment burial of low-$\delta^{13}C$ POC. The transient imbalance between weathering and burial fluxes can thus cause profound changes in both marine and atmospheric $\delta^{13}C$, and moreover provides an important feedback for the longterm marine carbon cycle (Tschumi et al., 2011; Roth et al., 2014). In our

experiment, an efficient biological pump leads to a global ~ 6 % decrease in the amount of air–sea gas exchange F_{u+d} because of efficient export of carbon to depth, thereby lowering the net upward advection of carbon. A mirrored but weaker response is modelled for a decrease in biological pump efficiency: halving the POC sinking rate leads to a 13 ppm increase in pCO_2^{atm} (of which 23 % can be explained by the SO) and a more negative atmospheric $\delta^{13}C$ (-6.7 ‰) and 7 % increased F_{u+d} (Table 2, Fig. S3).

Surface ocean $\delta^{13}C$ is mostly influenced by the changes in productivity and the vertical displacement of the POC remineralisation depth. The deepening of the remineralisation depth has been extensively discussed in the literature (Boyle, 1988; Keir, 1991; Mulitza et al., 1998; Roth et al., 2014) and likely explains lowered mid-depth glacial $\delta^{13}C$ together with changes in ocean circulation (for example, Toggweiler, 1999). POC sinking removes nutrients and preferentially light ^{12}C carbon from the surface ocean, while exporting them to the deep ocean. If POC sinking rates are high, this increases the mean surface ocean $\delta^{13}C$ (contributing to the $\delta^{13}C^{atm}$ increase) by 0.12 ‰ and lowers mean deep ocean $\delta^{13}C$ by 0.01 ‰ (Fig. 6) – with values corrected for the overall 0.15 ‰ increase in marine $\delta^{13}C$, which occurs due to transient imbalance between weathering and sediment burial. Therefore, even though the absolute export production is globally reduced by 26 %, the biological pump is more efficient as any new nutrients in the surface ocean will immediately be used and exported. With a halving of the POC sinking rate, the remineralisation is confined closer to the surface ocean (Fig. 4). The net effect is that surface ocean $\delta^{13}C$ is reduced (by a mean of 0.21 ‰ – corrected for the mean ocean change of 0.04 ‰) throughout the ocean (Fig. 4), because the fractionation effect during photosynthesis is counteracted by the remineralisation of POC (which would normally have occurred at depth). The SO plays a relatively minor role in the sensitivity to the POC experiments (Fig. 6b). Changes in deep ocean $\delta^{13}C$ depend on the water mass age (Fig. 6c): old water (North Pacific) has a larger remineralisation signal when the biological pump is efficient. Independent of the biological pump efficiency, the relatively young

waters of the deep North Atlantic generally adopt about the same $\delta^{13}C$ signal as the surface ocean $\delta^{13}C$, which is set by air–sea gas exchange. This is in agreement with a relatively low $\delta^{13}C_{bio}^{perc}$ estimate for the deep North Atlantic (~ 30 %).

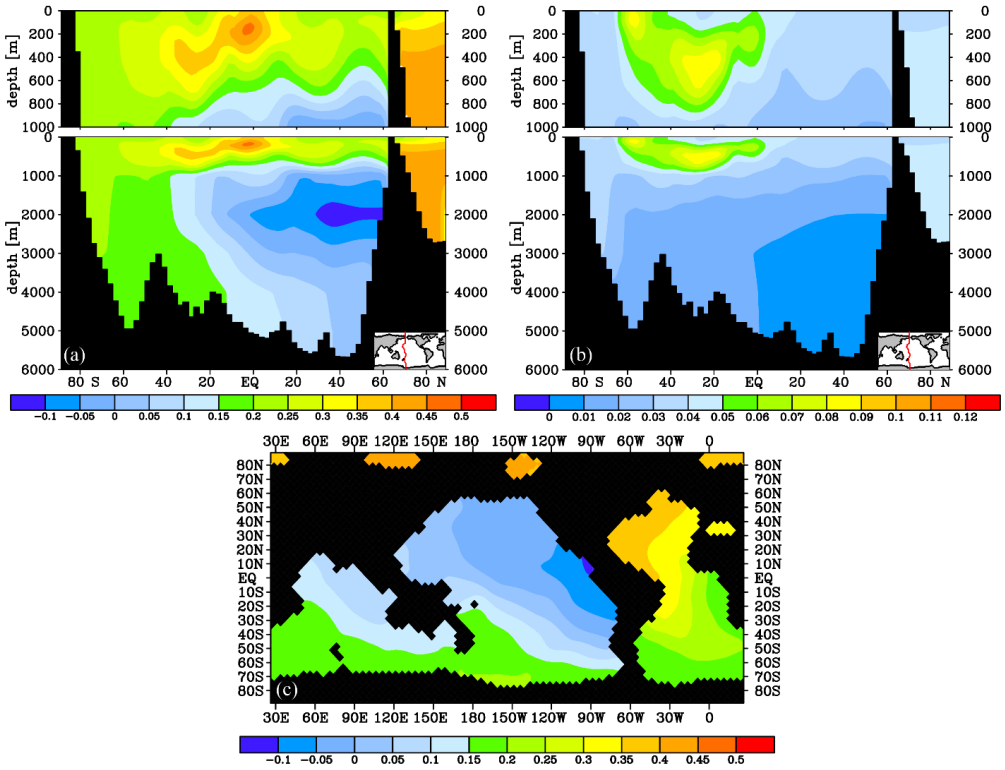

Figure 6. $\delta^{13}C$ of DIC (‰) difference after 2000 years for the POC sinking rate experiments (experiment control): (a) the global efficient biological pump (high POC sinking rate) experiment for a Pacific transect and (b) the SO-only efficient biological pump experiment for a Pacific transect and (c) the global efficient biological pump experiment at 3000 m depth. Note the different scales.

The sensitivity of $\Delta\delta^{13}C$ to changes in POC sinking rate depends strongly on location (Figs. 4 and 6). In general, the $\Delta\delta^{13}C$ is strengthened for an increased biological pump efficiency (Fig. 5), and this effect is stronger with water mass age (Figs. 6c and 4). The downward shift of the remineralisation depth of low-$\delta^{13}C$ POC drives this increase in $\Delta\delta^{13}C$, a mechanism discussed by Boyle (1988) and Mulitza et al. (1998), among others, to understand glacial $\Delta\delta^{13}C$ increase. Our results show that the vertical displacement of the $\delta^{13}C$ profile is most pronounced in the North and South Pacific (Fig. 4). The North Atlantic $\Delta\delta^{13}C$ is much less affected as these waters are mostly

influenced by air–sea gas exchange. Instead, the entire North Atlantic profile is shifted more than in the other ocean basins (Fig. 4). $\Delta\delta^{13}C$ weakens for a reduced biological pump efficiency (Figs. 4 and 5), especially in older water where $\delta^{13}C_{bio}^{perc}$ is higher (Fig. 2a). It is worth noting, however, that the changes in $\Delta\delta^{13}C$ in the SO are comparably small because the vertical mixing in the SO of the low-$\delta^{13}C$ deep water mostly causes shifts in the entire $\delta^{13}C$ profile, not a change in the gradient (Fig. 4).

3.3.3 The biological pump: SO nutrient depletion

Consistent with previous studies (Sarmiento et al., 2004; Marinov et al., 2006; Primeau et al., 2013), we find a large atmospheric impact of our SO nutrient depletion experiment. The high SO nutrient uptake efficiency (i.e. an efficient biological pump) causes a 44 ppm reduction in pCO_2^{atm} after 2000 years. The V_{max} experiment reaches quasi-equilibrium after ~ 800 years, as seen from the time evolution of pCO_2^{atm} and $\delta^{13}C^{atm}$ (Fig. S3). $\delta^{13}C^{atm}$ increases to -6.1 ‰ due to the increased surface ocean $\delta^{13}C$ (Fig. 7a). This 0.4 ‰ increase is high compared to the results of Menviel et al. (2015), who found a $\delta^{13}C^{atm}$ sensitivity of 0.1 ‰–0.2 ‰ in response to changes in SO nutrient utilisation. The different development time compared to the fast POC sinking rate experiment is explained by the absence of longterm loss of carbon to the sediments in the V_{max} experiment, because transport and water-column remineralisation within the SO limits an increase in POC burial there. In the SO, net carbon uptake (F_{net}) increases fourfold to 1.5 Gt C yr^{-1} (Fig. S6) because the high nutrient and carbon consumption transport carbon into the ocean interior and do not permit CO_2 to escape to the atmosphere.

SO export production of POC is increased (Fig. S7) by a factor of 2.4, causing global POC export production to increase by 15 %, albeit reducing lower-latitude productivity (non-SO up to ~ 35° N) by 13 %. This relocation of global POC export production in response to SO increased nutrient uptake efficiency is in agreement with earlier studies (Marinov et al., 2006; Primeau et al., 2013). The increased surface ocean $\delta^{13}C$ signature everywhere north of the SO sea ice edge (Fig. 7a) is in the SO

attributed to increased POC export production counteracted by a decreased F_{u+d} (which would reduce $\delta^{13}C_{surface}$ in the SO because of the negative $\delta^{13}C_{diseq}$; Figs. 3 and S5). At lower latitudes, the decreased F_{u+d} (which increases $\delta^{13}C_{surface}$ in lower latitudes because of the positive $\delta^{13}C_{diseq}$; Figs. 3 and S5) dominates the effect of the 13 % lower POC export production on $\delta^{13}C_{surface}$.

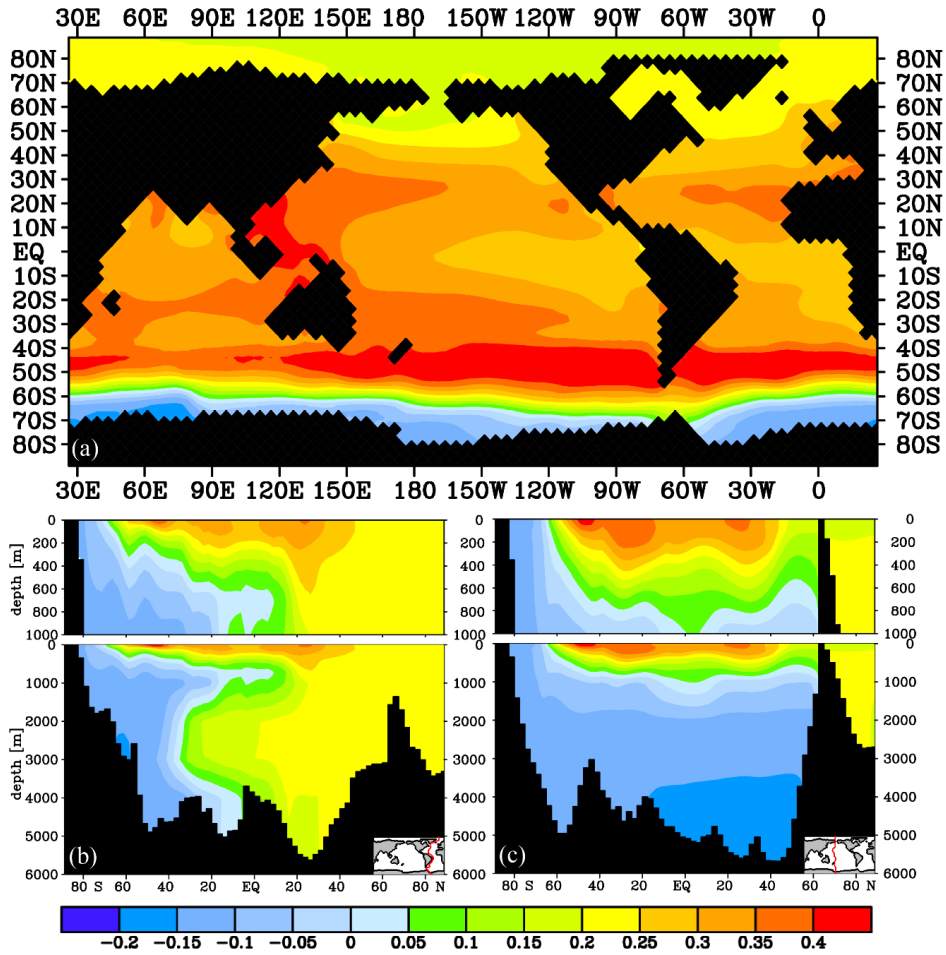

Figure 7. $\delta^{13}C$ of DIC (‰) difference after 2000 years for the V_{max} nutrient depletion experiment (experiment control): (a) at 25 m depth and for (b) an Atlantic transect and (c) a Pacific transect.

At depth and under the sea ice in the Antarctic, where deep water upwells, the imprint of additional POC remineralisation at depth decreases $\delta^{13}C$ of DIC (Fig. 7). This decrease in $\delta^{13}C$ is only visible in water masses downstream of the SO (Fig. 7b and c)

and is most pronounced in the deep North Pacific (Fig. 7c). The increased nutrient uptake rate in the SO increases global mean $\Delta\delta^{13}C$ by 0.4 ‰ (Fig. 5) as well as increasing $\Delta\delta^{13}C$ in all ocean basins (Fig. 4), as seen for the fast POC sinking rate experiment. $\Delta\delta^{13}C$ is affected more in older waters, where a more pronounced remineralisation imprint has developed (Fig. 4). Besides effects on the $\delta^{13}C$ distribution (Fig. 7), the O_2 and PO_3^{4-} distributions change as well: the O_2 distribution is reorganised such that surface ocean O_2 is increased (by up to 20 µmol kg^{-1}, with largest changes in the SO), while deep ocean O_2 is reduced downstream of the SO (by up to 40 µmol kg^{-1}). Surface ocean PO_3^{4-} is reduced mostly in the SO (by up to 0.8 µmol kg^{-1}). This signal is, however, too small to significantly increase mean deep ocean PO_3^{4-}. This implies a reduction in global preformed phosphate governed by the efficient nutrient uptake in the SO; see also Primeau et al. (2013). SO nutrient drawdown can thus cause negligible mean (deep) ocean PO_3^{4-} and $\delta^{13}C$ changes, despite causing large changes in local $\delta^{13}C$ and $\Delta\delta^{13}C$ through the interplay between biology and air–sea gas exchange. Interesting in light of glacial proxy interpretation, the fit to the $\delta^{13}C$: PO_3^{4-} relationship is improved throughout the ocean for the V_{max} experiment, similar to the effects of the "Gas slow" experiment (Fig. 8). Changes in the goodness of fit of $\delta^{13}C$ and PO_3^{4-} data to the $\delta^{13}C$: PO_3^{4-} relationship (i.e. $\delta^{13}C_{bio} = 3.18 - 1.05 \times PO_3^{4-}$, Sect. 2) are usually interpreted as changes in ventilation or air–sea gas exchange (Lear et al., 2016; Eide et al., 2017b). However, here we show that changes in the fit represent the relative importance of biology and air–sea gas exchange in determining $\delta^{13}C$, as both changes in $\delta^{13}C_{diseq}$ (i.e. gas exchange rate experiments) and changes in the biological pump can affect the goodness of fit to the $\delta^{13}C$: PO_3^{4-} relationship (Fig. 8).

3.3.4 Southern Ocean sea ice cover

The sea ice cover of the SO changes considerably over glacial–interglacial cycles, as well as on seasonal timescales (Crosta, 2009) and Fig. A22 therein). In general, the model sea ice cover will inhibit light penetration into the surface ocean and limit air–

sea gas exchange based on its thickness (Sect. 2). In the sensitivity experiments we assume complete inhibition of both light and air–sea carbon exchange by the sea ice. In this section we thus explore the effect of both biological production and air–sea gas exchange in two extreme cases, (i) the largest realistic sea ice cover based on the glacial maximum winter extreme (50° S) and (ii) the smallest sea ice cover based on the contemporary summer minimum sea ice extent (70° S).

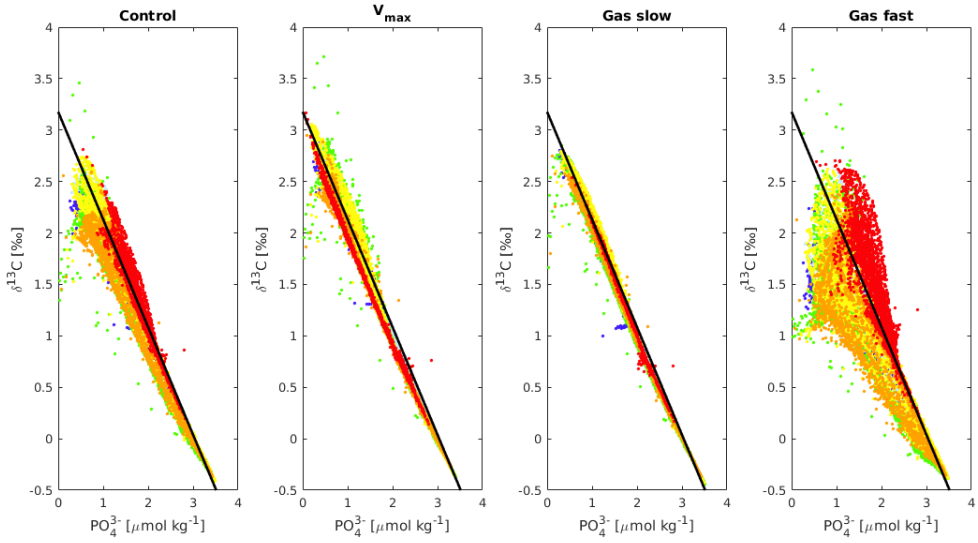

Figure 8. $\delta^{13}C$ versus PO_3^{4-} for the control, V_{max}, "gas slow" and "gas fast" experiments for all ocean basins except the Nordic Seas (i.e. basins A to F in Fig. S8). Dark blue = A/North Atlantic, Light blue = B/South Atlantic, Red = C/Southern Ocean, Yellow = D/South Pacific, Green = E/North Pacific, Orange = F/Indian Ocean. The black line is the $\delta^{13}Cbio = 3.18 - 1.05 \times PO_3^{4-}$ relationship, i.e. the relationship between $\delta^{13}C$ and PO_3^{4-} expected if only biology affected $\delta^{13}C$ (Sect. 2). Deviations from the black line represent the relative importance of air–sea gas exchange compared to biology for $\delta^{13}C$.

Note that there is a constant sea ice cover about north of 70° N and south of 60° S in the control run of the model. Therefore, the strongest marine $\delta^{13}C$ change is expected south of 60° S for a decreased sea ice cover and between 50° and 60° S for an increased sea ice cover, as this is the area where ice cover is altered relative to the control run. Ocean circulation changes that could result from a changed sea ice cover are not taken into account, as we want to study the potential isolated effect of sea ice on $\delta^{13}C$ through biological and air–sea gas exchange changes. Both local and global air–sea carbon fluxes are influenced by a change in the SO sea ice cover, which results

in changes in pCO_2^{atm} and $\delta^{13}C^{atm}$. In our experiment, pCO_2^{atm} increases by 9 ppm for an increased sea ice cover and decreases by 6 ppm for a decreased sea ice cover (Table 2, Fig. S3). As noted in Sect. 3.3.1, a change in pCO_2^{atm} is governed by a transient change in the net air–sea gas exchange flux F_{net} until a new equilibrium is established. An extended ice cover causes more CO_2 to remain in the atmosphere because the additional ice covers a part of the SO that is a sink for CO_2 (Fig. S4 – Control). As the net global air–sea gas exchange F_{net} approaches equilibrium, the non-SO ocean therefore becomes a smaller source for carbon. This reduces the net gas exchange F_{net} inside and outside of the SO by ~ 40 %–50 %. Our results show that the effects of a changed sea ice cover on pCO_2^{atm} are yet to be fully understood: Stephens and Keeling (2000) for example modelled a strong decrease in pCO_2^{atm} in response to an increased sea ice cover south of the Antarctic Polar Front, because they mostly cover a part of the SO that is a source of carbon to the atmosphere. In our study, the reduction in pCO_2^{atm} by 6 ppm due to a reduced sea ice cover is attributable to the POC production in the previously ice-covered area between ~ 60° and 70° S. In a sensitivity experiment where the ice cover influences air–sea gas exchange only, the sea ice retreat leads to an increase in pCO_2^{atm} because the region below the ice is strongly supersaturated in carbon with respect to the atmosphere. The increased sea ice cover leads to a complete suppression of air–sea gas exchange south of 50° S. Since this region is in negative carbon isotopic disequilibrium with the atmosphere ($\delta^{13}C < \delta^{13}Ceq$), the ice cover inhibits a $\delta^{13}C$ flux into the ocean. As a result, pCO_2^{atm} increases to -6.2 ‰, while the opposite happens for a reduced sea ice cover, leading to a lowered pCO_2^{atm} (-6.6 ‰).

The increased sea ice cover over the SO results in a surface ocean $\delta^{13}C$ reduction relative to the control of -0.5 ‰ to -0.1 ‰ in the SO (Figs. 4 and 9), while $\delta^{13}C$ increases outside of the SO by 0 ‰–0.2 ‰ (Fig. 9a). The reduction is especially pronounced between 40 and 60° S. The ~ 40 % reduced POC export production in the SO due to light inhibition by the sea ice cover causes a major part of the SO surface $\delta^{13}C$ reduction, as the absence of photosynthesis will cause lower surface ocean $\delta^{13}C$.

Next to that, the reduced air–sea gas exchange F_{u+d} in the SO also leads to a lowered surface ocean $\delta^{13}C$ signature. About the opposite happens when we simulate a strongly decreased sea ice cover (only ice south of 70 S): a small reduction of $\delta^{13}C$ is modelled outside the SO, but the SO $\delta^{13}C_{surface}$ locally becomes up to ~ 0.8 ‰ higher relative to the control (Fig. 9b) as the increased amount of air–sea gas exchange F_{u+d} decreases the carbon isotopic disequilibrium and increases POC production in the newly exposed area, both acting to increase $\delta^{13}C$ of DIC.

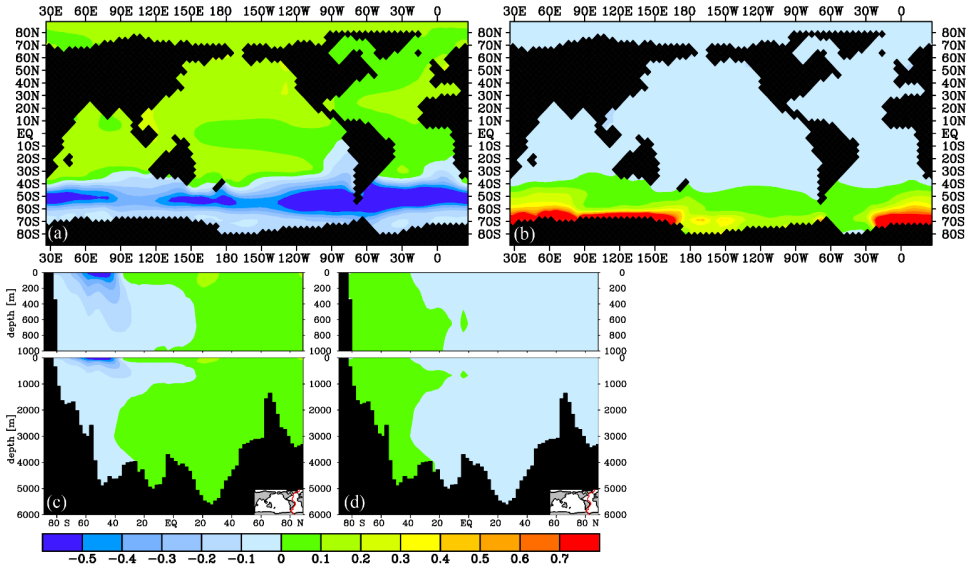

Figure 9. $\delta^{13}C$ of DIC (‰) difference after 2000 years for the Antarctic sea ice cover experiments (experiment control): the effect of a large (a, c) and small (b, d) Antarctic sea ice cover, for 25 m depth (a, b) and an Atlantic transect (c, d).

The effect of a changed ice cover on deep ocean $\delta^{13}C$ is less than ~ 0.1 ‰ (Fig. 9c, d) as the surface signal is diluted while it follows the general ocean circulation. As for air– sea gas exchange (Sect. 3.3.1), no pronounced deep ocean $\delta^{13}C$ signal is found outside of the SO due to sea ice cover changes (this is opposed to interpretations by Lear et al., 2016). Global mean $\Delta\delta^{13}C$ is not significantly affected by changes in the SO sea ice cover (Fig. 5) because the low- and high-latitude effects on $\delta^{13}C_{surface}$ cancel each other out. The SO $\Delta\delta^{13}C$, however, weakens considerably to 0.4 ‰ when the 50–60° S region becomes covered with sea ice and strengthens to 1 ‰ if the sea ice is

removed between 60 and 70° S (Fig. 4). The presence or absence of a sea ice cover should thus be clearly visible in especially planktic SO $\delta^{13}C$ sediment records. The effect on $\Delta\delta^{13}C$ spreads downstream of the SO, where $\Delta\delta^{13}C$ is increased by up to 0.2 ‰ in the Pacific Ocean for an increased SO sea ice cover (Fig. 4).

3.4 Modelled versus observed $\Delta\delta^{13}C$ variations

The variations in $\Delta\delta^{13}C$ on glacial–interglacial timescales provide researchers with a tracer to study the biogeochemical state of the past global ocean, under the condition that we can interpret (variations in) $\Delta\delta^{13}C$. The idealised perturbations made to the (Southern) Ocean in this study show that global mean $\Delta\delta^{13}C$ is particularly sensitive to an increased gas exchange rate and changes in the efficiency of the biological pump. Global mean $\Delta\delta^{13}C$ varies by up to about ±0.35 ‰ around the pre-industrial model reference (1.2 ‰) in response to biogeochemical change (Fig. 5) – under the assumption of a constant ocean circulation. However, the sensitivity of $\Delta\delta^{13}C$ to biogeochemical changes depends strongly on location for all sensitivity experiments (Fig. 4), possibly explaining part of the incoherency of reconstructed planktic and benthic foraminiferal $\delta^{13}C$ from sediment cores (Oliver et al., 2010). In general, such $\Delta\delta^{13}C$ reconstructions show $\Delta\delta^{13}C$ variations in ~ 1 ‰ over the past 350 000 years (Shackleton et al., 1983; Shackleton and Pisias, 1985; Boyle, 1988; Charles et al., 2010; Oliver et al., 2010; Ziegler et al., 2013). Ocean circulation changes explain at least part of these variations in $\Delta\delta^{13}C$ (Oppo et al., 1990; Heinze et al., 1991; Heinze and Hasselmann, 1993; Toggweiler 1999; Charles et al., 2010; Jansen, 2017). However, the changes in the biogeochemical state of the ocean imposed in our experiments show that variations in $\Delta\delta^{13}C$ could be strongly influenced by (SO) biogeochemistry as well. $\Delta\delta^{13}C$ is increased during glacials and reduced during interglacials across a large set of sediment cores (Boyle, 1988; Charles et al., 2010; Oliver et al., 2010; Ziegler et al., 2013). Rapid and large changes have been documented for SO $\Delta\delta^{13}C$ records (Ziegler et al., 2013), and here we show that biogeochemical changes in the SO affect $\Delta\delta^{13}C$ globally. Our results show that an increase in mean $\Delta\delta^{13}C$ could biogeochemically

result from slower gas exchange, increased POC sinking rates, or an increased nutrient uptake rate in the SO (Figs. 4 and 5). Such biogeochemical changes have been associated with glacial periods (for example, Ziegler et al., 2013) and are potential candidates to explain part of the $\Delta\delta^{13}C$ increase in interplay with stronger ocean stratification. Sedimentcore reconstructions of $\Delta\delta^{13}C$ show that an increased $\Delta\delta^{13}C$ can originate from a downward shift of the metabolic imprint of low-$\delta^{13}C$ POC, which would increase shallow $\delta^{13}C$ (Boyle, 1988; Mulitza et al., 1998; Toggweiler, 1999; Charles et al., 2010), and/or a deep ocean $\delta^{13}C$ decrease (Broecker, 1982; Boyle, 1988; Oliver et al., 2010), with little variation recorded for surface ocean $\delta^{13}C$. The absence of a clear surface $\delta^{13}C$ signal could in the SO be the net effect of an increased sea ice cover (locally decreasing $\delta^{13}C$; Figs. 4 and 9a) and an increased biological pump efficiency (locally increasing $\delta^{13}C_{surface}$; Figs. 6a and b, 7a) or increased SO thermodynamic equilibrium (Fig. 3a and b) – if these opposing signals get mixed. A pronounced deep ocean $\delta^{13}C$ decrease is associated with an efficient biological pump and older water masses in our study (Fig. 4). Interestingly, large local changes in deep ocean $\delta^{13}C$ and $\Delta\delta^{13}C$ do not necessarily imply changes in mean deep ocean PO_3^{4-} (Sect. 3.3.3).

The local character of the $\Delta\delta^{13}C$ sensitivity (Fig. 4) implies that correlations between sediment core $\Delta\delta^{13}C$ / $\delta^{13}C$ variations and global parameters (e.g. pCO_2) are not easily extrapolated to other sediment cores over large distances. Analysis of SO $\Delta\delta^{13}C$ reconstructions from sediment cores, at 42 and 46° S (Charles et al., 2010) for example, shows that there is a strong correlation between these cores and Northern Hemisphere climate fluctuations. We expect that this strong correlation does not exist for cores further south in the SO because our results indicate that the SO south of ~ 50–60° S often has a different $\Delta\delta^{13}C$ response to biogeochemical change than the rest of the ocean.

Interglacial periods are generally thought to be associated with a decrease in the efficiency of the biological pump and increased deep-ocean ventilation via southern-

sourced water masses (Gottschalk et al., 2016). Increased deep-ocean ventilation might be driven by increased winds (Tschumi et al., 2011), which would (apart from changing the SO circulation pattern) also increase gas exchange rates. Each of these processes indeed reduces mean $\Delta\delta^{13}C$ in our experiments (Fig. 5), although this is less pronounced in the SO (Fig. 4). However, the interglacial reduction of $\Delta\delta^{13}C$ seems to originate from a deep ocean $\delta^{13}C$ increase compared to the glacial deep ocean $\delta^{13}C$ (Broecker, 1982; Charles et al., 2010; Oliver et al., 2010). Our results show that neither an inefficient biological pump nor fast gas exchange can be associated with a pronounced deep sea $\delta^{13}C$ increase relative to our control, because their effects are restricted to the surface ocean. On the other hand, the interglacial decrease in $\Delta\delta^{13}C$ is a decrease compared to the glacial state: if glacial SO nutrient uptake was higher (V_{max}), a return to the "normal" state (i.e. the model control run) would result in a major decrease in $\Delta\delta^{13}C$ (Figs. 4 and 5).

3.5 The relationship between $\Delta\delta^{13}C$, $\delta^{13}C^{atm}$, and pCO_2^{atm}

One would expect variations in $\delta^{13}C^{atm}$ as well as $\Delta\delta^{13}C$ to correlate with variations in pCO_2^{atm}, because similar processes (biology and air–sea gas exchange) steer their distribution and concentrations (Shackleton and Pisias, 1985; this article). $\Delta\delta^{13}C$ is considered a promising proxy for reconstructions of pCO_2^{atm} for times predating icecore records (Lisiecki, 2010). Here we show that a positive linear relationship between $\delta^{13}C^{atm}$ and global mean $\Delta\delta^{13}C$ (Fig. 10a) holds over a wide range of biogeochemical states, as simulated in the sensitivity experiments. However, the negative linear relationship between pCO_2^{atm} and global mean $\Delta\delta^{13}C$ (Fig. 10b) is weak ($R^2 = 0.39$). Yet, previous studies do show the existence of a correlation between local $\Delta\delta^{13}C$ and pCO_2^{atm} (such as found by for example Dickson et al., 2008), and correlation of modified $\Delta\delta^{13}C$ between ocean basins with pCO_2^{atm} (Lisiecki, 2010). The effects of ocean circulation on glacial–interglacial $\delta^{13}C^{atm}$ changes, not studied here, are most pronounced in response to Antarctic Bottom Water formation rate variations and are of the order of 0 ‰–0.15 ‰ (Menviel et al., 2015). Our results show that $\delta^{13}C^{atm}$ varies

by up to about ±0.5 ‰ in response to biogeochemical changes (Table 2). Changes in the POC sinking rate lie approximately along a line in $\delta^{13}C^{atm}$: $\Delta\delta^{13}C$ space (Fig. 10a), suggesting that changes in the biological pump efficiency are important for the $\delta^{13}C^{atm}$: $\Delta\delta^{13}C$ relationship. Likewise, both the gas exchange rate and biological pump experiments lie along an approximate lines in pCO_2^{atm} : $\Delta\delta^{13}C$ space (Fig. 10b, albeit a different one – leading to a low total correlation).

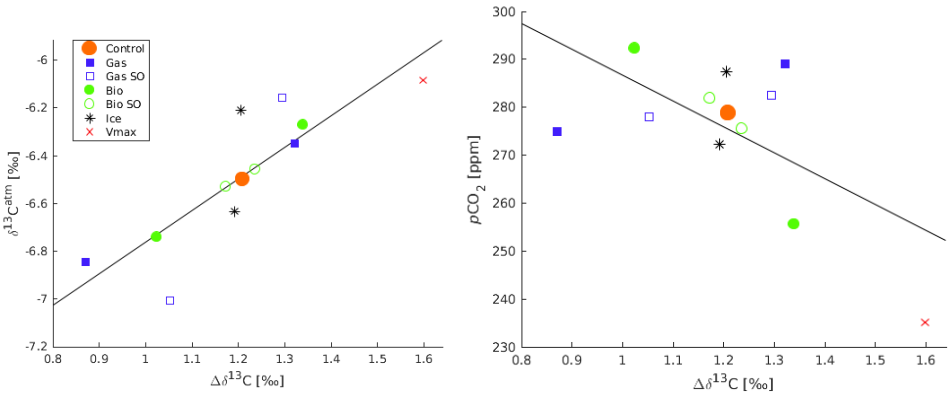

Figure 10. Relationships between global mean $\Delta\delta^{13}C$, $\delta^{13}C^{atm}$, and pCO_2^{atm}. (a) Global mean $\Delta\delta^{13}C$ versus $\delta^{13}C^{atm}$ of the different sensitivity experiments. R^2 of the best-fit line is 0.71, and the line is described by y = 1.3x - 8.1. (b) Global mean $\Delta\delta^{13}C$ versus pCO_2^{atm} of the different sensitivity experiments. R^2 of the best-fit line is 0.39, and the line is described by y = -54x + 341.

Changes in air–sea gas exchange (as simulated in the gas exchange and sea ice cover experiments) affect $\delta^{13}C^{atm}$ more than $\Delta\delta^{13}C$. This confirms the idea that $\Delta\delta^{13}C$ is governed by biological processes and will also set $\delta^{13}C^{atm}$, unless air–sea gas exchange gets the chance to dominate $\delta^{13}C^{atm}$. The high potential of SO air–sea gas exchange to change $\delta^{13}C^{atm}$ (Table 2: sea ice and gas exchange rate experiments) complements recent studies showing that increased SO ventilation of deep ocean carbon is a likely candidate for glacial–interglacial $\delta^{13}C^{atm}$ excursions – which are of the order of 0.5 ‰ (Lourantou et al., 2010; Menviel et al., 2015; Bauska et al., 2016; Eggleston et al., 2016).

4 Summary and conclusions

This study addresses the sensitivity of modelled marine and atmospheric $\delta^{13}C$ and $\Delta\delta^{13}C$ to changes in biogeochemical parameters under constant ocean circulation, focusing on the contribution of the SO (the ocean south of 45° S, 22 % of the global ice-free ocean area). Variations in $\Delta\delta^{13}C$ recorded in sediment records are sensitive to ocean circulation changes as shown in previous studies, but here we show that the biogeochemical state of the (Southern) Ocean can also have large effects on $\Delta\delta^{13}C$ across all ocean basins. Using the ocean biogeochemistry general circulation model HAMOCC2s, a set of sensitivity experiments was carried out, which focuses on the biogeochemical aspects known to be important for $\delta^{13}C$ and $\Delta\delta^{13}C$. Specifically, the experiments explore changes in air–sea gas exchange rate, sea ice extent (influencing both biological production and the air–sea gas exchange of carbon), and the efficiency of the biological pump through the POC sinking rate and nutrient uptake rate.

The results show the important role of the SO in determining global $\delta^{13}C$ and $\Delta\delta^{13}C$ sensitivities, as well as the strong spatial differences in these. A new quasi-equilibrium state developed mostly within the first 100–800 years of the sensitivity experiments, except for the POC sinking experiment, where an imbalance between weathering and burial causes a long-term drift. The $\delta^{13}C$ signature is governed by different processes depending on location: air–sea gas exchange sets surface ocean $\delta^{13}C$ in all ocean basins, contributing 60 %–100 % to the $\delta^{13}C$ signature. At depth and with increasing water mass age, the influence of biology increases to 50 % in the oldest water masses (North Pacific) due to POC remineralisation. This spatial pattern behind the $\delta^{13}C$ signature of a water parcel results in a non-uniform sensitivity of $\delta^{13}C$ to biogeochemical change. Global mean $\Delta\delta^{13}C$ varies by up to about ±0.35 ‰ due to biogeochemical state changes in our experiments (at a constant ocean circulation) (Fig. 5). This amplitude is almost half of the reconstructed variation in $\Delta\delta^{13}C$ on glacial–interglacial timescales (1 ‰), and could thus contribute to variations in $\Delta\delta^{13}C$ together with ocean circulation changes. However, $\Delta\delta^{13}C$ can have a different

response on a basin scale: the ocean's oldest water (North Pacific) responds most to biological changes, the young deep water (North Atlantic) responds strongly to air–sea gas exchange changes, and the vertically well-mixed water (SO) has a low or even reversed $\Delta\delta^{13}C$ sensitivity compared to the other basins. The amplitude of the $\Delta\delta^{13}C$ sensitivity can be higher at decreasing scale, as seen from a maximum sensitivity of about -0.6 ‰ on ocean basin scale (Fig. 4). Interestingly, the direction of both glacial (intensification of $\Delta\delta^{13}C$) and interglacial (weakening of $\Delta\delta^{13}C$) $\Delta\delta^{13}C$ change matches changes in biogeochemical processes thought to be associated with these periods. This supports the idea that biogeochemistry explains part of the reconstructed variations in $\Delta\delta^{13}C$, in addition to changes in ocean circulation.

An increased gas exchange rate has the potential to reduce the biologically induced $\Delta\delta^{13}C$ through the reduction of surface ocean and atmospheric $\delta^{13}C$. Increased gas exchange, however, only reduces $\Delta\delta^{13}C$ in the low latitudes: in high latitudes, increased gas exchange will increase $\Delta\delta^{13}C$ (by increasing $\delta^{13}C_{surface}$) because of the negative disequilibrium $\delta^{13}C_{diseq}$ (i.e. $\delta^{13}C < \delta^{13}Ceq$) in this region, and thus potentially increase $\delta^{13}C_{surface}$ (Sect. 3.3.1). Notably, pCO_2^{atm}, $\delta^{13}C^{atm}$, and marine $\delta^{13}C$ are shown to be disproportionally sensitive to SO gas exchange rate changes.

Changes in the efficiency of the biological pump also have a major potential to alter $\Delta\delta^{13}C$ as well as pCO_2^{atm} and $\delta^{13}C^{atm}$. The globally increased POC sinking rate experiment shows that $\Delta\delta^{13}C$ strengthens in low latitudes (and more so in older waters) by deepening the low-$\delta^{13}C$ signature of remineralised POC, while SO $\Delta\delta^{13}C$ is not very sensitive to POC sinking rates. The SO effects are comparably small because the vertical mixing in the SO of the low-$\delta^{13}C$ deep water only causes shifts in the entire $\delta^{13}C$ profile, not a change in the gradient (Fig. 4). Increased POC sinking causes a longterm imbalance between weathering and sediment burial which leads to an increase in mean $\delta^{13}C$ and $\delta^{13}C^{atm}$ (of about 0.15 ‰) after 2000 years. Increased nutrient uptake in the SO (V_{max} experiment) results in 13 % lower non-SO POC export production up to ~ 35° N, in agreement with previous studies on the role of the SO

biological pump in lower-latitude productivity. Interestingly, the increase in $\Delta\delta^{13}C$ in all ocean basins occurs without significantly changing mean (deep) ocean PO_3^{4-}, which advocates for increased SO nutrient uptake to explain (part of) glacial–interglacial $\Delta\delta^{13}C$ variations. Furthermore, our results show that improved goodness of fit of the model data to the $\delta^{13}C : PO_3^{4-}$ relationship can be driven by reduced gas exchange as well as biological uptake efficiency in the SO, since both increase the importance of biology relative to air– sea gas exchange for $\delta^{13}C$. Caution should thus be exercised when interpreting changes in the fit of observations to the $\delta^{13}C : PO_3^{4-}$ relationship as changes in ocean ventilation or air–sea gas exchange alone.

A significant linear relationship was found across the sensitivity experiments between $\delta^{13}C^{atm}$ and $\Delta\delta^{13}C$ ($R^2 = 0.71$), and a weaker one ($R^2 = 0.39$) for pCO_2^{atm} and $\Delta\delta^{13}C$. This result shows that paleo-reconstructions of $\delta^{13}C^{atm}$ based on $\Delta\delta^{13}C$ could be valid for a wide range of biogeochemical states. Previous studies have shown good correlation between pCO_2^{atm} and local $\Delta\delta^{13}C$, but our results suggest that the relationship may not be valid if both biological and gas exchange rate changes occur. The maximum response of $\delta^{13}C^{atm}$ to the biogeochemical changes imposed in our experiments (up to 0.5 ‰) is larger than the idealised maximum effect of ocean circulation changes on $\delta^{13}C^{atm}$ (0 ‰– 0.15 ‰; Menviel et al., 2015), which underlines the potential importance of biogeochemical processes for variations in $\delta^{13}C^{atm}$. The high potential of SO air–sea gas exchange to steer $\delta^{13}C^{atm}$ (Table 2: sea ice and gas exchange rate experiments) complements recent studies showing that increased SO ventilation of deep ocean carbon is a likely candidate for glacial–interglacial $\delta^{13}C^{atm}$ excursions.

As an outlook, the use of a more complex model with a higher horizontal and vertical resolution and a shorter time step (resolving seasonal variations) could provide valuable additional information. For example, the role of different regions within the SO on the global $\delta^{13}C$ distribution could be better studied with a more complex model. Sediment corebased reconstructions of the global carbon cycle could possibly be aided by a more complex model with a finer grid and higher time resolution, by

providing more detailed information on the contribution of biogeochemical processes to local ocean tracers. Next to that, exploring the effect on $\Delta\delta^{13}C$ of a glacial model circulation field could provide a way to quantify the maximum combined effect of circulation and biogeochemical change on $\Delta\delta^{13}C$.

Code and data availability. The model and model output can be made available upon request to the main author.

Supplement. The supplement related to this article is available online at: https://doi.org/10.5194/bg-15-7205-2018-supplement.

Author contributions. CH provided the HAMOCC2s model. ALM and CH designed the model experiments and ALM carried them out. ALM analyzed the results and prepared the paper, with feedback and supervision from JS and CH.

Competing interests. The authors declare that they have no conflict of interest.

Special issue statement. This article is part of the special issue "The 10th International Carbon Dioxide Conference (ICDC10) and the 19th WMO/IAEA Meeting on Carbon Dioxide, other Green-house Gases and Related Measurement Techniques (GGMT-2017) (AMT/ACP/BG/CP/ESD inter-journal SI)". It is a result of the 10th International Carbon Dioxide Conference, Interlaken, Switzerland, 21–25 August 2017.

Acknowledgements. The authors would like to thank two anony-mous reviewers for their constructive and helpful comments, which improved this paper. This study is a contribution to the project "Earth system modelling of climate variations in the Anthropocene" (EVA; grant no. 229771) as well as the project "Overturning circulation and its implications for global carbon cycle in coupled models" (ORGANIC; grant no. 239965) which are both funded by the Research Council of Norway. This is a contribution to the Bjerknes Centre for Climate Research (Bergen, Norway). Storage resources were provided by the Norwegian storage infrastructure of Sigma2 (NorStore project ns2980k). Anne L. Morée is grateful for PhD funding through the

Faculty for Mathematics and Natural Sciences of the University of Bergen and the Meltzer Foundation. Christoph Heinze acknowledges sabbatical support from the Faculty for Mathematics and Natural Sciences of the University of Bergen.

Edited by: Fortunat Joos

Reviewed by: two anonymous referees

References

Bauska, T. K., Baggenstos, D., Brook, E. J., Mix, A. C., Marcott, S. A., Petrenko, V. V., Schaefer, H., Severinghaus, J. P., and Lee, J. E.: Carbon isotopes characterize rapid changes in atmospheric carbon dioxide during the last deglaciation, P. Natl. Acad. Sci. USA, 113, 3465–3470, https://doi.org/10.1073/pnas.1513868113, 2016.

Boyle, E. A.: The role of vertical chemical fractionation in controlling late Quaternary atmospheric carbon dioxide, J. Geophys. Res.Oceans, 93, 15701-15714, https://doi.org/10.1029/JC093iC12p15701, 1988.

Broecker, W. S.: Ocean chemistry during glacial time, Geochim. Cosmochim. Ac., 46, 1689–1705, https://doi.org/10.1016/0016-7037(82)90110-7, 1982.

Broecker, W. S. and Maier-Reimer, E.: The influence of air and sea exchange on the carbon isotope distribution in the sea, Global Biogeochem. Cy., 6, 315–320, https://doi.org/10.1029/92GB01672, 1992.

Broecker, W. S. and McGee, D.: The ^{13}C record for atmospheric CO_2: What is it trying to tell us?, Earth Planet. Sci. Lett., 368, 175–182, https://doi.org/10.1016/j.epsl.2013.02.029, 2013.

Broecker W, S. and Peng, T. H.: Gas exchange rates between air and sea, Tellus, 26, 21–35, https://doi.org/10.1111/j.2153-3490.1974.tb01948.x, 1974.

Broecker, W. S. and Peng, T. H.: The role of CaCO3 compensation in the glacial to interglacial atmospheric CO_2 change, Global Biogeochem. Cy., 1, 15-29, https://doi.org/10.1029/GB001i001p00015, 1987.

Charles, C. D., Pahnke, K., Zahn, R., Mortyn, P. G., Ninnemann, U., and Hodell, D. A.: Millennial scale evolution of the Southern Ocean chemical divide, Quaternary Science Reviews, 29, 399-409, https://doi.org/10.1016/j.quascirev.2009.09.021, 2010.

Craig, H.: Isotopic standards for carbon and oxygen and correction factors for mass-spectrometric analysis of carbon dioxide, Geochim. Cosmochim. Ac., 12, 133–149, https://doi.org/10.1016/0016-7037(57)90024-8, 1957.

Crosta, X.: Antarctic Sea Ice History, Late Quaternary, in: Encyclopedia of Paleoclimatology and Ancient Environments, edited by: Gornitz, V., Springer Netherlands, Dordrecht, the Netherlands, 31–34, 2009.

Crucifix, M.: Distribution of carbon isotopes in the glacial ocean: A model study, Paleoceanography, 20, PA4020, https://doi.org/10.1029/2005PA001131, 2005.

Curry, W. B. and Oppo, D. W.: Glacial water mass geometry and the distribution of $\delta^{13}C$ of ΣCO_2 in the western Atlantic Ocean, Paleoceanography, 20, PA1017, https://doi.org/10.1029/2004PA001021, 2005.

DeVries, T., Primeau, F., and Deutsch, C.: The sequestration efficiency of the biological pump, Geophys. Res. Lett., 39, L13601, https://doi.org/10.1029/2012GL051963, 2012.

Dickson, A. J., Leng, M. J., and Maslin, M. A.: Mid-depth South Atlantic Ocean circulation and chemical stratification during MIS-10 to 12: implications for atmospheric CO_2, Clim. Past, 4, 333– 344, https://doi.org/10.5194/cp-4-333-2008, 2008.

Dunne, J. P., Sarmiento, J. L., and Gnanadesikan, A.: A synthesis of global particle export from the surface ocean and cycling through the ocean interior and on the seafloor, Global Biogeochem. Cy., 21, GB4006, https://doi.org/10.1029/2006GB002907, 2007.

Duplessy, J. C., Shackleton, N. J., Fairbanks, R. G., Labeyrie, L., Oppo, D., and Kallel, N.: Deepwater source variations during the last climatic cycle and their impact on the global deepwater circulation, Paleoceanography, 3, 343–360, https://doi.org/10.1029/PA003i003p00343, 1988.

Eggleston, S., Schmitt, J., Bereiter, B., Schneider, R., and Fischer, H.: Evolution of the stable carbon isotope composition of atmospheric CO_2 over the last glacial cycle, Paleoceanography, 31, 434–452, https://doi.org/10.1002/2015PA002874, 2016.

Eide, M., Olsen, A., Ninnemann, U. S., and Eldevik, T.: A global estimate of the full oceanic $\delta^{13}C$ Suess effect since the preindustrial, Global Biogeochem. Cy., 31, 492–514, https://doi.org/10.1002/2016GB005472, 2017a.

Eide, M., Olsen, A., Ninnemann, U. S., and Johannessen, T.: A global ocean climatology of preindustrial and modern ocean $\delta^{13}C$, Global Biogeochem. Cy., 31, 515–534, https://doi.org/10.1002/2016GB005473, 2017b.

Emerson, S. and Hedges, J.: Chemical oceanography and the marine carbon cycle, Cambridge University Press, Cambridge, UK, xi, 453 pp. of col. plates pp., 2008.

Galbraith, E. D., Kwon, E. Y., Bianchi, D., Hain, M. P., and Sarmiento, J. L.: The impact of atmospheric pCO_2 on carbon isotope ratios of the atmosphere and ocean, Global Biogeochem. Cy., 29, 307–324, https://doi.org/10.1002/2014GB004929, 2015.

Gottschalk, J., Skinner, L. C., Lippold, J., Vogel, H., Frank, N., Jaccard, S. L., and Waelbroeck, C.: Biological and physical controls in the Southern Ocean on past millennial-scale atmospheric CO_2 changes, Nat. Commun., 7, 11539, https://doi.org/10.1038/ncomms11539, 2016.

Gruber, N. and Keeling, C. D.: An improved estimate of the isotopic air-sea disequilibrium of CO_2: Implications for the oceanic uptake of anthropogenic CO_2, Geophys. Res. Lett., 28, 555–558, https://doi.org/10.1029/2000GL011853, 2001.

Gruber, N., Keeling, C. D., Bacastow, R. B., Guenther, P. R., Lueker, T. J., Wahlen, M., Meijer, H. A. J., Mook, W. G., and Stocker, T. F.: Spatiotemporal patterns of carbon-13 in the global surface oceans and the oceanic suess effect, Global Biogeochem. Cy., 13, 307–335, https://doi.org/10.1029/1999GB900019, 1999.

Heinze, C.: Assessing the importance of the Southern Ocean for natural atmospheric pCO_2 variations with a global biogeochemical general circulation model, DeepSea Res. Pt. II, 49, 3105–3125, https://doi.org/10.1016/S0967-0645(02)00074-7, 2002.

Heinze, C., and Hasselmann, K.: Inverse Multiparameter Modeling of Paleoclimate Carbon Cycle Indices, Quaternary Res., 40, 281– 296, https://doi.org/10.1006/qres.1993.1082, 1993.

Heinze, C. and Maier-Reimer, E.: The Hamburg Oceanic Carbon Cycle Circulation Model Version "HAMOCC2s" for long time integrations, Max-Planck-Institut für Meteorologie, Hamburg REPORT 20, 1999.

Heinze, C., Maier-Reimer, E., and Winn, K.: Glacial pCO_2 Reduction by the World Ocean: Experiments With the Hamburg Carbon Cycle Model, Paleoceanography, 6, 395–430, https://doi.org/10.1029/91PA00489, 1991.

Heinze, C., Hoogakker, B. A. A., and Winguth, A.: Ocean carbon cycling during the past 130 000 years – a pilot study on inverse palaeoclimate record modelling, Clim. Past, 12, 1949– 1978, https://doi.org/10.5194/cp-12-1949-2016, 2016.

Hilting, A. K., Kump, L. R., and Bralower, T. J.: Variations in the oceanic vertical carbon isotope gradient and their implications for the Paleocene-Eocene biological pump, Paleoceanography, 23, PA3222, https://doi.org/10.1029/2007PA001458, 2008.

Holden, P. B., Edwards, N. R., Müller, S. A., Oliver, K. I. C., Death, R. M., and Ridgwell, A.: Controls on the spatial distribution of oceanic $^{13}C_{DIC}$, Biogeosciences, 10, 1815–1833, https://doi.org/10.5194/bg-10-1815-2013, 2013.

Hollander, D. J. and McKenzie, J. A.: CO_2 control on carbon-isotope fractionation during aqueous photosynthesis: A paleo-pCO_2 barometer, Geology, 19, 929–932, https://doi.org/10.1130/0091-7613(1991)019<0929:ccocif>2.3.co;2, 1991.

Hoogakker, B. A. A., Elderfield, H., Schmiedl, G., McCave, I. N., and Rickaby, R. E. M.: Glacial-interglacial changes in bottom-water oxygen content on the Portuguese margin, Nat. Geosci., 8, 40–43, https://doi.org/10.1038/ngeo2317, 2015.

Jahn, A., Lindsay, K., Giraud, X., Gruber, N., Otto-Bliesner, B. L., Liu, Z., and Brady, E. C.: Carbon isotopes in the ocean model of the Community Earth System Model (CESM1), Geosci. Model Dev., 8, 2419–2434, https://doi.org/10.5194/gmd-8-2419-2015, 2015.

Jansen, M. F.: Glacial ocean circulation and stratification explained by reduced atmospheric temperature, P. Natl. Acad. Sci. USA, 114, 45–50, https://doi.org/10.1073/pnas.1610438113, 2017.

Jones, D. C., Ito, T., Takano, Y., and Hsu, W. C.: Spatial and seasonal variability of the air-sea equilibration timescale of carbon dioxide, Global Biogeochem. Cy., 28, 1163–1178, https://doi.org/10.1002/2014GB004813, 2014.

Keir, R. S.: The effect of vertical nutrient redistribution on surface ocean $\delta^{13}C$, Global Biogeochem. Cy., 5, 351–358, https://doi.org/10.1029/91GB01913, 1991.

Kroopnick, P.: The distribution of ^{13}C in the Atlantic Ocean, Earth Planet. Sc. Lett., 49, 469–484, https://doi.org/10.1016/0012-821X(80)90088-6, 1980.

Kroopnick, P. M.: The distribution of ^{13}C of ΣCO_2 in the world oceans, Deep-Sea Res., 32, 57–84, https://doi.org/10.1016/0198-0149(85)90017-2, 1985.

Laws, E. A., Bidigare, R., R., and Popp, B. N.: Effects of growth rate and CO_2 concentration on carbon isotopic fractionation by the marine diatom Phaeodactylum tricornutum, Limnol. Oceanogr., 42, 1552–1560, 1997.

Lear, C. H., Billups, K., Rickaby, R. E. M., Diester-Haass, L., Mawbey, E. M., and Sosdian, S. M.: Breathing more deeply: Deep ocean carbon storage during the mid-Pleistocene climate transition, Geology, 44, 1035–1038, https://doi.org/10.1130/G38636.1, 2016.

Lisiecki, L. E.: A benthic $\delta^{13}C$-based proxy for atmospheric pCO_2 over the last 1.5 Myr, Geophys. Res. Lett., 37, L21708, https://doi.org/10.1029/2010GL045109, 2010.

Lourantou, A., Lavricˇ Jošt, V., Köhler, P., Barnola, J. M., Paillard, D., Michel, E., Raynaud, D., and Chappellaz, J.: Constraint of the CO_2 rise by new atmospheric carbon isotopic measurements during the last deglaciation, Global Biogeochem. Cy., 24, GB2015, https://doi.org/10.1029/2009GB003545, 2010.

Lutz, M. J., Caldeira, K., Dunbar, R. B., and Behrenfeld, M. J.: Seasonal rhythms of net primary production and particulate organic carbon flux to depth describe the efficiency of biological pump in the global ocean, J. Geophys. Res. Oceans, 112, C10011, https://doi.org/10.1029/2006JC003706, 2007.

Lynch-Stieglitz, J., Stocker, T. F., Broecker, W. S., and Fairbanks, R. G.: The influence of air-sea exchange on the isotopic composition of oceanic carbon: Observations and modeling, Global Biogeochem. Cy., 9, 653–665, https://doi.org/10.1029/95GB02574, 1995.

MacCready, P. and Quay, P.: Biological export flux in the Southern Ocean estimated from a climatological nitrate budget, Deep-Sea Res. Pt. II, 48, 4299–4322, https://doi.org/10.1016/S0967-0645(01)00090-X, 2001.

Mackenzie, F. T. and Lerman, A.: Isotopic Fractionation of Carbon: Inorganic and Biological Processes, in: Carbon in the Geobiosphere – Earth's Outer Shell –, edited by: Mackenzie, F. T. and Lerman, A., Springer Netherlands, Dordrecht, the Netherlands, 165–191, 2006.

Marchal, O., Stocker, T. F., and Joos, F.: A latitude-depth, circulation-biogeochemical ocean model for paleoclimate studies. Development and sensitivities, Tellus B, 50, 290–316, https://doi.org/10.1034/j.1600-0889.1998.t01-2-00006.x, 1998.

Marinov, I., Gnanadesikan, A., Toggweiler, J. R., and Sarmiento, J. L.: The Southern Ocean biogeochemical divide, Nature, 441, 964–967, 2006.

Menviel, L., Mouchet, A., Meissner, K. J., Joos, F., and England, M. H.: Impact of oceanic circulation changes on atmospheric $^{13}CO_2$, Global Biogeochem. Cy., 29, 1944–1961, https://doi.org/10.1002/2015GB005207, 2015.

Menviel, L., Yu, J., Joos, F., Mouchet, A., Meissner, K. J., and England, M. H.: Poorly ventilated deep ocean at the Last Glacial Maximum inferred from carbon isotopes: A data-model comparison study, Paleoceanography, 32, 2–17, https://doi.org/10.1002/2016PA003024, 2016.

Milliman, J. D. and Droxler, A. W.: Neritic and pelagic carbonate sedimentation in the marine environment: ignorance is not bliss, Geol. Rundsch., 85, 496–504, https://doi.org/10.1007/BF02369004, 1996.

Mook, W. G.: ^{13}C in atmospheric CO_2, Neth. J. Sea Res., 20, 211– 223, https://doi.org/10.1016/0077-7579(86)90043-8, 1986.

Mulitza, S., Rühlemann, C., Bickert, T., Hale, W., Pätzold, J., and Wefer, G.: Late Quaternary $\delta^{13}C$ gradients and carbonate accumulation in the western equatorial Atlantic, Earth Planet Sci. Lett., 155, 237–249, https://doi.org/10.1016/S0012-821X(98)00012-0, 1998.

Murnane, R. J. and Sarmiento, J. L.: Roles of biology and gas exchange in determining the $\delta^{13}C$ distribution in the ocean and the preindustrial gradient in atmospheric $\delta^{13}C$, Global Biogeochem. Cy., 14, 389–405, https://doi.org/10.1029/1998GB001071, 2000.

Nevison, C. D., Keeling, R. F., Kahru, M., Manizza, M., Mitchell, B. G., and Cassar, N.: Estimating net community production in the Southern Ocean based on atmospheric potential oxygen and satellite ocean color data, Global Biogeochem. Cy., 26, GB1020, https://doi.org/10.1029/2011GB004040, 2012.

Oliver, K. I. C., Hoogakker, B. A. A., Crowhurst, S., Henderson, G. M., Rickaby, R. E. M., Edwards, N. R., and Elderfield, H.: A synthesis of marine sediment core $\delta^{13}C$ data over the last 150 000 years, Clim. Past, 6, 645–673, https://doi.org/10.5194/cp-6-645-2010, 2010.

Oppo, D. W., Fairbanks, R. G., and Gordon, A. L.: Late Pleistocene Southern Ocean $\delta^{13}C$ variability, Paleoceanography, 5, 43–54, https://doi.org/10.1029/PA005i001p00043, 1990.

Primeau, F. W., Holzer, M., and DeVries, T.: Southern Ocean nutrient trapping and the efficiency of the biological pump, J. Geophys. Res. Oceans, 118, 2547–2564, https://doi.org/10.1002/jgrc.20181, 2013.

Quay, P., Sonnerup, R., Westby, T., Stutsman, J., and Mc-Nichol, A.: Changes in the $^{13}C/^{12}C$ of dissolved inorganic carbon in the ocean as a tracer of anthropogenic CO_2 uptake, Global Biogeochem. Cy., 17, 4-1–4-20, https://doi.org/10.1029/2001GB001817, 2003.

Roth, R., Ritz, S. P., and Joos, F.: Burial-nutrient feedbacks amplify the sensitivity of atmospheric carbon dioxide to changes in organic matter remineralisation, Earth Syst. Dynam., 5, 321–343, https://doi.org/10.5194/esd-5-321-2014, 2014.

Sarmiento, J. L., Gruber, N., Brzezinski, M. A., and Dunne, J. P.: High-latitude controls of thermocline nutrients and low latitude biological productivity, Nature, 427, 56–60, 2004.

Schlitzer, R.: Carbon Export Fluxes in the Southern Ocean: Results from Inverse Modeling and Comparison with Satellite Estimates, Deep-Sea Res., 2, 1623–1644, 2002.

Schmittner, A. and Somes, C. J.: Complementary constraints from carbon (^{13}C) and nitrogen (^{15}N) isotopes on the glacial ocean's soft-tissue biological pump, Paleoceanography, 31, 669–693, https://doi.org/10.1002/2015PA002905, 2016.

Schmittner, A., Gruber, N., Mix, A. C., Key, R. M., Tagliabue, A., and Westberry, T. K.: Biology and air–sea gas exchange controls on the distribution of carbon isotope ratios ($\delta^{13}C$) in the ocean, Biogeosciences, 10, 5793–5816, https://doi.org/10.5194/bg-10-5793-2013, 2013.

Shackleton, N. J., Hall, M. A., Line, J., and Shuxi, C.: Carbon isotope data in core V19-30 confirm reduced carbon dioxide concentration in the ice age atmosphere, Nature, 306, 319–322, https://doi.org/10.1038/306319a0, 1983.

Shackleton, N. J. and Pisias, N. G.: Atmospheric carbon dioxide, orbital forcing, and climate, in: The Carbon cycle and atmospheric CO_2: natural variations archean to present, edited by: Sundquist,

E. T., and Broecker, W. S., Geophysical Monograph, American Geophysical Union, Washington, USA, 303–317, 1985.

Sonnerup, R. E. and Quay, P. D.: ^{13}C constraints on ocean carbon cycle models, Global Biogeochem. Cy., 26, GB2014, https://doi.org/10.1029/2010GB003980, 2012.

Stephens, B. B. and Keeling, R. F.: The influence of Antarctic sea ice on glacial–interglacial CO_2 variations, Nature, 404, 171–174, https://doi.org/10.1038/35004556, 2000.

Tagliabue, A. and Bopp, L.: Towards understanding global variability in ocean carbon-13, Global Biogeochem. Cy., 22, GB1025, https://doi.org/10.1029/2007GB003037, 2008.

Toggweiler, J. R.: Variation of atmospheric CO_2 by ventilation of the ocean's deepest water, Paleoceanography, 14, 571–588, https://doi.org/10.1029/1999PA900033, 1999.

Tréguer, P.: Silica and the cycle of carbon in the ocean, C. R. Geosci., 334, 3–11, https://doi.org/10.1016/S1631-0713(02)01680-2, 2002.

Tschumi, T., Joos, F., Gehlen, M., and Heinze, C.: Deep ocean ventilation, carbon isotopes, marine sedimentation and the deglacial CO_2 rise, Clim. Past, 7, 771–800, https://doi.org/10.5194/cp-7-771-2011, 2011.

Zahn, R., Winn, K., and Sarnthein, M.: Benthic foraminiferal $\delta^{13}C$ and accumulation rates of organic carbon: Uvigerina Peregrina group and Cibicidoides Wuellerstorfi, Paleoceanography, 1, 27–42, https://doi.org/10.1029/PA001i001p00027, 1986.

Zeebe, R. and Wolf-Gladrow, D.: CO_2 in Seawater: Equilibrium, Kinetics, Isotopes, Elsevier Oceanography Series, edited by: Halpern, D., Elsevier Science B.V., Amsterdam, the Netherlands, 346 pp., 2001.

Zhang, J., Quay, P. D., and Wilbur, D. O.: Carbon isotope fractionation during gas-water exchange and dissolution of CO_2, Geochim. Cosmochim. Ac., 59, 107–114, https://doi.org/10.1016/0016-7037(95)91550-D, 1995.

Ziegler, M., Diz, P., Hall, I. R., and Zahn, R.: Millennial-scale changes in atmospheric CO_2 levels linked to the Southern Ocean carbon isotope gradient and dust flux, Nat. Geosci., 6, 457–461, https://doi.org/10.1038/ngeo1782, 2013.

Supplement to Paper I

Southern Ocean controls of the vertical marine $\delta^{13}C$ gradient – a modelling study

Morée, A. L., J. Schwinger, and C. Heinze

Biogeosciences, **15**, 7205-7223, 10.5194/bg-15-7205-2018

2018

SI 1A Particulate organic carbon cycling in HAMOCC2s

Particle export production in the surface layer (the euphotic zone), P_{POC}, P_{opal} or P_{CaCO3} [mol L^{-1} yr^{-1}], is described by Michaelis-Menten kinetics for nutrient uptake as follows:

$$P_{POC} = \frac{V_{max}^{POC} \cdot [PO_4^{3-}]^2 \cdot r_{C:P}}{K_S^{POC} + [PO_4^{3-}]}, \qquad P_{opal} = \frac{V_{max}^{opal} \cdot \left[Si(OH)_4\right]^2}{K_S^{opal} + \left[Si(OH)_4\right]}, \text{and}$$

$$P_{CaCO3} = P_{POC} \cdot R \cdot (1 - \frac{{}^{P_{opal}}/_{P_{POC}}}{S_{opal}}),$$

where K_S^{POC} and K_S^{opal} are the half saturation constants for POC and opal respectively, $r_{C:P}$ is the Redfield ratio between carbon (C) and phosphorus (P) and V_{max}^{POC} and V_{max}^{opal} [yr^{-1}] are the maximum uptake rate of phosphate and silicic acid respectively. *R* is the maximum rain ratio C($CaCO_3$):C(POC) and is set to the constant value 0.3405. P_{CaCO3} increases when ${}^{P_{opal}}/_{P_{POC}}$ lowers below threshold value for onset of $CaCO_3$ production S_{opal}. Furthermore, V_{max}^{POC}, V_{max}^{opal}, K_S^{POC} and K_S^{opal} are prescribed depending on sea surface temperature following Heinze et al. (2003).

The sinking of the exported biogenic particles is described by a mass balance between gains and losses, for POC:

$\frac{dPOC_{settle}}{dt} = gains - losses$. With

$\frac{dPOC_{settle}}{dt} = P_{POC} - \frac{w}{\Delta z_0} \cdot POC_{settle} - r_{POC} \cdot POC_{settle}$, for the surface layer,

$\frac{dPOC_{settle}}{dt} = w \cdot \frac{\partial POC_{settle}}{\partial z} - r_{POC} \cdot POC_{settle}$, for all layers below the surface layer

This is done in the same way for $CaCO_3$, opal, and clay – although clay is considered chemically inert and thus not degraded or dissolved. In the above set of equations,

gains equal P_{POC}, P_{opal} or P_{CaCO3} and dust input for clay. Losses in the surface layer come from sinking and degradation/remineralisation, where the sinking term involves the sinking velocity w (3 m d^{-1} in the control run, adjusted in the POC sinking rate experiments) and the thickness of the euphotic zone Δz_0 (50 m). The degradation term consists of a constant degradation rate r_{POC} (2.69 yr^{-1}) - with equivalents r_{opal} (1.23 yr^{-1}) or r_{CaCO3} (6.76 yr^{-1}) for the other biogenic particles. Below the surface layer, gains are determined by the input of sinking particles from above (for POC, $w \cdot \frac{\partial POC_{settle}}{\partial z}$) and continued losses to inorganic carbon and nutrients through degradation/remineralisation (for POC, $r_{POC} \cdot POC_{settle}$). Remineralisation of POC requires oxygen availability above a minimum of $1e^{-5}$ moles/l. In addition to degradation $CaCO_3$ and opal dissolution is simulated, which depends on carbonate saturation and opal saturation respectively.

Throughout the water column, POC losses are mirrored by source terms for the inorganic dissolved species of the water column (for TAlk, DIC, phosphate, and oxygen). The remainder of particles which are not subject to degradation within the water column are deposited onto the ocean sediments. Here, the lowermost water column layer and topmost sediment layer directly interact through a sediment balance of deposition and redissolution/remineralisation.

SI 1B Calculation of gas transfer fluxes

Separate fluxes F_{up} and F_{down} are calculated by splitting the gas transfer formulation into two parts. The gas transfer formulation for CO_2 can be described as: $F_A = k_w ([A]_{water} - [A]_{air})$, where for $A=CO_2$, k_w is the specific gas exchange rate, $[A]_{water}$ is the model surface-ocean free CO_2 concentration, and $[A]_{air}$ is the atmospheric CO_2 concentration. In the model, $F_{up}=k_w*[A]_{water}$ and $F_{down}=k_w*[A]_{air}$ and $F_{net} = F_A = F_{up}-F_{down}$. This splitting up is useful for the calculation of air-sea fractionation of the carbon isotopes, as the equilibrium fractionation factor only needs to be multiplied with F_{up}

when calculating the effects of the air-sea gas exchange on $\delta^{13}C$. It also proved to be useful for our discussion, because the total amount of exchange F_{u+d} influences $\delta^{13}C$.

The freely evolving atmospheric concentration of O_2, $^{13}CO_2$ and CO_2 is modelled by a one-layer box over each grid point, for which zonal average atmospheric concentrations are calculated at every time-step. Because of the annual model time-step, gas transport is simulated through meridional diffusion only, where the assumption is that the atmosphere is longitudinally well-mixed.

SI 2 Figures

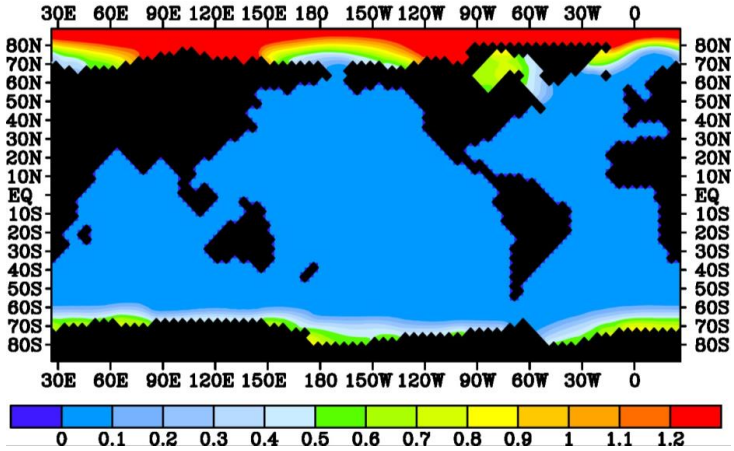

Figure S1 Surface map of the annually constant sea ice thickness in the model in meter.

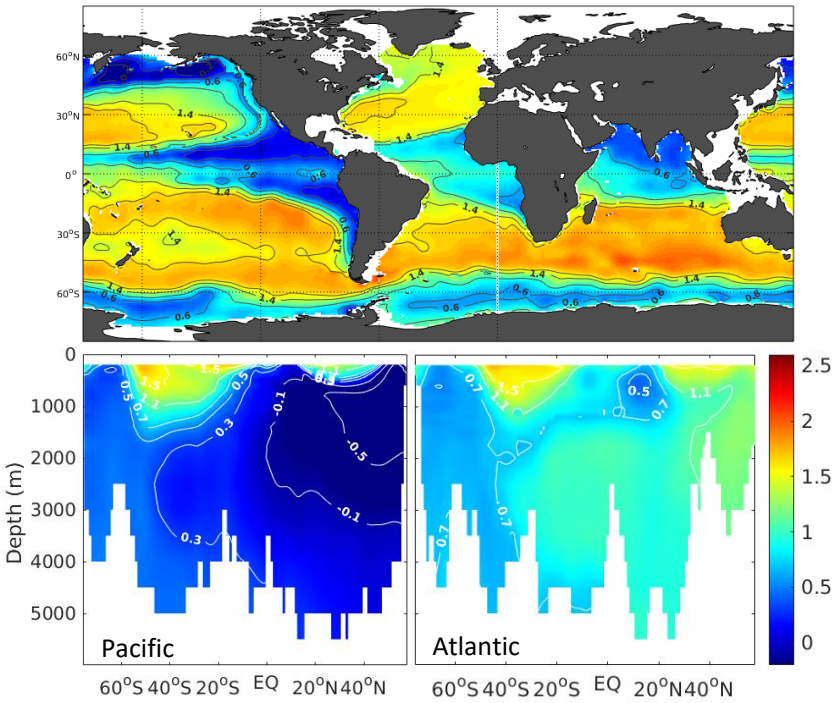

Figure S2 Pre-industrial $\delta^{13}C$ data based on Eide et al. (2017b) at 200 m depth (top), a Pacific transect at 150° W (bottom left) and an Atlantic transect at 30° W (bottom right)

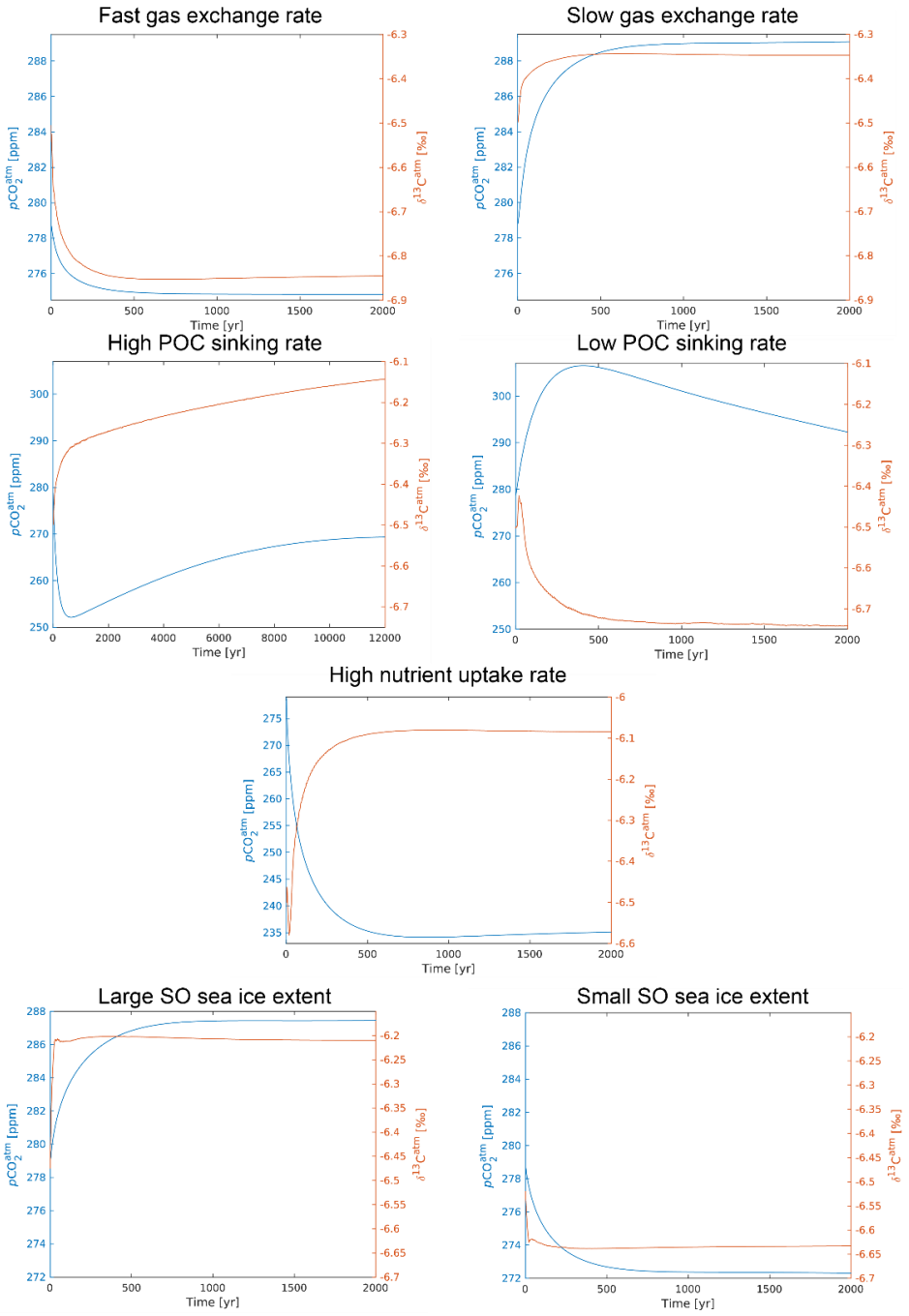

Figure S3 Atmospheric development of $\delta^{13}C^{atm}$ and pCO_2^{atm} during the (Global) sensitivity experiments. Note that the high POC sinking rate experiment was continued for an additional 10 000 years as compared to the other experiments. Small ongoing drift for 100 000s of years occurs in all experiments due to the very long equilibration timescale between burial and weathering for $\delta^{13}C$ (Roth et al., 2014).

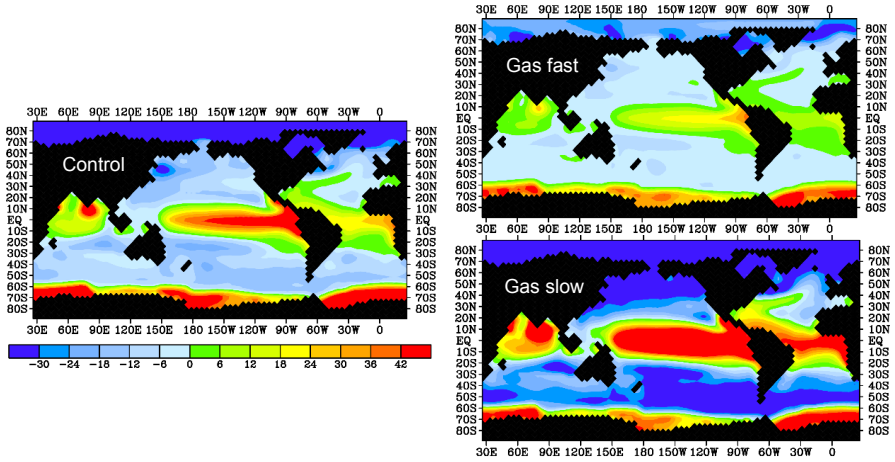

Figure S4 The pCO_2 difference [ppm] between the surface ocean and the atmosphere for the model control run, 'Gas fast' and 'Gas slow' experiments. Negative values indicate a carbon flux into the ocean. The actual flux depends amongst others on the size of the pCO_2 difference and the air-sea gas exchange rate.

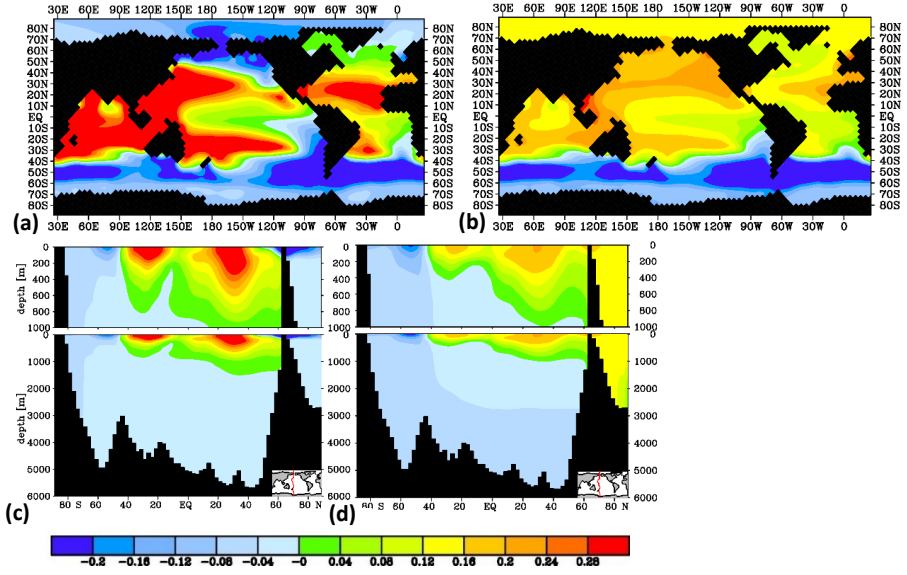

Figure S5 Modelled slow gas exchange sensitivity experiment $\delta^{13}C$ of DIC [‰] difference with the model control run: global experiments (a) and (c) and SO-only experiments (b) and (d), at 25 m depth (a) and (b) and as a Pacific transect of $\delta^{13}C$ difference (c) and (d). The sign of the change equals the sign of the $\delta^{13}C_{diseq}$.

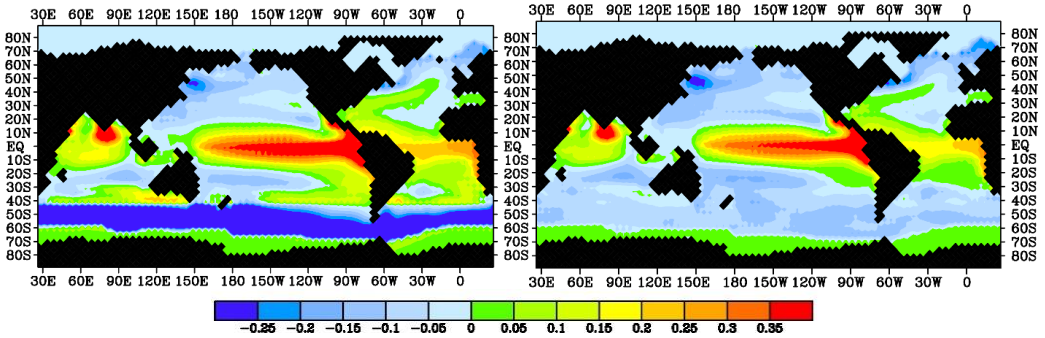

Figure S6 Air-sea ^{13}C [gC m^{-2} yr^{-1}] flux for the V_{max} experiment (left) and model control run (right). Negative values indicate carbon uptake by the ocean.

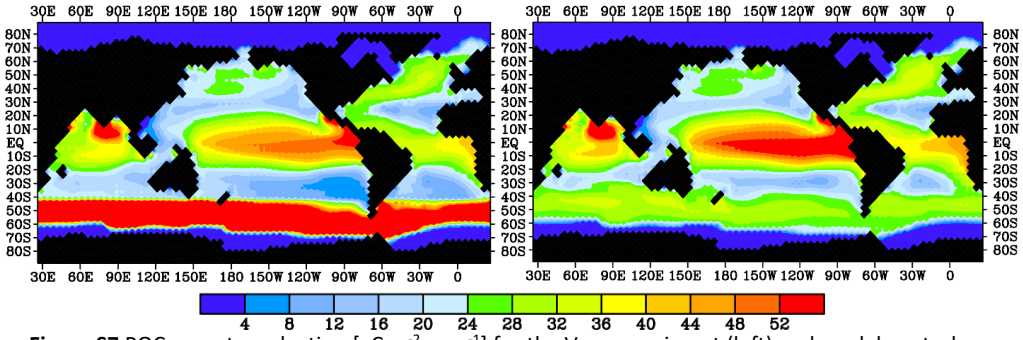

Figure S7 POC export production [gC m^{-2} $year^{-1}$] for the V_{max} experiment (left) and model control run (right).

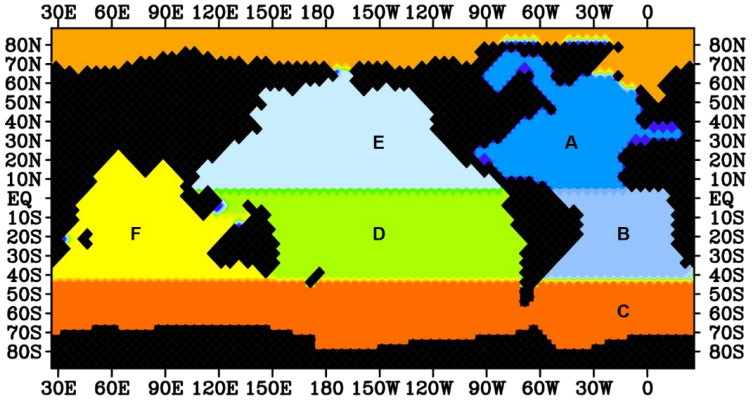

Figure S8 The basins used to make Fig. 4. A=North Atlantic, B=South Atlantic, C=Southern Ocean, D=South Pacific, E=North Pacific, F=Indian Ocean.

SI 3 References

Heinze, C., Hupe, A., Maier-Reimer, E., Dittert, N., and Ragueneau, O.: Sensitivity of the marine biospheric Si cycle for biogeochemical parameter variations, Global Biogeochemical Cycles, 17, 1086, doi:10.1029/2002GB001943, 2003.

Heinze, C., Hoogakker, B. A. A., and Winguth, A.: Ocean carbon cycling during the past 130 000 years – a pilot study on inverse palaeoclimate record modelling, Clim. Past, 12, 1949-1978, 10.5194/cp-12-1949-2016, 2016.

Paper II

II

A Last Glacial Maximum forcing dataset for ocean modelling

Morée, A. L., and J. Schwinger

Revised version of

Earth Syst. Sci. Data Discuss., 10.5194/essd-2019-79

2019

A Last Glacial Maximum forcing dataset for ocean modelling

Anne L. Morée[1], Jörg Schwinger[2]

[1]Geophysical Institute, University of Bergen and Bjerknes Centre for Climate Research, Bergen, 5007, Norway

[2]NORCE Climate, Bjerknes Centre for Climate Research, 5007 Bergen, Norway

Correspondence to: Anne L. Morée (anne.moree@uib.no)

Abstract. Model simulations of the Last Glacial Maximum (LGM, ~21 000 years before present) can aid the interpretation of proxy records, help to gain an improved mechanistic understanding of the LGM climate system and are valuable for the evaluation of model performance in a different climate state. Ocean-ice only model configurations forced by prescribed atmospheric data (referred to as "forced ocean models") drastically reduce the computational cost of paleoclimate modelling as compared to fully coupled model frameworks. While feedbacks between the atmosphere and ocean-sea-ice compartments of the Earth system are not present in such model configurations, many scientific questions can be addressed with models of this type. The data presented here are derived from fully coupled paleoclimate simulations of the Palaeoclimate Modelling Intercomparison Project (PMIP3). The data are publicly accessible at the NIRD Research Data Archive at https://doi.org/10.11582/2019.00019 (Morée and Schwinger, 2019). They consist of 2-D anomaly forcing fields suitable for use in ocean models that employ a bulk forcing approach and are optimized for use with CORE forcing fields. The data include specific humidity, downwelling longwave and shortwave radiation, precipitation, wind (v and

u components), temperature and sea surface salinity (SSS). All fields are provided as climatological mean anomalies between LGM and pre-industrial times. These anomaly data can therefore be added to any pre-industrial ocean forcing data set in order to obtain forcing fields representative of LGM conditions as simulated by PMIP3 models. These forcing data provide a means to simulate the LGM in a computationally efficient way, while still taking advantage of the complexity of fully coupled model set-ups. Furthermore, the dataset can be easily updated to reflect results from upcoming and future paleo model intercomparison activities.

1 Introduction

The LGM (~21 kya) is of interest to the climate research community because of the relative abundance of proxy data, and because it is the most recent profoundly different climatic state of our planet. For these reasons, the LGM is extensively studied in modelling frameworks (Menviel et al., 2017; Brady et al., 2012; Otto-Bliesner et al., 2007). Model simulations of the past ocean can not only provide a method to gain a mechanistic understanding of marine proxy records, they can also inform us about model performance in a different climatic state of the Earth system (Braconnot et al., 2012). Typical state-of-the-art tools to simulate the (past) Earth system are climate or Earth system models as, for example, used in the Coupled Model Intercomparison Project phase 5 (CMIP5; Taylor et al. (2011)). Besides simulating our present climate, these CMIP5 models are also used to simulate past climate states (such as the LGM) in the Palaeoclimate Modelling Intercomparison Project 3 (PMIP3). However, the computational costs and run-time of such fully coupled model frameworks are a major obstacle for their application to palaeoclimate modelling. Palaeoclimate modelling optimally requires long (thousands to ten thousands of years) simulations in order to provide the necessary time for relevant processes to emerge (e.g. CaCO3 compensation) (Braconnot et al., 2007). Complex fully coupled models can typically not be run into full equilibrium (which requires hundreds to thousands of years of integration) due to computational costs (Eyring et

al., 2016). Therefore, the PMIP3 models exhibit model drift (especially in the deep ocean, e.g. Marzocchi and Jansen (2017)). The 3rd phase of the PMIP project (PMIP3; Braconnot et al. (2012)) limits global mean sea-surface temperature drift to under 0.05 K per century and requires the Atlantic Meridional Overturning Circulation to be stable (Kageyama et al., 2018).

The use of PMIP output as ocean forcing is an accepted practice in ocean modelling (e.g., Muglia and Schmittner (2015)). We refer to a "forced ocean model" as a model of the ocean-sea-ice-atmosphere system in which the atmosphere is represented by prescribed 2-D forcing fields. It can be used whenever ocean-atmosphere feedbacks are of minor importance and has the advantage of reducing the computational costs – making longer or more model runs feasible. We present 2-D (surface) anomaly fields of CMIP5/PMIP3 experiments 'lgm' minus 'piControl' calculated from monthly climatological PMIP3 output. The PMIP3 output is the result of global boundary conditions and forcings (such as insolation and ice sheet cover) applied in the fully coupled PMIP3 models (Braconnot et al., 2012). Our dataset (Morée and Schwinger, 2019) is a unique compilation of existing data, processed and reformatted such that it can be readily applied in a forced ocean model framework that uses a bulk forcing approach similar to Large and Yeager (2004). Since this approach has been popularized through coordinated model intercomparison activities (Griffies et al., 2009), a majority of forced ocean models today uses this approach. The 2-D anomaly fields presented here can be added to the pre-industrial forcing of a forced ocean model in order to obtain an atmospheric forcing representative of the LGM. The data are climatological mean anomalies, and as such suitable for equilibrium LGM 'time-slice' modelling of the ocean. The description of the procedure followed to make this dataset (Sect. 3) should support any extension of the dataset with additional (PMIP-derived) variables if needed. The PMIP4 guidelines (Kageyama et al., 2017) can support users in designing a specific model set-up, for example regarding the land-sea mask, trace gas concentrations, river runoff or other conditions and forcing one would

want to apply to a model. In Sect. 2, a general description of the dataset and data sources is provided alongside with an overview of the variables (Table 1).

Table 1: Summary of the data showing variable description, units, format (lon×lat, time), Notes, NetCDF variable name(s) and the original PMIP3 variable name(s). Formats follow CORE conventions (Large and Yeager, 2004). The wind component variables are provided in separate files (Morée and Schwinger, 2019). In each NetCDF file (i.e., for each variable) the model spread is provided alongside the anomaly field named 'variablename_spread'.

Variable description	Units	Resolution (lon×lat), time	Notes	Variable name	PMIP3 variable name(s)
Specific humidity	kg kg^{-1}	192×94, 1460	Re-referenced to 10 m	huss_10m	huss
Downwelling longwave radiation	W m^{-2}	192×94, 365		rlds	rlds
Downwelling shortwave radiation	W m^{-2}	192×94, 365		rsds	rsds
Precipitation	mm day^{-1}	192×94, 12		pr	pr
Wind (u and v components)	m s^{-1}	192×94, 1460		uas and vas	uas and vas
Temperature	K	192×94, 1460	Re-referenced to 10 m	tas_10m	tas
Sea surface salinity	psu	360×180, 12		sos	so

2 General description of the dataset

The data presented in this article are 2-D anomaly fields of the LGM versus pre-industrial state (experiment 'lgm' minus experiment 'piControl') based on the PMIP3 (Braconnot et al., 2012). These anomaly fields can be used as atmospheric LGM forcing fields for ocean-only model set-ups when added to pre-industrial forcing fields, and are optimized for use in combination with Coordinated Ocean-ice Reference Experiments (CORE) forcing fields (Griffies et al., 2009). The use of an anomaly forcing implies the assumption that no changes in temporal or spatial

variability occurred between the lgm and piControl states beyond changes in the mean. We note that by adding multi model mean anomalies to forcing fields, dynamical inconsistencies (e.g. between wind and temperature fields) could be created. A forcing data set would typically be dynamically consistent if the forcing would be the outcome of an advanced atmospheric reanalysis. However, the CORE forcing is a mixture of reanalysis and observational data products, and we assume that the addition of our anomaly fields will be a minor contribution to the dynamical inconsistencies already present in the CORE forcing fields (Large and Yeager, 2004). The basis of this data is monthly climatological PMIP3 output. Any variables presented on sub-monthly time resolution are therefore time-interpolated. Since this is a limitation of the available data, we have to assume that any sub-monthly variability (e.g. the diurnal cycle) is preserved from the preindustrial climate state to the LGM state. The anomalies are calculated as the mean of the difference between monthly climatologies of the 'lgm' and 'piControl' PMIP3 model runs. The calculation of such a model mean will dampen uncorrelated variability across the different models. However, for the sake of achieving long integration times (e.g., for paleo studies), we expect this approach is justifiable. Moreover, the calculated anomalies are generally small as compared to the forcing field itself. In cases where modelling groups provided more than one ensemble member, we included only the first member in our calculations. Even though PMIP3 simulations have limitations and a large inter-model spread, PMIP3 is the state of the art for modelling of past climates at present (Braconnot et al., 2012; Braconnot and Kageyama, 2015). Furthermore, no global proxy-based reconstructions of the variables presented here are available to provide a proxy-based LGM forcing dataset. Using mean coupled model output as forcing is thus considered the best available option for use in forced ocean models. The data is the mean anomaly of five PMIP3 models (CNRM-CM5, IPSL-CM5A-LR, GISS-E2-R, MIROC-ESM and MRI-CGCM3: Table 2), as only these models provide output for all variables.

The variables are i) specific humidity at 10 meters, ii) downwelling longwave radiation, iii) downwelling shortwave radiation, iv) precipitation, v) wind (v and u components), vi) temperature at 10 meters, and vii) sea surface salinity (SSS) (Table 1). The SSS anomaly field can be used to apply SSS restoring in LGM simulations.

Table 2: PMIP3 models used in this study

Model name	Modelling group	Reference	Source data reference
CNRM-CM5	CNRM-CERFACS (France)	Voldoire et al. (2013)	piControl: Sénési et al. (2014a) lgm: Sénési et al. (2014b)
IPSL-CM5A-LR	IPSL (Institut Pierre Simon Laplace, France)	Dufresne et al. (2013)	piControl: Caubel et al. (2016) lgm: Kageyama et al. (2016)
MIROC-ESM	MIROC (JAMSTEC and NIES, Japan)	Sueyoshi et al. (2013)	piControl: JAMSTEC et al. (2015a) lgm: JAMSTEC et al. (2015b)
MRI-CGCM3	MRI (Meteorological Research Institute, Japan)	Yukimoto et al. (2012)	piControl: Yukimoto et al. (2015a) lgm: Yukimoto et al. (2015b)
GISS-E2-R	NASA/GISS (Goddard Institute for Space Studies, USA)	Schmidt et al. (2014)	piControl: NASA-GISS (2014a) lgm: NASA-GISS (2014b)

All variables (Sect. 3.1-7) of the monthly climatological PMIP3 output have been regridded (Table 3, #1), averaged (Table 3, #2), and differenced (Table 3, #3) to calculate the anomaly fields. Additional procedures for each variable are provided in the respective part of Sect. 3, together with a figure of each variable's yearly mean anomaly and model spread. Alongside the lgm-piControl anomaly for each variable, the model spread across all five models is made available. This inter-model disagreement is described for each variable in Sect. 3, and could for example be used to guide adjustments of the amplitude of the forcing anomaly for model tuning

purposes. Additionally, proxy-base reconstructions are available for some of the variables (e.g., temperature), which can constrain potential adjustments to the forcing anomaly fields. We leave it to the individual modelling groups to make such adjustments to their forcing fields.

Table 3: Package commands applied in this study. Detailed information on these commands can be found in the respective NCO and CDO documentation online. All operations were performed with either CDO version 1.9.3 (Schulzweida, 2019) or NCO version 4.6.9. The complete list of commands is available in the NetCDF files as global attribute 'history'.

#	CDO or NCO command
1	cdo remapbil,t62grid
2	cdo ensmean
3	cdo sub
4	cdo setmisstodis
5	ncap2
6	cdo inttime

All operations were performed with NetCDF toolkits CDO version 1.9.3 (Schulzweida, 2019) or NCO version 4.6.9. The main functions used are documented in Table 3, and referred to in the text at the first occurrence. The atmospheric anomaly data are on a Gaussian grid, with 192×94 (lon×lat) grid-points. The SSS fields is on a regular 360×180 (lon×lat) grid. Regridding any of the files to a different model grid should be straightforward (e.g., Table 3, #1), as it was ensured that all files contain the information needed for re-gridding. The variables, grid and time resolution are chosen to be compatible with the CORE forcing fields (Large and Yeager, 2004), which have been extensively used in the ocean modelling community (e.g. Griffies et al. (2009); Schwinger et al. (2016)). We anticipate that the variables selected here should be useful in different model set-ups as well. We intend to provide a data set that is flexible with respect to the use of different land-ocean masks in different models. Therefore, we account for changes in sea-level (i.e. a larger land area in the LGM), which can affect variables in coastline areas, by applying the following masking

procedure: i) masking the multi-model mean anomaly with the maximum lgm land mask across all models, then ii) extrapolating the variable over land using a distance-weighted average (Table 3, #4), and iii) finally masking the data with a present-day land mask (based on the World Ocean Atlas 2013 1° resolution land mask), but with the ocean extended in a 1.5 degrees radius over land. This choice ensures that the anomaly forcing data can be used with any pre-industrial land-sea mask. Through following this procedure, the grid points affected by land-sea mask changes are thus filled with the extrapolated model mean anomaly from the LGM coastaln ocean. In the case of NorESM-OC (Schwinger et al., 2016), the atmospheric anomaly fields were added to its CORE normal-year forcing fields (Large and Yeager, 2004) to obtain an LGM normal-year forcing, under the assumption of an unchanged spatial and temporal variability for the respective variable. Note that the addition of the anomaly fields to the user's own model forcing could lead to physically unrealistic/not-meaningful results for some variables (such as negative precipitation or radiation). This must be corrected for by capping off sub-zero values (Table 3, #5) after addition of the anomaly.

3 The variables

3.1 Specific humidity anomaly

The monthly climatology of near-surface specific humidity is provided at 2 meters height in PMIP3. The bulk forcing method of Large and Yeager (2004) requires specific humidity (and temperature) at the same height as the wind forcing (10 meters). Therefore, specific humidity was re-referenced to 10 meters height for each of the four models following the procedure detailed in Large and Yeager (2004). The re-referencing required the use of wind (u and v components), sea level pressure (CMIP variable 'psl') and skin temperature ('ts', representing sea surface temperature over the open ocean), which were taken from the respective 'piControl' and 'lgm' CMIP5/PMIP3 output for each model. The mean anomaly over the four models was time interpolated (Table 3, #6) to a 6-hour time resolution from the monthly

climatological PMIP3 output. The annual mean lgm-piControl anomaly field (Fig. 1) shows a global decrease in specific humidity, as expected from decreased air temperatures (Sect. 3.6). The anomaly is most pronounced around the equator, where we see a decrease of 2-3 kg kg^{-1}, while the anomaly is near-zero towards both poles. The model spread of the anomaly shows a disagreement between the PMIP3 models generally in the order of 1-2 kg kg^{-1}, without any strong spatial pattern (Fig. 1).

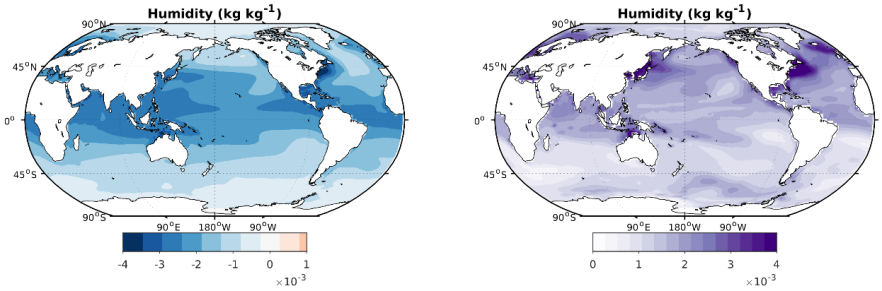

Figure 1: Annual mean 10-meter height specific humidity lgm-piControl anomaly (left) and model spread (right) in kg kg^{-1}.

3.2 Downwelling longwave radiation anomaly

The anomaly for surface downwelling longwave radiation is time-interpolated (Table 3, #6) to a daily time resolution. The annual mean anomaly field (Fig. 2) shows globally decreased downwelling longwave radiation in the 'lgm' experiment as compared to the 'piControl' experiment, in the order of 10-30 W m^{-2} over most of the ocean due to a generally cooler atmosphere (Sect. 3.6). The largest anomalies lie close to the northern ice sheets, with up to -90 W m^{-2} lower radiation in the 'lgm' experiment than in the 'piControl' experiment. Ice is likely also the main contributor to the high (60-90 W m^{-2}) inter-model spread in North Atlantic and Southern Oceans. The remainder of the ocean exhibits a better agreement, with inter-model spreads generally below 20 W m^{-2} (Fig. 2).

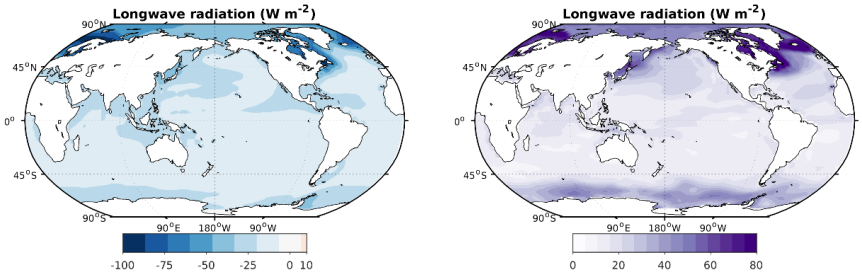

Figure 2: Annual mean downwelling longwave radiation lgm-piControl anomaly (left) and model spread (right) in W m^{-2}.

3.3 Downwelling shortwave radiation anomaly

The surface downwelling shortwave radiation anomaly field is time-interpolated (Table 3, #6) to daily fields as done for downwelling longwave radiation. The annual mean anomaly is especially pronounced around the Laurentide and Scandinavian ice sheets, where strong positive anomalies of over ~30 W m^{-2} exist (Fig. 3).

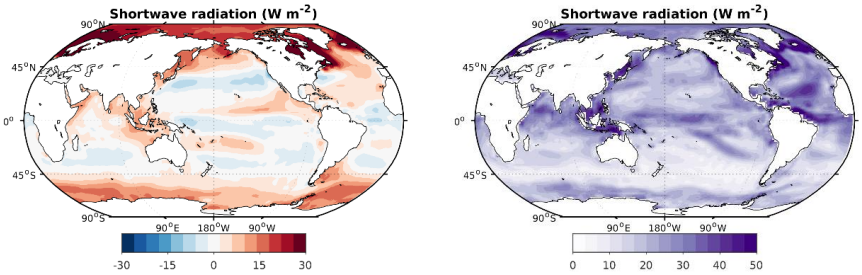

Figure 3: Annual mean downwelling shortwave radiation lgm-piControl anomaly (left) and model spread (right) in W m^{-2}.

Globally, the annual mean downwelling shortwave radiation anomaly generally falls in a range of -15 to +15 W m^{-2} over the ocean. The anomaly field shows negative anomalies as well positive ones in an alternating spatial pattern approximately symmetrically around the equator in the Pacific basin. The inter-model spread is largest in the North Atlantic region and along the equator (Fig. 3). Due to the large model disagreement of up to 50 W m^{-2} for this variable, the inter-model spread and

mean anomaly are of similar magnitude although a consistent pattern is present in the anomaly field.

3.4 Precipitation anomaly

The anomaly presented here is the lgm-piControl precipitation anomaly at the air-sea interface and includes both the liquid and solid phases from all types of clouds (both large-scale and convective), and excludes evaporation. The units were converted to mm day^{-1} to comply with the CORE forcing format (causing a deviation from the CF-1.6 convention). The resulting annual mean anomaly generally falls in the range of -2 to 2 mm day^{-1}, and is most pronounced along the equator (Fig. 4).

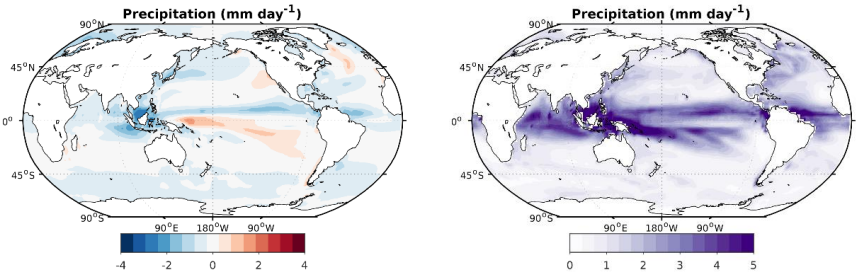

Figure 4: Annual mean precipitation lgm-piControl anomaly (left) and model spread (right) in mm day^{-1}.

The models show a mean increase in precipitation directly south of the equator in the Pacific basin, as well as in the Pacific subtropics off the western North-American coast. The North Atlantic also receives a mean positive precipitation anomaly, offsetting part of the positive salinity anomaly there, which is potentially relevant for the simulation of deep water formation in this region (Sect. 3.7). Negative mean precipitation anomalies are most pronounced directly north of the equator and north of ~40° N in the Pacific basin as well as in the Atlantic Arctic. The inter-model spread is up to ~5 mm day^{-1} around the equator, likely due to the model disagreement about the sign and location of changes in the inter-tropical convergence zone (Fig. 4). Related to precipitation fluxes, river runoff fluxes also changed between the lgm and piControl

model experiments. As river routing and flux calculations are very model specific, we expect modelling groups to find a suitable solution for their setup themselves, and recommend consulting the PMIP guidelines when doing so (Kageyama et al., 2017).

3.5 Wind anomalies, u and v components

Both for the u and v component of the wind speed, the lgm-piControl anomaly is time-interpolated to 6-hourly fields. The annual mean meridional wind velocity (v, southerly winds) anomaly shows a pronounced increase (~3-5 m s^{-1}) in southerly winds around the NW edge of the Laurentide ice sheet as well as over the NW edge of the Scandinavian ice sheet (Fig. 5). Alongside that, a pronounced decrease (~ 3-5 m s^{-1}) in southerly winds is simulated along the eastern North American coast and the Canadian archipelago. The open ocean anomalies are generally small (at most ±1 m s^{-1}). The inter-model spread has no pronounced pattern but is sizable, with ~ 1-5 m s^{-1} disagreement between the PMIP3 models. The mean zonal wind velocity (u, westerly winds) anomaly shows alternating negative and positive anomaly bands with an approximate ±2 m s^{-1} range (Fig. 6). This pattern is stronger in the Northern Hemisphere north of ~45° N. The inter-model spread (~1-3 m s^{-1}) has little structure except for the ~4-5 m s^{-1} disagreement in the Southern Ocean south of ~40° S, and the ~3-5 m s^{-1} disagreement in the North Atlantic (Fig. 6).

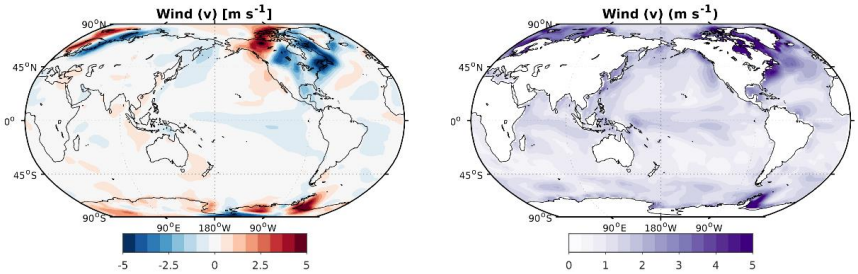

Figure 5: Annual mean meridional wind velocity lgm-piControl anomaly (left) and model spread (right) in m s^{-1}.

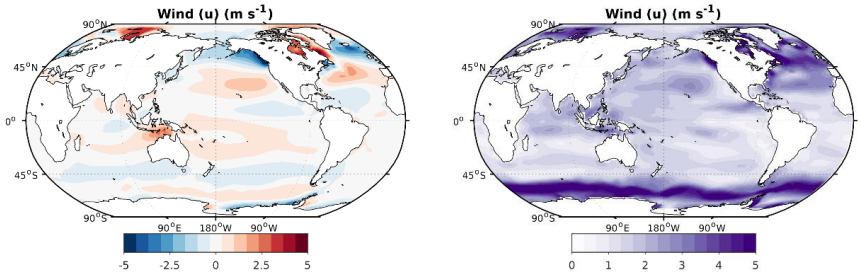

Figure 6: Annual mean zonal wind velocity lgm-piControl anomaly (left) and model spread (right) in m s^{-1}.

3.6 Temperature anomaly

The near-surface atmospheric temperature at 2 m height from PMIP3 is re-referenced to 10 meters (as done for specific humidity, Sect. 3.1), and time-interpolated to calculate the 6-hourly mean anomaly for temperature. The annual mean anomaly is most pronounced in the North Atlantic, where open ocean anomalies exceed 10 K. Elsewhere, the annual mean temperature generally is around 2.5 K. There is a clear pattern in the model spread: The models show a large spread (>10 K) north of ~45° N, as well as south of ~40° S (5-10 K), likely due to the disagreement about ice cover. At lower latitudes and over the ocean the model spread is generally smaller (0-3 K) (Fig. 7).

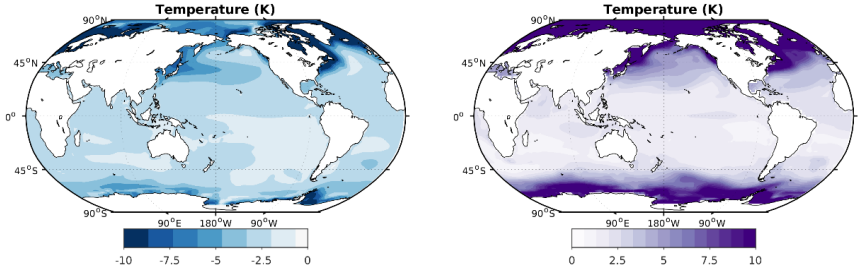

Figure 7: Annual mean 10-meter height temperature lgm-piControl anomaly (left) and model spread (right) in K.

3.7 Sea surface salinity anomaly

Global mean salinity is initialized in PMIP3 models with a 1 psu higher salinity to account for the concentrating effect of the decrease in sea level (Kageyama et al., 2017). Sea surface salinity however, shows a more variable annual mean lgm-piControl change due to changes in the global hydrological cycle (Fig. 8). The sea surface salinity anomaly is presented on a regular 1x1 grid for ease of use. The resulting annual mean SSS anomaly (Fig. 8) shows an increase in sea surface salinity (~1 psu) over the Southern Ocean south of ~55° S, as well as in the Arctic (>3 psu) and the Northern Indian Ocean (~1 psu). A ~2 psu anomaly is simulated in the Canadian Archipelago, the Labrador Sea and across the North Atlantic between what is now Canada and Europe (Fig. 8). Freshening is simulated close to some continents, and is especially pronounced around Scandinavia (about -3 psu). Simulated ocean circulation can be very sensitive to fresh water forcing and thus SSS, especially in the North Atlantic (e.g. Rahmstorf (1996), Spence et al. (2008)). Application of SSS restoring using the SSS anomaly field should therefore be done with caution and attention to its effects on the meridional overturning circulation. Tuning of the salinity anomaly in important deep-water formation regions of up to about ±1 psu, such as done by for example Winguth et al. (1999), may be required to obtain a satisfactory circulation field in reasonable agreement with proxy data. Such adjustments fall well within the PMIP3 model spread (Fig. 8), and show the current limitations of fully coupled PMIP3 models to simulate the LGM hydrological cycle consistent with proxy records of ocean circulation.

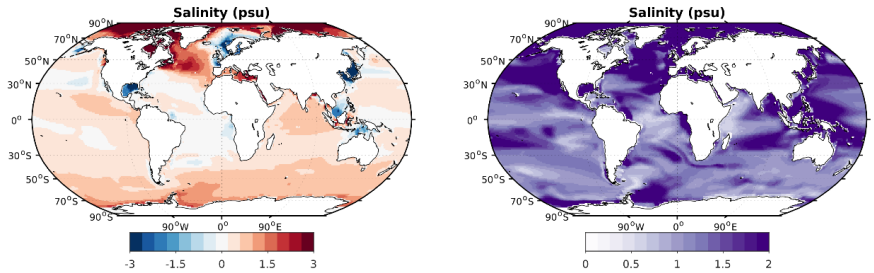

Figure 8: Annual mean sea surface salinity lgm-piControl anomaly (left) and model spread (right) in psu.

4 Data availability

The data are publicly accessible at the NIRD Research Data Archive at https://doi.org/10.11582/2019.00019 (Morée and Schwinger, 2019). The .md5 files contain an md5 checksum, which can be used to check whether changes have been made to the respective .nc files.

5 Summary and Conclusions

The output of the fully coupled PMIP3 simulations of CNRM-CM5, IPSL-CM5A-LR, MIROC-ESM and MRI-CGCM3 is converted to anomaly datasets intended for use in forced ocean modelling of the LGM. All anomalies are calculated as the difference between the 'lgm' and 'piControl' PMIP3 experiments. In addition, all data are formatted in a way that further conversions (of for example units or the grid) can be applied in a straightforward way. The variables are provided in NetCDF format in separate files, and distributed by the NIRD Research Data Archive (Morée and Schwinger, 2019). A climatological LGM forcing data set can be created for any forced ocean model by addition of the presented 2-D anomaly fields to the model's pre-industrial forcing. This approach enables the scientific community to simulate the LGM ocean state in a forced model set-up. We expect that if additional forcing is needed for a specific model, the same approach as described above can be followed. This process is simplified by providing all main CDO and NCO commands used in creating the dataset (Table 3). All data represent a climatological year, i.e. one annual cycle per variable. The application of the data is thus suitable for 'time-slice' equilibrium simulations of the LGM, and optimised for use with the CORE forcing format (Large and Yeager, 2004).

The uncertainty of our anomaly forcing (approximated by the model spread of the PMIP3 models) is generally of similar magnitude as the multi-model annual mean. The attribution of the model spread to specific processes is beyond the scope of this article, but our results show that there is considerable uncertainty involved in the

magnitude of the anomaly for all variables presented here. Nevertheless, all mean anomalies show a distinct spatial pattern that we expect to be indicative of the LGM-PI changes. Finally, there is no other way to reconstruct most of these variables than model simulations with state-of-the-art models such as those applied in the PMIP3 experiments. For modelling purposes, the inter-model disagreement of PMIP3 provides the user with leeway to adjust the amplitude of the forcing (guided by the size of the model spread, which is therefore provided alongside the variables in the dataset). Such adjustments can improve model-proxy data agreements, such as described for salinity in Sect. 3.7.

Author contributions. AM prepared, visualized and analyzed the data and wrote the original draft of the manuscript. AM and JS together conceptualized the method and revised the manuscript. JS provided supervision throughout the study.

Competing interests. The authors declare that they have no conflict of interest.

Acknowledgements. We acknowledge the World Climate Research Programme's Working Group on Coupled Modelling, which is responsible for CMIP, and we thank the climate modelling groups (Table 2) for producing and making available their model output. For CMIP the U.S. Department of Energy's Program for Climate Model Diagnosis and Intercomparison provides coordinating support and led development of software infrastructure in partnership with the Global Organization for Earth System Science Portals. This is a contribution to the Bjerknes Centre for Climate Research (Bergen, Norway). Storage resources were provided by UNINETT Sigma2 - the National Infrastructure for High Performance Computing and Data Storage in Norway (project number ns2980k). Anne L. Morée is grateful for PhD funding through the Faculty for Mathematics and Natural Sciences of the University of Bergen. Jörg Schwinger acknowledges funding through the Research Council of Norway (project INES (270061)). This study is a contribution to the project "Coordinated Research in Earth Systems and Climate: Experiments, kNowledge, Dissemination and Outreach"

(CRESCENDO; EU Horizon2020 Programme grant no. 641816) which is funded by the European Commission.

References

Braconnot, P., Otto-Bliesner, B., Harrison, S., Joussaume, S., Peterchmitt, J. Y., Abe-Ouchi, A., Crucifix, M., Driesschaert, E., Fichefet, T., Hewitt, C. D., Kageyama, M., Kitoh, A., Laîné, A., Loutre, M. F., Marti, O., Merkel, U., Ramstein, G., Valdes, P., Weber, S. L., Yu, Y., and Zhao, Y.: Results of PMIP2 coupled simulations of the Mid-Holocene and Last Glacial Maximum; Part 1: experiments and large-scale features, Clim. Past, 3, 261-277, 10.5194/cp-3-261-2007, 2007.

Braconnot, P., Harrison, S., Kageyama, M., Bartlein, P., Masson-Delmotte, V., Abe-Ouchi, A., Otto-Bliesner, B., and Zhao, Y.: Evaluation of climate models using palaeoclimatic data, Nature Climate Change, 2, 417-424, doi: 10.1038/nclimate1456, 2012.

Braconnot, P., and Kageyama, M.: Shortwave forcing and feedbacks in Last Glacial Maximum and Mid-Holocene PMIP3 simulations, Philosophical Transactions of the Royal Society A: Mathematical, Physical and Engineering Sciences, 373, 20140424, 10.1098/rsta.2014.0424, 2015.

Brady, E. C., Otto-Bliesner, B. L., Kay, J. E., and Rosenbloom, N.: Sensitivity to Glacial Forcing in the CCSM4, Journal of Climate, 26, 1901-1925, 10.1175/JCLI-D-11-00416.1, 2012.

Caubel, A., Denvil, S., Foujols, M. A., Marti, O., Dufresne, J.-L., Bopp, L., Cadule, P., Ethé, C., Idelkadi, A., Mancip, M., Masson, S., Mignot, J., Ionela, M., Balkanski, Y., Bekki, S., Bony, S., Braconnot, P., Brockman, P., Codron, F., Cozic, A., Cugnet, D., Fairhead, L., Fichefet, T., Flavoni, S., Guez, L., Guilyardi, E., Hourdin, F., Ghattas, J., Kageyama, M., Khodri, M., Labetoulle, S., Lefebvre, M.-P., Levy, C., Li, L., Lott, F., Madec, G., Marchand, M., Meurdesoif, Y., Rio, C., Schulz, M., Swingedouw, D., Szopa, S., Viovy, N., and Vuichard, N.: IPSL-CM5A-LR model output prepared for CMIP5 piControl experiment, served by ESGF,WDCC at DKRZ, doi:10.1594/WDCC/CMIP5.IPILpc, 2016.

Dufresne, J. L., Foujols, M. A., Denvil, S., Caubel, A., Marti, O., Aumont, O., Balkanski, Y., Bekki, S., Bellenger, H., Benshila, R., Bony, S., Bopp, L., Braconnot, P., Brockmann, P., Cadule, P., Cheruy, F., Codron, F., Cozic, A., Cugnet, D., de Noblet, N., Duvel, J. P., Ethé, C., Fairhead, L., Fichefet, T., Flavoni, S., Friedlingstein, P., Grandpeix, J. Y., Guez, L., Guilyardi, E., Hauglustaine, D., Hourdin, F., Idelkadi, A., Ghattas, J., Joussaume, S., Kageyama, M., Krinner, G., Labetoulle, S., Lahellec, A., Lefebvre, M. P., Lefevre, F., Levy, C., Li, Z. X., Lloyd, J., Lott, F., Madec, G., Mancip, M., Marchand, M., Masson, S., Meurdesoif, Y., Mignot, J., Musat, I., Parouty, S., Polcher, J., Rio, C., Schulz, M., Swingedouw, D., Szopa, S., Talandier, C., Terray, P., Viovy, N., and Vuichard, N.: Climate change projections using the IPSL-CM5 Earth System Model: from CMIP3 to CMIP5, Clim Dyn, 40, 2123-2165, 10.1007/s00382-012-1636-1, 2013.

Eyring, V., Bony, S., Meehl, G. A., Senior, C. A., Stevens, B., Stouffer, R. J., and Taylor, K. E.: Overview of the Coupled Model Intercomparison Project Phase 6 (CMIP6) experimental design and organization, Geosci. Model Dev., 9, 1937-1958, 10.5194/gmd-9-1937-2016, 2016.

Griffies, S. M., Biastoch, A., Böning, C., Bryan, F., Danabasoglu, G., Chassignet, E. P., England, M. H., Gerdes, R., Haak, H., Hallberg, R. W., Hazeleger, W., Jungclaus, J., Large, W. G., Madec, G., Pirani, A., Samuels, B. L., Scheinert, M., Gupta, A. S., Severijns, C. A., Simmons, H. L., Treguier, A. M., Winton, M., Yeager, S., and Yin, J.: Coordinated Ocean-ice Reference Experiments (COREs), Ocean Modelling, 26, 1-46, https://doi.org/10.1016/j.ocemod.2008.08.007, 2009.

JAMSTEC, AORI, and NIES: MIROC-ESM model output prepared for CMIP5 piControl, served by ESGF, doi:10.1594/WDCC/CMIP5.MIMEpc 2015a.

JAMSTEC, AORI, and NIES: MIROC-ESM model output prepared for CMIP5 lgm, served by ESGF, doi:10.1594/WDCC/CMIP5.MIMElg, 2015b.

Kageyama, M., Denvil, S., Foujols, M. A., Caubel, A., Marti, O., Dufresne, J.-L., Bopp, L., Cadule, P., Ethé, C., Idelkadi, A., Mancip, M., Masson, S., Mignot, J., Ionela, M., Balkanski, Y., Bekki, S.,

Bony, S., Braconnot, P., Brockman, P., Codron, F., Cozic, A., Cugnet, D., Fairhead, L., Fichefet, T., Flavoni, S., Guez, L., Guilyardi, E., Hourdin, F., Ghattas, J., Khodri, M., Labetoulle, S., Lefebvre, M.-P., Levy, C., Li, L., Lott, F., Madec, G., Marchand, M., Meurdesoif, Y., Rio, C., Schulz, M., Swingedouw, D., Szopa, S., Viovy, N., and Vuichard, N.: IPSL-CM5A-LR model output prepared for CMIP5 lgm experiment, served by ESGF,WDCC at DKRZ doi:10.1594/WDCC/CMIP5.IPILlg, 2016.

Kageyama, M., Albani, S., Braconnot, P., Harrison, S. P., Hopcroft, P. O., Ivanovic, R. F., Lambert, F., Marti, O., Peltier, W. R., Peterschmitt, J. Y., Roche, D. M., Tarasov, L., Zhang, X., Brady, E. C., Haywood, A. M., LeGrande, A. N., Lunt, D. J., Mahowald, N. M., Mikolajewicz, U., Nisancioglu, K. H., Otto-Bliesner, B. L., Renssen, H., Tomas, R. A., Zhang, Q., Abe-Ouchi, A., Bartlein, P. J., Cao, J., Li, Q., Lohmann, G., Ohgaito, R., Shi, X., Volodin, E., Yoshida, K., Zhang, X., and Zheng, W.: The PMIP4 contribution to CMIP6 – Part 4: Scientific objectives and experimental design of the PMIP4-CMIP6 Last Glacial Maximum experiments and PMIP4 sensitivity experiments, Geosci. Model Dev., 10, 4035-4055, 10.5194/gmd-10-4035-2017, 2017.

Kageyama, M., Braconnot, P., Harrison, S. P., Haywood, A. M., Jungclaus, J. H., Otto-Bliesner, B. L., Peterschmitt, J. Y., Abe-Ouchi, A., Albani, S., Bartlein, P. J., Brierley, C., Crucifix, M., Dolan, A., Fernandez-Donado, L., Fischer, H., Hopcroft, P. O., Ivanovic, R. F., Lambert, F., Lunt, D. J., Mahowald, N. M., Peltier, W. R., Phipps, S. J., Roche, D. M., Schmidt, G. A., Tarasov, L., Valdes, P. J., Zhang, Q., and Zhou, T.: The PMIP4 contribution to CMIP6 – Part 1: Overview and overarching analysis plan, Geosci. Model Dev., 11, 1033-1057, 10.5194/gmd-11-1033-2018, 2018.

Large, W. G., and Yeager, S. G.: Diurnal to decadal global forcing for ocean and sea-ice models: the data sets and flux climatologies, Tech. Note NCAR/TN-460+STR. National Center of Atmospheric Research, Boulder, Colorado, USA, http://opensky.ucar.edu/islandora/object/technotes:434, 2004.

Marzocchi, A., and Jansen, M. F.: Connecting Antarctic sea ice to deep-ocean circulation in modern and glacial climate simulations, Geophysical Research Letters, 44, 6286-6295, 10.1002/2017GL073936, 2017.

Menviel, L., Yu, J., Joos, F., Mouchet, A., Meissner, K. J., and England, M. H.: Poorly ventilated deep ocean at the Last Glacial Maximum inferred from carbon isotopes: A data-model comparison study, Paleoceanography, 32, 2-17, 10.1002/2016pa003024, 2017.

Morée, A., Schwinger, J.: PMIP3-based Last Glacial Maximum (LGM) pre-industrial (PI) anomaly fields for addition to PI ocean model forcing, version 2, Norstore, https://doi.org/10.11582/2019.00019, 2019.

Muglia, J., and Schmittner, A.: Glacial Atlantic overturning increased by wind stress in climate models, Geophysical Research Letters, 42, 9862-9868, doi:10.1002/2015gl064583, 2015.

NASA-GISS: GISS-E2-R model output prepared for CMIP5 pre-industrial control, served by ESGF WDCC at DKRZ, doi:10.1594/WDCC/CMIP5.GIGRpc, 2014a.

NASA-GISS: GISS-E2-R model output prepared for CMIP5 last glacial maximum, served by ESGF WDCC at DKRZ, doi:10.1594/WDCC/CMIP5.GIGRlg, 2014b.

Otto-Bliesner, B. L., Hewitt, C. D., Marchitto, T. M., Brady, E., Abe-Ouchi, A., Crucifix, M., Murakami, S., and Weber, S. L.: Last Glacial Maximum ocean thermohaline circulation: PMIP2 model intercomparisons and data constraints, Geophysical Research Letters, 34, 10.1029/2007GL029475, 2007.

Rahmstorf, S.: On the freshwater forcing and transport of the Atlantic thermohaline circulation, Clim Dyn, 12, 799-811, 10.1007/s003820050144, 1996.

Schmidt, G. A., Kelley, M., Nazarenko, L., Ruedy, R., Russell, G. L., Aleinov, I., Bauer, M., Bauer, S. E., Bhat, M. K., Bleck, R., Canuto, V., Chen, Y.-H., Cheng, Y., Clune, T. L., Del Genio, A., de Fainchtein, R., Faluvegi, G., Hansen, J. E., Healy, R. J., Kiang, N. Y., Koch, D., Lacis, A. A., LeGrande, A. N., Lerner, J., Lo, K. K., Matthews, E. E., Menon, S., Miller, R. L., Oinas, V., Oloso, A. O., Perlwitz, J. P., Puma, M. J., Putman, W. M., Rind, D., Romanou, A., Sato, M., Shindell, D. T., Sun, S., Syed, R. A., Tausnev, N., Tsigaridis, K., Unger, N., Voulgarakis, A., Yao, M.-S., and Zhang, J.:

Configuration and assessment of the GISS ModelE2 contributions to the CMIP5 archive, Journal of Advances in Modeling Earth Systems, 6, 141-184, 10.1002/2013MS000265, 2014.

Schulzweida, U.: CDO User Guide (Version 1.9.6), Max Planck Institute for Meteorology, Bundesstraße 53, 20146 Hamburg, Germany, http://doi.org/10.5281/zenodo.2558193, 215 pp., 2019.

Schwinger, J., Goris, N., Tjiputra, J. F., Kriest, I., Bentsen, M., Bethke, I., Ilicak, M., Assmann, K. M., and Heinze, C.: Evaluation of NorESM-OC (versions 1 and 1.2), the ocean carbon-cycle stand-alone configuration of the Norwegian Earth System Model (NorESM1), Geosci. Model Dev., 9, 2589-2622, 10.5194/gmd-9-2589-2016, 2016.

Sénési, S., Richon, J., Franchistéguy, L., Tyteca, S., Moine, M.-P., Voldoire, A., Sanchez-Gomez, E., Salas y Mélia, D., Decharme, B., Cassou, C., Valcke, S., Beau, I., Alias, A., Chevallier, M., Déqué, M., Deshayes, J., Douville, H., Madec, G., Maisonnave, E., Planton, S., Saint-Martin, D., Szopa, S., Alkama, R., Belamari, S., Braun, A., Coquart, L., and Chauvin, F.: CNRM-CM5 model output prepared for CMIP5 piControl, served by ESGF,WDCC at DKRZ, doi:10.1594/WDCC/CMIP5.CEC5pc, 2014a.

Sénési, S., Richon, J., Franchistéguy, L., Tyteca, S., Moine, M.-P., Voldoire, A., Sanchez-Gomez, E., Salas y Mélia, D., Decharme, B., Cassou, C., Valcke, S., Beau, I., Alias, A., Chevallier, M., Déqué, M., Deshayes, J., Douville, H., Madec, G., Maisonnave, E., Planton, S., Saint-Martin, D., Szopa, S., Alkama, R., Belamari, S., Braun, A., Coquart, L., and Chauvin, F.: CNRM-CM5 model output prepared for CMIP5 lgm, served by ESGF,WDCC at DKRZ, doi:10.1594/WDCC/CMIP5.CEC5lg, 2014b.

Spence, J. P., Eby, M., and Weaver, A. J.: The Sensitivity of the Atlantic Meridional Overturning Circulation to Freshwater Forcing at Eddy-Permitting Resolutions, Journal of Climate, 21, 2697-2710, 10.1175/2007JCLI2103.1, 2008.

Sueyoshi, T., Ohgaito, R., Yamamoto, A., Chikamoto, M. O., Hajima, T., Okajima, H., Yoshimori, M., Abe, M., O'Ishi, R., Saito, F., Watanabe, S., Kawamiya, M., and Abe-Ouchi, A.: Set-up of the PMIP3 paleoclimate experiments conducted using an Earth system model, MIROC-ESM, Geosci. Model Dev., 6, 819-836, 10.5194/gmd-6-819-2013, 2013.

Taylor, K. E., Stouffer, R. J., and Meehl, G. A.: An Overview of CMIP5 and the Experiment Design, Bulletin of the American Meteorological Society, 93, 485-498, 10.1175/BAMS-D-11-00094.1, 2011.

Voldoire, A., Sanchez-Gomez, E., Salas y Mélia, D., Decharme, B., Cassou, C., Sénési, S., Valcke, S., Beau, I., Alias, A., Chevallier, M., Déqué, M., Deshayes, J., Douville, H., Fernandez, E., Madec, G., Maisonnave, E., Moine, M. P., Planton, S., Saint-Martin, D., Szopa, S., Tyteca, S., Alkama, R., Belamari, S., Braun, A., Coquart, L., and Chauvin, F.: The CNRM-CM5.1 global climate model: description and basic evaluation, Clim Dyn, 40, 2091-2121, 10.1007/s00382-011-1259-y, 2013.

Winguth, A. M. E., Archer, D., Duplessy, J. C., Maier-Reimer, E., and Mikolajewicz, U.: Sensitivity of paleonutrient tracer distributions and deep-sea circulation to glacial boundary conditions, Paleoceanography, 14, 304-323, 10.1029/1999PA900002, 1999.

Yukimoto, S., Adachi, Y., Hosaka, M., Sakami, T., Yoshimura, H., Hirabara, M., Tanaka, T. Y., Shindo, E., Tsujino, H., Deushi, M., Mizuta, R., Yabu, S., Obata, A., Nakano, H., Koshiro, T., Ose, T., and Kitoh, A.: A New Global Climate Model of the Meteorological Research Institute: MRI-CGCM3;Model Description and Basic Performance, Journal of the Meteorological Society of Japan. Ser. II, 90A, 23-64, 10.2151/jmsj.2012-A02, 2012.

Yukimoto, S., Adachi, Y., Hosaka, M., Sakami, T., Yoshimura, H., Hirabara, M., Tanaka, T., Shindo, E., Tsujino, H., Deushi, M., Mizuta, R., Yabu, S., Obata, A., Nakano, H., Koshiro, T., Ose, T., and Kitoh, A.: MRI-CGCM3 model output prepared for CMIP5 piControl, served by ESGF,WDCC at DKRZ, doi:10.1594/WDCC/CMIP5.MRMCpc, 2015a.

Yukimoto, S., Adachi, Y., Hosaka, M., Sakami, T., Yoshimura, H., Hirabara, M., Tanaka, T., Shindo, E., Tsujino, H., Deushi, M., Mizuta, R., Yabu, S., Obata, A., Nakano, H., Koshiro, T., Ose, T., and Kitoh, A.: MRI-CGCM3 model output prepared for CMIP5 lgm, served by ESGF,WDCC at DKRZ, doi:10.1594/WDCC/CMIP5.MRMClg, 2015b.

Paper III

Evaluating the Biological Pump Efficiency of the Last Glacial Maximum Ocean using $\delta^{13}C$

Morée, A. L., J. Schwinger, U. Ninneman,

A. Jeltsch-Thömmes, I. Bethke, and C. Heinze

Submitted to Climate of the Past

III

Evaluating the Biological Pump Efficiency of the Last Glacial Maximum Ocean using $\delta^{13}C$

Anne L. Morée[1], Jörg Schwinger[2], Ulysses S. Ninneman[3], Aurich Jeltsch-Thömmes[4], Ingo Bethke[1], Christoph Heinze[1]

[1]Geophysical Institute, University of Bergen and Bjerknes Centre for Climate Research, Bergen, 5007, Norway

[2]NORCE Norwegian Research Centre and Bjerknes Centre for Climate Research, Bergen, 5838, Norway

[3]Department of Earth Science, University of Bergen and Bjerknes Centre for Climate Research, Bergen, 5007, Norway

[4]Climate and Environmental Physics, Physics Institute and Oeschger Centre for Climate Change Research, University of Bern, Bern, Switzerland

Correspondence to: Anne L. Morée (anne.moree@uib.no)

Abstract. Although both physical and biological marine changes are required to explain the 100 ppm lower atmospheric pCO_2 of the Last Glacial Maximum (LGM, ~21 ka) as compared to pre-industrial (PI) times, their exact contributions are debated. Proxies of past marine carbon cycling (such as $\delta^{13}C$) document these changes, and thus provide constraints for quantifying the drivers of long-term carbon cycle variability. This modelling study explores the relative roles of physical and biological changes in the ocean needed to simulate an LGM ocean in satisfactory agreement with proxy data, and here especially $\delta^{13}C$. We prepared a PI and LGM ocean model

state (NorESM-OC) with full biogeochemistry (including the carbon isotopes $\delta^{13}C$ and radiocarbon) and dynamic sea ice. The modelled LGM-PI differences are evaluated against a wide range of physical and biogeochemical proxy data, and show agreement for key aspects of the physical ocean state within the data uncertainties. However, the lack of a simulated increase of regenerated nutrients for the LGM indicates that additional biogeochemical changes are required to simulate an LGM ocean in agreement with proxy data. In order to examine these changes, we explore the theoretical effects of different global mean biological pump efficiencies on the simulated marine biogeochemical tracer distributions. We estimate that (besides changes in ocean circulation) an approximate doubling of the global mean biological pump efficiency from 38 % (PI) to 75 % (LGM) reduces model-proxy biases the most. The remaining absolute model-proxy error in $\delta^{13}C$ (which is 0.07 ‰ larger than the 0.19 ‰ data uncertainty) indicates that additional changes in ocean dynamics are needed to simulate an LGM ocean in agreement with proxy data, such as increased aging or volume of Southern Source Waters. Besides that, our theoretical approach of increasing the biological pump efficiency may be too simplified to capture the vertical redistribution of regenerated nutrients – also suggested by a too weak chemocline. Our results underline that only those coupled climate models that contain the processes and/or components that realistically change both ocean circulation and biogeochemistry will be able to simulate an LGM ocean in satisfactory agreement with proxy data – and hence be reliable for use in climate projections. Therefore, future research should aim to identify the exact physical and biogeochemical processes that could have doubled the global mean biological pump efficiency (i.e., the interior regenerated signature) between the PI and LGM, with a likely central role for Southern Source Waters.

1 Introduction

Model and proxy reconstructions of the Last Glacial Maximum (LGM) suggest major redistributions of marine biogeochemical tracers and water masses as compared to

pre-industrial (PI) times, as well as lower carbon storage in both the land biosphere and atmosphere. The culmination of these changes into a ~100 ppm lower LGM atmospheric pCO_2 concentration (EPICA Project Members, 2004) has driven extensive research to identify, understand, and quantify the processes contributing to these major atmospheric pCO_2 variations (e.g., Broecker, 1982; Broecker and Peng, 1986; Heinze and Hasselmann, 1993; Heinze et al., 2016; Sigman et al., 2010; Adkins, 2013; Jeltsch-Thömmes et al., 2019). The oceans are of particular interest as they form the largest carbon reservoir available for atmospheric exchange on millennial timescales, and in addition need to have stored the extra carbon coming from the land biosphere and atmosphere during the LGM. Both physical (circulation, solubility) and biological processes (biological pump efficiency) likely played a role in the differences between the LGM and PI oceans, although their relative importance is under debate: Between ~25 and ~60 % is attributed to biological processes and the remainder to physical changes (Bouttes et al., 2011; Buchanan et al., 2016; Khatiwala et al., 2019).

Here, we explore the relative roles of marine physical and biological changes needed to simulate an LGM ocean in optimal agreement with proxy data. We use the concept of the biological pump efficiency (defined as the ability of marine organisms to consume surface ocean phosphate, or more specifically the ratio of global mean regenerated to total phosphate, Sect. 2.4) to examine its effect on LGM marine biogeochemical tracer distributions in concert with physical changes. The global mean efficiency of the biological pump is strongly and nearly linearly correlated with atmospheric CO_2 concentrations (Ito and Follows, 2005) and is considered a key concept to understand the atmospheric CO_2 drawdown potential of the ocean (Ödalen et al., 2018) through its influence on the vertical gradient of marine dissolved inorganic carbon (DIC). In our evaluation and discussion, we pay particular attention to the role of Southern Source Waters (SSW, waters originating in the Southern Ocean), which are thought to be a key component in altering ocean interior tracer distributions and glacial atmospheric pCO_2 drawdown (e.g., Lynch-Stieglitz et al.,

2016; Schmitt et al., 2012; Moy et al., 2019; Sigman et al., 2010; Ferrari et al., 2014; Morée et al., 2018; Khatiwala et al., 2019).

Our work represents the first LGM simulation using a forced isopycnic ocean model (NorESM-OC; Schwinger et al., 2016; Tjiputra et al., 2020), where all atmospheric forcing fields have been adjusted to represent the LGM (Sect. 2). Besides a general ocean circulation model (MICOM), NorESM-OC simulates full biogeochemistry including the ^{13}C and ^{14}C carbon isotopes (model HAMOCC), as well as dynamic sea ice (model CICE) and a prognostic box atmosphere. The simulation of the carbon isotopes is particularly useful here as they i) can be directly compared to data from sediment cores (e.g., Gebbie et al., 2015; Skinner et al., 2017), ii) are influenced by both biological and physical processes (e.g., Broecker and McGee, 2013), iii) give an indication which oceanic regions could be most relevant (Schmitt et al., 2012; Morée et al., 2018; Skinner et al., 2017)), and, given the above, iv) are useful in model evaluation (Schmittner et al., 2013; Braconnot et al., 2012). We focus on the standardized $^{13}C/^{12}C$ carbon isotope ratio ($\delta^{13}C$; Zeebe and Wolf-Gladrow (2001)), for which relatively many LGM data are available (e.g., Peterson et al., 2014; Oliver et al., 2010). In addition, the $^{14}C/^{12}C$ carbon isotope ratio (expressed as $\Delta^{14}C$) provides the model with an age tracer (radiocarbon age), which can be used to understand water mass ventilation and circulation rates, and for comparison with reconstructed $\Delta^{14}C$ (Skinner et al., 2017; Gebbie and Huybers, 2012). We furthermore evaluate the LGM simulation against proxy and/or model reconstructions of water mass distributions, sea surface temperature, salinity, sea ice extent, export production, vertical nutrient redistribution, atmospheric pCO_2, the change in marine dissolved inorganic carbon, and O_2 (Sect. 3.2). We apply the concept of True Oxygen Utilization (TOU; Ito et al., 2004) instead of Apparent Oxygen Utilization (AOU) and make use of the explicit simulation of preformed biogeochemical tracers in our model (Tjiputra et al., 2020). This approach makes it possible to separate physical and biogeochemical drivers of the tracer distributions more thoroughly, and accounts for the role of the air-sea carbon disequilibrium pump (Khatiwala et al., 2019). We acknowledge that without a

land source of C in our simulated LGM ocean (of ~ 850 Gt C, Jeltsch-Thömmes et al., 2019), nor sediments that could alter $CaCO_3$ cycling and long-term organic matter burial (Sigman et al., 2010), we do not expect to simulate the full range of processes contributing to glacial-interglacial pCO_2^{atm} changes. Rather, we include estimates of these carbon reservoir changes in our evaluation of the LGM biological pump efficiency (Sect. 3.3).

The evaluation against proxy data allows us to evaluate both the physical and biological changes needed for simulating the LGM ocean. Notably, in fully coupled paleo Earth System Modelling such as in the most recent Paleo Modelling Intercomparison Project 3 (PMIP3), only two out of nine Earth System Models included marine biogeochemistry in their LGM simulation (IPSL-CM5A-LR (Dufresne et al., 2013) and MIROC-ESM (Sueyoshi et al.,2013)). Earth System Models of intermediate complexity (and coarse resolution ocean model studies) have shown that changes in model (biogeochemical) parameterizations are needed to simulate glacial-interglacial cycles in agreement with proxy records (e.g., Jeltsch-Thömmes et al., 2019; Ganopolski and Brovkin, 2017; Buchanan et al., 2016; Heinze et al., 1991; Heinze and Hasselmann, 1993; Heinze et al., 2016). In our forced ocean model setup, we are able to reveal aspects important for modelling the LGM and relevant for improving the agreement between fully coupled paleo modelling and proxy data. Moreover, our work will help to gain insight in the changes (i.e. physical and biological) needed to simulate a different climate state (such as the LGM) - which also applies to Earth System Model-based climate projections.

2 Methods

2.1 Model description

We apply the ocean carbon-cycle stand-alone configuration of the Norwegian Earth System Model (NorESM) as described by Schwinger et al. (2016), but with several modifications for the next generation NorESM version 2 already included. The

physical ocean component MICOM (Miami Isopycnic Coordinate Ocean Model; Bentsen et al., 2013) has been updated as described in Guo et al. (2019). The biogeochemistry component HAMOCC (HAMburg Ocean Carbon Cycle model; Maier-Reimer, 1993; Maier-Reimer et al., 2005) adopted for use with the isopycnic MICOM (Assmann et al., 2010; Tjiputra et al., 2013; Schwinger et al., 2016) has undergone a few minor technical improvements (e.g. updated initialisation based on latest data products, additional diagnostic tracers) and employs a new tuning of the ecosystem parameterization as described in Tjiputra et al. (2020).

In addition to these changes, the carbon isotopes (^{13}C and ^{14}C) are implemented in HAMOCC (Tjiputra et al. (2020)), a prognostic box atmosphere is made available for atmospheric CO_2 (including $^{13}CO_2$ and $^{14}CO_2$; Tjiputra et al., 2020), and an LGM setup is made (Sect. 2.2). This is an ocean-only modelling study, where the atmospheric forcing is prescribed from a data set (except atmospheric CO_2, $\delta^{13}C$ and $\Delta^{14}C$, which evolve freely; Sect. 2.2). All simulations in this study are done without the sediment module of HAMOCC (this is done in order to avoid prohibitively long spin-up times, especially for the carbon isotopes; an acceleration method for the model spin-up including interactive water column-sediment interaction is work in progress for a separate manuscript). Applying the current setup, detritus arriving at the sediment-water interface is evenly redistributed over the entire water column, while opal and $CaCO_3$ are dissolved immediately in the bottom-most mass containing layer. Riverine input of carbon and nutrient is also turned off. Furthermore, nitrogen deposition, denitrification and nitrogen fixation are excluded from our simulations, as these processes cause a long-term drift in the alkalinity inventory of the ocean (and thereby the pCO_2 of the prognostic atmosphere).

The two main isotopes of carbon, ^{13}C and ^{14}C, are newly implemented in HAMOCC (Tjiputra et al., 2020). The model includes fractionation during air-sea gas exchange and photosynthesis, as well as radiocarbon decay. Fractionation during $CaCO_3$ formation is small as compared to the effects of air-sea gas exchange and

photosynthesis, as well as uncertain (Zeebe and Wolf-Gladrow, 2001) and is therefore omitted (e.g., Schmittner et al., 2013; Lynch-Stieglitz et al., 1995). Air-sea gas exchange fractionation (~8-11 ‰) is a function of surface ocean temperature and the CO_3^{2-} fraction of total DIC such that fractionation increases with decreasing temperatures (Zhang et al., 1995; Mook, 1986). Biological fractionation (~19 ‰) increases surface water $\delta^{13}C$ of DIC while producing low-$\delta^{13}C$ organic matter. In the interior ocean, this light isotope signal from organic matter is released back into the water column during remineralization and respiration, thereby creating a vertical gradient. HAMOCC applies the parameterization by Laws et al. (1997), where the biological fractionation ε_{bio} depends on the ratio between phytoplankton growth rate and the aqueous CO_2 concentration. For ^{14}C, each fractionation factor is set to the quadratic of the respective ^{13}C value (i.e., $\alpha_{14C} = \alpha^2_{13C}$). In addition, ^{14}C is radioactive and decays with a half-life of 5730 years to ^{14}N.

In order to evaluate the carbon isotopes against observations, we derive $\delta^{13}C$ and $\Delta^{14}C$. $\delta^{13}C$ is calculated using the standard equation $\delta^{13}\mathrm{C} = \left(\frac{^{13}C/^{12}C}{(^{13}C/^{12}C)_{standard}} - 1\right) * 1000\ ‰$,where $(^{13}C/^{12}C)_{standard}$ is the Pee Dee Belemnite standard ratio (0.0112372; Craig (1957)). $\Delta^{14}C$ is calculated by standardizing $DI^{14}C$ following $\delta^{14}\mathrm{C} = \left(\frac{^{14}C/C}{(^{14}C/C)_{standard}} - 1\right) * 1000\ ‰$, where $(^{14}C/C)_{standard}$ is the NBS standard ($1.170 \cdot e^{-12}$; Orr et al., 2017). $\Delta^{14}C$ is then calculated from $\delta^{14}C$, following $\Delta^{14}\mathrm{C} = \delta^{14}\mathrm{C} - 2 * (\delta^{13}\mathrm{C} + 25) * (1 + \frac{\delta^{14}\mathrm{C}}{1000})$. $\Delta^{14}C$ age presented in this study is derived from $\Delta^{14}C$ of DIC following ($\Delta^{14}C_{age} = -8033 * \ln(-8033 * \Delta^{14}\mathrm{C}/1000) + 1$) and is based on calibrated $\Delta^{14}C$ of DIC using an atmospheric value of 0 ‰ for both the LGM and PI spinup (Tjiputra et al., 2020). This approach facilitates comparison with the radiocarbon disequilibrium data by Skinner et al. (2017).

2.2 Last Glacial Maximum setup

Several adjustments were made to the model in order to obtain an LGM circulation field. First, the land-sea mask and ocean bathymetry were adjusted for the ~120 m lower sea level in the LGM caused by the increased land ice volume as compared to the PI. Following the PMIP4 guidelines in Kageyama et al. (2017) the Bering Strait is closed, and the Canadian Archipelago (including Borrow Strait and Nares Strait), Barents Sea, Hudson Bay, Black Sea, Red Sea, as well as the Baltic and North Seas are defined as land in the LGM. The PI land-sea mask formed the basis for the LGM land-sea mask, through shifting the PI bathymetry 116 m upwards. If the resulting depth in a grid cell was between 0-25 meters, the depth was set to 25 m and negative depths were set to land grid points. After this, any channels with a width of only one grid cell were closed off as well, as these inhibit sea ice movement in the sea ice model causing unrealistic sea ice build-up. LGM freshwater runoff is routed to the nearest ocean grid cell but otherwise unadjusted.

Changes in isopycnal densities and sea surface salinity restoring are applied in the LGM model setup in order to ensure an adequate vertical model resolution and ocean circulation. A net LGM increase in density due to decreased ocean temperatures and increased ocean salinity required increasing all 53 isopycnal layer densities by 1.3 kg m^{-3} in the LGM setup as compared to the PI model setup. NorESM-OC uses salinity restoring to avoid long-term drift away from a predefined SSS state. Here, this predefined state is chosen, consistent with the atmospheric forcing (see below) as the mean of the LGM minus PI SSS anomaly modelled by PMIP3 models added to a PI SSS climatology. However, the unadjusted application of the PMIP3-based SSS anomaly caused an Atlantic water mass distribution and overturning strength in poor agreement with proxy reconstructions (SM 2). Earlier studies have shown a high sensitivity of models to SSS restoring, especially in the North Atlantic (Rahmstorf, 1996; Spence et al., 2008; Bopp et al., 2017). Indeed, the density contrast between Northern and Southern source waters drives the simulated Atlantic Meridional

Overturning Circulation (AMOC) strength in many of the PMIP2 models (Weber et al., 2007), and is therefore important for the simulation of overturning strength in agreement with proxy records. Therefore, we adjust the SSS restoring present in NorESM-OC to obtain a circulation field in better agreement with proxy reconstructions: In addition to the PMIP3-based SSS anomaly, we apply a region of -0.5 psu in the North Atlantic and +0.5 psu in the Southern Ocean (for specifics, see SM 1), as done similarly by Winguth et al. (1999) or through freshwater fluxes by Menviel et al. (2017) and Bopp et al. (2017).

An atmospheric LGM forcing for NorESM-OC was created by adding anomalies (relative to the pre-industrial state) derived from PMIP3 models (Morée and Schwinger, 2019; version 1) to the CORE Normal Year Forcing (NYF; Large and Yeager, 2004). The use of mean PMIP/CMIP anomalies to force stand-alone models is a standard approach that has been tested before (Mitchell et al., 2017; Chowdhury and Behera, 2019; Muglia et al., 2015; Muglia et al., 2018). Through this approach, the effect of the presence of sea ice on the atmospheric state is included in the forcing, but the sea ice model handles the actual formation/melt of sea ice. Compared to the PI CORE-NYF, the LGM forcing over the ocean has a lower specific humidity (especially in the tropics), decreased downwelling longwave radiation, precipitation and air temperature, and a heterogeneous change in downwelling shortwave radiation and zonal and meridional winds. In addition to the adjustments to the NYF, the dust fluxes of Lambert et al. (2015) are used in the LGM model setup, following PMIP4 guidelines (Kageyama et al., 2017). The PI setup uses the Mahowald et al. (2006) dust dataset.

2.3 Initialization and tuning

All marine biogeochemical tracers were initialized in the LGM as done for the PI spin-up using the WOA and GLODAPv2 data sets. For the LGM, consistent with the decreased ocean volume, all biogeochemical tracer concentration are increased at initialization by 3.26 %. Similarly, ocean salinity is uniformly increased by 1 psu, following PMIP recommendations. The carbon isotopes (Sect. 2.1) are only enabled

after an initial spin-up of the model in order to first obtain reasonably stabilized total carbon tracer distributions. DI^{13}C is initialized after 1000 years using the correlation between δ^{13}C and apparent oxygen utilization (AOU) in combination with the model's DIC distribution. We applied the δ^{13}C:AOU relationship of the pre-industrial Eide et al. (2017) data ($\delta^{13}C_{PI} = -0.0075 \cdot \mathrm{AOU} + 1.72$) and converted to absolute model ^{13}C using model DIC and AOU. As this approach uses the model's 'native' AOU and DIC, the equilibration time of δ^{13}C was reduced as compared to initialisation with a δ^{13}C data product such as that of Eide et al. (2017). Model DI^{14}C is initialized after 4000 years by first calculating δ^{14}C using a combination of pre-industrial δ^{13}C (Eide et al., 2017) (with the missing upper 200m copied from 200m depth to all empty surface layers) and the observational-based estimate of pre-industrial Δ^{14}C (Key et al., 2004). Then, model DI^{14}C is derived from the δ^{14}C by rewriting and solving the standardization equation ($\delta^{14}C = \left(\frac{^{14}C/C}{(^{14}C/C)_{standard}} - 1\right) * 1000$ ‰, with model DIC as C). Subsequently, isotopic DOC, POC, phytoplankton C, and zooplankton C are initialized as done for the corresponding total carbon variable, but multiplied with 0.98 (as an estimate of the photosynthetic fractionation effect) and the respective DI^{13}C/DI^{12}C or DI^{14}C/DI^{12}C ratio. Isotopic $CaCO_3$ is initialized as for total carbon, multiplied with DI^{13}C/DI^{12}C or DI^{14}C/DI^{12}C, as we do not consider fractionation during $CaCO_3$ formation.

The prognostic atmospheric pCO_2 is initialized at 278 ppm for both spin-ups. At initialization of the carbon isotopes, atmospheric δ^{13}C is set to -6.5 ‰ and atmospheric Δ^{14}C is set to 0 ‰. Atmospheric pCO_2 at the time of initialization is then used to calculate the absolute ^{13}C and ^{14}C model concentrations ($^{13}C^{atm}$ and $^{14}C^{atm}$, in ppm).

Two main spin-ups have been made with NorESM-OC: One for the LGM and one for the PI, designed as described in Sect. 2.1-2.3. Both the PI and LGM simulations are run for a total of 5600 years.

2.4 Analysis of the biological pump efficiency

Here, we explore the effect of an increase in the global mean biological pump efficiency ($\overline{BP_{eff}}$, Eq. 1), which we define, following Ito and Follows (2005), as the ratio between global mean regenerated phosphate ($\overline{PO_4^{reg}}$) and global mean total phosphate ($\overline{PO_4}$).

$$\overline{BP_{eff}} = \overline{PO_4^{reg}}/\overline{PO_4} \quad (1)$$

Regenerated phosphate is calculated as the difference between total phosphate and preformed phosphate (PO_4^{pref}). PO_4^{pref} is explicitly simulated in the model (Tjiputra et al., 2020), and represents phosphate that leaves the mixed layer in inorganic form (unutilized by biology).

We work with the global mean value of $\overline{BP_{eff}}$ as this governs pCO_2^{atm} (Ito and Follows, 2005; Ödalen et al., 2018). However, we note that major local differences in the ratio of regenerated to total phosphate exist in the ocean, for example between North Atlantic Deep Water (high-ratio) and Antarctic Bottom Water (low-ratio) (Ito and Follows, 2005; DeVries et al., 2012), which thus indicate the differences in potential to sequester carbon and nutrients in the ocean interior. Here, changes in $\overline{BP_{eff}}$ are calculated in a theoretical framework (off-line) to better understand the LGM redistribution of carbon between the land, atmosphere and ocean, and its effects on marine biogeochemistry (and corresponding proxy data). Our approach also allows us to give an upper estimate of the $\overline{BP_{eff}}$ of the LGM ocean.

Simulated $\overline{BP_{eff}}$ can be adjusted to any assumed $\overline{BP_{eff}}$ by changing $\overline{PO_4^{reg}}$ ($\overline{PO_4^{reg}}_{new} = \overline{BP_{eff}}_{new} \times \overline{PO_4}$). The assumed change in PO_4^{reg} (ΔPO_4^{reg}) is used to estimate the effects on DIC, O_2 and $\delta^{13}C$ using the following relationships:

$$O_2{}^{new} = O_2 - \Delta PO_4^{reg} \times r_{O:P} \quad (2)$$

$$DIC^{new} = DIC + \Delta PO_4^{reg} \times r_{C:P} \quad (3)$$

$$\delta^{13}C^{new} = \delta^{13}C - R_{\delta^{13}C:PO_4^{reg}} \times \Delta PO_4^{reg} \quad (4)$$

Model Redfield ratios $r_{O_2:P}$ and $r_{C:P}$ are set to 172 and 122, respectively (following Takahashi et al., 1985). $R_{\delta^{13}C:PO_4^{reg}}$ is the slope of the $\delta^{13}C$: PO_4^{reg} relationship, which is found to be 0.67 in the model (R^2=0.76).

The spatial distribution of ΔPO_4^{reg} is an important consideration. We therefore explore ΔPO_4^{reg} by applying three different methods: The first method (method 'add') equally distributes the mean change in ΔPO_4^{reg} over the entire ocean ($PO_4^{reg}{}_{new} = PO_4^{reg}{}_{model} + \overline{\Delta PO_4^{reg}}$). The second method (method 'factor') takes into account the original distribution of $PO_4^{reg}{}_{model}$ (by calculating $\overline{\Delta PO_4^{reg}} = \overline{PO_4^{reg}}_{new} / \overline{PO_4^{reg}}_{model}$ and calculating for every grid cell $PO_4^{reg}{}_{new} = PO_4^{reg}{}_{model} \times \overline{\Delta PO_4^{reg}}$). The third method is as the first, additive, method but only adding the extra regenerated tracers to SSW as determined from the conservative PO tracer (method 'SSW', see Sect. 3.2 for the LGM PO tracer distribution).

It is important to note that $\overline{BP_{eff}}$ can be changed by several processes: through the soft- and hard tissue biological pumps, the solubility pump (Heinze et al., 1991; Volk and Hoffert, 1985) and by changes in the physical carbon pump (circulation/stratification of the water column).

3 Results and discussion

The results presented in Sect. 3.1 and Sect. 3.2 are the annual mean climatologies over the last 30 years of the 5600-year PI and LGM spin-ups. We present an evaluation of the PI (Sect. 3.1) and LGM (Sect. 3.2) spin-ups and compare the latter to proxy reconstructions, and discuss the LGM-PI changes in a theoretical framework exploring the efficiency of the biological pump (Sect. 3.3).

3.1 The simulated pre-industrial ocean

The simulated pre-industrial ocean state has a maximum AMOC strength of ~18 ± 0.5 Sv north of 20° N, which compares favourably to the mean observational estimates of 17.2-18.7 Sv (Srokosz and Bryden, 2015; McCarthy et al., 2015), especially when noting the wide range of modelled AMOC strengths in similar forced ocean setups (Danabasoglu et al., 2014). The interannual variability of the simulated AMOC is small compared to observations (about ±4 Sv; Srokosz and Bryden, 2015), due to the annually repeating forcing. Drake Passage transport is simulated at ~114 Sv, lower than recent observational estimate of 173.3 ± 10.7 Sv (Donohue et al., 2016). The depth of the transition between the upper and lower overturning cells at 30° S lies at ~2700 m, comparable to other model estimates (Weber et al., 2007). Temperature biases are generally modest (smaller than ± 1.5°C) for most of the ocean above 3000m, except for a warm bias related to a too deep tropical and subtropical thermocline. At depth (>3000 m) there is a widespread cold bias that originates from the Southern Ocean (too much deep mixing and associated heat loss to the atmosphere). Salinity biases are generally small, except for a positive bias related to a too strong Mediterranean outflow at mid-depth in the Atlantic. Furthermore, the ocean is ~0.2-0.3 psu too fresh at depths over ~3 km. The mixed layer depth (MLD) is generally simulated too deep (compared to the observational estimates of De Boyer Montégut et al. (2004)). In the high latitudes, winter month MLD biases in excess of 200 metres are present in our model. In low latitudes, MLD is about 20 metres too deep year-round. The simulated biogeochemistry of the PI ocean is described in more detail in Schwinger et al. (2016) although there have been some improvements due to the model updates mentioned above as described in Tjiputra et al. (2020). Some features of relevance for this study are summarized here: The spatial pattern of primary production (PP) compares well with observation-based estimates with the exception of the tropical Pacific upwelling, where PP is too high, and the subtropical gyres where PP is generally too low. Because of too high PP and export in the equatorial Pacific, a far too large oxygen minimum zone (OMZ) with elevated concentrations of

regenerated phosphate develops in the model. Otherwise, the global nutrient concentrations are in reasonable agreement with modern observations (WOA, Glodapv2). $\overline{BP_{eff}}$ is 38 % for the simulated PI ocean, in good agreement with observational estimates of 32-46 % (Ito and Follows, 2005; Primeau et al., 2013).

3.2 The simulated LGM ocean

3.2.1 The physical ocean state

Proxy-based reconstructions describe an LGM circulation that includes a shoaling of the upper circulation cell in the Atlantic (Glacial NADW) and expansion and slow-down of a cooler and more saline lower circulation cell (Glacial AABW; Adkins, 2013; Sigman et al., 2010; Ferrari et al., 2014). In this study, we assume these aspects of the LGM ocean to be qualitatively correct, and therefore aim for a model simulation in agreement with these features. We note that discussion continues as to the magnitude and veracity of these change (e.g., Gebbie, 2014). Most reconstructions estimate a weakened AMOC for the LGM as compared to the PI state, although estimates vary between a 50 % weakening and an invigoration of AMOC (McManus et al., 2004; Kurahashi-Nakamura et al., 2017; Böhm et al., 2014; Lynch-Stieglitz et al., 2007; Muglia et al., 2018). The maximum overturning strength north of 20° N simulated by NorESM-OC is 15.6 Sv (~7 % weaker than simulated for our PI ocean, which we attribute to our adjustments and tuning of the salinity restoring). Higher uncertainties are involved with reconstructions of the strength of the Antarctic Circumpolar Current (ACC), with consensus leaning towards a slight invigoration (Lynch-Stieglitz et al., 2016; Lamy et al., 2015; McCave et al., 2013; Mazaud et al., 2010; Buchanan et al., 2016). We simulate a Drake Passage transport of 129 Sv, which is about 13 % stronger than simulated for the PI ocean. The simulated transition between the Atlantic overturning cells shoals by ~350m, which falls within the uncertainty of reconstructions (Gebbie, 2014; Adkins, 2013; Oppo et al., 2018) (Fig. S5). Specifically, the transition lies well above the main bathymetric features of the Atlantic Ocean in our LGM simulation (as visible from the transition line in the PO

tracer; Fig. 1). This could have been an important feature of the glacial Atlantic water mass configuration due to reduced mixing along topography (Adkins, 2013; Ferrari et al., 2014) - i.e., shifting water mass boundaries away from the regions of intense internal mixing increases chemical and tracer stratification. The changes in water mass circulation cause an increased SSW volume contribution to the Atlantic and Pacific basins, as visible from the conservative PO tracer (Fig. 1, and Fig. S4 for Pacific) (Broecker, 1974), and in agreement with proxy reconstructions. Radiocarbon age increases at depth (Fig. 1c and Fig. S4), with a global volume-weighted mean increase of 269 years. This is low compared to the estimate of Skinner et al. (2017) of 689±53 years, and we find the majority of our radiocarbon age bias to lie at depth in the Atlantic (not shown) indicating too strong ventilation and/or biased equilibration of these waters (which have a southern source, Fig 1a-b). Furthermore, SSW salinity increases (Fig. S6) – also in good agreement with proxy reconstructions (Adkins, 2013).

Also relevant for the water mass circulation as well as marine biogeochemistry, are the low LGM atmospheric temperatures that cause a mean ocean temperature decrease of 1.9 °C in the model. This is less than the 2.57 ± 0.24 °C estimated from proxy reconstructions of mean ocean temperature (Bereiter et al., 2018), likely because the SSW may not carry a strong enough temperature decrease from the atmosphere into the interior ocean in our simulation (Fig. S7) – implying an underestimation of negative buoyancy fluxes. While the differences between our simulated LGM-PI changes in SST (Fig. S8) do not exhibit the same amount of heterogeneity as observed in proxy reconstructions (MARGO Project Members, 2009), the simulated mean SST change (-1.97 °C) seems reasonable when taking into account the uncertainty of SST reconstructions (MARGO Project Members (2009) estimate -1.9 ± 1.8 °C; Ho and Laepple, 2015). Further, the general pattern of stronger SST cooling outside of the polar regions is captured which is important for the air-sea disequilibrium pump (Khatiwala et al., 2019). We simulate an increase in Southern Ocean sea ice cover for both summer and winter (Fig. S9), but less than is inferred

from proxy-based reconstructions for the LGM (Gersonde et al., 2005) – similar to PMIP models (Roche et al., 2012). Southern Ocean sea ice may have played a major role in LGM marine biogeochemistry and interior ocean carbon storage (Ferrari et al., 2014; Marzocchi and Jansen, 2017; Stephens and Keeling, 2000), and could therefore explain some of the model biases. Examples are the lack of stratification in the Southern Ocean which is thought to be driven by brine rejection from sea ice (Jansen, 2017), and affect air-sea equilibration of biogeochemical tracers such as DIC and O_2 (Gottschalk et al., 2016a).

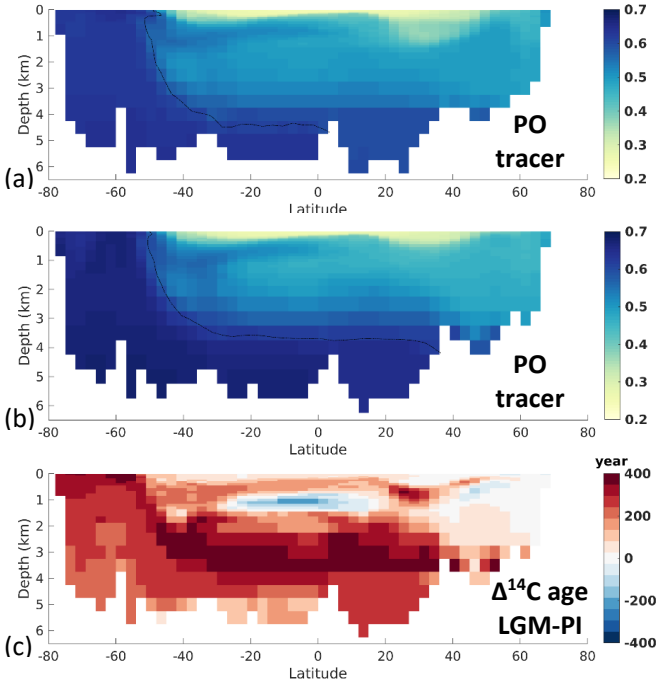

Figure 1 Atlantic zonal mean PO (25-35° W) for (a) the PI and (b) the LGM model states. PO = O_2 + 172 * PO_4 (Broecker, 1974). The line represents the respective end-member PO of the Southern source waters (mean Southern Ocean surface PO), and thus the extent of Southern source water. (c) The change in radiocarbon age between the LGM and PI. See Fig. S4 for the corresponding Pacific zonal mean transects.

3.2.2. The biogeochemical ocean state

Proxies for the past biogeochemical state of the ocean (such as export production, oxygen concentrations, $\delta^{13}C$) allow us to make a further evaluation of our simulated

LGM ocean (Fig. 2). The global mean efficiency of the biological pump $\overline{BP_{eff}}$ decreases from 38 % in the PI simulation to 33 % in the LGM simulation, as opposed to reconstructions which infer an increased regenerated signature in the interior ocean (Jaccard et al., 2009; Umling et al., 2018; Freeman et al., 2016). The simulated increase in preformed phosphate (Fig. 2) represents an increased (but unused) potential for the ocean to draw down atmospheric pCO_2 (Ödalen et al., 2018). We can attribute our simulated decrease in $\overline{BP_{eff}}$ to the increase in SSW volume (Fig. 1), as SSW has a low regenerated signature (Ito and Follows, 2005). Despite the decrease in $\overline{BP_{eff}}$, simulated pCO_2^{atm} is 21 ppm lower in our LGM setup as compared to the PI setup. We attribute this change to the net effect of the i) smaller ocean volume, causing the concentration of alkalinity, DIC and salinity and a reportedly ~16 ppm pCO_2^{atm} increase (Sarmiento and Gruber, 2006), and ii) the decrease in water temperature, which drives a pCO_2^{atm} drawdown of ~30 ppm (Sigman and Boyle, 2000). As we made no additional changes to the marine biogeochemical model (except for an LGM dust input field), and have no sediment or land model included in our simulation, the ~20 ppm pCO_2^{atm} drawdown as well as limited changes in regenerated nutrient inventories is expected and found in earlier studies (e.g., Buchanan et al., 2016). Similarly, the atmospheric $\delta^{13}C$ change due to glacial land-vegetation loss is not simulated because we only simulate the ocean.

Simulated changes in Atlantic total phosphate (Fig. 2) agree well qualitatively with reconstructed nutrient redistributions, which describe a deep ocean nutrient increase and mid-to surface decrease (Buchanan et al., 2016; Gebbie, 2014; Marchitto and Broecker, 2006; Oppo et al., 2018). North Pacific waters >2.5 km depth exhibit a lower LGM phosphate (and DIC) as compared to the PI, due to the lack of accumulated regenerated phosphate (Fig. S10). In agreement with the expectation of increased interior carbon storage, simulated interior DIC increases - especially in SSW (Fig. 2). As for phosphate, this increase is driven by the physical carbon pump only, through higher saturation of surface DIC in the Southern Ocean driven by lower T and increased alkalinity (not shown).

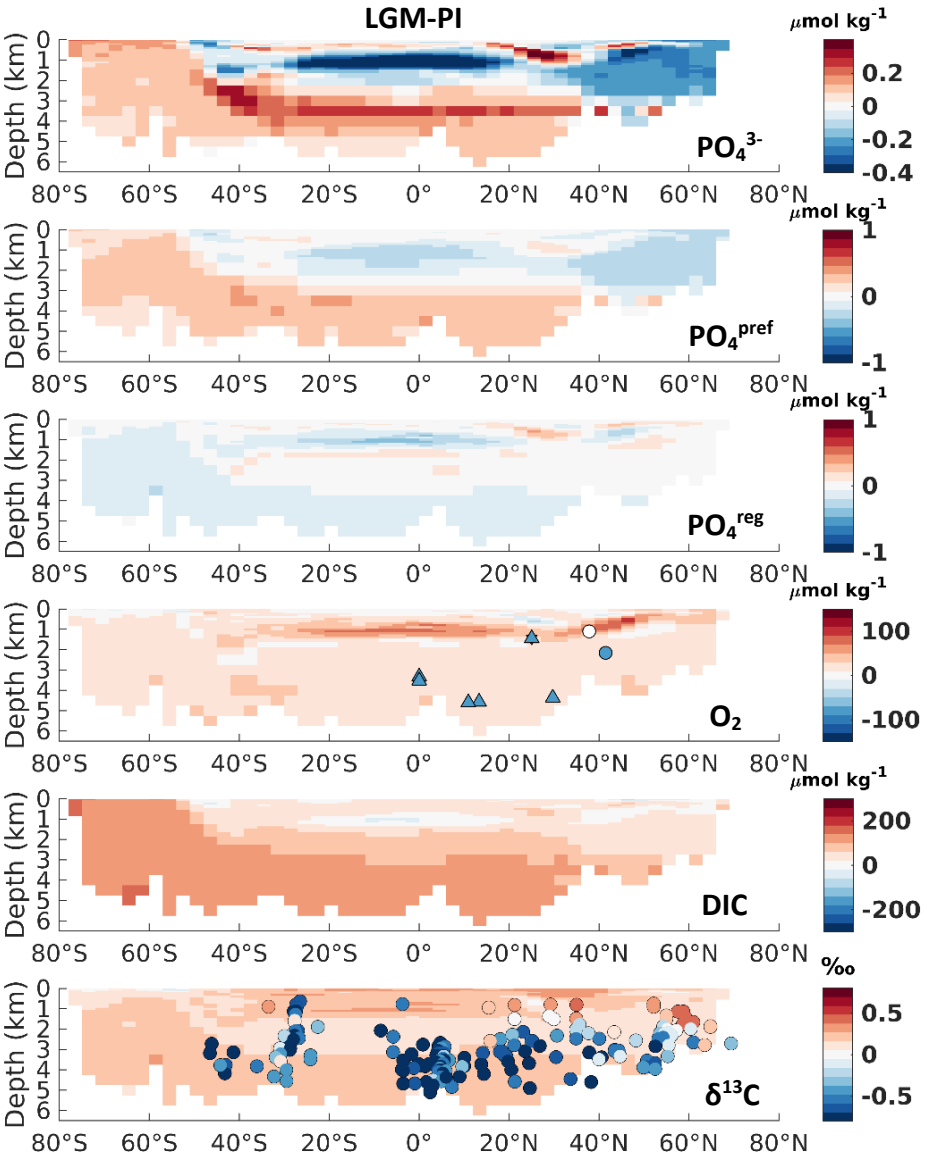

Figure 2 Atlantic zonal mean (25-35° W) of LGM-PI changes for the original model output. See Fig. S10 for the corresponding Pacific sections. Overlay on O_2 is qualitative estimates of LGM-PI changes in O_2 within 30° from 30° W, with blue being a decrease, white indicating unclear changes and red indicating an increase in O_2 (Jaccard and Galbraith, 2011). Simulated LGM-PI $\delta^{13}C$ is compared to a compilation of LGM minus Late Holocene $\delta^{13}C$ data within 30° from 30° W (Peterson et al., 2014; Muglia et al., 2018; Molina-Kescher et al., 2016; Sikes et al., 2016; Burckel et al., 2016; Gottschalk et al., 2016b-c; Hodell and Channell, 2016; Howe and Piotrowski, 2017).

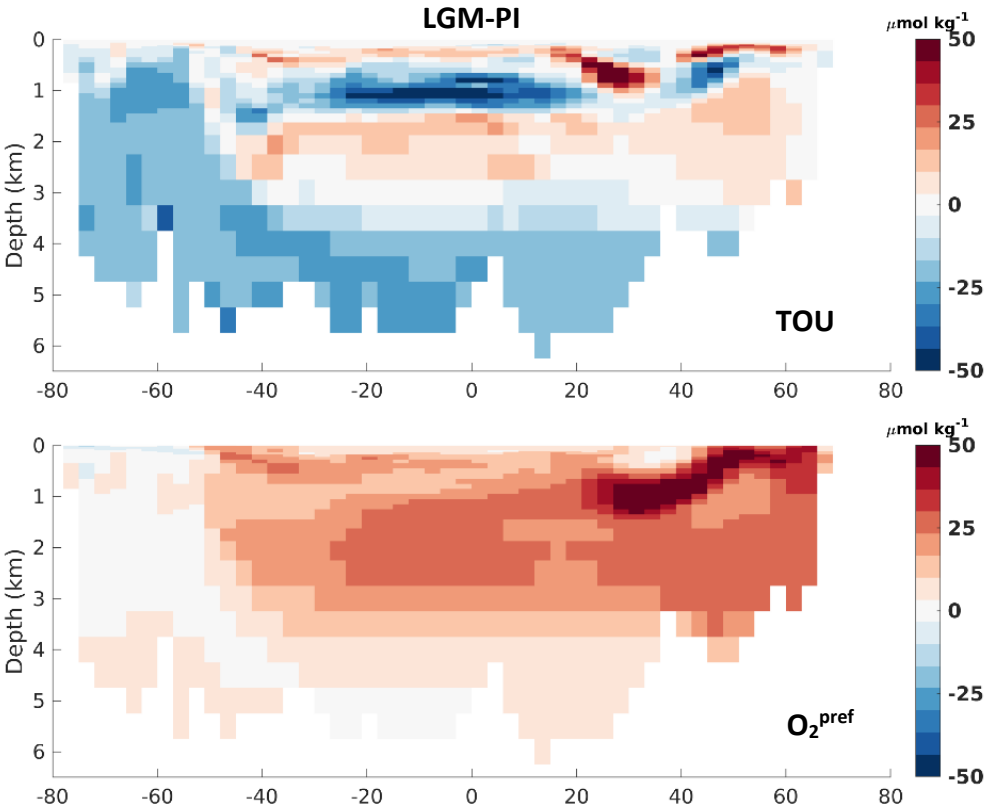

Figure 3 Atlantic zonal mean of simulated LGM-PI O_2 components True Oxygen Utilization (TOU= O_2^{pref}- O_2) (Ito et al., 2004) and preformed O_2 (O_2^{pref}), which is simulated as the O_2 concentration that leaves the surface ocean, and is thus different from saturated O_2 (Tjiputra et al., 2020).

However, the biases in simulated O_2 and $\delta^{13}C$ LGM-PI changes and their respective proxy reconstructions are large (Fig. 2). Any mismatch in the absolute values of $\delta^{13}C$ is not shown here because we compare LGM-PI differences in both the sediment cores and model. In line with decreased remineralisation and increased O_2 solubility due to lower temperatures in the model, O_2 concentrations increase throughout the ocean (Fig. 2). There is a notable difference between Northern and Southern end-members in the Atlantic: Northern-source deep waters have increased O_2 concentrations due to physical O_2 pumping (colder waters have higher O_2 solubility) as visible in preformed O_2, while SSW O_2 increases due to a lack of remineralisation at depth due to low oxygen utilization (Fig. 3). The general increase in O_2 concentrations,

mostly due to the lack of biological O_2 consumption at depth (Fig. 3), is in disagreement with proxy reconstructions (Jaccard and Galbraith, 2011) and shows the missing regenerated nutrients should mostly come from lacking biological processes (remineralization). $\delta^{13}C$ of DIC is governed by both ocean circulation (ventilation rate) and the efficiency of the biological pump (respiration rate), and their relative importance depends on location (Gruber et al., 1999; Schmittner et al., 2013; Eide et al., 2017).

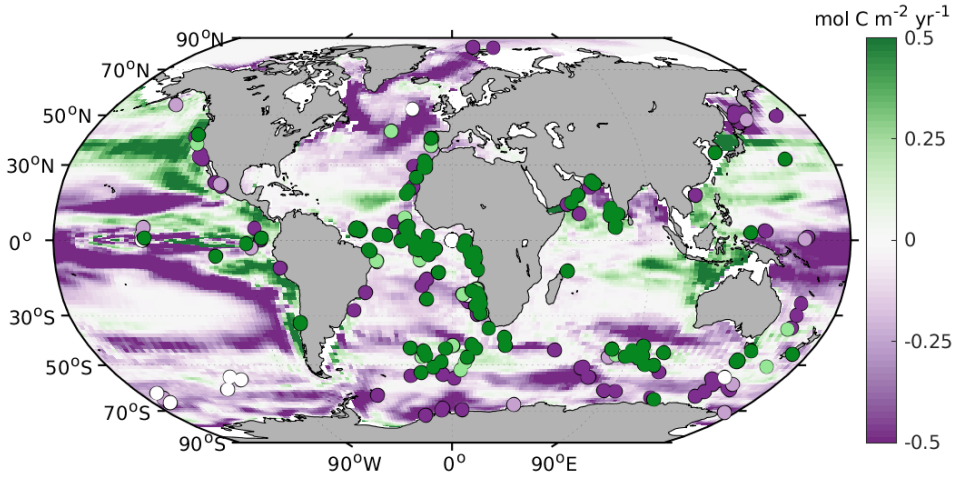

Figure 4 Comparison between the simulated LGM-PI change in export production at 100m depth and Kohfeld et al. (2005) qualitative data (dots: dark purple=decrease, light purple=small decrease, white=no change, light green=light increase, dark green=increase).

As for O_2, the overall increase in simulated $\delta^{13}C$ of DIC contradicts $\delta^{13}C$ records from sediment cores, in which the strengthening of the vertical gradient is a main feature (Fig. 2). Deep $\delta^{13}C$ and its vertical gradient is for an important part governed by biological processes (Morée et al., 2018). As a last comparison, we evaluate our modelled changes in export production against proxy data, even though such data have poor global coverage and large spatial heterogeneity, and are largely qualitative (Kohfeld et al., 2005). LGM export production generally decreases outside of upwelling zones in our model (Fig. 4) and increases in upwelling zones (model and proxy data, Fig. 4). We conclude that the simulated export production increase may

be too weak in the sub-Antarctic and is lacking in the tropical Atlantic (Fig. 4). Especially Southern Ocean export production has a large potential to affect interior and lower latitude nutrient and DIC concentrations (Sarmiento et al., 2004; Primeau et al., 2013), and likely contributes to the simulated low $\overline{BP_{eff}}$ and low-regenerated signature in the biogeochemical tracer distributions. Considering the large influence of SSW nutrient supply on lower latitude productivity we anticipate a key role for SSW here - as supported by proxy data (e.g., Winckler et al., 2016; Costa et al., 2016), although local changes in iron fertilization may play an additional role depending on local iron limitation (e.g., Oka et al., 2011).

3.3 The potential of the biological pump

A decrease in pCO_2^{atm} and increase in regenerated nutrients, despite an increase in low regenerated nutrient SSW volume, is likely to occur through the increase of BP_{eff} (and thus regenerated nutrients) of SSW (Jaccard et al., 2009). In addition, an increase in the (Southern Ocean) air-sea disequilibrium of DIC may have kept more carbon sequestered in the deep ocean, through increased stratification and inhibition of air-sea gas exchange by for example sea ice (Jansen, 2017). An increase in the regenerated signature of northern source water would have further contributed to a global increase in regenerated carbon and nutrients in the interior ocean (Yu et al., 2019), although occupying a smaller volume. As natural preformed concentrations in SSW are high (Ito and Follows, 2005), there is a high potential for these waters to obtain a stronger regenerated signature, and thereby facilitate pCO_2^{atm} drawdown (Ödalen et al., 2018). Our model results for the LGM-PI change in O_2 and $\delta^{13}C$ show a strong miss-match with proxy records (Sect. 3.2.2 and Fig. 2). Here, we explore the effect of a theoretical ('offline') increase of regenerated nutrients in the ocean, by increasing regenerated phosphate and updating O_2, DIC and $\delta^{13}C$ accordingly (Sect. 2.4). The increase is projected on the same simulated physical ocean state presumed to represent LGM conditions (i.e. Sect 3.2.1). To the extent that this state represents true glacial conditions, it allows for an assessment of the magnitude and nature of

marine biogeochemical changes needed for lowering LGM pCO_2^{atm}. In our approach, the additional regenerated phosphate is taken from preformed phosphate, thus leaving the total phosphate inventory unchanged. Proxy reconstructions of global LGM phosphate, however, show that LGM phosphate was redistributed as well as elevated (Tamburini and Föllmi, 2009; Filippelli et al., 2007). As we consider a closed system (no sediments or land input of phosphate or other elements), only redistributions of phosphate can be captured in our model setup.

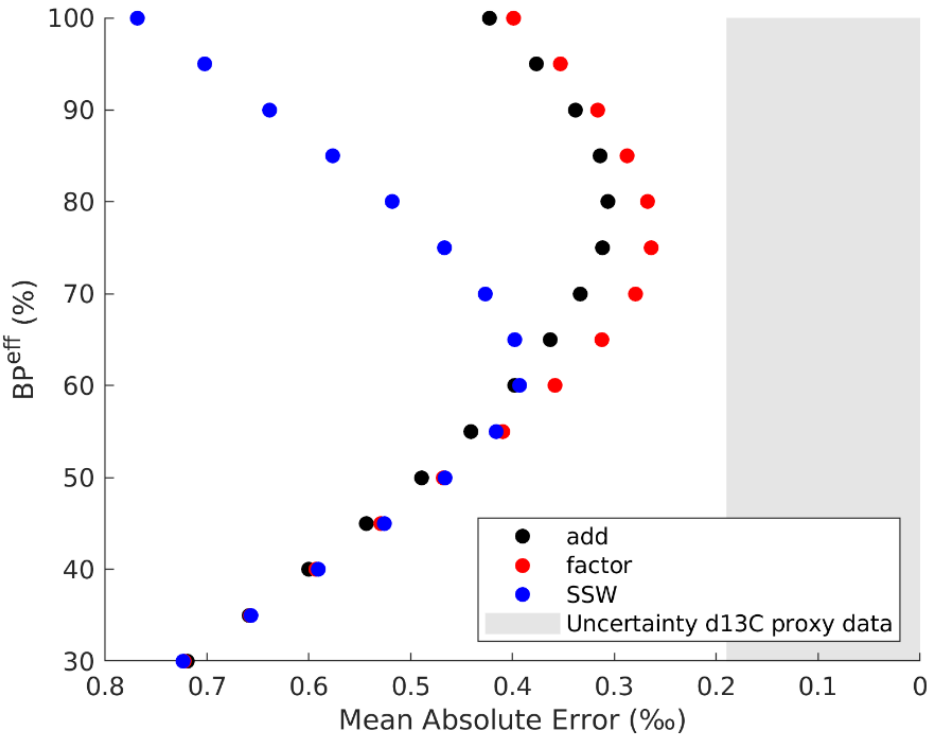

Figure 5 Efficiency of the biological pump ($\overline{\boldsymbol{BP}_{\boldsymbol{eff}}}$) versus the mean absolute error between all $\delta^{13}C$ proxy data and the nearest model grid-cell $\delta^{13}C$, for different methods (Sect. 2.4). Note that the original LGM $\overline{\boldsymbol{BP}_{\boldsymbol{eff}}}$ is 33 %. The $\delta^{13}C$ sediment core data have an uncertainty of ~0.19‰, shaded in grey (Peterson et al., 2014).

We compare the mean error between the model and the $\delta^{13}C$ proxy data across a wide range of $\overline{BP_{eff}}$ (20-100 %, Fig. 5), and for the different methods of adding regenerated $\delta^{13}C$ (Sect. 2.4). Besides the physical and biogeochemical constraints and evaluation (Sect. 3.2), we also estimate the LGM-PI change in marine DIC (ΔDIC) by

applying the Bern3D Earth System Model of Intermediate Complexity v.2.0s following Jeltsch-Thömmes et al. (2019) (SM 3). Mean ΔDIC is ~4000 Gt C (1 sigma range: 3350 to 4480 Gt C) based on the constraints given to the Bern3D model (pCO_2^{atm}, $\delta^{13}C^{atm}$, marine $\delta^{13}C$ of DIC, and deep equatorial Pacific CO_3^{2-}). Contributions to ΔDIC as evaluated in the framework of Jeltsch-Thömmes et al. (2019) arise from removal of carbon from the ocean by sedimentation-weathering imbalances, coral reef growth, increase of the terrestrial carbon storage, and increase in atmospheric CO_2 from the LGM to PI. The wide spread in the ΔDIC estimate by the Bern3D model highlights uncertainties connected to particularly the weathering-burial cycle of carbon over glacial-interglacial timescales.

Using NorESM-OC, the best fit between the modelled and sediment core LGM-PI changes in $\delta^{13}C$ is found for a $\overline{BP_{eff}}$ of 75 % (Fig. 5). A $\overline{BP_{eff}}$ of 75 % would lead to the adjusted tracer distributions shown in Fig. 6 (applying Eq. 2-4). This is true for the approach 'factor' (described in Sect. 2.4), indicating that taking the distribution of the original simulated LGM PO_4^{reg} and strengthening that regenerated signal gives the best agreement with sediment core data. The $\overline{BP_{eff}}$ of 75 % corresponds to an LGM-PI ΔDIC of ~1850 Gt C. This ΔDIC estimate falls below the overall range (2400 to 5500 Gt C) given by the Bern3D model and its constraints. If using only one of the above constraints, however (pCO_2^{atm}, $\delta^{13}C^{atm}$, marine $\delta^{13}C$ of DIC, and deep equatorial Pacific CO_3^{2-}), the ΔDIC estimate of ~1850 Gt C lies in the range of Bern3D results (see SM 3 for details). Furthermore, we expect that values given by the Bern3D model likely lie at the high end of estimates (see also discussion in Jeltsch-Thömmes et al., 2019 and SM3). Using their idealized model setup, Schmittner and Somes (2016) estimated an LGM $\overline{BP_{eff}}$ of 54-59 % (41 % in PI) and a ΔDIC of 590-790 Gt C by exploring the effects of a uniform change in the maximum growth rate of phytoplankton. A direct comparison between these studies is complicated by the large differences between the models, but the differences indicate remaining uncertainties in the magnitude of both ΔDIC and LGM $\overline{BP_{eff}}$. Nevertheless, LGM $\overline{BP_{eff}}$ seems to have been about 18

(i.e. 59-41) % and up to 37 (i.e. 75-38) % higher than in the PI. We note that the total marine ΔDIC (~1850 Gt C) estimate points towards a central role for the Pacific basin to store glacial carbon, if we consider Atlantic LGM storage >3 km depth to be in the order of 50 Gt C (Yu et al., 2016).

In addition to evaluating the model-data fit of $\delta^{13}C$, we evaluate the effect of the tracer adjustments on O_2. The decrease in O_2 for an adjusted $\overline{BP_{eff}}$ (Fig. 6) shows better agreement with qualitative proxy data in the Atlantic (Compare Figs. 2 and 6; Jaccard and Galbraith, 2011) as well as the estimated 175±20 µmol kg^{-1} LGM-PI decrease in Sub-Antarctic Atlantic bottom-water (Gottschalk et al., 2016a). Absolute LGM O_2 (Fig. S11) would decrease to sub-zero O_2 concentrations in the North Pacific (ca. -100 µmol kg^{-1}), which is of a similar magnitude as the size of the PI model-observation bias in this area (Tjiputra et al., 2020), but may be too extreme as indicated by qualitative proxy data that describe an LGM-PI O_2 increase for the North Pacific above 3 km depth (Fig. S10; Jaccard and Galbraith, 2011). An increase in denitrification could have played a role here, but cannot be evaluated in our model setup. Additional (quantitative) estimates of LGM-PI O_2 for major water masses would thus help to provide further constraints on LGM $\overline{BP_{eff}}$.

Our mean absolute error in $\delta^{13}C$ decreases from 0.67 ‰ for the original LGM state estimate (Fig. 2) to 0.26 ‰ for the 75% $\overline{BP_{eff}}$ ocean (Fig. 5 and 6). The remaining absolute $\delta^{13}C$ error is therefore 0.07 ‰ larger than the proxy data uncertainty. This remaining model-data $\delta^{13}C$ mismatch of 0.07 ‰ (Fig. 5) as well as the possibly too low Pacific O_2 (Fig. S10) indicate that projecting changes in $\overline{BP_{eff}}$ onto the simulated glacial circulation field still does not fully align with the actual LGM state - despite exploring different approaches for the redistribution of the regenerated nutrients (Sect. 2.4). Specifically, even though a 75 % $\overline{BP_{eff}}$ and the reorganised circulation captures most of the magnitude of the LGM-PI $\delta^{13}C$ change, the strength of the glacial chemocline (the vertical $\delta^{13}C$ gradient) remains too weak (Fig. 6). Other modelling studies of the glacial ocean show similar biases (e.g., Heinze et al., 2016; Schmittner

and Somes, 2016). This suggests additional processes, which would allow stronger chemical stratification between intermediate and deep waters, are missing in the model(s) and are not explained in a simple way by intensification of the biological pump or our simulated changes in circulation. We recognize that optimizing the model $\overline{BP_{eff}}$ to additional (quantitative) proxies such as the nitrogen isotopes could provide more constraints (Schmittner and Somes, 2016).

Here, we discuss several processes that could contribute to the remaining model-proxy error. First, our results may indicate that the water mass production processes in the model are not (yet) fully adequate. Interior $\delta^{13}C$ is influenced by the source of deep waters as well as intermediate waters, the extent of deep convection as well as mixing processes between interior water masses (e.g., Duplessy et al., 1988), partly on spatial and temporal scales possibly not resolved by our model. The PI simulation of a generally too deep Southern Ocean MLD as well as Southern Ocean- attributed model-observational biases in biogeochemical tracers (Sect. 3.1; Tjiputra et al., 2020) suggest that deep water formation processes indeed are not simulated in full agreement with observational data. The lack of a reliable glacial freshwater forcing is likely to be partly responsible for errors in the LGM simulation. Too strong exchange (mixing) in the LGM ocean between the deep and intermediate waters in models could also maintain a too weak glacial chemocline. Our simulated SSW radiocarbon ages are too young compared to reconstructions (Fig. 1), consistent with inadequate isolation of these waters in the simulation. Aging of these SSW could increase the regenerated signature in these waters (consuming O_2, and decreasing $\delta^{13}C$ of DIC) and steepen the chemocline while additionally improving agreement with the Bern3D model ΔDIC estimate and radiocarbon age. The simulation of increased Southern Ocean sea ice extent and/or formation rate (Nadeau et al., 2019) may be a key player for improving simulations of a more stratified and isolated SSW (Ferrari et al., 2014; Jansen 2017), which would create older waters with higher regenerated signatures and increase the air-sea disequilibrium of biogeochemical tracers such as DIC and O_2 (Gottschalk et al., 2016a) further lowering atmispheric CO_2 (Khatiwala et al., 2019).

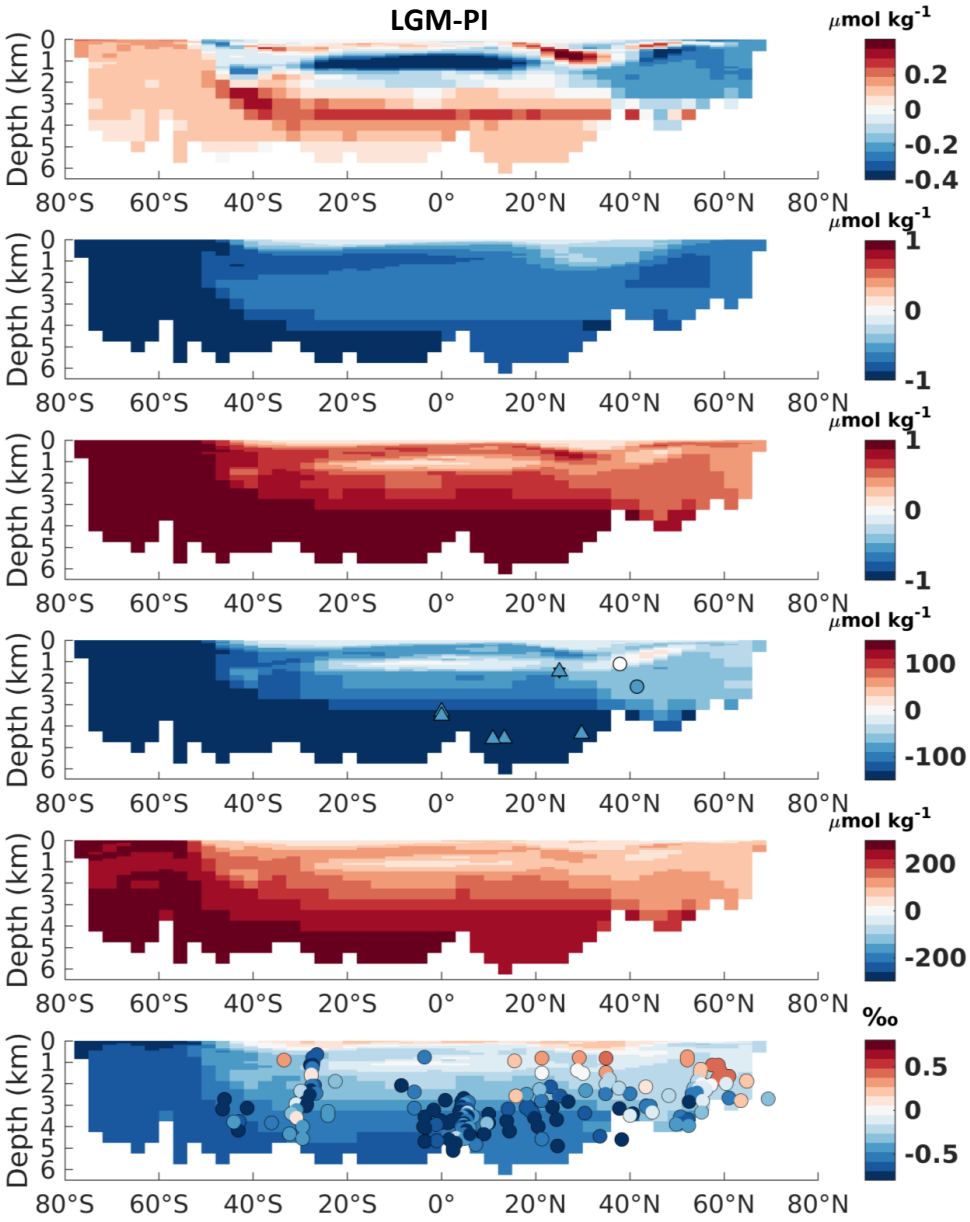

Figure 6 As Figure 2, but for an adjusted $\overline{BP_{eff}}$ of 75 %.

4 Conclusions

We present a model simulation of the pre-industrial and Last Glacial Maximum (LGM) oceans. We use the simulations to explore the relative roles of physical and biological marine changes needed to simulate an LGM ocean in satisfactory agreement with proxy data. Despite the good agreement between (qualitative and quantitative) proxy reconstructions and our simulation of different LGM and pre-industrial (PI) ocean circulation, our model is unable to simulate the complete set of biogeochemical changes implied by proxy data. Therefore, our results (mainly the lack of increased regenerated nutrients) confirm the idea that both biogeochemical (beyond those represented by the model) and physical changes must have been at play in the ocean to create the LGM pCO_2^{atm} drawdown (Heinze et al., 2016; Bouttes et al., 2011; Buchanan et al., 2016). Comparison between a range of qualitative and quantitative proxy data and simulated biogeochemical tracers (specifically total dissolved inorganic carbon, regenerated phosphate, True Oxygen Utilization, O_2 and $\delta^{13}C$) reveals that there is a too small signature of regenerated nutrients in our simulated LGM ocean. We conduct a theoretical exploration of the effects of changes in the global mean biological pump efficiency and quantify its effect on the global mean absolute error between simulated $\delta^{13}C$ and proxy $\delta^{13}C$ data. The smallest error is found for an approximate doubling in the global mean efficiency of the biological pump $\overline{BP_{eff}}$ (from 38 % in the PI ocean to ~75 % in the LGM). Such a change minimizes the simulated global mean absolute error for $\delta^{13}C$ from 0.67 ‰ (for the originally simulated 33 % $\overline{BP_{eff}}$ of the LGM) to 0.26 ‰ - only distinguishable by 0.07 ‰ from the $\delta^{13}C$ data uncertainty. It additionally improves the agreement with both qualitative and quantitative O_2 reconstructions. Much of the remaining model-proxy $\delta^{13}C$ data mismatch is due to a too weak vertical chemocline in glacial simulations. Therefore, scaling of the biological pump efficiency does not fully explain the glacial ocean proxy data using the modelled circulation field thought to most closely represent the glacial state. We see different explanations of the bias that could strengthen the glacial chemocline, such as the further aging (by isolation and

stratification) of interior waters through improved simulation of deep-water formation, which would increase the regenerated signature of the interior LGM ocean. Especially Southern Source Waters would have a large potential (due to their large volume contribution) to increase global interior radiocarbon ages and regenerated signatures of the interior ocean.

The estimated $\overline{BP_{eff}}$ increase to 75 % corresponds to an increase in oceanic DIC (ΔDIC) of ~1850 Gt C. This lies in the range of estimates as derived by the Bern3D Earth System Model of Intermediate Complexity constrained by single proxy targets (pCO_2^{atm}, $\delta^{13}C^{atm}$, marine $\delta^{13}C$ of DIC, or deep equatorial Pacific CO_3^{2-}). If all four targets are used as constraints, the range of ΔDIC estimates based on the Bern3D model is higher than 1850 Gt C (see Fig. S3 and SM3). In order to disentangle and understand the processes contributing to ΔDIC, especially the large contribution from sedimentation-weathering imbalances, further work seems necessary.

The general agreement between our model results and proxy data for ocean circulation (within the uncertainty of reconstructions), after adjustments to the sea surface salinity field, demonstrates an advantage of our forced ocean model setup, and its flexibility, over fully coupled Earth System Models in exploring different circulation and biological pump scenarios for explaining glacial CO_2 changes. We conclude that a large PI-to-LGM increase in the efficiency of the biological pump (from 38 to ~75 %) as well as a reorganization of ocean circulation/stratification are essential for simulating an LGM ocean in optimal agreement with proxy data. Based on this, we expect that only fully coupled models that contain the processes and/or components that realistically change these aspects will be able to simulate an LGM ocean in satisfactory agreement with proxy data.

Data availability. The model output data for the PI and LGM simulations is available at the NIRD Research Data Archive (*AT PUBLICATION; DOI).*

Author contributions. ALM, JS and CH conceptualized the study and developed the methodology in cooperation with IB and contribution from AJT. ALM did the formal analysis of the data and wrote the original draft for which she visualized the results. ALM, JS, CH, AJT and UN investigated the results. All authors contributed to the review and editing of the original draft. JS and ALM curated the data, contributed to the software and validated the results. CH and JS supervised the project, and provided the resources and funding acquisition needed for this work.

Competing interests. The authors declare that they have no conflict of interest.

Disclaimer. This article reflects only the authors' view – the funding agencies as well as their executive agencies are not responsible for any use that may be made of the information that the article contains.

Acknowledgments. This is a contribution to the Bjerknes Centre for Climate Research (Bergen, Norway). Storage and computing resources were provided by UNINETT Sigma2 - the National Infrastructure for High Performance Computing and Data Storage in Norway (project numbers nn/ns2980k and nn/ns2345k). AM is grateful for PhD funding through the Faculty for Mathematics and Natural Sciences of the University of Bergen (UoB) as well as support by the Meltzer fund of UoB and Erasmus Mundus to stay at ETH Zürich for part of this work. JS acknowledges funding through the Research Council of Norway (project INES 270061). The NorESM components were upgraded with support from project EVA (Earth system modelling of climate Variations in the Anthropocene, grant no. 229771, Research Council of Norway) and, CRESCENDO (Coordinated Research in Earth Systems and Climate: Experiments, kNowledge, Dissemination and Outreach; Horizon 2020 European Union's Framework Programme for Research and Innovation, grant no. 641816, European Commission). AJT acknowledges support from the Swiss National Science Foundation (# 200020_172476) and the Oeschger Centre for Climate Change Research.

References

Adkins J. F.: The role of deep ocean circulation in setting glacial climates, Paleoceanography, 28, 539-561, 10.1002/palo.20046, 2013.

Assmann, K. M., Bentsen, M., Segschneider, J., and Heinze, C.: An isopycnic ocean carbon cycle model, Geosci. Model Dev., 3, 143-167, 10.5194/gmd-3-143-2010, 2010.

Bentsen, M., Bethke, I., Debernard, J. B., Iversen, T., Kirkevåg, A., Seland, Ø., Drange, H., Roelandt, C., Seierstad, I. A., Hoose, C., and Kristjánsson, J. E.: The Norwegian Earth System Model, NorESM1-M – Part 1: Description and basic evaluation of the physical climate, Geosci. Model Dev., 6, 687-720, 10.5194/gmd-6-687-2013, 2013.

Bereiter, B., Shackleton, S., Baggenstos, D., Kawamura, K., and Severinghaus, J.: Mean global ocean temperatures during the last glacial transition, Nature, 553, 39, 10.1038/nature25152, 2018.

Bopp, L., Resplandy, L., Untersee, A., Le Mezo, P., and Kageyama, M.: Ocean (de)oxygenation from the Last Glacial Maximum to the twenty-first century: insights from Earth System models, Philos Trans A Math Phys Eng Sci, 375, 20160323, 10.1098/rsta.2016.0323, 2017.

Bouttes, N., Paillard, D., Roche, D. M., Brovkin, V., and Bopp, L.: Last Glacial Maximum CO_2 and $\delta^{13}C$ successfully reconciled, Geophysical Research Letters, 38, 10.1029/2010GL044499, 2011.

Braconnot, P., Harrison, S., Kageyama, M., Bartlein, P., Masson-Delmotte, V., Abe-Ouchi, A., Otto-Bliesner, B., and Zhao, Y.: Evaluation of climate models using palaeoclimatic data, Nature Climate Change, 2, 417-424, 10.1038/nclimate1456, 2012.

Broecker, W. S.: "NO", a conservative water-mass tracer, Earth and Planetary Science Letters, 23, 100-107, 10.1016/0012-821X(74)90036-3, 1974.

Broecker, W. S.: Glacial to interglacial changes in ocean chemistry, Progress in Oceanography, 11, 151-197, 10.1016/0079-6611(82)90007-6, 1982.

Broecker, W. S., and McGee, D.: The ^{13}C record for atmospheric CO_2: What is it trying to tell us?, Earth and Planetary Science Letters, 368, 175-182, 10.1016/j.epsl.2013.02.029, 2013.

Broecker, W. S., and Peng, T.-H.: Carbon Cycle: 1985 Glacial to Interglacial Changes in the Operation of the Global Carbon Cycle, Radiocarbon, 28, 309-327, 10.1017/S0033822200007414, 1986.

Buchanan, P. J., Matear, R. J., Lenton, A., Phipps, S. J., Chase, Z., and Etheridge, D. M.: The simulated climate of the Last Glacial Maximum and insights into the global marine carbon cycle, Climate of the Past, 12, 2271-2295, 10.5194/cp-12-2271-2016, 2016.

Burckel, P., Waelbroeck, C., Luo, Y., Roche, D. M., Pichat, S., Jaccard, S. L., Gherardi, J.-M., Govin, A., Lippold, J., and Thil, F.: The Atlantic Meridional Overturning Circulation during the last glacial. In: Supplement to: Burckel, P et al. (2016): Changes in the geometry and strength of the Atlantic meridional overturning circulation during the last glacial (20-50 ka). Climate of the Past, 12(11), 2061-2075, 10.5194/cp-12-2061-2016, PANGAEA, 2016.

Böhm, E., Lippold, J., Gutjahr, M., Frank, M., Blaser, P., Antz, B., Fohlmeister, J., Frank, N., Andersen, M. B., and Deininger, M.: Strong and deep Atlantic meridional overturning circulation during the last glacial cycle, Nature, 517, 73, 10.1038/nature14059, 2014.

Chowdhury, P., and Behera, M. R.: Evaluation of CMIP5 and CORDEX derived wave climate in Indian Ocean, Climate Dynamics, 52, 4463-4482, 10.1007/s00382-018-4391-0, 2019.

Costa, K. M., McManus, J. F., Anderson, R. F., Ren, H., Sigman, D. M., Winckler, G., Fleisher, M. Q., Marcantonio, F., and Ravelo, A. C.: No iron fertilization in the equatorial Pacific Ocean during the last ice age, Nature, 529, 519-522, 10.1038/nature16453, 2016.

Craig, H.: Isotopic standards for carbon and oxygen and correction factors for mass-spectrometric analysis of carbon dioxide, Geochimica et Cosmochimica Acta, 12, 133-149, 10.1016/0016-7037(57)90024-8, 1957.

Danabasoglu, G., Yeager, S. G., Bailey, D., Behrens, E., Bentsen, M., Bi, D., Biastoch, A., Böning, C., Bozec, A., Canuto, V. M., Cassou, C., Chassignet, E., Coward, A. C., Danilov, S., Diansky, N., Drange, H., Farneti, R., Fernandez, E., Fogli, P. G., Forget, G., Fujii, Y., Griffies, S. M., Gusev, A., Heimbach, P., Howard, A., Jung, T., Kelley, M., Large, W. G., Leboissetier, A., Lu, J., Madec, G.,

Marsland, S. J., Masina, S., Navarra, A., George Nurser, A. J., Pirani, A., y Mélia, D. S., Samuels, B. L., Scheinert, M., Sidorenko, D., Treguier, A.-M., Tsujino, H., Uotila, P., Valcke, S., Voldoire, A., and Wang, Q.: North Atlantic simulations in Coordinated Ocean-ice Reference Experiments phase II (CORE-II). Part I: Mean states, Ocean Modelling, 73, 76-107, 10.1016/j.ocemod.2013.10.005, 2014.

De Boyer Montégut, C., Madec, G., Fischer, A. S., Lazar, A., and Iudicone, D.: Mixed layer depth over the global ocean: An examination of profile data and a profile-based climatology, Journal of Geophysical Research: Oceans, 109, 10.1029/2004JC002378, 2004.

DeVries, T., Primeau, F., and Deutsch, C.: The sequestration efficiency of the biological pump, Geophysical Research Letters, 39, L13601, 10.1029/2012GL051963, 2012.

Donohue, K. A., Tracey, K. L., Watts, D. R., Chidichimo, M. P., and Chereskin, T. K.: Mean Antarctic Circumpolar Current transport measured in Drake Passage, Geophysical Research Letters, 43, 11,760-711,767, 10.1002/2016GL070319, 2016.

Duplessy, J. C., Shackleton, N. J., Fairbanks, R. G., Labeyrie, L., Oppo, D., and Kallel, N.: Deepwater source variations during the last climatic cycle and their impact on the global deepwater circulation, Paleoceanography, 3, 343-360, 10.1029/PA003i003p00343, 1988.

Eide, M., Olsen, A., Ninnemann, U. S., and Johannessen, T.: A global ocean climatology of preindustrial and modern ocean $\delta^{13}C$, Global Biogeochemical Cycles, 31, 515-534, 10.1002/2016GB005473, 2017.

EPICA Project Members: Eight glacial cycles from an Antarctic ice core, Nature, 429, 623-628, 10.1038/nature02599, 2004.

Ferrari, R., Jansen, M. F., Adkins, J. F., Burke, A., Stewart, A. L., and Thompson, A. F.: Antarctic sea ice control on ocean circulation in present and glacial climates, Proceedings of the National Academy of Sciences, 111, 8753, 10.1073/pnas.1323922111, 2014.

Filippelli, G. M., Latimer, J. C., Murray, R. W., and Flores, J.-A.: Productivity records from the Southern Ocean and the equatorial Pacific Ocean: Testing the glacial Shelf-Nutrient Hypothesis, Deep Sea Research Part II: Topical Studies in Oceanography, 54, 2443-2452, 10.1016/j.dsr2.2007.07.021, 2007.

Freeman, E., Skinner, L. C., Waelbroeck, C., and Hodell, D.: Radiocarbon evidence for enhanced respired carbon storage in the Atlantic at the Last Glacial Maximum, Nature Communications, 7, 11998, 10.1038/ncomms11998, 2016.

Ganopolski, A., and Brovkin, V.: Simulation of climate, ice sheets and CO_2 evolution during the last four glacial cycles with an Earth system model of intermediate complexity, Climate of the Past, 13, 1695-1716, 10.5194/cp-13-1695-2017, 2017.

Gebbie, G., and Huybers, P.: The Mean Age of Ocean Waters Inferred from Radiocarbon Observations: Sensitivity to Surface Sources and Accounting for Mixing Histories, Journal of Physical Oceanography, 42, 291-305, 10.1175/jpo-d-11-043.1, 2012.

Gebbie, G.: How much did Glacial North Atlantic Water shoal?, Paleoceanography, 29, 190-209, 10.1002/2013PA002557, 2014.

Gebbie, G., Peterson, C. D., Lisiecki, L. E., and Spero, H. J.: Global-mean marine $\delta^{13}C$ and its uncertainty in a glacial state estimate, Quaternary Science Reviews, 125, 144-159, 10.1016/j.quascirev.2015.08.010, 2015.

Gersonde, R., Crosta, X., Abelmann, A., and Armand, L.: Sea-surface temperature and sea ice distribution of the Southern Ocean at the EPILOG Last Glacial Maximum—a circum-Antarctic view based on siliceous microfossil records, Quaternary Science Reviews, 24, 869-896, 10.1016/j.quascirev.2004.07.015, 2005.

Gottschalk, J., Skinner, L. C., Lippold, J., Vogel, H., Frank, N., Jaccard, S. L., and Waelbroeck, C.: Biological and physical controls in the Southern Ocean on past millennial-scale atmospheric CO_2 changes, Nature Communications, 7, 11539, 10.1038/ncomms11539, 2016a.

Gottschalk, J., Vázquez Riveiros, N., Waelbroeck, C., Skinner, L. C., Michel, E., Duplessy, J.-C., Hodell, D. A., and Mackensen, A.: Stable oxygen and carbon isotopes of C. wuellerstorfi, C. kullenbergi and Uvigerina spp. from MD07-3076Q (sub-Antarctic Atlantic) over the last 22 kyrs. In: In

supplement to: Gottschalk, J et al. (2016): Carbon isotope offsets between benthic foraminifer species of the genus Cibicides (Cibicidoides) in the glacial sub-Antarctic Atlantic. Paleoceanography, 31(12), 1583-1602, 10.1002/2016PA003029, PANGAEA, 2016b.

Gottschalk, J., Vázquez Riveiros, N., Waelbroeck, C., Skinner, L. C., Michel, E., Duplessy, J.-C., Hodell, D. A., and Mackensen, A.: Stable oxygen and carbon isotopes of C. wuellerstorfi, C. kullenbergi and Uvigerina spp. from TN057-6GC (sub-Antarctic Atlantic) over the last 29 kyrs. In: In supplement to: Gottschalk, J et al. (2016): Carbon isotope offsets between benthic foraminifer species of the genus Cibicides (Cibicidoides) in the glacial sub-Antarctic Atlantic. Paleoceanography, 31(12), 1583-1602, 10.1002/2016PA003029, PANGAEA, 2016c.

Gruber, N., Keeling, C. D., Bacastow, R. B., Guenther, P. R., Lueker, T. J., Wahlen, M., Meijer, H. A. J., Mook, W. G., and Stocker, T. F.: Spatiotemporal patterns of carbon-13 in the global surface oceans and the oceanic suess effect, Global Biogeochemical Cycles, 13, 307-335, 10.1029/1999GB900019, 1999.

Guo, C., Bentsen, M., Bethke, I., Ilicak, M., Tjiputra, J., Toniazzo, T., Schwinger, J., and Otterå, O. H.: Description and evaluation of NorESM1-F: a fast version of the Norwegian Earth System Model (NorESM), Geoscientific Model Development, 12, 343-362, 10.5194/gmd-12-343-2019, 2019.

Heinze, C., Maier-Reimer, E., and Winn, K.: Glacial pCO_2 Reduction by the World Ocean: Experiments With the Hamburg Carbon Cycle Model, Paleoceanography, 6, 395-430, 10.1029/91PA00489, 1991.

Heinze, C., and Hasselmann, K.: Inverse Multiparameter Modeling of Paleoclimate Carbon Cycle Indices, Quaternary Research, 40, 281-296, 10.1006/qres.1993.1082, 1993.

Heinze, C., Hoogakker, B. A. A., and Winguth, A.: Ocean carbon cycling during the past 130 000 years – a pilot study on inverse palaeoclimate record modelling, Climate of the Past, 12, 1949-1978, 10.5194/cp-12-1949-2016, 2016.

Ho, S., and Laepple, T.: Glacial cooling as inferred from marine temperature proxies TEXH86 and UK'37, Earth and Planetary Science Letters, 409, 15-22, 10.1016/j.epsl.2014.10.033, 2015.

Hodell, D. A., and Channell, J. E. T.: Stable isotope ratios of Cibicidoides wuellerstorfi from IODP Site 303-U1304. In: In supplement to: Hodell, DA; Channell, JET (2016): Mode transitions in Northern Hemisphere glaciation: co-evolution of millennial and orbital variability in Quaternary climate. Climate of the Past, 12(9), 1805-1828, 10.5194/cp-12-1805-2016, PANGAEA, 2016.

Howe, J. N. W., and Piotrowski, A. M.: (Table S2) Stable carbon and oxygen isotopic composition of benthic foraminifera of ODP Site 154-929. In: In supplement to: Howe, JNW; Piotrowski, AM: Atlantic deep water provenance decoupled from atmospheric CO_2 concentration during the lukewarm interglacials. Nature Communications, 10.1038/s41467-017-01939-w, PANGAEA, 2017.

Ito, T., Follows, M. J., and Boyle, E. A.: Is AOU a good measure of respiration in the oceans?, Geophysical Research Letters, 31, 10.1029/2004GL020900, 2004.

Ito, T., and Follows, M. J.: Preformed phosphate, soft tissue pump and atmospheric CO_2, Journal of Marine Research, 63, 813-839, 10.1357/0022240054663231, 2005.

Jaccard, S. L., Galbraith, E. D., Sigman, D. M., Haug, G. H., Francois, R., Pedersen, T. F., Dulski, P., and Thierstein, H. R.: Subarctic Pacific evidence for a glacial deepening of the oceanic respired carbon pool, Earth and Planetary Science Letters, 277, 156-16510.1016/j.epsl.2008.10.017, 2009.

Jaccard, S. L., and Galbraith, E. D.: Large climate-driven changes of oceanic oxygen concentrations during the last deglaciation, Nature Geoscience, 5, 151, 10.1038/ngeo1352, 2011.

Jansen, M. F.: Glacial ocean circulation and stratification explained by reduced atmospheric temperature, Proceedings of the National Academy of Sciences, 114, 45-50, 10.1073/pnas.1610438113, 2017.

Jeltsch-Thömmes, A., Battaglia, G., Cartapanis, O., Jaccard, S. L., and Joos, F.: Low terrestrial carbon storage at the Last Glacial Maximum: constraints from multi-proxy data, Climate of the Past, 15, 849-879, 10.5194/cp-15-849-2019, 2019.

Kageyama, M., Albani, S., Braconnot, P., Harrison, S. P., Hopcroft, P. O., Ivanovic, R. F., Lambert, F., Marti, O., Peltier, W. R., Peterschmitt, J. Y., Roche, D. M., Tarasov, L., Zhang, X., Brady, E. C., Haywood, A. M., LeGrande, A. N., Lunt, D. J., Mahowald, N. M., Mikolajewicz, U., Nisancioglu, K. H., Otto-Bliesner, B. L., Renssen, H., Tomas, R. A., Zhang, Q., Abe-Ouchi, A., Bartlein, P. J., Cao, J., Li, Q., Lohmann, G., Ohgaito, R., Shi, X., Volodin, E., Yoshida, K., Zhang, X., and Zheng, W.: The PMIP4 contribution to CMIP6 – Part 4: Scientific objectives and experimental design of the PMIP4-CMIP6 Last Glacial Maximum experiments and PMIP4 sensitivity experiments, Geoscientific Model Development, 10, 4035-4055, 10.5194/gmd-10-4035-2017, 2017.

Khatiwala, S., Schmittner, A., and Muglia, J.: Air-sea disequilibrium enhances ocean carbon storage during glacial periods, Science Advances, 5, eaaw4981, 10.1126/sciadv.aaw4981, 2019.

Key, R. M., Kozyr, A., Sabine, C. L., Lee, K., Wanninkhof, R., Bullister, J. L., Feely, R. A., Millero, F. J., Mordy, C., and Peng, T. H.: A global ocean carbon climatology: Results from Global Data Analysis Project (GLODAP), Global Biogeochemical Cycles, 18, GB4031, 10.1029/2004GB002247, 2004.

Kohfeld, K. E., Quéré, C. L., Harrison, S. P., and Anderson, R. F.: Role of Marine Biology in Glacial-Interglacial CO_2 Cycles, Science, 308, 74-78, 10.1126/science.1105375, 2005.

Kurahashi-Nakamura, T., Paul, A., and Losch, M.: Dynamical reconstruction of the global ocean state during the Last Glacial Maximum, Paleoceanography, 32, 326-350, 10.1002/2016PA003001, 2017.

Lamy, F., Arz, H. W., Kilian, R., Lange, C. B., Lembke-Jene, L., Wengler, M., Kaiser, J., Baeza-Urrea, O., Hall, I. R., Harada, N., and Tiedemann, R.: Glacial reduction and millennial-scale variations in Drake Passage throughflow, Proceedings of the National Academy of Sciences, 112, 13496, 10.1073/pnas.1509203112, 2015.

Laws, E. A., Bidigare, R., R., and Popp, B. N.: Effects of growth rate and CO_2 concentration on carbon isotopic fractionation by the marine diatom Phaeodactylum tricornutum, Limnology and Oceanography, 42, 1552-1560, 10.4319/lo.1997.42.7.1552, 1997.

Lynch-Stieglitz, J., Stocker, T. F., Broecker, W. S., and Fairbanks, R. G.: The influence of air-sea exchange on the isotopic composition of oceanic carbon: Observations and modeling, Global Biogeochemical Cycles, 9, 653-665, 10.1029/95GB02574, 1995.

Lynch-Stieglitz, J., Adkins, J. F., Curry, W. B., Dokken, T., Hall, I. R., Herguera, J. C., Hirschi, J. J. M., Ivanova, E. V., Kissel, C., Marchal, O., Marchitto, T. M., McCave, I. N., McManus, J. F., Mulitza, S., Ninnemann, U., Peeters, F., Yu, E.-F., and Zahn, R.: Atlantic Meridional Overturning Circulation During the Last Glacial Maximum, Science, 316, 66, 10.1126/science.1137127, 2007.

Lynch-Stieglitz, J., Ito, T., and Michel, E.: Antarctic density stratification and the strength of the circumpolar current during the Last Glacial Maximum, Paleoceanography, 31, 539-552, 10.1002/2015PA002915, 2016.

Mahowald, N. M., Muhs, D. R., Levis, S., Rasch, P. J., Yoshioka, M., Zender, C. S., and Luo, C.: Change in atmospheric mineral aerosols in response to climate: Last glacial period, preindustrial, modern, and doubled carbon dioxide climates, Journal of Geophysical Research: Atmospheres, 111, 10.1029/2005JD006653, 2006.

Maier-Reimer, E.: Geochemical cycles in an ocean general circulation model. Preindustrial tracer distributions, Global Biogeochemical Cycles, 7, 645-677, 10.1029/93GB01355, 1993.

Maier-Reimer, E., Kriest, I., Segschneider, J., and Wetzel, P.: The Hamburg Oceanic Carbon Cycle Circulation model HAMOCC5.1 – Technical Description Release 1.1, Max Planck Institute for Meteorology, Hamburg, Germany, 2005.

Marchitto, T. M., and Broecker, W. S.: Deep water mass geometry in the glacial Atlantic Ocean: A review of constraints from the paleonutrient proxy Cd/Ca, Geochemistry, Geophysics, Geosystems, 7, 10.1029/2006GC001323, 2006.

MARGO Project Members: Constraints on the magnitude and patterns of ocean cooling at the Last Glacial Maximum, Nature Geoscience, 2, 127, 10.1038/ngeo411, 2009.

Marzocchi, A., and Jansen, M. F.: Connecting Antarctic sea ice to deep-ocean circulation in modern and glacial climate simulations, Geophysical Research Letters, 44, 6286-6295, 10.1002/2017GL073936, 2017.

Mazaud, A., Michel, E., Dewilde, F., and Turon, J. L.: Variations of the Antarctic Circumpolar Current intensity during the past 500 ka, Geochemistry, Geophysics, Geosystems, 11, 10.1029/2010GC003033, 2010.

McCarthy, G. D., Smeed, D. A., Johns, W. E., Frajka-Williams, E., Moat, B. I., Rayner, D., Baringer, M. O., Meinen, C. S., Collins, J., and Bryden, H. L.: Measuring the Atlantic Meridional Overturning Circulation at 26°N, Progress in Oceanography, 130, 91-111, 10.1016/j.pocean.2014.10.006, 2015.

McCave, I. N., Crowhurst, S. J., Kuhn, G., Hillenbrand, C. D., and Meredith, M. P.: Minimal change in Antarctic Circumpolar Current flow speed between the last glacial and Holocene, Nature Geoscience, 7, 113, 10.1038/ngeo2037, 2013.

McManus, J. F., Francois, R., Gherardi, J. M., Keigwin, L. D., and Brown-Leger, S.: Collapse and rapid resumption of Atlantic meridional circulation linked to deglacial climate changes, Nature, 428, 834-837, 10.1038/nature02494, 2004.

Menviel, L., Yu, J., Joos, F., Mouchet, A., Meissner, K. J., and England, M. H.: Poorly ventilated deep ocean at the Last Glacial Maximum inferred from carbon isotopes: A data-model comparison study, Paleoceanography, 32, 2-17, 10.1002/2016pa003024, 2017.

Mitchell, D., AchutaRao, K., Allen, M., Bethke, I., Beyerle, U., Ciavarella, A., Forster, P. M., Fuglestvedt, J., Gillett, N., Haustein, K., Ingram, W., Iversen, T., Kharin, V., Klingaman, N., Massey, N., Fischer, E., Schleussner, C. F., Scinocca, J., Seland, Ø., Shiogama, H., Shuckburgh, E., Sparrow, S., Stone, D., Uhe, P., Wallom, D., Wehner, M., and Zaaboul, R.: Half a degree additional warming, prognosis and projected impacts (HAPPI): background and experimental design, Geosci. Model Dev., 10, 571-583, 10.5194/gmd-10-571-2017, 2017.

Molina-Kescher, M., Frank, M., Tapia, R., Ronge, T. A., Nürnberg, D., and Tiedemann, R.: Radiogenic neodymium, strontium and lead isotopes of authigenic and detrital sedimentary phases and stable oxygen and carbon isotopes of benthic foraminifera from gravity cores SO213-59-2 and SO213-60-1 (central South Pacific). In: Supplement to: Molina-Kescher, M et al. (2016): Reduced admixture of North Atlantic Deep Water to the deep central South Pacific during the last two glacial periods. Paleoceanography, 10.1002/2015PA002863, PANGAEA, 2016.

Mook, W. G.: ^{13}C in atmospheric CO_2, Netherlands Journal of Sea Research, 20, 211-223, 10.1016/0077-7579(86)90043-8, 1986.

Morée, A. L., Schwinger, J., and Heinze, C.: Southern Ocean controls of the vertical marine $\delta^{13}C$ gradient – a modelling study, Biogeosciences, 15, 7205-7223, 10.5194/bg-15-7205-2018, 2018.

Morée, A. L., and Schwinger, J.: A Last Glacial Maximum forcing dataset for ocean modelling, Earth Syst. Sci. Data Discuss., 2019, 1-14, 10.5194/essd-2019-79, 2019.

Moy, A. D., Palmer, M. R., Howard, W. R., Bijma, J., Cooper, M. J., Calvo, E., Pelejero, C., Gagan, M. K., and Chalk, T. B.: Varied contribution of the Southern Ocean to deglacial atmospheric CO_2 rise, Nature Geoscience, 10.1038/s41561-019-0473-9, 2019.

Muglia, J., and Schmittner, A.: Glacial Atlantic overturning increased by wind stress in climate models, Geophysical Research Letters, 42, 9862-9868, 10.1002/2015gl064583, 2015.

Muglia, J., Skinner, L. C., and Schmittner, A.: Weak overturning circulation and high Southern Ocean nutrient utilization maximized glacial ocean carbon, Earth and Planetary Science Letters, 496, 47-56, 10.1016/j.epsl.2018.05.038, 2018.

Nadeau, L.-P., Ferrari, R., and Jansen, M. F.: Antarctic Sea Ice Control on the Depth of North Atlantic Deep Water, Journal of Climate, 32, 2537-2551, 10.1175/JCLI-D-18-0519.1, 2019.

Oka, A., Abe-Ouchi, A., Chikamoto, M. O., and Ide, T.: Mechanisms controlling export production at the LGM: Effects of changes in oceanic physical fields and atmospheric dust deposition, Global Biogeochemical Cycles, 25, 10.1029/2009GB003628, 2011.

Oliver, K. I. C., Hoogakker, B. A. A., Crowhurst, S., Henderson, G. M., Rickaby, R. E. M., Edwards, N. R., and Elderfield, H.: A synthesis of marine sediment core $\delta^{13}C$ data over the last 150 000 years, Climate of the Past, 6, 645-673, 10.5194/cp-6-645-2010, 2010.

Oppo, D. W., Gebbie, G., Huang, K.-F., Curry, W. B., Marchitto, T. M., and Pietro, K. R.: Data Constraints on Glacial Atlantic Water Mass Geometry and Properties, Paleoceanography and Paleoclimatology, 33, 1013-1034, 10.1029/2018PA003408, 2018.

Peterson, C. D., Lisiecki, L. E., and Stern, J. V.: Deglacial whole-ocean $\delta^{13}C$ change estimated from 480 benthic foraminiferal records, Paleoceanography, 29, 549-563, 10.1002/2013PA002552, 2014.

Primeau, F. W., Holzer, M., and DeVries, T.: Southern Ocean nutrient trapping and the efficiency of the biological pump, Journal of Geophysical Research: Oceans, 118, 2547-2564, 10.1002/jgrc.20181, 2013.

Rahmstorf, S.: On the freshwater forcing and transport of the Atlantic thermohaline circulation, Climate Dynamics, 12, 799-811, 10.1007/s003820050144, 1996.

Roche, D. M., Crosta, X., and Renssen, H.: Evaluating Southern Ocean sea-ice for the Last Glacial Maximum and pre-industrial climates: PMIP-2 models and data evidence, Quaternary Science Reviews, 56, 99-106, 10.1016/j.quascirev.2012.09.020, 2012.

Sarmiento, J. L., Gruber, N., Brzezinski, M. A., and Dunne, J. P.: High-latitude controls of thermocline nutrients and low latitude biological productivity, Nature, 427, 56-60, 10.1038/nature02127, 2004.

Sarmiento, J. L., and Gruber, N.: Ocean biogeochemical dynamics, Princeton University Press Princeton, 2006.

Schmitt, J., Schneider, R., Elsig, J., Leuenberger, D., Lourantou, A., Chappellaz, J., Köhler, P., Joos, F., Stocker, T. F., Leuenberger, M., and Fischer, H.: Carbon Isotope Constraints on the Deglacial CO_2 Rise from Ice Cores, Science, 336, 711-714, 10.1126/science.1217161, 2012.

Schmittner, A., Gruber, N., Mix, A. C., Key, R. M., Tagliabue, A., and Westberry, T. K.: Biology and air-sea gas exchange controls on the distribution of carbon isotope ratios ($\delta^{13}C$) in the ocean, Biogeosciences, 10, 5793-5816, 10.5194/bg-10-5793-2013, 2013.

Schmittner, A., and Somes, C. J.: Complementary constraints from carbon (^{13}C) and nitrogen (^{15}N) isotopes on the glacial ocean's soft-tissue biological pump, Paleoceanography, 31, 669-693, 10.1002/2015PA002905, 2016.

Schwinger, J., Goris, N., Tjiputra, J. F., Kriest, I., Bentsen, M., Bethke, I., Ilicak, M., Assmann, K. M., and Heinze, C.: Evaluation of NorESM-OC (versions 1 and 1.2), the ocean carbon-cycle stand-alone configuration of the Norwegian Earth System Model (NorESM1), Geoscientific Model Development, 9, 2589-2622, 10.5194/gmd-9-2589-2016, 2016.

Sigman, D. M., and Boyle, E. A.: Glacial/interglacial variations in atmospheric carbon dioxide, Nature, 407, 859-869, 10.1038/35038000, 2000.

Sigman, D. M., Hain, M. P., and Haug, G. H.: The polar ocean and glacial cycles in atmospheric CO_2 concentration, Nature, 466, 47, 10.1038/nature09149, 2010.

Sikes, E. L., Elmore, A. C., Allen, K. A., Cook, M. S., and Guilderson, T. P.: Glacial water mass structure and rapid $\delta^{18}O$ and $\delta^{13}C$ changes during the last glacial termination in the Southwest Pacific, Earth and Planetary Science Letters, 456, 87-97, 10.1016/j.epsl.2016.09.043, 2016.

Skinner, L. C., Primeau, F., Freeman, E., de la Fuente, M., Goodwin, P. A., Gottschalk, J., Huang, E., McCave, I. N., Noble, T. L., and Scrivner, A. E.: Radiocarbon constraints on the glacial ocean circulation and its impact on atmospheric CO_2, Nature Communications, 8, 16010, 10.1038/ncomms16010, 2017.

Spence, J. P., Eby, M., and Weaver, A. J.: The Sensitivity of the Atlantic Meridional Overturning Circulation to Freshwater Forcing at Eddy-Permitting Resolutions, Journal of Climate, 21, 2697-2710, 10.1175/2007JCLI2103.1, 2008.

Srokosz, M. A., and Bryden, H. L.: Observing the Atlantic Meridional Overturning Circulation yields a decade of inevitable surprises, Science, 348, 10.1126/science.1255575, 2015.

Stephens, B. B., and Keeling, R. F.: The influence of Antarctic sea ice on glacial–interglacial CO_2 variations, Nature, 404, 171-174, 10.1038/35004556, 2000.

Takahashi, T., Broecker, W. S., and Langer, S.: Redfield ratio based on chemical data from isopycnal surfaces, Journal of Geophysical Research: Oceans, 90, 6907-6924, 10.1029/JC090iC04p06907, 1985.

Tamburini, F., and Föllmi, K. B.: Phosphorus burial in the ocean over glacial-interglacial time scales, Biogeosciences, 6, 501-513, 10.5194/bg-6-501-2009, 2009.

Tjiputra, J. F., Roelandt, C., Bentsen, M., Lawrence, D. M., Lorentzen, T., Schwinger, J., Seland, Ø., and Heinze, C.: Evaluation of the carbon cycle components in the Norwegian Earth System Model (NorESM), Geoscientific Model Development 6, 301-325, 10.5194/gmd-6-301-2013, 2013.

Tjiputra, J. F., Schwinger, J., Bentsen, M., Morée, A. L., Gao, S., Bethke, I., Heinze, C., Goris, N., Gupta, A., He, Y., Olivié, D., Seland, Ø., and Schulz, M.: Ocean biogeochemistry in the Norwegian Earth System Model version 2 (NorESM2), Geosci. Model Dev. Discuss., 2020, 1-64, 10.5194/gmd-2019-347, 2020.

Umling, N. E., Thunell, R. C., and Bizimis, M.: Deepwater Expansion and Enhanced Remineralization in the Eastern Equatorial Pacific During the Last Glacial Maximum, Paleoceanography and Paleoclimatology, 33, 563-578, 10.1029/2017PA003221, 2018.

Volk, T., and Hoffert, M. I.: Ocean Carbon Pumps: Analysis of Relative Strengths and Efficiencies in Ocean-Driven Atmospheric CO_2 Changes, in: The Carbon Cycle and Atmospheric CO_2: Natural Variations Archean to Present, American Geophysical Union, 99-110, 1985.

Weber, S. L., Drijfhout, S. S., Abe-Ouchi, A., Crucifix, M., Eby, M., Ganopolski, A., Murakami, S., Otto-Bliesner, B., and Peltier, W. R.: The modern and glacial overturning circulation in the Atlantic ocean in PMIP coupled model simulations, Climate of the Past, 3, 51-64, 10.5194/cp-3-51-2007, 2007.

Winckler, G., Anderson, R. F., Jaccard, S. L., and Marcantonio, F.: Ocean dynamics, not dust, have controlled equatorial Pacific productivity over the past 500,000 years, Proceedings of the National Academy of Sciences, 113, 6119, 10.1073/pnas.1600616113, 2016.

Winguth, A. M. E., Archer, D., Duplessy, J. C., Maier-Reimer, E., and Mikolajewicz, U.: Sensitivity of paleonutrient tracer distributions and deep-sea circulation to glacial boundary conditions, Paleoceanography, 14, 304-323, 10.1029/1999PA900002, 1999.

Yu, J., Menviel, L., Jin, Z. D., Thornalley, D. J. R., Barker, S., Marino, G., Rohling, E. J., Cai, Y., Zhang, F., Wang, X., Dai, Y., Chen, P., and Broecker, W. S.: Sequestration of carbon in the deep Atlantic during the last glaciation, Nature Geoscience, 9, 319-324, 10.1038/ngeo2657, 2016.

Yu, J., Menviel, L., Jin, Z. D., Thornalley, D. J. R., Foster, G. L., Rohling, E. J., McCave, I. N., McManus, J. F., Dai, Y., Ren, H., He, F., Zhang, F., Chen, P. J., and Roberts, A. P.: More efficient North Atlantic carbon pump during the Last Glacial Maximum, Nature Communications, 10, 2170, 10.1038/s41467-019-10028-z, 2019.

Zeebe, R., and Wolf-Gladrow, D.: CO_2 in Seawater: Equilibrium, Kinetics, Isotopes, Elsevier Oceanography Series, edited by: Halpern, D., Elsevier Science B.V., Amsterdam, The Netherlands, 346 pp., 2001.

Zhang, J., Quay, P. D., and Wilbur, D. O.: Carbon isotope fractionation during gas-water exchange and dissolution of CO_2, Geochimica et Cosmochimica Acta, 59, 107-114, 10.1016/0016-7037(95)91550-D, 1995.

Ödalen, M., Nycander, J., Oliver, K. I. C., Brodeau, L., and Ridgwell, A.: The influence of the ocean circulation state on ocean carbon storage and CO_2 drawdown potential in an Earth system model, Biogeosciences, 15, 1367-1393, 10.5194/bg-15-1367-2018, 2018.

Supplement to Paper III

Evaluating the Biological Pump Efficiency of the Last Glacial Maximum Ocean using $\delta^{13}C$

Morée, A. L., J. Schwinger, U. Ninneman,

A. Jeltsch-Thömmes, I. Bethke, and C. Heinze

Submitted to Climate of the Past

1 Sea surface salinity restoring

We compare the ocean circulation after 1000 years of simulation in an LGM spinup with and without extra adjustments to the sea surface salinity (SSS) reference field used for salinity restoring. The adjusted spinup is the one used in our study and described in the main text. If unadjusted, the LGM SSS reference field is derived from the PI SSS reference field through the addition of a PMIP3-based sea surface salinity anomaly (Morée and Schwinger, 2019a; Morée and Schwinger, 2019b) (Fig. S1a). For the unadjusted setup NorESM-OC simulated an AMOC of 21 Sv (17 Sv for the adjusted spinup), and a Drake Passage through flow of 112 Sv (134 Sv for the adjusted spinup). The SSW profoundly decrease their volume in the Atlantic (Fig. S2). As especially the retreat of SSW is in disagreement with proxy-based reconstructions (see main text), we applied an adjustment to the SSS relaxation of -0.5 psu in the North Atlantic in the region where the anomaly was largest, as well as in the Southern Ocean (Fig. S1a). The simulated SSS for the adjusted run is shown in Fig. S1b.

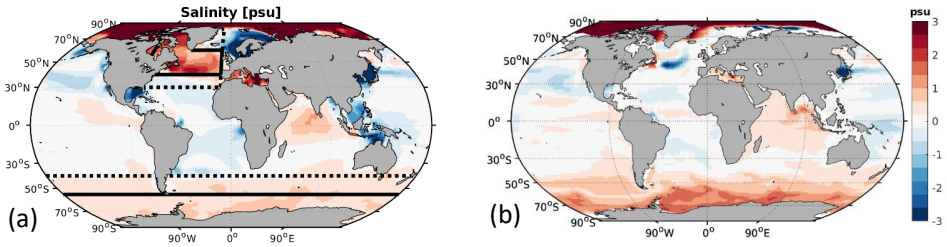

Figure S1 Sea surface salinity anomaly between the LGM and PI, with regions of salinity relaxation adjustment. (a) SSS anomaly in model forcing. In addition, the North Atlantic region, which is decreased by 0.5 psu, extends between 90°W and 45°W from 40°N to 80°N, and between 45°W to 10°W from 40°N to 60°N. The additional anomaly is linearly ramped off to zero at the line along 30°N and to the point 80°N 10°W. In the Southern Ocean, 0.5 psu is added south of 55°S, and ramped off to zero until 40°S. (b) Simulated SSS LGM-PI change.

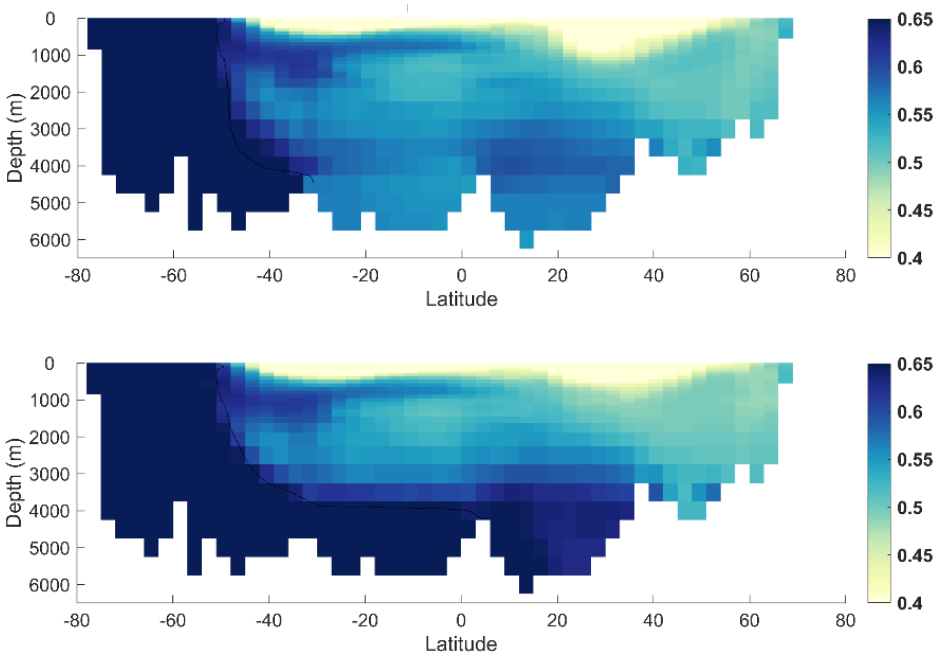

Figure S2 Atlantic PO tracer (as Fig. 1) after 1000 years of spinup without salinity adjustment (upper) and with salinity adjustment (lower).

2 LGM Normal Year Forcing

The PMIP3-based atmospheric anomaly fields which were used to obtain an atmospheric forcing representative of the LGM (Morée and Schwinger, 2019a; Morée and Schwinger, 2019b) received an update (version 2, retrievable in Morée and Schwinger, 2019a) after the model simulations for this study were finished. Version 2 is based on PMIP3 models CNRM-CM5, IPSL-CM5A-LR, GISS-E2-R, MIROC-ESM and MRI-CGCM3 for all variables including SSS. In version 1, GISS-E2-R was not included and the SSS anomaly was based on CNRM-CM5 and MIROC-ESM. We evaluated the differences in the LGM spinup after 500 model years between version 1 and version 2 of these anomaly fields. We note that the modelled circulation is not fully equilibrated yet at this stage, but limit our comparison due to computational costs. We conclude that the SSS tuning applied as described in SM1 is specific to version 1 of the forcing anomaly, and should be adjusted for version 2.

3 Calculation of LGM-PI ΔDIC

We estimate the LGM-PI change in marine DIC content by applying the same approach used to estimate Δland in Jeltsch-Thömmes et al. (2019). To this end, the forcing-response relationships of seven generic deglacial carbon cycle mechanisms in regard to LGM-PI changes in four observational targets (pCO_2^{atm}, $\delta^{13}C^{atm}$, marine $\delta^{13}C$ of DIC, or deep equatorial Pacific CO_3^{2-}) and DIC are investigated with the Bern3D Earth System Model of Intermediate Complexity. The seven processes cover physical mechanisms, mechanisms related to oceanic carbonate and organic matter, and changes in the land biosphere carbon inventory (for details please see Jeltsch-Thömmes et al., 2019). These seven generic deglacial carbon cycle mechanisms were varied individually by systematic parameter variations in addition to well-established forcings such as orbital parameters, greenhouse gas radiative forcing, land ice albedo, coral reef regrowth, and North Atlantic freshwater forcing. In a next step, Latin hypercube parameter sampling was used to vary the processes in combination and probe for nonlinear interactions and use the results to adjust the above forcing-response relationships. A simple emulator of the form

$$\Delta T = a^T + b^T * (\sum_{i=1}^{7} \Delta p_i * S_i^T),$$

where $S_i^T = \partial T / \partial p_i$ is the sensitivity for each target T to each mechanism i and the corresponding parameter change Δp_i is derived. a^T is the offset and b^T the slope of the respective linear fit from the multi-parameter adjustment. We use the same half a million parameter combinations as used in Jeltsch-Thömmes et al. (2019) and with ΔDIC as target. The four proxy targets (pCO_2^{atm}, $\delta^{13}C^{atm}$, marine $\delta^{13}C$ of DIC, or deep equatorial Pacific CO_3^{2-}) are used as constraints.

Applying single constraints only, yields similar ranges for ΔDIC for each constraint. Considering all four proxy targets simultaneously shifts the estimate of ΔDIC to higher values (Fig. S3a). We can further disentangle contributions to ΔDIC: Sedimentation-weathering imbalances contribute the most to ΔDIC and with the largest uncertainty

(Fig. S3b). The contribution from corals reflects the uncertainty of the estimated amount of coral reef growth. The estimates range from 380 Gt C (Vecsei and Berger, 2004) to 1200 Gt C and more (Milliman, 1993; Kleypas, 1997; Ridgwell et al., 2003). For the discussion of the contribution from the land biosphere the reader is referred to Jeltsch-Thömmes et al. (2019). The atmospheric contribution is a result of the prescribed LGM to PI CO_2 target of 80-100 ppm. The results point to an important role and large contribution from sedimentation-weathering imbalances to ΔDIC estimates over glacial/interglacial timescales, however, with a large uncertainty.

It has to be noted that in order to use the cost-efficient emulator and explore a large parameter space only the change between LGM and PI was considered. Including the spatio-temporal evolution of several proxies in transient model simulations will help to further gain understanding into governing processes and narrow down the ΔDIC estimate but is beyond the scope of this manuscript.

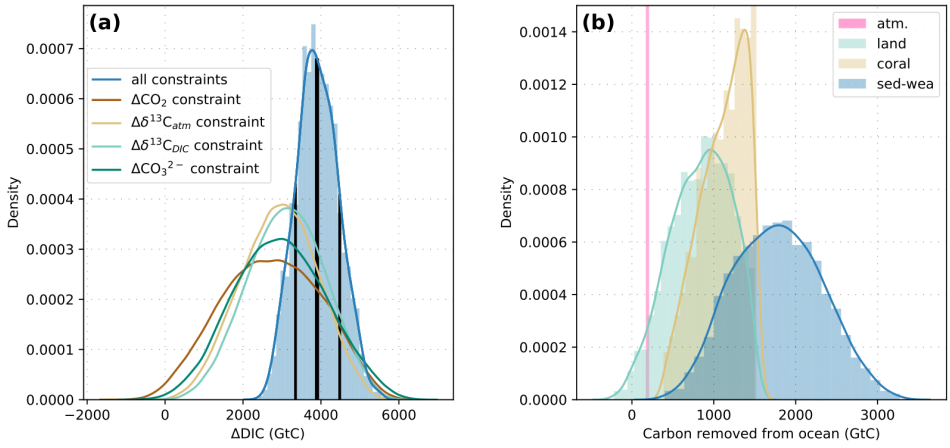

Figure S3 LGM-PI multi-constraint ΔDIC determined using the Bern3D model. The (a) total estimate and (b) contributions from atmosphere, land, coral and sedimentation-weathering imbalances.

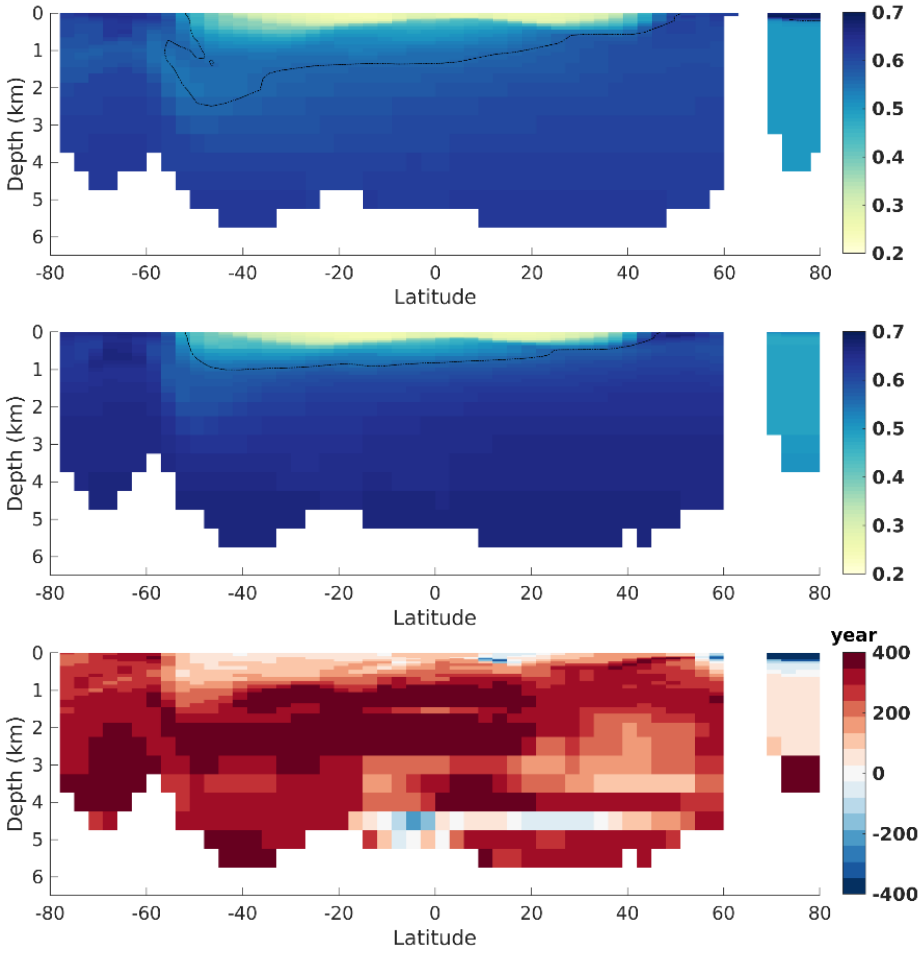

Figure S4 PO tracer Pacific zonal mean transect for the PI (top) and LGM (middle) simulation as well as Pacific change in radiocarbon age (bottom), as Fig. 1.

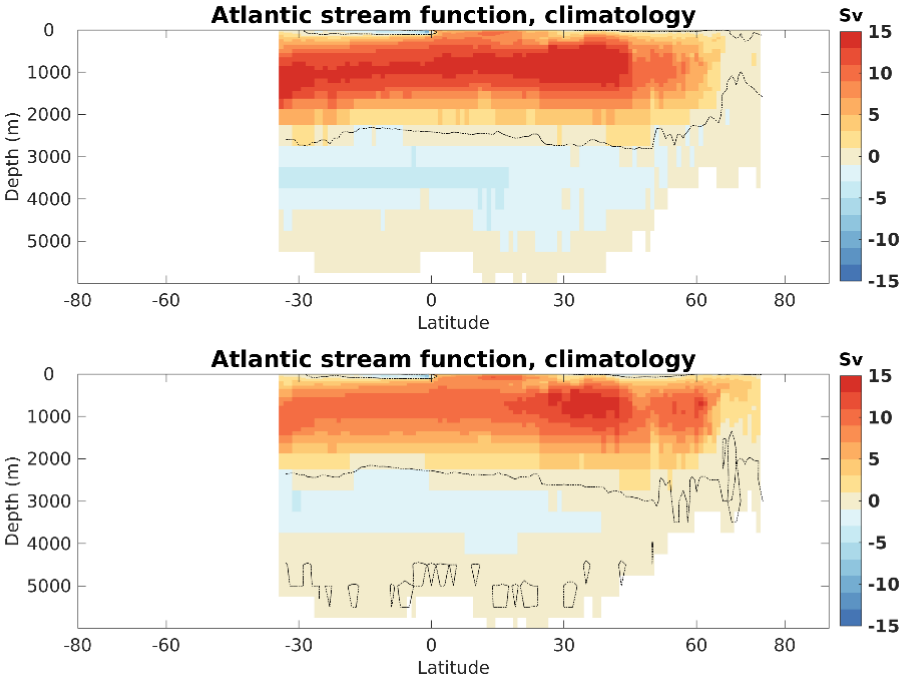

Figure S5 Atlantic stream functions for the PI (top) and LGM (bottom). The depth of the transition between the Atlantic overturning cells, as indicated by the depth of the zero Sv contour at 30°S, shallowed by ~350 m in our LGM setup as compared to the PI spinup.

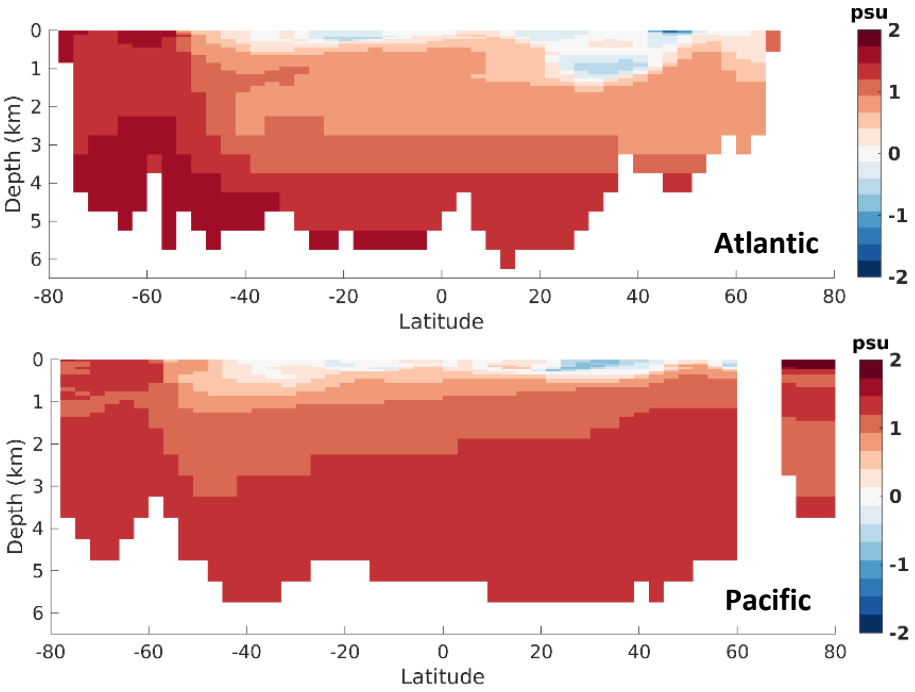

Figure S6 Simulated LGM-PI change in salinity.

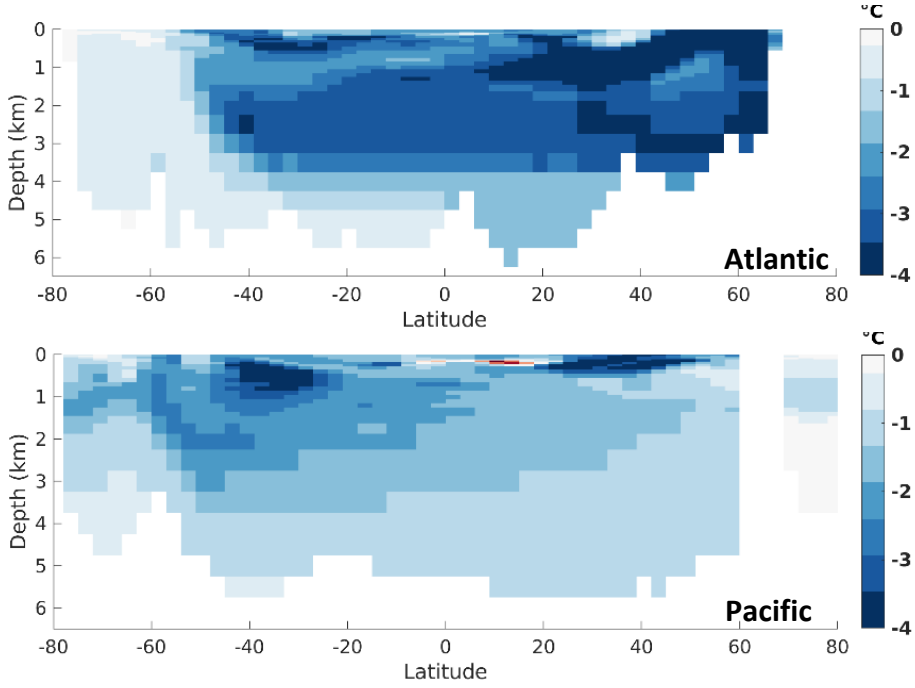

Figure S7 Simulated LGM-PI change in temperature.

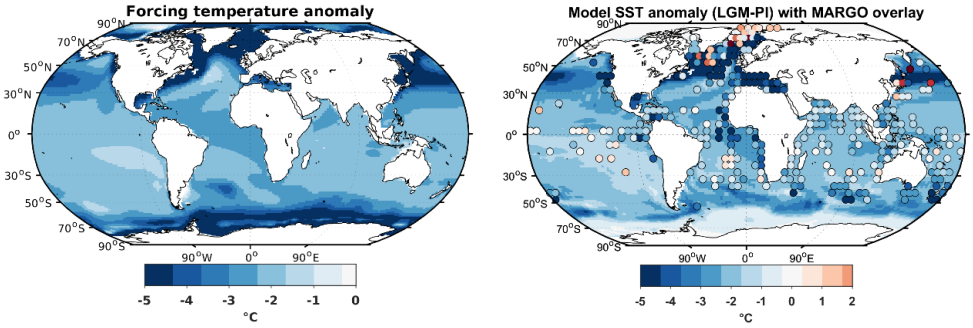

Figure S8 Atmospheric forcing (annual mean) (left) and simulated SST anomaly (right) with overlay of MARGO SST reconstruction data (Margo Project Members, 2009)

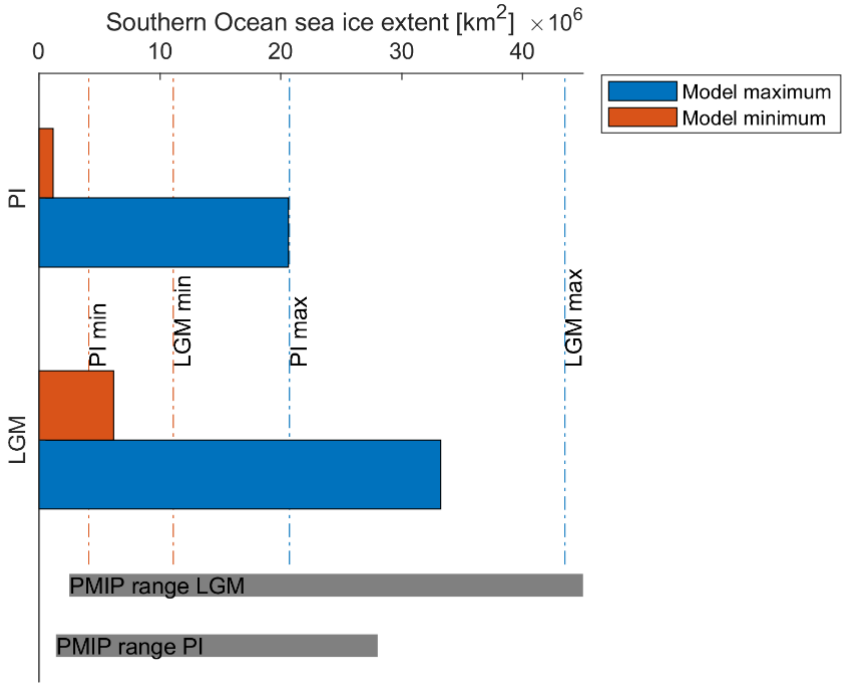

Figure S9 Southern Ocean sea ice extent (area of sea ice with a concentration of >15%) for the PI and LGM simulations. PMIP and observational estimate data from Roche et al. (2012) and Marzocchi and Jansen (2017).

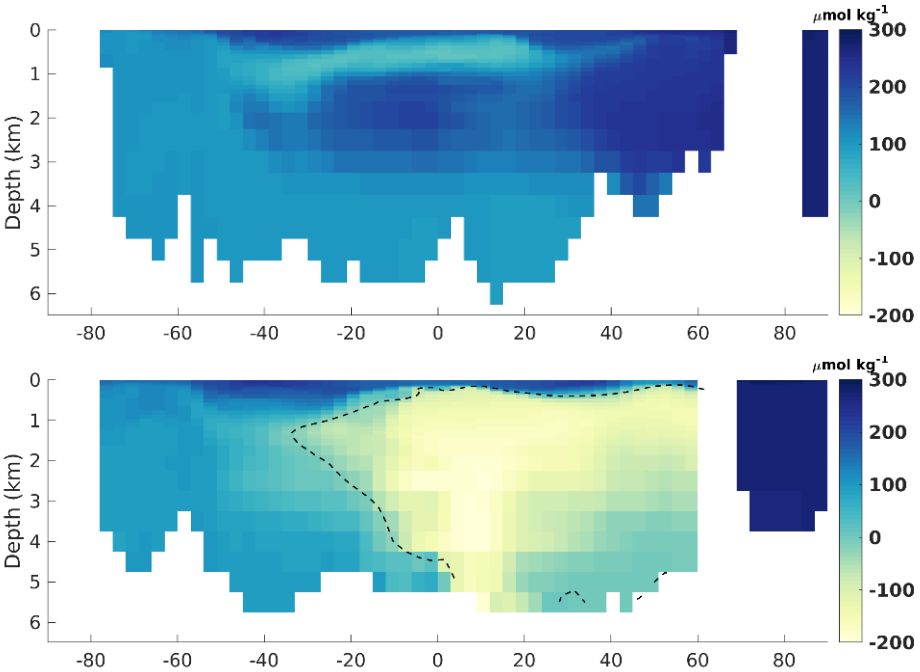

Figure S11 Simulated LGM O_2 concentrations for a 75 % $\overline{BP_{eff}}$, with a zero contour line.

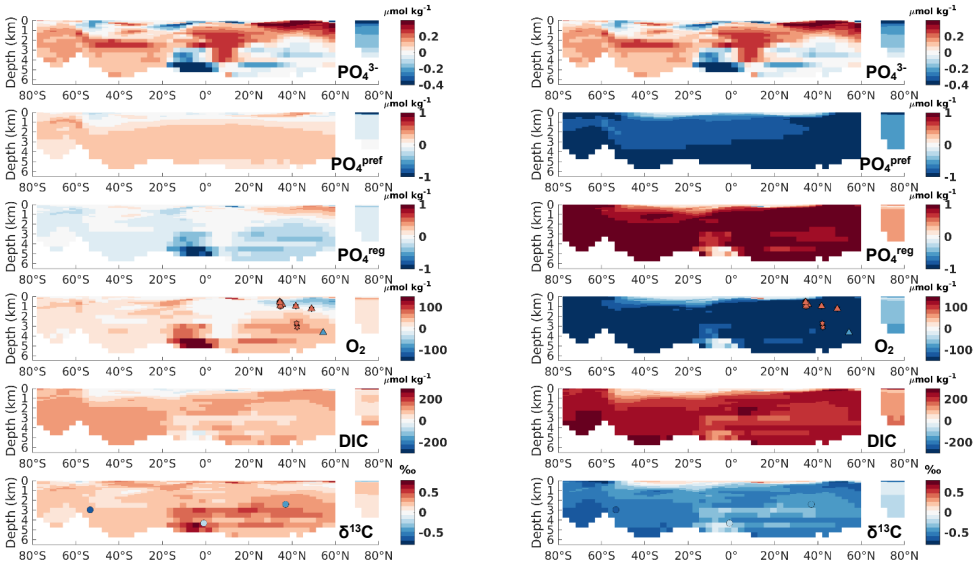

Figure S10 Pacific LGM-PI changes for the original model output (left-hand column) and adjusted to a biological pump efficiency of 75% (right-hand column). Otherwise as in Fig. 2 and 5.

References

Jeltsch-Thömmes, A., Battaglia, G., Cartapanis, O., Jaccard, S. L., and Joos, F.: Low terrestrial carbon storage at the Last Glacial Maximum: constraints from multi-proxy data, Climate of the Past, 15, 849-879, 10.5194/cp-15-849-2019, 2019.

Kleypas, J. A.: Modeled estimates of global reef habitat and carbonate production since the last glacial maximum, Paleoceanography, 12, 533–545, 10.1029/97PA01134, 1997.

Marzocchi, A., and Jansen, M. F.: Connecting Antarctic sea ice to deep-ocean circulation in modern and glacial climate simulations, Geophysical Research Letters, 44, 6286-6295, 10.1002/2017GL073936, 2017.

Milliman, J. D.: Production and accumulation of calcium carbonate in the ocean: budget of a nonsteady state, Global Biogeochemical Cycles, 7, 927–957, 1993.

Morée, A., and Schwinger, J.: Last Glacial Maximum minus pre-industrial anomaly fields for use in forced ocean modelling, based on PMIP3 [Dataset]. Norstore, 2019a.

Morée, A. L., and Schwinger, J.: A Last Glacial Maximum forcing dataset for ocean modelling, Earth Syst. Sci. Data Discuss., 2019, 1-14, 10.5194/essd-2019-79, 2019b.

Ridgwell, A. J., Watson, A. J., Maslin, M. A., and Kaplan, J. O.: Implications of coral reef buildup for the controls on atmospheric CO_2 since the Last Glacial Maximum, Paleoceanography, 18, 7 pp., 10.1029/2003PA000893, 2003.

Roche, D. M., Crosta, X., and Renssen, H.: Evaluating Southern Ocean sea-ice for the Last Glacial Maximum and pre-industrial climates: PMIP-2 models and data evidence, Quaternary Science Reviews, 56, 99-106, https://doi.org/10.1016/j.quascirev.2012.09.020, 2012.

Vecsei, A. and Berger, W. H.: Increase of atmospheric CO_2 during deglaciation: Constraints on the coral reef hypothesis from patterns of deposition, Global Biogeochemical Cycles, 18, 1–7, 10.1029/2003GB002147, 2004.

Paper IV

Cancellation of the precessional cycle in benthic $\delta^{18}O$ records during the Early Pleistocene

Morée, A. L., T. Sun, A. Bretones, E.O. Straume, K. Nisancioglu, and G. Gebbie

Under review at Geophysical Research Letters

IV

Cancellation of the precessional cycle in $\delta^{18}O$ records during the Early Pleistocene

Anne L. Morée[1], Tianyi Sun[2†], Anais Bretones[3], Eivind O. Straume[4], Kerim Nisancioglu[3,4], Geoffrey Gebbie[5]

[1]Geophysical Institute, University of Bergen and the Bjerknes Centre for Climate Research, 5007 Bergen, Norway.

[2]Institute for Geophysics, Jackson School of Geosciences, the University of Texas at Austin, Austin, Texas.

[3]Department of Earth Science, University of Bergen and the Bjerknes Centre for Climate Research, 5007 Bergen, Norway.

[4]Centre for Earth Evolution and Dynamics (CEED), Department of Geosciences, University of Oslo, Norway.

[5]Department of Physical Oceanography, Woods Hole Oceanographic Institution, Woods Hole, MA, USA.

Corresponding author: Anne L. Morée (anne.moree@uib.no)

† Current affiliation: Environmental Defense Fund, New York, NY.

Key Points:

- Glacial-interglacial cycles are incompletely recorded in the ocean due to cancellation of hemispherically anti-phased signals
- Precessional cancellation develops due to mixing of North Atlantic and Southern Ocean $\delta^{18}O$ signals at depth
- Our model experiments show wide-spread precessional cancellation for the Early Pleistocene

Abstract

The dominant pacing of glacial-interglacial cycles in deep-ocean $\delta^{18}O$ records changed substantially during the Mid Pleistocene Transition. The precessional cycle (~23 ky) is absent during the Early Pleistocene, which we show can be explained by cancellation of the hemispherically anti-phased precessional cycle in the Early Pleistocene interior ocean. Such cancellation develops due to mixing of North Atlantic and Southern Ocean $\delta^{18}O$ signals at depth. We explore the cancellation potential for different North Atlantic and Southern Ocean deep-water source $\delta^{18}O$ values using a tracer transport ocean model. Cancellation of precession occurs for all signal strengths and is widespread for a signal strength typical for the Early Pleistocene. Early Pleistocene precessional power is therefore likely incompletely archived in deep-sea $\delta^{18}O$ records, concealing the true periodicity of the glacial cycles in the two hemispheres.

Plain Language Summary

$\delta^{18}O$ records from deep-sea sediments show a pronounced difference in periodicity between the Early (~2-1 Million years ago) and Late (~1-0 Million years ago) Pleistocene - the Mid-Pleistocene Transition, MPT. Representing changes in ice volume and temperature, these $\delta^{18}O$ records are an important source for our understanding of long-term climate variability. A central conclusion based on these $\delta^{18}O$ records is that glacial-interglacial cycles considerably changed their rhythm during the Mid-Pleistocene. Curiously, the ~23 000 year (precessional) cycle of solar insolation is absent in Early Pleistocene $\delta^{18}O$ records - despite its presence in solar insolation forcing to the ice sheets. Climate feedbacks involving (sea) ice, geological processes and carbon cycling may have contributed to the MPT. We, however, show that the absence of an Early Pleistocene precession signal in deep-sea $\delta^{18}O$ records could be the result of destructive interference in the deep ocean, caused by the anti-phasing of the precessional cycle between the North Atlantic and Southern Ocean deep-water sources. We explored the potential for cancellation with an ocean model and show that interference can indeed cause widespread cancellation, particularly in

the Early Pleistocene. We, therefore, conclude that the $\delta^{18}O$ incompletely archives climatic cycles, challenging our understanding of long-term climate variability.

1. Introduction

Changes in the Earth's orbital parameters cause variations in solar insolation, the Milankovitch cycles, on the time scales of precession (~ 23 ky), obliquity (~ 41 ky) and eccentricity (~ 100 ky) (Milanković, 1920). In the early 1980s, it became clear that the orbital parameters strongly correlate with the dramatic variations in marine sediment $\delta^{18}O$ records during the Pleistocene (Imbrie et al., 1984). As marine $\delta^{18}O$ relates to ice sheet volume and temperature (Elderfield et al., 2012), Pleistocene glacial-interglacial variations were postulated to be driven by the Milankovitch cycles (Hays et al., 1976; Imbrie et al., 1984). $\delta^{18}O$ proxy records, however, show a pronounced change in dominant Milankovitch periodicities from the Early to Late Pleistocene, at the Mid Pleistocene Transition (MPT). The Early Pleistocene (here taken as 2-1.2 Ma) is referred to as 'the 41 ky world' (Raymo & Nisancioglu, 2003) due to the dominance of the 41 ky obliquity periodicity in the proxy records. The Late Pleistocene (here taken as 0.8-0 Ma) is referred to as 'the 100 ky world' because of the dominance of periodicities between 80 and 120ky, and has all three Milankovitch cycles represented in deep-sea $\delta^{18}O$ records.

The transition from the 41 ky to the 100 ky world (i.e., the MPT) is not yet fully understood. Most hypotheses explain the MPT by changes in global or hemispheric ice sheet volume, where smaller ice sheets are considered to respond on shorter timescales (i.e. 23 and 41 ky cycles), whereas larger ice sheets respond on longer timescales (i.e. 100 ky cycles). A higher atmospheric pCO_2 is reconstructed for the Early Pleistocene as compared to the Late Pleistocene, particularly for the glacials (Hönisch et al., 2009; Seki et al., 2010). This comparatively high Early Pleistocene atmospheric pCO_2 is associated with smaller ice sheets, while lower atmospheric pCO_2 favors colder climates and larger ice sheets in the Late Pleistocene. The relatively smaller Early Pleistocene ice sheet volume could also be related to the existence and

slow erosion of a relatively soft regolith bed beneath the Laurentide ice sheet, inhibiting the build-up of larger ice volume pre-MPT (Clark et al., 2006; Clark & Pollard, 1998). Sea ice may have played a role: the activation of the 'sea ice switch' during the MPT due to general Pleistocene climate cooling could have paced a ~100 ky rhythm of the ice ages post-MPT through its influence on atmospheric temperature and moisture fluxes (Gildor & Tziperman, 2000). Alternatively, the change in periodicity could be explained by climate variability on timescales beyond the Pleistocene, where the MPT triggered a different cyclic variability through the albedo discontinuity at the snow-ice edge (Crowley & Hyde, 2008). Recently however, studies increasingly stress the importance of long-term atmospheric pCO_2 and temperature decline, interacting with regolith removal and/or Southern Ocean iron fertilization as the driver of the MPT (Berger et al., 1999; Chalk et al., 2017; McClymont et al., 2013; Willeit et al., 2019).

2. The Antiphase Hypothesis

An alternative view of both 'the 41 ky world' and the MPT is that part of the change in periodicity observed in the $\delta^{18}O$ proxy records is due to the cancellation of the cyclic precessional signals in the interior ocean (Raymo et al., 2006). We build on the work by Raymo et al. (2006) and test the feasibility of cancellation of the hemispherically anti-phased precessional signal in deep-sea $\delta^{18}O$ records (the "Antiphase Hypothesis") (Shakun et al., 2016), and note strong spatial variations in the occurrence of such cancellation. According to the Antiphase Hypothesis, precessional cancellation occurs before the MPT only (i.e., in the Early Pleistocene). This contrast in the occurrence of precessional cancellation across the MPT is explained by variations in the relative $\delta^{18}O$ source signal strengths from the two main deep-water formation regions (in the North Atlantic and Southern Ocean) - which influence the strength of precession relative to obliquity at depth. Consequently, the change in source-signal strengths is recorded in the $\delta^{18}O$ of marine sediments as an apparent change in dominant periodicity.

There are several lines of evidence in favor of the Antiphase Hypothesis. For example, one would expect a prominent precessional influence throughout the Pleistocene based on classic Milankovitch theory. In addition, evidence for precession-driven Northern Hemispheric ice volume (Raymo et al., 2006; Shakun et al., 2016) implies a prominent precessional component in $\delta^{18}O$ records throughout the Pleistocene. Under the Antiphase Hypothesis, both of these dynamical expectations would hold, as long as both poles contribute a precession $\delta^{18}O$ signal to the interior ocean. Given new proxy data, we will be able to verify to what extent deep-sea $\delta^{18}O$ indeed represents surface climatic oscillations by using proxies of ice volume not influenced by interior cancellation of precession - such as $\delta^{18}O$ records from Antarctic ice core records across the MPT (Dahl-Jensen, 2018).

3. Results

3.1 Southern versus northern influence

Assuming that deep-water formation mostly occurs during the winter season in both hemispheres, we hypothesize that the mixing of deep-water from the two main deep-water formation regions (the Southern Ocean and North Atlantic; Figure 1) can lead to cancellation of the precessional signal in deep-sea $\delta^{18}O$ sediment records. This is due to the hemispheric anti-phasing of the precessional signal in insolation for a given season (Milanković, 1920), and because of the inflow of meltwater from the ice sheets into the Southern Ocean and North Atlantic deep-water formation regions (Figure 1).

The relative amplitude of the southern versus northern deep-water signals (the S/N ratio) is key for the potential of precessional cancellation in $\delta^{18}O$ proxy records. The S/N ratio depends on the interplay between: i) the respective deep-water volume contribution of the northern and southern sources and their overturning rates; ii) the $\delta^{18}O$ source signature of the northern and southern ice sheets; and iii) the amplitude and the variability of the northern and southern ice sheet volumes. We consider the net effect of these different aspects through the S/N ratio, as they individually are not

well constrained over the course of the Pleistocene. Shifts in the S/N ratio can have implications for other water column tracers as well, especially if changes occur in the deep-water volume contributions from the northern and southern source regions (Marinov et al., 2008). Such changes would induce variations in the interior storage of carbon and atmospheric pCO_2 (Marinov et al., 2008; Toggweiler, 1999) - and therefore the greenhouse effect, which again would influence ice sheet volume and temperature.

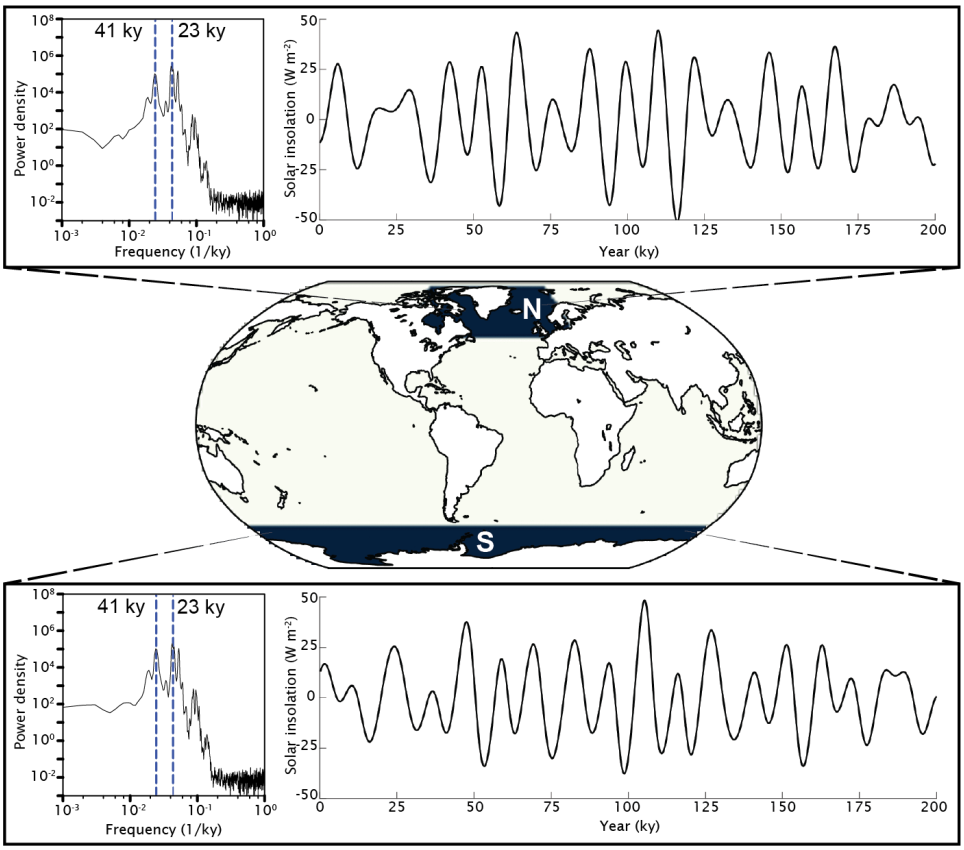

Figure 1. Scaled insolation forcing (W m^2) at 65°N and 65°S with the corresponding power density spectrum (W^2 m^{-4} ky) of the northern (i.e. North Atlantic, within 50-80°N and 100°W-20°E) and southern (i.e. Southern Ocean, ≥ 60°S) source regions. These two source regions are named N and S on the map.

As we anticipate that the S/N ratio is key for the potential of precessional cancellation, we expect a profound change in the S/N ratio during the MPT – causing precessional cancellation in the $\delta^{18}O$ records before the MPT, but not after. Indeed, the influence

of the southern and northern hemisphere on global climate variability varied greatly over the past 35 My (De Vleeschouwer et al., 2017), showing potential for large shifts in the S/N ratio. Since deep-sea $\delta^{18}O$ records are strongly correlated with sea level changes (Spratt & Lisiecki, 2016), reconstructions of glacial-interglacial ice sheet volume variability expressed as sea level equivalents (s.l.e.) can be used to understand past changes in the S/N ratio. Before the Early Pleistocene '41 ky world' (i.e., > ~2-1.2 Ma), we expect a large S/N ratio since it precedes the onset of Northern Hemisphere glaciation (which occurred ~3.6-2.4 Ma; Mudelsee and Raymo (2005)) (i.e., S/N>>6).

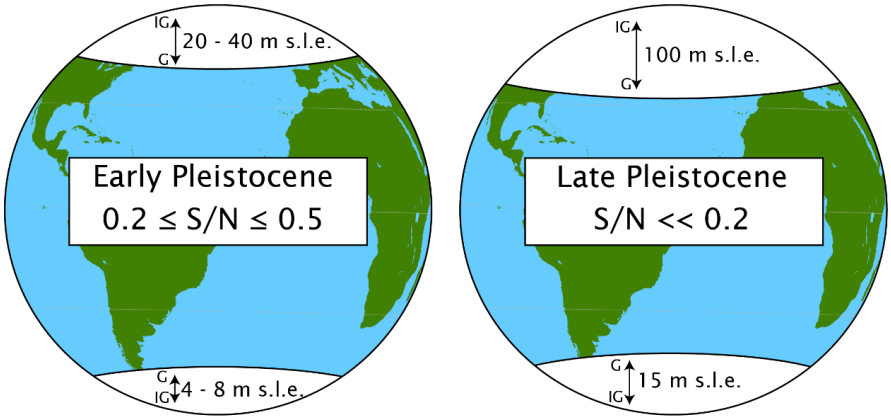

Figure 2. Concept of the decrease in S/N ratio from the Early to the Late Pleistocene, as based on s.l.e. reconstructions. The S/N ratio is determined by the relative contribution of the northern versus southern signals (Figure 1).

For the Early Pleistocene, a best (but uncertain) estimate of the S/N ratio is in the range of 0.2-0.5: the northern ice sheet contributed ~20-40 m s.l.e. to glacial-interglacial sea level variability (Berger et al., 1999; Willeit et al., 2015). At the same time, total sea level generally varied by at most ~50 m, of which the Antarctic ice sheet contributed 4-8 m s.l.e. (Sutter et al. (2019); Figure 2). After the MPT, global ice sheet volume increased (Berger et al., 1999; Elderfield et al., 2012), with a glacial-interglacial sea level variability reaching ~120 m (Spratt & Lisiecki, 2016) causing a further decrease in the S/N ratio (S/N<<0.2). In this period, the Late Pleistocene, the Antarctic ice sheet likely did not contribute more than ~15 m s.l.e. to glacial-interglacial sea

level changes, due to the relative stability of the West Antarctic ice sheet (DeConto & Pollard, 2016; Sutter et al., 2019).

Using a tracer transport model of modern ocean circulation, we explore how an absent precessional signal could develop in the $\delta^{18}O$ records, as a function of S/N ratios. In order to do so, we prescribe the model's North Atlantic and Southern Ocean surface water end-members with their respective solar insolation (at 65°N and 65°S) over the past 200 ky (Figure 1) for a large range of S/N ratios (for details on experiment design, see SI Text S1). The range of S/N ratios represents the range of $\delta^{18}O$ source water properties that could exist over time. Note that the spectrum of the forcing contains a similar power for the obliquity and precessional cycles. We apply the Total Matrix Intercomparison model (TMI) (Gebbie & Huybers, 2012) to explore the fate of the cyclic northern and southern surface forcing signals in the interior ocean (SI Text S2). The respective deep-water volume contribution of the northern and southern sources to the interior are kept constant and represent over ~75% of the total bottom water volume in the model (Figure S1). The importance of boundary conditions for the interior tracer distribution has been explored extensively with the TMI model, including on palaeoclimatic time scales (Oppo et al., 2018). However, the deep-water formation sites and overturning rates may have varied over the Pleistocene (Hasenfratz et al., 2019; Kleiven et al., 2003). We evaluate the potential effects of changes in circulation strength (advection and diffusion) and find that they do not change the basic process behind the Antiphase Hypothesis (SI Text S3).

3.2 Cancellation of precession

Cancellation or weakening of the precessional amplitude relative to obliquity amplitude occurs in the ocean interior for any non-zero S/N ratio (Figure 3 and S2), suggesting that such cancellation could occur at any point in Earth's history where deep-waters from the two hemispheres (with an anti-phased signature) mix in the interior ocean. Our estimate of the Pleistocene S/N ratio is less than 0.5 based on sea level reconstructions (Figure 2). For the Early Pleistocene, the estimated S/N ratio of

~0.2-0.5 makes it likely that cancellation of precession played a major role in $\delta^{18}O$ records, particularly at depth in the Pacific basin (Figure 3 and S2). In the Late Pleistocene S/N decreased to values <<0.2, for which we do not expect widespread cancellation (Figure 3 and S2), causing precession to re-appear in the post-MPT $\delta^{18}O$ records.

A stronger amplitude of the southern sourced signal (i.e., high S/N ratio) generally pushes the region of cancellation northward in all ocean basins (Figure S2). At the same time, the areal extent of the bottom water cancellation is greatly reduced when it migrates from the Pacific into the Atlantic basin. The dominant contribution of the southern source waters in the Pacific (Gebbie (2012)*;* Figure S1) results in widespread Pacific cancellation only when the amplitude of the southern source is relatively weak (S/N<1). For high S/N ratios (S/N>6, as expected before the onset of glaciation in the Northern Hemisphere), precessional cancellation is limited to the mid-Atlantic interior ocean (Figure 3). Also for an S/N ratio of ~1-2, we expect no cancellation of precession in the Pacific and very limited cancellation in the Atlantic and Indian Oceans (Figure S2). The amplitude of the southern source signal relative to the northern deep-water source is therefore key in the development of cancellation. An improved estimate of end-member values (i.e., $\delta^{18}O$ from ice released into the ocean) for the Early and Late Pleistocene would help to determine the importance of cancellation for each of these distinct periods.

There is a notable exception to the dominance of southern source waters in the mid and high latitude North Atlantic. Here, the >75% contribution of northern source waters dominates the interior signal and prevents cancellation of the precessional signal relative to obliquity north of ~40°N, regardless of the strength of the southern source amplitude (Figure 3). Interestingly, a weak precessional amplitude off the southwestern African coast is present for nearly any S/N ratio (Figure S2).

The area prone to cancellation of precession has a vertical structure (Figure 3 and S3, S4). This shows that most of the interior ocean is prone to cancellation, or weakening

of the precessional signal relative to obliquity, but that the cancellation is not spatially uniform.

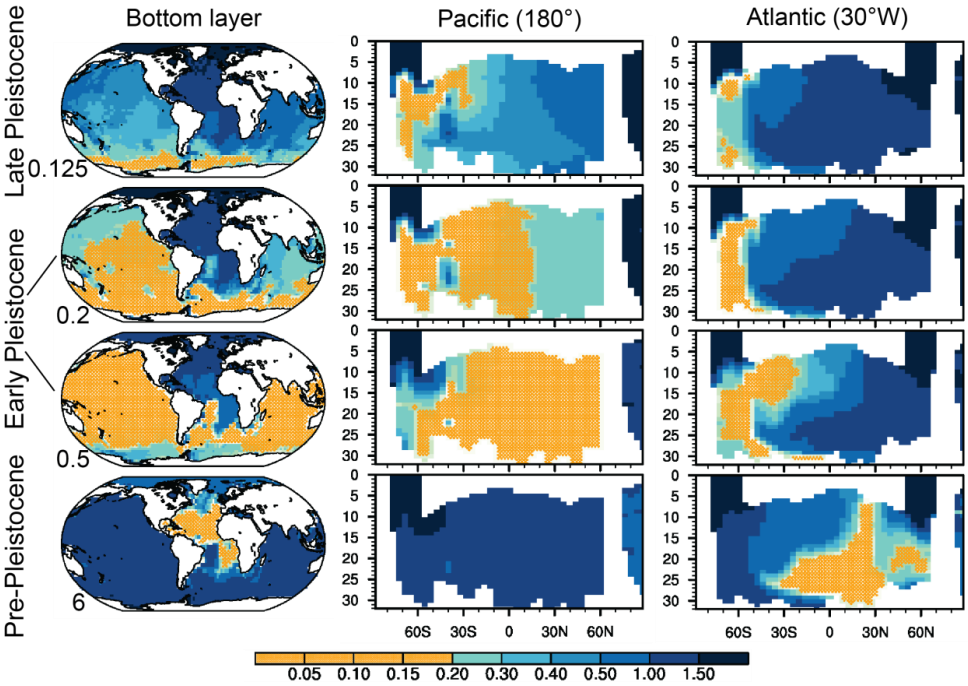

Figure 3. Ratio of precessional to obliquity spectral power, as received from the northern and southern sources (Figure 1). Data are normalized by the 41 ky obliquity power at each grid point (SI Text S1) and presented for the S/N ratios 0.125, 0.2, 0.5 and 6 as denoted to the lower left of the respective maps. The area were the spectral power is less than 0.2 is hatched (in orange) to show the potential extent of cancellation of precessional power relative to obliquity. White regions received no signal from either the northern or southern sources (Figure 1). Data are presented at the bottom layer, an Atlantic section (at 30°W) and a Pacific section (at 180°). The vertical axis of the sections is in hundreds of meters. The full range of S/N experiments are presented in Figure S2 (bottom layer), Figure S3 (Atlantic) and Figure S4 (Pacific).

We conclude that in the South Atlantic, Indian and Pacific Ocean basins, the Early Pleistocene absence of a strong precessional power in $\delta^{18}O$ records could be explained by the mixing of North Atlantic and Southern Ocean sourced deep-water masses. Moreover, this result is robust with respect to changes in circulation strength (SI Text S3 and Figure S5). If the S/N ratio decreased during the Pleistocene, as suggested by reconstructions of ice sheet volume variability, such cancellation would disappear in the Late Pleistocene - explaining the transition from the '41 ky' to the

'100 ky' worlds observed across the Mid Pleistocene Transition in the deep-sea $\delta^{18}O$ records.

3.3 Artificial sediment cores

Location is fundamental for the potential of any S/N ratio to locally reduce precessional power relative to obliquity (Figure 3). Artificial sediment cores taken at the locations of ODP849 (mid-Pacific) and DSDP607 (North Atlantic) show the asymmetry in basin response to different S/N ratios (Figure 4). The mid-Pacific ODP849 core shows cancellation for S/N ratios 0.375 and 0.5. In contrast, the North Atlantic DSDP607 core shows no weakening strong enough to explain a cancellation of the precessional signal within the Pleistocene range of S/N ratios (Figure 4). This asymmetry is a direct consequence of the circulation and water mass contributions, with the Pacific dominated by southern source waters, and the North Atlantic dominated by northern source waters (Figure S1). Cancellation is more sensitive to differences in source signal strengths (Figure 3) than to changes in circulation strength (Figure S5) – highlighting that changes in S/N ratio are decisive for the cancellation at a particular core location. The basin asymmetry reveals a possible challenge with the interpretation of global stacks of $\delta^{18}O$ records: if interpreted as a whole (Lisiecki & Raymo, 2005), any inter-basin asymmetries in spectral power sensitivity to changes in S/N ratio are not considered. The spectra of the ODP849 and DSDP607 sediment core $\delta^{18}O$ time series show the absence of precessional power at both sites during the Early Pleistocene (Figure 4). This appears to be at odds with the Antiphase Hypothesis, given that the simulated North Atlantic and mid-Pacific $\delta^{18}O$ time series respond differently to a change in S/N ratio (Figure 4). We show that cancellation of precession played a major role in the interior Pacific during the Early Pleistocene ($0.2 \leq S/N \leq 0.5$, Figure 3, Figure S2 and Figure 4).

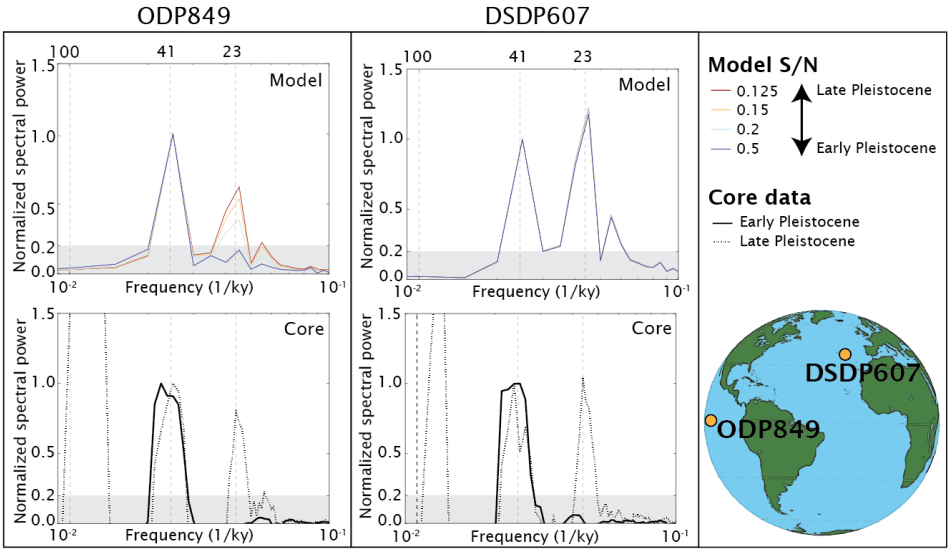

Figure 4. Power spectrum of the model sensitivity experiments and sediment core $\delta^{18}O$ data at core sites ODP849 and DSDP607, after Figure S1 in Raymo et al. (2006). Cancellation is defined at a normalized precessional power < 0.2, and is indicated by the grey area. Spectral noise is subtracted from the sediment core data in order to reveal the dominant frequencies (SI Text S4).

The Atlantic, north of ~40°N, does not exhibit cancellation for typical Pleistocene S/N ice volume ratios (S/N≤0.5, see DSDP607 in Figure 4), but this could change if the influence of southern source waters increased. Such an increased southern influence could develop through shoaling of the upper Atlantic overturning cell – increasing the volume contribution of the southern source waters to the North Atlantic. Such a shoaling and northward extension of southern source waters is indeed reconstructed for cold periods during the Pleistocene (Böhm et al., 2014). Another important factor is the potential for changes in the relative strength of the precession and obliquity signal in the two end-members. As postulated by (Raymo et al., 2006), the Antarctic ice sheet transitioned from a largely land-based ice sheet to a marine-based ice sheet at the MPT. This is not only expected to have changed the amplitude of the Southern Hemisphere signal, but also the relative strength of obliquity and precession. Typically, marine based ice sheets are expected to respond less to precession given that the relative contribution from seasonal surface melt is reduced. Thus, the absence of a pronounced precessional power in Early Pleistocene deep sea $\delta^{18}O$

records is a complex combination of multiple causes, and resolving the changes in the glacial cycles at the MPT relies on careful consideration of the location and depth of the marine sediment cores.

Our results show that precessional cancellation, expected from the Antiphase Hypothesis, occurs for all S/N ratios and persists across different circulation strengths. This causes an incomplete recording of hemispheric anti-phased glacial-interglacial cycles in the deep-sea $\delta^{18}O$ records. Accounting for this cancellation is therefore crucial for the correct interpretation of $\delta^{18}O$ records across the MPT at specific core locations as well as when stacking different deep-sea sediment records to estimate variations in global ice volume.

Acknowledgments

The authors acknowledge P. Huybers and M. Raymo for discussions that helped improve this manuscript. AM, TS, AB and EOS also want to thank the organization of Advanced Climate Dynamics Course (ACDC) for creating a nurturing and inspiring environment. This work developed from the ACDC2018 summer school and by funding of TS and EOS to visit Bergen through their Bjerknes Visiting Fellowship. AM thanks the University of Bergen for her stipend, EOS acknowledges support from the Research Council of Norway through its Centers of Excellence funding scheme (project 223272). TS was supported by U.S. National Science Foudation Climate and Large-Scale Dynamics Program (AGS-1302346) and the Ewing-Worzel Fellowship at Institute for Geophysics, University of Texas at Austin. Storage and computing resources were provided by UNINETT Sigma2 - the National Infrastructure for High Performance Computing and Data Storage in Norway (project number ns2980k). GG is supported by U.S. National Science Foundation award OCE-1536380. Data availability: The model experiment data are publicly accessible in NetCDF format at the NIRD Research Data Archive at (*DOI be added after review: currently available at http://ns2980k.web.sigma2.no/moree/TMI_results/TMI_results.tar.gz.gpg)*. The

sediment core analysis scripts can be made available upon request to AB. The TMI model version 7 is available upon request to GG.

References

Berger, A., Li, X. S., & Loutre, M. F. (1999). Modelling northern hemisphere ice volume over the last 3Ma. *Quaternary Science Reviews, 18*(1), 1-11. http://www.sciencedirect.com/science/article/pii/S027737919800033X

Berger, A., & Loutre, M. (1992). Astronomical Solutions for Paleoclimate Studies over the Last 3 Million Years. *Earth Planet. Sci. Lett., 111*(2-4), 369-382.

Böhm, E., Lippold, J., Gutjahr, M., Frank, M., Blaser, P., Antz, B., et al. (2014). Strong and deep Atlantic meridional overturning circulation during the last glacial cycle. *Nature, 517*, 73. https://doi.org/10.1038/nature14059

Chalk, T. B., Hain, M. P., Foster, G. L., Rohling, E. J., Sexton, P. F., Badger, M. P. S., et al. (2017). Causes of ice age intensification across the Mid-Pleistocene Transition. *Proceedings of the National Academy of Sciences, 114*, 13114-13119.

Clark, P. U., Archer, D., Pollard, D., Blum, J. D., Rial, J. A., Brovkin, V., et al. (2006). The middle Pleistocene transition: characteristics, mechanisms, and implications for long-term changes in atmospheric pCO_2. *Quaternary Science Reviews, 25*(23), 3150-3184. http://www.sciencedirect.com/science/article/pii/S0277379106002332

Clark, P. U., & Pollard, D. (1998). Origin of the Middle Pleistocene Transition by ice sheet erosion of regolith. *Paleoceanography, 13*(1), 1-9. https://agupubs.onlinelibrary.wiley.com/doi/abs/10.1029/97PA02660

Crowley, T. J., & Hyde, W. T. (2008). Transient nature of late Pleistocene climate variability. *Nature, 456*, 226. https://doi.org/10.1038/nature07365

Dahl-Jensen, D. (2018). Drilling for the oldest ice. *Nature Geoscience, 11*(10), 703-704. https://doi.org/10.1038/s41561-018-0241-2

De Vleeschouwer, D., Vahlenkamp, M., Crucifix, M., & Pälike, H. (2017). Alternating Southern and Northern Hemisphere climate response to astronomical forcing during the past 35 m.y. *Geology, 45*(4), 375-378. https://doi.org/10.1130/G38663.1

DeConto, R. M., & Pollard, D. (2016). Contribution of Antarctica to past and future sea-level rise. *Nature, 531*, 591. Article. https://doi.org/10.1038/nature17145

Elderfield, H., Ferretti, P., Greaves, M., Crowhurst, S., McCave, I. N., Hodell, D., & Piotrowski, A. M. (2012). Evolution of Ocean Temperature and Ice Volume Through the Mid-Pleistocene Climate Transition. *Science, 337*, 704-709.

Gebbie, G. (2012). Tracer transport timescales and the observed Atlantic-Pacific lag in the timing of the Last Termination. *Paleoceanography, 27*(3).

Gebbie, G., & Huybers, P. (2011). How is the ocean filled? *Geophysical Research Letters*.

Gebbie, G., & Huybers, P. (2012). The Mean Age of Ocean Waters Inferred from Radiocarbon Observations: Sensitivity to Surface Sources and Accounting for Mixing Histories. *Journal of Physical Oceanography, 42*(2), 291-305. https://journals.ametsoc.org/doi/abs/10.1175/JPO-D-11-043.1

Gildor, H., & Tziperman, E. (2000). Sea ice as the glacial cycles' Climate switch: role of seasonal and orbital forcing. *Paleoceanography, 15*(6), 605-615. https://agupubs.onlinelibrary.wiley.com/doi/abs/10.1029/1999PA000461

Gouretski, V., & Koltermann, K. (2004). *WOCE Global Hydrographic Climatology*. Retrieved from Hamburg, Germany:

Hasenfratz, A. P., Jaccard, S. L., Martínez-García, A., Sigman, D. M., Hodell, D. A., Vance, D., et al. (2019). The residence time of Southern Ocean surface waters and the 100,000-year ice age cycle. *Science, 363*, 1080-1084.

Hays, J. D., Imbrie, J., & Shackleton, N. J. (1976). Variations in the Earth's Orbit: Pacemaker of the Ice Ages. *Science, 194*(4270), 1121. http://science.sciencemag.org/content/194/4270/1121.abstract

Huybers, P. (2007). Glacial Variability Over the Last Two Million Years: An Extended Depth-Derived Agemodel, Continuous Obliquity Pacing, and the Pleistocene Progression. *Quaternary Science Reviews, 26*(1-2), 37-55.

Huybers, P. (2018). Matlab code to calculate Milankovitch cycles of solar insolation, modified from J. Levine (2001). UC Berkeley and Harvard, USA.

Hönisch, B., Hemming, N. G., Archer, D., Siddall, M., & McManus, J. F. (2009). Atmospheric Carbon Dioxide Concentration Across the Mid-Pleistocene Transition. *Science, 324*, 1551-1554.

Imbrie, J., Hays, J. D., Martinson, D. G., McIntyre, A., Mix, A. C., Morley, J. J., et al. (1984). The orbital theory of Pleistocene climate: support from a revised chronology of the marine $\delta^{18}O$ record. In A. Berger, J. Imbrie, J. Hays, G. Kukla, & B. Saltzman (Eds.), *Milankovitch and Climate, Part 1* (pp. 269-305). Dordrecht, The Netherlands: D. Reidel Publishing Company.

Key, R. M., Kozyr, A., Sabine, C. L., Lee, K., Wanninkhof, R., Bullister, J. L., et al. (2004). A global ocean carbon climatology: Results from Global Data Analysis Project (GLODAP). *Global Biogeochemical Cycles, 18*(4), GB4031. http://dx.doi.org/10.1029/2004GB002247

Kleiven, H. F., Jansen, E., Curry, W. B., Hodell, D. A., & Venz, K. (2003). Atlantic Ocean thermohaline circulation changes on orbital to suborbital timescales during the mid-Pleistocene. *Paleoceanography, 18*(1). https://doi.org/10.1029/2001PA000629

Legrande, A. N., & Schmidt, G. A. (2006). Global gridded data set of the oxygen isotopic composition in seawater. *Geophysical Research Letters, 33*(12), n/a-n/a.

Lisiecki, L. E., & Raymo, M. E. (2005). A Pliocene-Pleistocene stack of 57 globally distributed benthic $\delta^{18}O$ records. *Paleoceanography, 20*(1), PA1003. https://agupubs.onlinelibrary.wiley.com/doi/abs/10.1029/2004PA001071

Marinov, I., Gnanadesikan, A., Sarmiento, J. L., Toggweiler, J. R., Follows, M., & Mignone, B. K. (2008). Impact of oceanic circulation on biological carbon storage in the ocean and atmospheric pCO_2. *Global Biogeochemical Cycles, 22*(3), GB3007. http://dx.doi.org/10.1029/2007GB002958

McClymont, E. L., Sosdian, S. M., Rosell-Melé, A., & Rosenthal, Y. (2013). Pleistocene sea-surface temperature evolution: Early cooling, delayed glacial intensification, and implications for the mid-Pleistocene climate transition. *Earth-Science Reviews, 123*, 173-193. http://www.sciencedirect.com/science/article/pii/S0012825213000809

Milanković, M. (1920). *Théorie mathématique des phénomènes thermiques produits par la radiation solaire*. Paris: Gauthier-Villars et Cie.

Mudelsee, M., & Raymo, M. E. (2005). Slow dynamics of the Northern Hemisphere glaciation. *Paleoceanography, 20*(4). https://doi.org/10.1029/2005PA001153

Oppo, D. W., Gebbie, G., Huang, K.-F., Curry, W. B., Marchitto, T. M., & Pietro, K. R. (2018). Data Constraints on Glacial Atlantic Water Mass Geometry and Properties. *Paleoceanography and Paleoclimatology, 33*(9), 1013-1034. https://doi.org/10.1029/2018PA003408

Raymo, M. E., Lisiecki, L. E., & Nisancioglu, K. H. (2006). Plio-Pleistocene Ice Volume, Antarctic Climate, and the Global $\delta^{18}O$ Record. *Science, 313*, 492-495.

Raymo, M. E., & Nisancioglu, K. H. (2003). The 41 kyr world: Milankovitch's other unsolved mystery. *Paleoceanography, 18*(1).

Seki, O., Foster, G. L., Schmidt, D. N., Mackensen, A., Kawamura, K., & Pancost, R. D. (2010). Alkenone and boron-based Pliocene pCO_2 records. *Earth and Planetary Science Letters, 292*(1), 201-211. http://www.sciencedirect.com/science/article/pii/S0012821X10000816

Shakun, J. D., Raymo, M. E., & Lea, D. W. (2016). An early Pleistocene Mg/Ca-$\delta^{18}O$ record from the Gulf of Mexico: Evaluating ice sheet size and pacing in the 41-kyr world. *Paleoceanography, 31*(7), 1011-1027.

Spratt, R. M., & Lisiecki, L. E. (2016). A Late Pleistocene sea level stack. *Clim. Past, 12*(4), 1079-1092. https://www.clim-past.net/12/1079/2016/

Sutter, J., Fischer, H., Grosfeld, K., Karlsson, N. B., Kleiner, T., Van Liefferinge, B., & Eisen, O. (2019). Modelling the Antarctic Ice Sheet across the Mid Pleistocene Transition - Implications for Oldest Ice. *The Cryosphere, 13*(7), 2023-2041.

Toggweiler, J. R. (1999). Variation of atmospheric CO_2 by ventilation of the ocean's deepest water. *Paleoceanography, 14*(5), 571-588. https://doi.org/10.1029/1999PA900033

Vaughan, S., Bailey, R., & Smith, D. (2011). Detecting cycles in stratigraphic data: Spectral analysis in the presence of red noise. *Paleoceanography and Paleoclimatology, 26*(4).

Willeit, M., Ganopolski, A., Calov, R., & Brovkin, V. (2019). Mid-Pleistocene transition in glacial cycles explained by declining CO_2 and regolith removal. *Science Advances, 5*.

Willeit, M., Ganopolski, A., Calov, R., Robinson, A., & Maslin, M. (2015). The role of CO_2 decline for the onset of Northern Hemisphere glaciation. *Quaternary Science Reviews, 119*, 22-34. http://www.sciencedirect.com/science/article/pii/S0277379115001572

Supplement to Paper IV

Cancellation of the precessional cycle in benthic $\delta^{18}O$ records during the Early Pleistocene

Morée, A. L., T. Sun, A. Bretones, E.O. Straume, K. Nisancioglu, and G. Gebbie

Under review at Geophysical Research Letters

Introduction

This Supporting Information supplies the reader with additional details on Experiment design (Text S1), the TMI model (Text S2), the model experiments on circulation changes (Text S3) and the analysis of the artificial and real sediment cores (Text S4). All model output was created during the period June-August 2019 and is available in NetCDF format. A spectral analysis has been done on these output data (details in Text S1), based on which we have presented our results (e.g., Fig. 3) and drawn our conclusions.

Text S1. Experiment design.

Two main global deep water formation areas are defined, one in the North Atlantic and one in the Southern Ocean (Figure 1). At the lowest model layer, the two water masses combined account for a majority (>70%) of the surface signal at the bottom layer for 86% of the grid cells (Figure S1). The North Atlantic source and Southern Ocean source both contribute similar amounts to the Atlantic basin, while the Southern Ocean deep water dominates the Pacific basin (Figure S1).

Model forcing is the May-July (N) mean spring-summer solar insolation at 65°N and the November-January (S) mean solar insolation at 65°S, respectively (Figure 1) (Huybers, 2018; Berger & Loutre, 1992). The forcing is dominated by the obliquity of the Earth's axis and the precession of the equinoxes (~41 and ~23 ky respectively), as these have the strongest power of the Milankovitch cycles (*36*). The insolation is scaled by subtracting the mean amplitude such that the mean of the forcing is zero. The solar insolation forcing is assumed to represent the respective hemispheric seasons that drive temperature and ice sheet volume, and thereby $\delta^{18}O$. We choose a reference case (S/N=1) where the amplitude difference is similar (Figure 1). In order to explore the effects of the relative contribution (i.e. amplitude) of the Northern and Southern source waters (Figure 1), we perform a set of sensitivity experiments across a wide range of S:N relative amplitudes (namely 0.125:1, 0.15:1, 0.2:1, 0.25:1, 0.375:1,

0.5:1, 0.75:1, 1:1, 1.1:1, 1.2:1, 1.25:1, 1.5:1, 2:1, 2.5:1, 3:1, 3.5:1, 4:1, 5:1, 6:1). The model is run forward for 200 ky using a 200 y time step. The model drift after 200 ky is negligible, although the variability in the surface forcing naturally causes cyclic behavior for as long as the model is run. After 200 ky of model runtime, we calculate the spectral power of the total signal received from the northern and southern sources (i.e., Figure 1) and plot the results in normalized form (e.g., Figure 3 and Figure S2-5). The spectral analysis is done using function 'specx_anal' from NCAR Command Language (NCL), which performs a forward Fourier transformation on a given time series after de-trending. The results are normalized to the obliquity power at each location in order to show the change in relative importance of precession to obliquity per grid cell. As the total power received by each grid cell increases with increasing S/N, this method facilitates comparison across all S/N experiments.

Text S2. Model description.

We apply the global ocean Total Matrix Intercomparison (TMI) transient tracer simulation model, version 7 (Gebbie & Huybers, 2011; Gebbie & Huybers, 2012). The horizontal resolution is 4° x 4°, and the ocean is vertically resolved in 33 layers, which correspond to the 33 vertical levels off the WOCE Global Hydrographic Climatology. The solution of TMI method represents the mean water mass age at each ocean interior point as based on inverse modelling using data of pre-industrial radiocarbon, temperature, seawater $\delta^{18}O$ ($\delta^{18}O_{sw}$), PO_4^{3-}, NO_3^-, O_2 and salinity ($\delta^{18}O_{sw}$ from GISS (Legrande & Schmidt, 2006); $\Delta^{14}C$ from GLODAP (Key et al., 2004); other tracers from the WOCE Global Hydrographic Climatology (Gouretski & Koltermann, 2004). The ocean circulation in the TMI model is therefore a constant, pre-industrial vector field of mean arrival times from any surface source box (2806 potential sources) to any point in the ocean interior. TMI version 7 considers the integrated effect of the water mass contributions (the sources) to any interior water mass, while in addition allowing for transient changes in the surface boundary forcing. As we are interested in a conservative tracer in this study ($\delta^{18}O_{sw}$), this transient setup of the model is suitable

for testing the effects of variable $\delta^{18}O_{sw}$ surface forcing on interior $\delta^{18}O_{sw}$ distributions. Moreover, it is computationally efficient and thus allows for long model runs as well as sensitivity experiments.

Text S3. Estimate of the effect of circulation changes.

In order to estimate the effect of a changing circulation on our results, we randomly vary the strength of global advective and diffusive fluxes within a 50-150% range of the original (pre-industrial) strength (Figure S5). Circulation strength is varied on an irregular timescale with a mean timescale of change of ~1600 y. Differences at the bottom ocean layer are small.

Text S4. Core analysis.

The sediment cores presented in Figure 4 (DSDP607 and ODP849) show benthic $\delta^{18}O$ records of the Pleistocene as well as artificial model equivalents for these locations. P. Huybers dated the sediment records with an age model constrained by geomagnetic events (Huybers, 2007). This is fundamental as many other cores are orbitally tuned (Lisiecki & Raymo, 2005) and can therefore not be used for our type of analysis. The sampling resolution of the original dataset was at most 4 ky, which was linearly interpolated to a constant 1 ky time step in order to allow Fourier analyses. The record average between 0.7 Ma and present was then subtracted to account for the local mean offset (Huybers, 2007). We separately analyzed the two periods of interest, i.e. the Early Pleistocene (taken as 2-1.2 Ma) and the Late Pleistocene (taken as 0.8-0 Ma). The power density spectra are calculated based on the multi-taper spectral analysis Matlab routine by P. Huybers, although adapted to Python (package scipy.fftpack). For each period, the power density spectrum was best fitted with a bending power law to find the density spectrum of the noise (Vaughan et al., 2011). The power density spectrum of the noise was then subtracted to reveal the significant frequencies. As for the model results, the core spectra were normalized by the periods maximum power density of obliquity (in the 30-45 ky range).

For the artificial model cores the spectrum was based on each of the full 200 ky model runs per S/N experiment at the nearest grid cell to the DSDP607 and ODP849 cores. The spectral power was calculated using a standard discrete Fourier transformation, without any additional corrections.

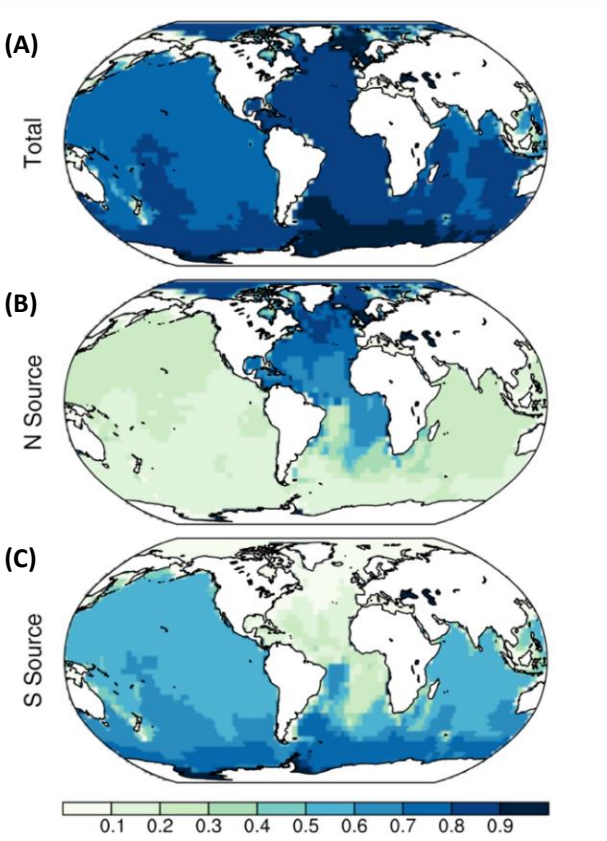

Figure S1. Volume contribution to the bottom layer of the model expressed as fraction of total grid cell volume. (A) Total contribution from northern and southern surface source regions, (B) northern source contribution, and (C) southern source contribution.

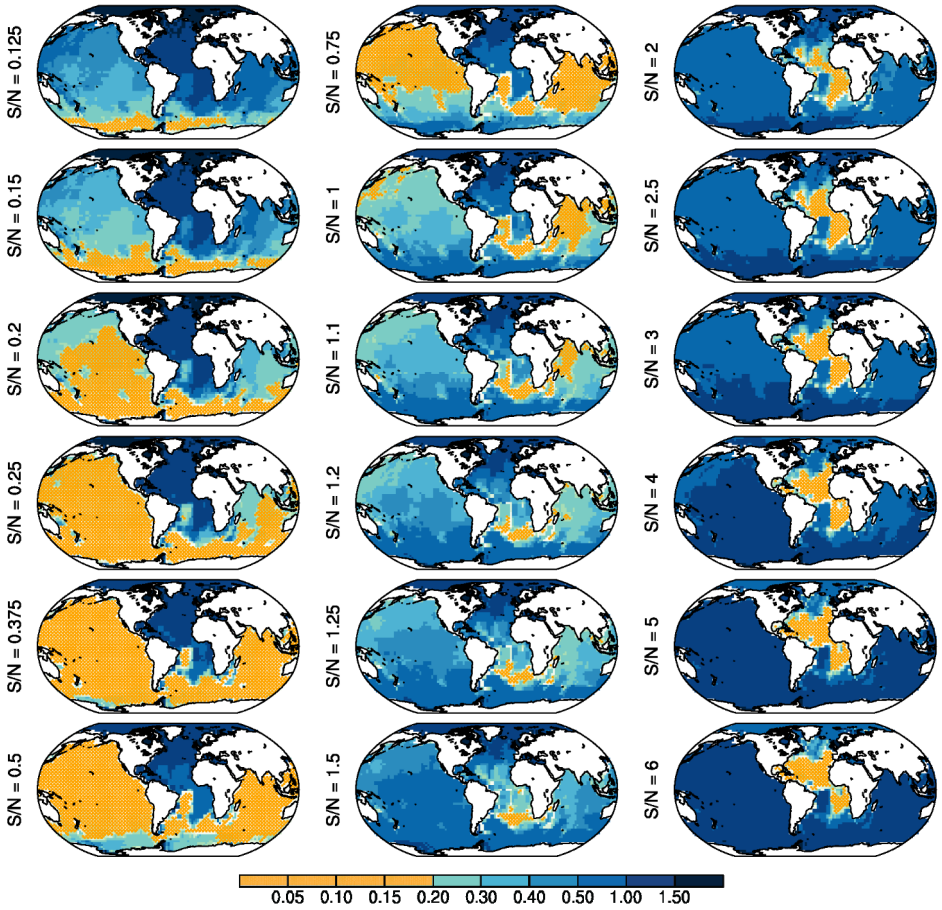

Figure S2. Bottom layer precessional power of the signal (normalized by the local 41 ky obliquity power) for all S/N experiments. A precessional power <0.2 is hatched to show the potential extent of cancellation.

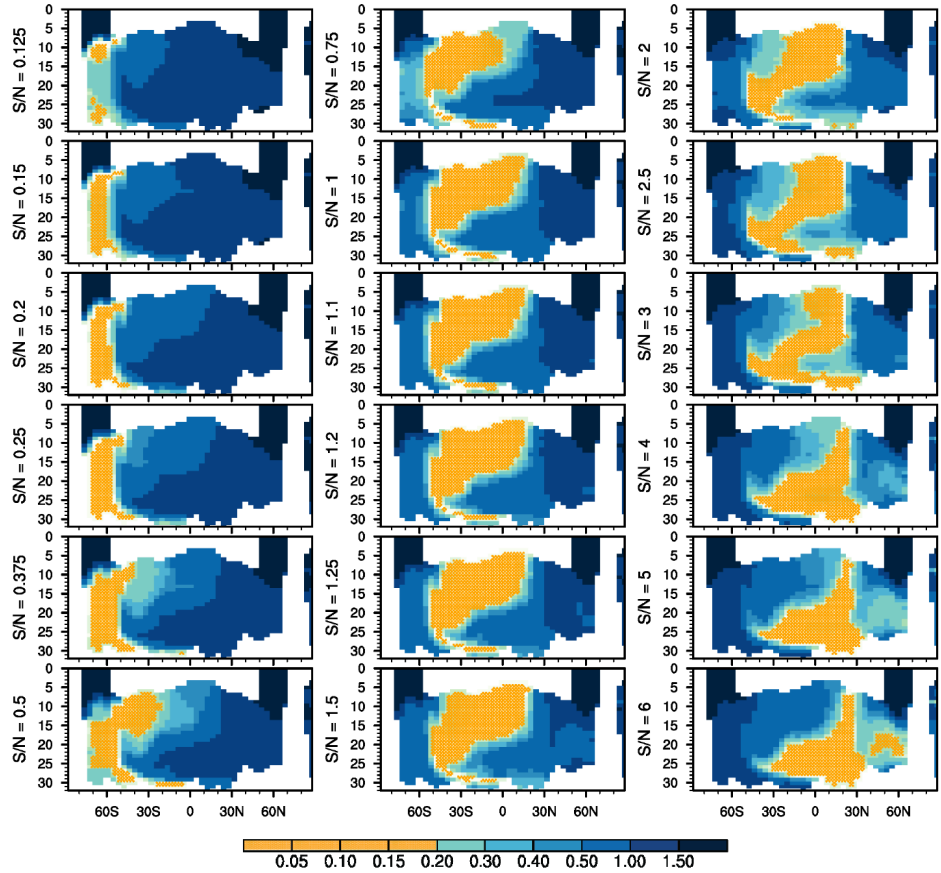

Figure S3. Atlantic (30° W) precessional power of the signal (normalized by the local 41 ky obliquity power) for all S/N experiments. A precessional power <0.2 is hatched to show the potential extent of cancellation. The vertical axis of the sections is in hundreds of meters.

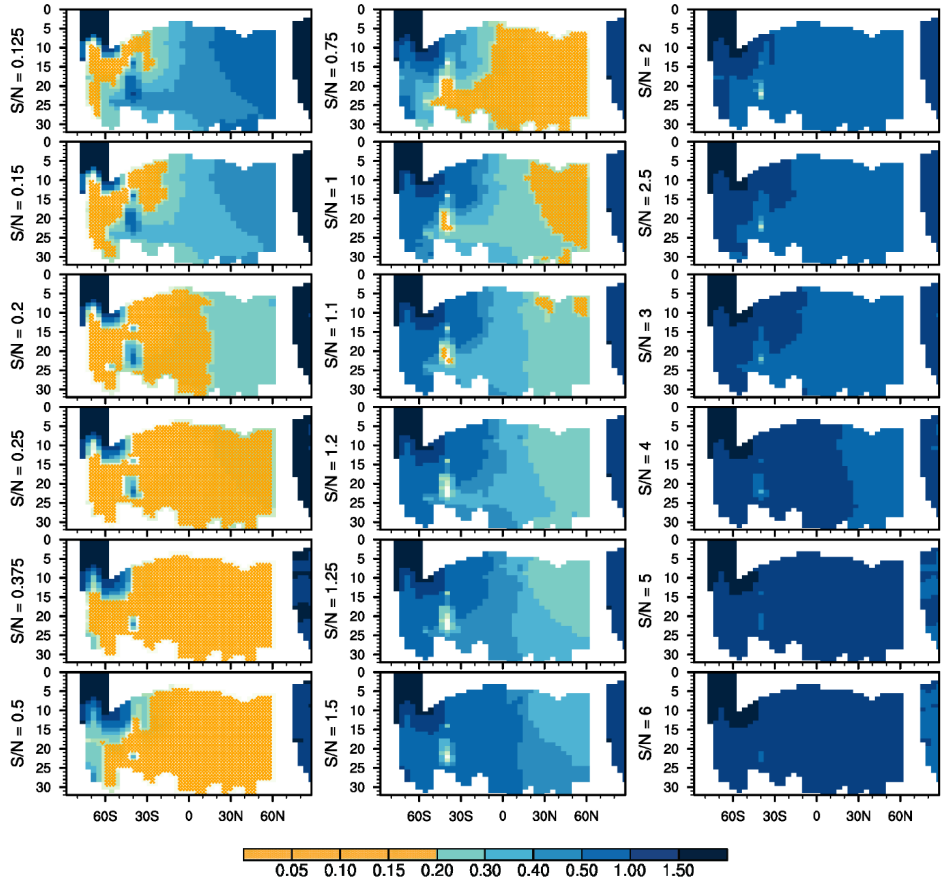

Figure S4. Pacific (180°) precessional power of the signal (normalized by the local 41 ky obliquity power) for all S/N experiments. A precessional power <0.2 is hatched to show the potential extent of cancellation. The vertical axis of the sections is in hundreds of meters.

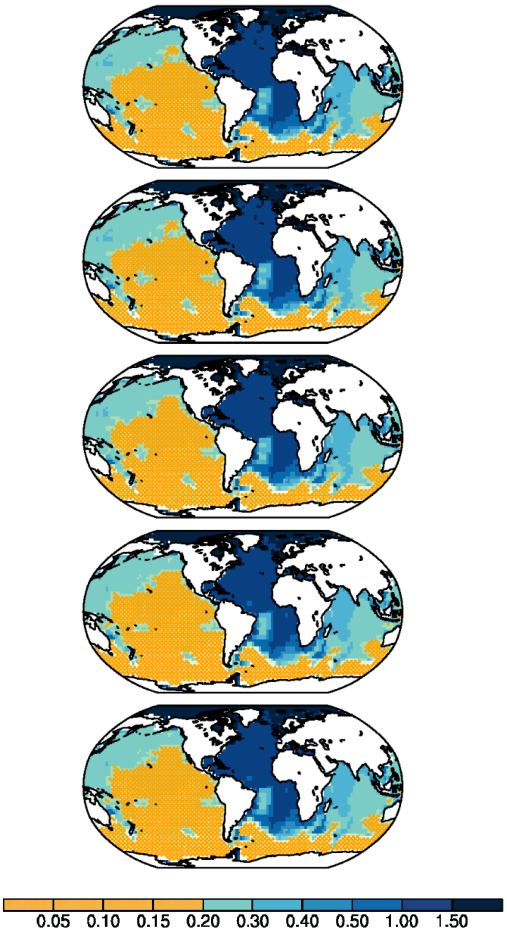

Figure S5. Five random variations of ocean circulation strength (advection and diffusion fluxes) for the S/N=0.2 experiment.

References

The references are listed in the main text following the formatting of GRL.

References of the synthesis

Abe-Ouchi, A., Saito, F., Kageyama, M., Braconnot, P., Harrison, S. P., Lambeck, K., Otto-Bliesner, B. L., Peltier, W. R., Tarasov, L., Peterschmitt, J. Y., and Takahashi, K.: Ice-sheet configuration in the CMIP5/PMIP3 Last Glacial Maximum experiments, Geoscientific Model Development, 8, 3621-3637, 10.5194/gmd-8-3621-2015, 2015.

Adkins, J. F.: The role of deep ocean circulation in setting glacial climates, Paleoceanography, 28, 539-561, 10.1002/palo.20046, 2013.

Ahn, S., Khider, D., Lisiecki, L. E., and Lawrence, C. E.: A probabilistic Pliocene–Pleistocene stack of benthic $\delta^{18}O$ using a profile hidden Markov model, Dynamics and Statistics of the Climate System, 2, 10.1093/climsys/dzx002, 2017.

Archer, D., and Maier-Reimer, E.: Effect of deep-sea sedimentary calcite preservation on atmospheric CO_2 concentration, Nature, 367, 260-263, 10.1038/367260a0, 1994.

Bauska, T. K., Baggenstos, D., Brook, E. J., Mix, A. C., Marcott, S. A., Petrenko, V. V., Schaefer, H., Severinghaus, J. P., and Lee, J. E.: Carbon isotopes characterize rapid changes in atmospheric carbon dioxide during the last deglaciation, P Natl Acad Sci USA, 113, 3465-3470, 10.1073/pnas.1513868113, 2016.

Belkin, I. M., and Gordon, A. L.: Southern Ocean fronts from the Greenwich meridian to Tasmania, Journal of Geophysical Research: Oceans, 101, 3675-3696, 10.1029/95JC02750, 1996.

Bouttes, N., Paillard, D., Roche, D. M., Brovkin, V., and Bopp, L.: Last Glacial Maximum CO_2 and $\delta^{13}C$ successfully reconciled, Geophysical Research Letters, 38, 10.1029/2010GL044499, 2011.

Braconnot, P., Harrison, S., Kageyama, M., Bartlein, P., Masson-Delmotte, V., Abe-Ouchi, A., Otto-Bliesner, B., and Zhao, Y.: Evaluation of climate models using palaeoclimatic data, Nature Climate Change, 2, 417-424, 10.1038/nclimate1456, 2012.

Broecker, W. S.: Glacial to interglacial changes in ocean chemistry, Progress in Oceanography, 11, 151-197, 10.1016/0079-6611(82)90007-6, 1982a.

Broecker, W. S.: Ocean chemistry during glacial time, Geochimica et Cosmochimica Acta, 46, 1689-1705, 10.1016/0016-7037(82)90110-7, 1982b.

Broecker, W. S., and Peng, T.-H.: Carbon Cycle: 1985 Glacial to Interglacial Changes in the Operation of the Global Carbon Cycle, Radiocarbon, 28, 309-327, 10.1017/S0033822200007414, 1986.

Broecker, W. S., and McGee, D.: The ^{13}C record for atmospheric CO_2: What is it trying to tell us?, Earth and Planetary Science Letters, 368, 175-182, 10.1016/j.epsl.2013.02.029, 2013.

Buchanan, P. J., Matear, R. J., Lenton, A., Phipps, S. J., Chase, Z., and Etheridge, D. M.: The simulated climate of the Last Glacial Maximum and insights into the global marine carbon cycle, Clim. Past, 12, 2271-2295, 10.5194/cp-12-2271-2016, 2016.

Charles, C. D., Pahnke, K., Zahn, R., Mortyn, P. G., Ninnemann, U., and Hodell, D. A.: Millennial scale evolution of the Southern Ocean chemical divide, Quaternary Science Reviews, 29, 399-409, 10.1016/j.quascirev.2009.09.021, 2010.

Ciais, P., Sabine, C., Bala, G., Bopp, L., Brovkin, V., Canadell, J., Chhabra, A., De Fries, R., Galloway, J., Heimann, M., Jones, C., Le Quéré, C., Myneni, R. B., Piao, S., and Thornton, P.: Carbon and Other Biogeochemical Cycles. Climate Change 2013: The Physical Science Basis. Contribution of Working Group I to the Fifth Assessment Report of the Intergovernmental Panel on Climate Change, in, edited by: Stocker, T. F., Qin, D., Plattner, G.-K., Tignor, M., Allen, S. K., Boschung, J., Nauels, A., Xia, Y., Bex, V., and Midgley, P. M., Cambridge University Press, Cambridge, United Kingdom and New York, NY, US, 2013.

Collins, M., R. , Knutti, J. A., J.-L. Dufresne, T. Fichefet, P. Friedlingstein, X. Gao, W.J. Gutowski, T. Johns, G., Krinner, M. Shongwe, C. Tebaldi, Weaver, A. J., and Wehner, M.: Long-term Climate Change: Projections, Commitments and Irreversibility. Climate Change 2013: The Physical Science Basis. Contribution of Working Group I to the Fifth Assessment Report of the Intergovernmental Panel on Climate Change, in, edited by: Stocker, T. F., Qin, D., Plattner, G.-K., Tignor, M., Allen, S. K., Boschung, J., Nauels, A., Xia, Y., Bex, V., and Midgley, P. M., Cambridge University Press, Cambridge, United Kingdom and New York, NY, US, 2013.

Coplen, T. B.: Reporting of stable hydrogen, carbon, and oxygen isotopic abundances, Geothermics, 24, 707-712, 10.1016/0375-6505(95)00024-0, 1995.

Curry, W. B., and Oppo, D. W.: Glacial water mass geometry and the distribution of $\delta^{13}C$ of ΣCO_2 in the western Atlantic Ocean, Paleoceanography, 20, PA1017, 10.1029/2004PA001021, 2005.

Donohue, K. A., Tracey, K. L., Watts, D. R., Chidichimo, M. P., and Chereskin, T. K.: Mean Antarctic Circumpolar Current transport measured in Drake Passage, Geophysical Research Letters, 43, 11,760-711,767, 10.1002/2016GL070319, 2016.

Downes, S. M., Farneti, R., Uotila, P., Griffies, S. M., Marsland, S. J., Bailey, D., Behrens, E., Bentsen, M., Bi, D., Biastoch, A., Böning, C., Bozec, A., Canuto, V. M., Chassignet, E., Danabasoglu, G., Danilov, S., Diansky, N., Drange, H., Fogli, P. G., Gusev, A., Howard, A., Ilicak, M., Jung, T., Kelley, M., Large, W. G., Leboissetier, A., Long, M., Lu, J., Masina, S., Mishra, A., Navarra, A., George Nurser, A. J., Patara, L., Samuels, B. L., Sidorenko, D., Spence, P., Tsujino, H., Wang, Q., and Yeager, S. G.: An assessment of Southern Ocean water masses and sea ice during 1988–2007 in a suite of interannual CORE-II simulations, Ocean Modelling, 94, 67-94, 10.1016/j.ocemod.2015.07.022, 2015.

Eggleston, S., Schmitt, J., Bereiter, B., Schneider, R., and Fischer, H.: Evolution of the stable carbon isotope composition of atmospheric CO_2 over the last glacial cycle, Paleoceanography, 31, 434-452, 10.1002/2015PA002874, 2016.

Eide, M., Olsen, A., Ninnemann, U. S., and Johannessen, T.: A global ocean climatology of preindustrial and modern ocean $\delta^{13}C$, Global Biogeochemical Cycles, 31, 515-534, 10.1002/2016GB005473, 2017.

Elderfield, H., Ferretti, P., Greaves, M., Crowhurst, S., McCave, I. N., Hodell, D., and Piotrowski, A. M.: Evolution of Ocean Temperature and Ice Volume Through the Mid-Pleistocene Climate Transition, Science, 337, 704-709, 10.1126/science.1221294, 2012.

EPICA Project Members: Eight glacial cycles from an Antarctic ice core, Nature, 429, 623-628, 10.1038/nature02599, 2004.

Ferrari, R., Jansen, M. F., Adkins, J. F., Burke, A., Stewart, A. L., and Thompson, A. F.: Antarctic sea ice control on ocean circulation in present and glacial climates, Proceedings of the National Academy of Sciences, 111, 8753, 10.1073/pnas.1323922111, 2014.

Ganopolski, A., and Brovkin, V.: Simulation of climate, ice sheets and CO_2 evolution during the last four glacial cycles with an Earth system model of intermediate complexity, Clim. Past, 13, 1695-1716, 10.5194/cp-13-1695-2017, 2017.

Gebbie, G., and Huybers, P. J.: The Mean Age of Ocean Waters Inferred from Radiocarbon Observations: Sensitivity to Surface Sources and Accounting for Mixing Histories, Journal of Physical Oceanography, 42, 10.1175/JPO-D-11-043.1, 2012.

Gruber, N., Keeling, C. D., Bacastow, R. B., Guenther, P. R., Lueker, T. J., Wahlen, M., Meijer, H. A. J., Mook, W. G., and Stocker, T. F.: Spatiotemporal patterns of carbon-13 in the global surface oceans and the oceanic suess effect, Global Biogeochemical Cycles, 13, 307-335, 10.1029/1999GB900019, 1999.

Gruber, N., Landschützer, P., and Lovenduski, N. S.: The Variable Southern Ocean Carbon Sink, Annual Review of Marine Science, 11, 159-186, 10.1146/annurev-marine-121916-063407, 2019.

Hauck, J., Völker, C., Wolf-Gladrow, D. A., Laufkötter, C., Vogt, M., Aumont, O., Bopp, L., Buitenhuis, E. T., Doney, S. C., Dunne, J., Gruber, N., Hashioka, T., John, J., Quéré, C. L., Lima, I. D., Nakano, H., Séférian, R., and Totterdell, I.: On the Southern Ocean CO_2 uptake and the role of the biological carbon pump in the 21st century, Global Biogeochemical Cycles, 29, 1451-1470, 10.1002/2015GB005140, 2015.

Hays, J. D., Imbrie, J., and Shackleton, N. J.: Variations in the Earth's Orbit: Pacemaker of the Ice Ages, Science, 194, 1121, 10.1126/science.194.4270.1121, 1976.

Heinze, C., Maier-Reimer, E., and Winn, K.: Glacial pCO_2 Reduction by the World Ocean: Experiments with the Hamburg Carbon Cycle Model, Paleoceanography, 6, 395-430, 10.1029/91PA00489, 1991.

Heinze, C., and Maier-Reimer, E.: The Hamburg Oceanic Carbon Cycle Circulation Model Version ''HAMOCC2s'' for long time integrations, Max-Planck-Institut für Meteorologie, Hamburg REPORT 20, 1999.

Heinze, C., Maier-Reimer, E., Winguth, A. M. E., and Archer, D.: A global oceanic sediment model for long-term climate studies, Global Biogeochemical Cycles, 13, 221-250, 10.1029/98GB02812, 1999.

Heinze, C., Hoogakker, B. A. A., and Winguth, A.: Ocean carbon cycling during the past 130 000 years – a pilot study on inverse palaeoclimate record modelling, Clim. Past, 12, 1949-1978, 10.5194/cp-12-1949-2016, 2016.

Heinze, C., Eyring, V., Friedlingstein, P., Jones, C., Balkanski, Y., Collins, W., Fichefet, T., Gao, S., Hall, A., Ivanova, D., Knorr, W., Knutti, R., Löw, A., Ponater, M., Schultz, M. G., Schulz, M., Siebesma, P., Teixeira, J., Tselioudis, G., and Vancoppenolle, M.: ESD Reviews: Climate feedbacks in the Earth system and prospects for their evaluation, Earth Syst. Dynam., 10, 379-452, 10.5194/esd-10-379-2019, 2019.

Hilting, A. K., Kump, L. R., and Bralower, T. J.: Variations in the oceanic vertical carbon isotope gradient and their implications for the Paleocene-Eocene biological pump, Paleoceanography, 23, PA3222, 10.1029/2007PA001458, 2008.

Imbrie, J., Hays, J. D., Martinson, D. G., McIntyre, A., Mix, A. C., Morley, J. J., Pisias, N. G., Prell, W. L., and Shackleton, N. J.: The orbital theory of Pleistocene climate: support from a revised chronology of the marine $\delta^{18}O$ record, in: Milankovitch and Climate, Part 1, edited by: Berger, A., Imbrie, J., Hays, J., Kukla, G., and Saltzman, B., D. Reidel Publishing Company, Dordrecht, The Netherlands, 269-305, 1984.

IPCC, 2014: Climate Change 2014: Synthesis Report. Contribution of Working Groups I, II and III to the Fifth Assessment Report of the Intergovernmental Panel on Climate Change [Core Writing Team, R.K. Pachauri and L.A. Meyer (eds.)]. IPCC, Geneva, Switzerland, 151 pp.

Ito, T., and Follows, M. J.: Preformed Phosphate, Soft Tissue Pump and Atmospheric CO_2, Journal of Marine Research, 63, 813-839, 10.1357/0022240054663231, 2005.

Jaccard, S. L., Galbraith, E. D., Sigman, D. M., Haug, G. H., Francois, R., Pedersen, T. F., Dulski, P., and Thierstein, H. R.: Subarctic Pacific evidence for a glacial deepening of the oceanic respired carbon pool, Earth and Planetary Science Letters, 277, 156-165, 10.1016/j.epsl.2008.10.017, 2009.

Jansen, M. F.: Glacial ocean circulation and stratification explained by reduced atmospheric temperature, Proceedings of the National Academy of Sciences, 114, 45-50, 10.1073/pnas.1610438113, 2017.

Jeltsch-Thömmes, A., Battaglia, G., Cartapanis, O., Jaccard, S. L., and Joos, F.: Low terrestrial carbon storage at the Last Glacial Maximum: constraints from multi-proxy data, Clim. Past, 15, 849-879, 10.5194/cp-15-849-2019, 2019.

Lambert, F., Tagliabue, A., Shaffer, G., Lamy, F., Winckler, G., Farias, L., Gallardo, L., and De Pol-Holz, R.: Dust fluxes and iron fertilization in Holocene and Last Glacial Maximum climates. In: Supplement to: Lambert, F et al. (2015): Dust fluxes and iron fertilization in Holocene and Last Glacial Maximum climates. Geophysical Research Letters, 42(14), 6014-6023, 10.1002/2015GL064250, PANGAEA, 2015.

Landschützer, P., Gruber, N., and Bakker, D. C. E.: An observation-based global monthly gridded sea surface pCO_2 product from 1982 onward and its monthly climatology (NCEI Accession 0160558) [2019-03-27]. NOAA National Centers for Environmental Information, 2017.

Large, W. G., and Yeager, S. G.: Diurnal to decadal global forcing for ocean and sea-ice models: the data sets and flux climatologies, Tech. Note NCAR/TN-460+STR. National Center of Atmospheric Research, Boulder, Colorado, USA, 2004.

Laufkötter, C., and Gruber, N.: Will marine productivity wane?, Science, 359, 1103, 10.1126/science.aat0795, 2018.

Le Quéré, C., Andrew, R. M., Friedlingstein, P., Sitch, S., Hauck, J., Pongratz, J., Pickers, P. A., Korsbakken, J. I., Peters, G. P., Canadell, J. G., Arneth, A., Arora, V. K., Barbero, L., Bastos, A., Bopp, L., Chevallier, F., Chini, L. P., Ciais, P., Doney, S. C., Gkritzalis, T., Goll, D. S., Harris, I., Haverd, V., Hoffman, F. M., Hoppema, M., Houghton, R. A., Hurtt, G., Ilyina, T., Jain, A. K., Johannessen, T., Jones, C. D., Kato, E., Keeling, R. F., Goldewijk, K. K., Landschützer, P., Lefèvre, N., Lienert, S., Liu, Z., Lombardozzi, D., Metzl, N., Munro, D. R., Nabel, J. E. M. S., Nakaoka, S. I., Neill, C., Olsen, A., Ono, T., Patra, P., Peregon, A., Peters, W., Peylin, P., Pfeil, B., Pierrot, D., Poulter, B., Rehder, G., Resplandy, L., Robertson, E., Rocher, M., Rödenbeck, C., Schuster, U., Schwinger, J., Séférian, R., Skjelvan, I., Steinhoff, T., Sutton, A., Tans, P. P., Tian, H., Tilbrook, B., Tubiello, F. N., van der Laan-Luijkx, I. T., van der Werf, G. R., Viovy, N., Walker, A. P., Wiltshire, A. J., Wright, R., Zaehle, S., and Zheng, B.: Global Carbon Budget 2018, Earth Syst. Sci. Data, 10, 2141-2194, 10.5194/essd-10-2141-2018, 2018.

Lenton, A., Tilbrook, B., Law, R. M., Bakker, D., Doney, S. C., Gruber, N., Ishii, M., Hoppema, M., Lovenduski, N. S., Matear, R. J., McNeil, B. I., Metzl, N., Fletcher, S. E. M., Monteiro, P. M. S., Rödenbeck, C., Sweeney, C., and Takahashi, T.: Sea–air CO_2 fluxes in the Southern Ocean for the period 1990–2009, Biogeosciences, 10, 4037-4054, 10.5194/bg-10-4037-2013, 2013.

Levy, M., Bopp, L., Karleskind, P., Resplandy, L., Ethe, C., and Pinsard, F.: Physical pathways for carbon transfers between the surface mixed layer and the ocean interior, Global Biogeochemical Cycles, 27, 1001-1012, 10.1002/gbc.20092, 2013.

Lisiecki, L. E., and Raymo, M. E.: A Pliocene-Pleistocene stack of 57 globally distributed benthic $\delta^{18}O$ records, Paleoceanography, 20, PA1003, 10.1029/2004pa001071, 2005.

Lourantou, A., Lavrič Jošt, V., Köhler, P., Barnola, J. M., Paillard, D., Michel, E., Raynaud, D., and Chappellaz, J.: Constraint of the CO_2 rise by new atmospheric carbon isotopic measurements during the last deglaciation, Global Biogeochemical Cycles, 24, 10.1029/2009GB003545, 2010.

Lynch-Stieglitz, J., Stocker, T. F., Broecker, W. S., and Fairbanks, R. G.: The influence of air-sea exchange on the isotopic composition of oceanic carbon: Observations and modeling, Global Biogeochemical Cycles, 9, 653-665, 10.1029/95GB02574, 1995.

Lüthi, D., Le Floch, M., Bereiter, B., Blunier, T., Barnola, J.-M., Siegenthaler, U., Raynaud, D., Jouzel, J., Fischer, H., Kawamura, K., and Stocker, T. F.: High-resolution carbon dioxide concentration record 650,000–800,000 years before present, Nature, 453, 379-382, 10.1038/nature06949, 2008.

Marchitto, T. M., and Broecker, W. S.: Deep water mass geometry in the glacial Atlantic Ocean: A review of constraints from the paleonutrient proxy Cd/Ca, Geochemistry, Geophysics, Geosystems, 7, 10.1029/2006GC001323, 2006.

Marinov, I., Gnanadesikan, A., Toggweiler, J. R., and Sarmiento, J. L.: The Southern Ocean biogeochemical divide, Nature, 441, 964-967, 10.1038/nature04883, 2006.

Marshall, J., and Speer, K.: Closure of the meridional overturning circulation through Southern Ocean upwelling, Nature Geoscience, 5, 171-180, 10.1038/ngeo1391, 2012.

Martin, J. H., Fitzwater, S. E., and Gordon, R. M.: Iron deficiency limits phytoplankton growth in Antarctic waters, Global Biogeochemical Cycles, 4, 5-12, 10.1029/GB004i001p00005, 1990.

Marzocchi, A., and Jansen, M. F.: Connecting Antarctic sea ice to deep-ocean circulation in modern and glacial climate simulations, Geophysical Research Letters, 44, 6286-6295, 10.1002/2017GL073936, 2017.

McClymont, E. L., Sosdian, S. M., Rosell-Melé, A., and Rosenthal, Y.: Pleistocene sea-surface temperature evolution: Early cooling, delayed glacial intensification, and implications for the mid-Pleistocene climate transition, Earth-Science Reviews, 123, 173-193, 10.1016/j.earscirev.2013.04.006, 2013.

Menviel, L., Mouchet, A., Meissner, K. J., Joos, F., and England, M. H.: Impact of oceanic circulation changes on atmospheric $\delta^{13}CO_2$, Global Biogeochemical Cycles, 29, 1944-1961, 10.1002/2015GB005207, 2015.

Milanković, M.: Théorie mathématique des phénomènes thermiques produits par la radiation solaire, Gauthier-Villars et Cie, Paris, 1-633 pp., 1920.

Mongwe, N. P., Vichi, M., and Monteiro, P. M. S.: The seasonal cycle of pCO_2 and CO_2 fluxes in the Southern Ocean: diagnosing anomalies in CMIP5 Earth system models, Biogeosciences, 15, 2851-2872, 10.5194/bg-15-2851-2018, 2018.

Moy, A. D., Palmer, M. R., Howard, W. R., Bijma, J., Cooper, M. J., Calvo, E., Pelejero, C., Gagan, M. K., and Chalk, T. B.: Varied contribution of the Southern Ocean to deglacial atmospheric CO_2 rise, Nature Geoscience, 10.1038/s41561-019-0473-9, 2019.

Muglia, J., and Schmittner, A.: Glacial Atlantic overturning increased by wind stress in climate models, Geophysical Research Letters, 42, 9862-9868, 10.1002/2015gl064583, 2015.

NOAA ESRL- Global Monitoring Division: Trends in Atmospheric Carbon Dioxide: https://www.esrl.noaa.gov/gmd/ccgg/trends/global.html, access: nov-13, 2019.

Nowicki, S. M. J., Payne, A., Larour, E., Seroussi, H., Goelzer, H., Lipscomb, W., Gregory, J., Abe-Ouchi, A., and Shepherd, A.: Ice Sheet Model Intercomparison Project (ISMIP6) contribution to CMIP6, Geosci. Model Dev., 9, 4521-4545, 10.5194/gmd-9-4521-2016, 2016.

Oppo, D. W., Gebbie, G., Huang, K.-F., Curry, W. B., Marchitto, T. M., and Pietro, K. R.: Data Constraints on Glacial Atlantic Water Mass Geometry and Properties, Paleoceanography and Paleoclimatology, 33, 1013-1034, 10.1029/2018PA003408, 2018.

Peltier, W. R., and Fairbanks, R. G.: Global glacial ice volume and Last Glacial Maximum duration from an extended Barbados sea level record, Quaternary Science Reviews, 25, 3322-3337, 10.1016/j.quascirev.2006.04.010, 2006.

Peterson, C. D., Lisiecki, L. E., and Stern, J. V.: Deglacial whole-ocean $\delta^{13}C$ change estimated from 480 benthic foraminiferal records, Paleoceanography, 29, 549-563, 10.1002/2013PA002552, 2014.

Primeau, F. W., Holzer, M., and DeVries, T.: Southern Ocean nutrient trapping and the efficiency of the biological pump, Journal of Geophysical Research: Oceans, 118, 2547-2564, 10.1002/jgrc.20181, 2013.

Rae, J. W. B., and Broecker, W.: What fraction of the Pacific and Indian oceans' deep water is formed in the Southern Ocean?, Biogeosciences, 15, 3779-3794, 10.5194/bg-15-3779-2018, 2018.

Rhein, M., Rintoul, S. R., Aoki, S., Campos, E., Chambers, D., Feely, R. A., Gulev, S., Johnson, G. C., Josey, S. A., Kostianoy, A., Mauritzen, C., Roemmich, D., Talley, L. D., and Wang, F.: Observations: Ocean, in: Climate Change 2013: The Physical Science Basis. Contribution of Working Group I to the Fifth Assessment Report of the Intergovernmental Panel on Climate Change, edited by: Stocker, T. F., Qin, D., Plattner, G.-K., Tignor, M., Allen, S. K., Boschung, J., Nauels, A., Xia, Y., Bex, V., and Midgley, P. M., Cambridge University Press, Cambridge, United Kingdom and New York, NY, USA, 2013.

Roth, R., Ritz, S. P., and Joos, F.: Burial-nutrient feedbacks amplify the sensitivity of atmospheric carbon dioxide to changes in organic matter remineralisation, Earth Syst Dynam, 5, 321-343, 10.5194/esd-5-321-2014, 2014.

Sarmiento, J. L., Gruber, N., Brzezinski, M. A., and Dunne, J. P.: High-latitude controls of thermocline nutrients and low latitude biological productivity, Nature, 427, 56-60, 10.1038/nature02127, 2004.

Sarmiento, J. L., and Gruber, N.: Ocean biogeochemical dynamics, Princeton University Press Princeton, 2006.

Schmittner, A., Gruber, N., Mix, A. C., Key, R. M., Tagliabue, A., and Westberry, T. K.: Biology and air-sea gas exchange controls on the distribution of carbon isotope ratios ($\delta^{13}C$) in the ocean, Biogeosciences, 10, 5793-5816, 10.5194/bg-10-5793-2013, 2013.

Schmittner, A., Bostock, H. C., Cartapanis, O., Curry, W. B., Filipsson, H. L., Galbraith, E. D., Gottschalk, J., Herguera, J. C., Hoogakker, B., Jaccard, S. L., Lisiecki, L. E., Lund, D. C., Martínez-Méndez, G., Lynch-Stieglitz, J., Mackensen, A., Michel, E., Mix, A. C., Oppo, D. W., Peterson, C. D., Repschläger, J., Sikes, E. L., Spero, H. J., and Waelbroeck, C.: Calibration of the carbon isotope composition ($\delta^{13}C$) of benthic foraminifera, Paleoceanography, 32, 512-530, 10.1002/2016PA003072, 2017.

Schwinger, J., Goris, N., Tjiputra, J. F., Kriest, I., Bentsen, M., Bethke, I., Ilicak, M., Assmann, K. M., and Heinze, C.: Evaluation of NorESM-OC (versions 1 and 1.2), the ocean carbon-cycle stand-alone configuration of the Norwegian Earth System Model (NorESM1), Geosci. Model Dev., 9, 2589-2622, 10.5194/gmd-9-2589-2016, 2016.

Shackleton, N. J., and Hall, M. A.: Oxygen and carbon isotope stratigraphy of Deep Sea Drilling Project Hole 552A: Plio-Pleistocene glacial history. Roberts, D., and Schnittker, D. (Eds.), Initial Reports of the Deep Sea Drilling Project, U.S. Govt. Printing Office, Washington 1984.

Sigman, D. M., Hain, M. P., and Haug, G. H.: The polar ocean and glacial cycles in atmospheric CO_2 concentration, Nature, 466, 47, 10.1038/nature09149, 2010.

Speer, K., Rintoul, S. R., and Sloyan, B.: The Diabatic Deacon Cell, Journal of Physical Oceanography, 30, 3212-3222, 10.1175/1520-0485, 2000.

Tagliabue, A., Bowie, A. R., Boyd, P. W., Buck, K. N., Johnson, K. S., and Saito, M. A.: The integral role of iron in ocean biogeochemistry, Nature, 543, 51-59, 10.1038/nature21058, 2017.

Takahashi, T., Sweeney, C., Hales, B., Chipman, D. W., Newberger, T., Goddard, J. G., Iannuzzi, R. A., and Sutherland, S. C.: The changing carbon cycle in the Southern Ocean, Oceanography, 25, 26-37, 10.5670/oceanog.2012.71, 2012.

Tamsitt, V., Drake, H. F., Morrison, A. K., Talley, L. D., Dufour, C. O., Gray, A. R., Griffies, S. M., Mazloff, M. R., Sarmiento, J. L., Wang, J., and Weijer, W.: Spiraling pathways of global deep waters to the surface of the Southern Ocean, Nature Communications, 8, 172, 10.1038/s41467-017-00197-0, 2017.

Tjiputra, J. F., Schwinger, J., Bentsen, M., Morée, A. L., Gao, S., Bethke, I., Heinze, C., Goris, N., Gupta, A., He, Y., Olivié, D., Seland, Ø., and Schulz, M.: Ocean biogeochemistry in the Norwegian Earth System Model version 2 (NorESM2), Geosci. Model Dev. Discuss., 2020, 1-64, 10.5194/gmd-2019-347, 2020.

Toggweiler, J. R.: Variation of atmospheric CO_2 by ventilation of the ocean's deepest water, Paleoceanography, 14, 571-588, 10.1029/1999PA900033, 1999.

Umling, N. E., Thunell, R. C., and Bizimis, M.: Deepwater Expansion and Enhanced Remineralization in the Eastern Equatorial Pacific During the Last Glacial Maximum, Paleoceanography and Paleoclimatology, 33, 563-578, 10.1029/2017PA003221, 2018.

Volk, T., and Hoffert, M. I.: Ocean Carbon Pumps: Analysis of Relative Strengths and Efficiencies in Ocean-Driven Atmospheric CO_2 Changes, in: The Carbon Cycle and Atmospheric CO_2: Natural Variations Archean to Present, American Geophysical Union, 99-110, 1985.

Watson, A. J., and Naveira Garabato, A. C.: The role of Southern Ocean mixing and upwelling in glacial-interglacial atmospheric CO_2 change, Tellus B: Chemical and Physical Meteorology, 58, 73-87, 10.1111/j.1600-0889.2005.00167.x, 2006.

Weber, S. L., Drijfhout, S. S., Abe-Ouchi, A., Crucifix, M., Eby, M., Ganopolski, A., Murakami, S., Otto-Bliesner, B., and Peltier, W. R.: The modern and glacial overturning circulation in the Atlantic ocean in PMIP coupled model simulations, Clim. Past, 3, 51-64, 10.5194/cp-3-51-2007, 2007.

Zeebe, R., and Wolf-Gladrow, D.: CO_2 in Seawater: Equilibrium, Kinetics, Isotopes, Elsevier Oceanography Series, edited by: Halpern, D., Elsevier Science B.V., Amsterdam, The Netherlands, 346 pp., 2001.

Zhang, J., Quay, P. D., and Wilbur, D. O.: Carbon isotope fractionation during gas-water exchange and dissolution of CO_2, Geochimica et Cosmochimica Acta, 59, 107-114, 10.1016/0016-7037(95)91550-D, 1995.

Zhang, Y. G., Pearson, A., Benthien, A., Dong, L., Huybers, P., Liu, X., and Pagani, M.: Refining the alkenone-pCO_2 method I: Lessons from the Quaternary glacial cycles, Geochimica et Cosmochimica Acta, 260, 177-191, 10.1016/j.gca.2019.06.032, 2019.

Abbreviations

AABW - Antarctic Bottom Water

ACC - Antarctic Circumpolar Current

CMIP - Coupled Model Intercomparison Project

CORE - Atmospheric forcing for ocean models (Large and Yeager, 2004)

DIC - Dissolved Inorganic Carbon

HAMOCC2s - Hamburg Oceanic Carbon Cycle Circulation Model Version 2s (Heinze and Maier-Reimer, 1999; Heinze et al., 2016)

LGM - Last Glacial Maximum

LGM-PI - LGM minus PI

MPT - Mid-Pleistocene Transition

NorESM - Norwegian Earth System Model

NorESM-OC - Stand-alone ocean carbon-cycle configuration of the Norwegian Earth System Model version 1.2 (Schwinger et al., 2016)

pCO_2^{atm} - Atmospheric pCO_2

PI - Pre-Industrial

PMIP - Paleoclimate Modelling Intercomparison Project

POC - Particulate Organic Carbon

SO - Southern Ocean

SSW - Southern Source Water

TMI - Total Matrix Intercomparison model version 7 (Gebbie and Huybers, 2012)

$\delta^{13}C_{DIC}$ - $\delta^{13}C$ of DIC, also denoted as $\delta^{13}C$

Graphic design: Communication Division, UiB / Print: Skipnes Kommunikasjon AS

uib.no

ISBN: 9788230847015 (print)
9788230847077 (PDF)